The Dissertation Committee for Raiyan Tripti Zaman
Certifies that this is the approved version of the following dissertation:

Efficacy of Hyper-osmotic Agent (100% Anhydrous Glycerol) in Tissue and Light-activated Micro-pattern Drug Delivery Device in *In Vivo* Rabbit Eye

Committee:

Henry G. Rylander, Supervisor

Ashley J. Welch

Thomas E. Milner

Xiaojing Zhang

Gracie Vargas

Efficacy of Hyper-osmotic Agent (100% Anhydrous Glycerol) in Tissue and Light-activated Micro-pattern Drug Delivery Device in *In Vivo* Rabbit Eye

by

Raiyan Tripti Zaman, BSE; MSE

Dissertation

Presented to the Faculty of the Graduate School of

The University of Texas at Austin

in Partial Fulfillment

of the Requirements

for the Degree of

Doctor of Philosophy

The University of Texas at Austin
May 2011

Dedication

To my mother Mahjuza Khanam, father Mohd. Amin Uz Zaman, and Grandfather Emdad Ali whose unconditional love, support, and prayers made it possible for me to make it as far as I have and who always told me that I could achieve anything if I put my mind to.

Acknowledgements

The celebrated cultural anthropologist Margaret Meade once admonished: "Never doubt that a small group of thoughtful, committed citizens can change the world…indeed it's the only thing that ever has". As I sit and write, sequestered many thousands of miles away from home in the comforts of American life, there is no doubt in my mind that I owe it to the rest of the world to become much more than a researcher. I used to pass many hours visiting the tiny hospital in Madhpur in my native Bangladesh. This hospital, which was named after my late grandmother, Gul Nahar was a remote gem of a healthcare institution that provided free medicine and primary care to poor mothers and their children. My frequent visits to this hospital taught me to never shrink from illness and injury, but rather to embrace the practical attitudes and methods of the medical professionals who help restore people to good health. However, restoring people to good health require expensive medical instruments which were not always affordable for most of the time in small village hospitals like the one I visited as a child.

So many of us, aspiring researchers balance our ambitions upon the idea of inventing novel concepts and ideas that may help people it has almost become clichéd. Yet having seen the blight of poverty, and the ways in which human resilience builds a path right through it, I am inspired to turn my own accomplishments as a Biomedical Engineer into the gift of hope. This is the hope that directs my future as a great researcher

in developing novel and affordable diagnostic and therapeutic instruments towards the care of the underprivileged; I do no more than my best.

The first step towards this incredible journey requires strong research background. As a graduate student of biomedical engineering the emphasis of my course work and research in medical optics and the propagation of light in chemically treated tissue for enhanced diagnostics and therapeutics opened the door for me to return the goodness that the world has given me. In this process I have meet many brilliant minds who helped me guide through the unknown path of research.

Thus, first and foremost I like to thank my supervising professors Dr. Ashley J. Welch (first three research projects) and Henry G. Rylander (last two research projects) for their unconditional support and guidance in every step of this journey. I am truly grateful for their thorough review of five of my journal papers, abstracts for many conferences over the weekends when I sent them at 2AM in the Saturday morning. They encouraged my when I lost my ways and never knew how I would move forward with my research. There were uncountable discussion and meetings leading to the successful completion of this thesis. They have mastered the art of managing graduate students while allowing us our independence in the laboratory. Both of them made it possible for me to participate in numerous conferences and allow me to write 6 peer reviewed journal papers. They also allowed me to help write research grants, provisional patent application through which I gained new insights into the world of academia. They always valued my opinion and treated my as peers rather than a graduate student. I have leaned patience when I almost gave up many hopes to complete experiments. They molded my mind as a

true researcher and taught me to think out of the box to find simple and elegant solutions to complicated problems.

I also want to thank the members of my dissertation committee. Dr. Gracie Vargas, not only offered much counsel along the way, but also treated me like a peer, rather than a student. Dr. John Zhang contributed many ideas and taught me to approach research problems in new ways. Dr. Thomas E. Milner taught me much about OCT techniques. All of these people were very receptive to my questions. I thank them all for willing to be part of my committee.

Although, Dr. James W. Tunnell was not on my committee, he made important contributions to my work: he educated me on various concepts of optical techniques such as diffuse optical and fluorescence spectroscopy and he allowed me to use equipments in his laboratory; and he participated in many helpful discussions. Also, I like to thank Dr. Anita Mahadevan-Jansen for providing me great insight in fluorescence spectroscopy. I appreciate Dr. Andrew K. Duunn's for teaching me the knowledge about laser speckle and two-photon imaging techniques.

I would like to thank my colleagues at the UT, Narasimhan Rajaram, Ashwin B. Parthasarathy, Bo Chen, Tianyi Wang, Jinze Qiu, Brandon S. Nichols made scientific contributions to my work by either assisting in experiments or offering technical expertise.

I am indebted to Kathryn Starr for helping me with my experiments by holding probe while I was taking the measurements. Without her help I would not be able to complete a lot of experiments. She became a great friend and a mentor. Jennifer Cassadey

taught me so much about animal care and regulations over the year and became my friend. Finally, Dr. Otto, without his generous offer with hardship money I would not able to complete my last research at UT.

Jim Pollard, Chris Cooper, Heidi Mellon, Christy Humphrey, and Carol Noriega deserve special thanks. If it wasn't for Jim, I could not have easily solved the computer troubles such as Matlab licensing problem or problem with remote login to the office computer from home. Also, Chris always helped me when I was locked out from my office several times. Heidi made enormous positive impact while she was in UT. She made my life so much easier that I could have easily continued on my research. Chris Humphrey, without whom I could never able to create the invoice order for renting the ophthalmic Nd:YAG laser. Also, Carol always helped me with academic regulations and deadline. I have to give a special thanks to Mr. Daniel Campbell who brought the laser from Dallas to Austin even when we could not use it due to campus shooting. Then he brought back again to complete the experiment.

Several institutions such as Vanderbilt University and Air Force Research Laboratory, Brooks City-Base have provided me with support in several occasions. I like to thank Dr. Jeffry Oliver for helping me with the thermal camera and providing me enucleated porcine eyes.

Most importantly, I am indebted to the support and encouragement I have received over the year from my parents, and my sisters. I am also grateful to my grandfather who taught me English when I was a child and told me I will do great things when I grow up. Although, he is not here with us anymore, his encouraging words still

give me strength. I am grateful to my husband, Syed Mohiul Alam, for his love and dedication. I like to thank my sisters Rownak Jyoti Zaman, Sitara Swati Zaman, and Rowshan Dipti Zaman. Also, like to thank my nephew Arik, and two nieces Inara and Samia for their unconditional love and respect.

My graduate school experience has been truly rewarding, both from academic and professional perspective. The University of Texas at Austin fosters professional development and growth of its graduate student community through numerous programs and activities. Thus, I am grateful to the UT system for providing me with such a great experience.

Efficacy of Hyper-osmotic Agent (100% Anhydrous Glycerol) in Tissue and Light-activated Micro-pattern Drug Delivery Device in *In Vivo* Rabbit Eye

Publication No._____

Raiyan Tripti Zaman, Ph.D.

The University of Texas at Austin, 2011

Supervisor: Henry Grady Rylander, III

My PhD research involves multi-disciplinary areas of study such as measuring perfusion of blood vessels in hamster dorsal skin using laser speckle imaging technique. In this study the changes were measured in blood flow velocity and diameters of micro vasculatures after the influence of glycerol application. The second study identifies the changes in morphology and optical properties of eye tissue after applying hyper-osmotic agent such as 100% anhydrous glycerol. Further investigation on the reversal process was performed without any application of 0.9% saline. The third study identified the variation in fluorescence in hamster dorsal skin tissue and enucleated porcine eyes with temperature. This study investigated the variation in fluorescence intensity with temperatures starting at 14°C and compared *in vivo* and *in vitro* results for consistency.

The fourth study investigated an implantable drug delivery package that was fabricated using PMMA and implanted between the sub-conjunctival and super-scleral space and release the content of the device by either mechanical pressure or light-activated ophthalmic Nd:YAG laser after optically clearing the eye tissue by topical application of a hyper-osmotic agent, 100% anhydrous glycerol. A hyper-osmotic agent creates a transport region in the conjunctiva and sclera to get visual access of the compartments in the drug delivery package. This new technology would provide the option to the patient of one time implantation of the carrier system containing the drug. Each time the patient requires medication a ND-YAG or other laser beam will propagate through the cleared eye tissue to release the drug in measurable doses at the discretion of the doctor from the package directly in to the vitreous humor. In this study we have measured half-life of the dye in the vitreous humor or posterior chamber and biocompatibility. The last study had drawn distinction between the fluorescence signals based on the location (anterior or posterior chamber) of the 10% Na fluorescence dye in the *in vivo* rabbit and *ex vivo* pig eyes.

Table of Contents

List of Tables

List of Figures

CHAPTER 1: INTRODUCTION

1.1. MOTIVATION

Light-based diagnostic and therapeutic procedures are an integral part of medical treatments. The goal of light-based techniques in medicine is either to (i) gain morphological information from biological tissue for diagnostic purposes or (ii) modify the properties of biological tissue in order to correct a medical condition by photo coagulation, photochemical. These light-based medical treatments rely on sufficient light delivery to in-depth biological targets of the tissue. Thus, research related to enhance light delivery to tissue is important to medicine due to the advantages of light-based techniques over traditional methods or are may be the only accepted methods to treat or non-invasively image biological abnormalities.

Often the limited penetration depth of light in biological tissue restricts the success of these treatment procedures. The penetration of light in most tissue varies from tens of microns in the ultraviolet and shorter visible wavelengths to several millimeters in the infrared region of the light spectrum. The distance a ray of light can travel in tissue is governed by light absorption and scattering properties of the tissue. Reducing the incidence of light scattering or absorption will increase the penetration depth of light in biological tissue. A technique that provides enhanced light penetration into normally opaque tissue can greatly improve the effectiveness of many optical diagnostic or

therapeutic techniques. Two requirements that must be fulfilled by such a technique is that the method be safe, and if any chemical or physical changes are involved or in another word any morphological changes, that the method be reversible in a short period of time.

In this dissertation a hyper-osmotic agent such as 100% anhydrous glycerol is introduced to increase the penetration depth of the normally opaque tissue and investigate the effects such as changes in blood flow velocity or optical properties of this optically cleared tissue. The technique renders local areas of tissue temporarily transparent and permits direct visualization of subsurface structures. This clearing technique further combined with a drug delivery system in rabbit eye for precise on demand delivery. Hydration of the sample reverses the optical effect. In addition to enhancement of diagnostic imaging techniques, focused light may be delivered at greater depths within tissue, potentially improving laser therapeutic techniques.

The increase in optical transparency leads us to ask why glycerol is able to induce the change in the manner. Clearly, glycerol modifies the optical properties of the skin, sclera, the white part of the eye but what mechanisms allow this? Is the skin/sclera changing at the microscopic level? Is glycerol replacing tissue water? Does glycerol act as an optical index matching fluid? Also significant is the question: How can we use the effects of this agent to enhance light delivery to deeper depths, thereby improving optically based medical techniques such as precise drug delivery to eye? The purpose of this dissertation is to answer these questions, to demonstrate the technique has the long

term potential for impacting several optically based medical techniques, and to broaden our knowledge of tissue and light-tissue interactions.

1.2. SPECIFIC AIMS

The primary objective of the research described in this dissertation is to explore the use of a specific hyper-osmotic chemical agent such as 100% anhydrous glycerol to reversibly reduce local light scattering in biological tissue for the purpose of enhancing therapeutic and diagnostic optical applications that require light delivery deep within the tissue.

My specific goals are:

I. **Measure perfusion of hamster skin**. It is important to measure the changes in blood flow velocity and diameters of micro vasculatures after glycerol application.

II. **Identify the changes in optical properties of eye tissue.** If hyper-osmotic agent could be used to improve treating ocular diseases, the changes in morphology and optical properties of sclera and choroidal layers need to be identified while the agent is being applied. Also, the safety or reversibility of this clearing process is important.

III. **Identify the variation in fluorescence in hamster dorsal skin tissue and enucleated porcine eyes with temperature.** This study investigated variations in

fluorescence intensity with temperatures starting at 14°C and compared *in vivo* and *in vitro* results for consistency.

IV. **Develop drug delivery device.** It is important to develop a drug delivery device that will be light activated to release measurable quantity of drugs from the device that is implanted in between the sub-conjunctiva and super-scleral space.

V. **Testing biocompatibility of the device by implanting the device in the in rabbit eye.** After implantation of the device every three days the animal will be observed for any sign of leaks from the device. Histology will be performed at the conclusion of the study to identify any adverse effect of the device on the eye tissue.

VI. **Drug release with ophthalmic Nd:YAG laser.** After the testing of biocompatibility we will implant the drug delivery device according to specific aim 2. Hyper-osmotic agent such as 100% anhydrous glycerol will be topically applied to conjunctiva to optically clear the tissue surrounding the device. Then, an ophthalmic portable pulsed Nd:YAG laser will be used to release the dye into the eye by ablating the membrane of the reservoir.

VII. **Half-life measurement of fluorescence dye.** We have measured the half-life of the fluorescence dye inside the eye by using a non-invasive fluorescence spectrometer system.

VIII. **Signal variation of the emission spectra of fluorescein dye.** The location of dye was detected by analyzing the emission spectra of the fluorescein dye.

1.3. DISSERTATION OVERVIEW

This dissertation is made up of seven chapters, four of which are research chapters (Chapters 3-6). A background chapter is first presented which covers subjects that will serve as an introduction for the experiments included in the rest of this dissertation (Chapter 2).

The experiments in this dissertation are summarized in four chapters that begin with *in vivo* blood dynamic changes in light scattering, when skin is subjected to glycerol (Chapter 3). The objective of this Chapter 3 is to quantify the effect of hyper-osmotic agent (glycerol) on blood velocity in hamster skin blood vessels measured with a dynamic imaging technique, laser speckle contrast imaging (LSCI). A dorsal skin-flap window was implanted on the hamster skin. The hyper-osmotic drug i.e. glycerol was delivered to the skin through the open dermal end of the window model. A two-dimensional map of blood flow of skin blood vessels was obtained from the speckle contrast (SC) images.

The mechanism of optical tissue clearing is addressed by the work presented in Chapter 4, where optical properties of tissue changes induced by glycerol, a hyper-osmotic agent, is determined. Light scattering in the normally white sclera prevents diagnostic imaging or delivery of a focused laser beam to target in the under lying choroid layer. In this chapter, we examine changes in optical properties and dynamics of blood owing to the application of the glycerol to the sclera of rabbits. Recovery dynamics are monitored after the application of saline. These measurements provide an estimate of the diffusion time of glycerol through the sclera and examine the hypothesis that glycerol

reduces blood flow. The speed of clearing for injection delivery is compared to the direct application of glycerol through an incision in the conjunctiva. A Diffuse Optical Spectroscopy (DOS) system provided spectral analysis of the remitted light every two minutes. Comparison of measurements to those obtained from phantoms with various absorptions and scattering properties provided estimates of the absorption coefficient and reduced scattering coefficient of rabbit eye tissue.

Chapter 5 investigated variations in fluorescence intensity with temperatures starting at 14°C and compared *in vivo* and *in vitro* results for consistency. A fiber optic based noninvasive system was used to characterize the temperature effect on tissue fluorescence in hamster dorsal skin *in vivo*, and in sclera and cornea of enucleated pig eyes *in vitro*. As tissue was allowed to progress through the range of 14°C to 42°C, the spectra of auto-fluorescence with respect to temperature was sampled every 1-2 minutes. A pulsed nitrogen laser was used to excite fluorescence through a fiber optic probe with a source-detector aperture separation of 370 μm. Fluorescence intensity decreased as temperature increased from 14°C to 42°C in a phantom containing Rhodamine B dye. Cooling a tissue increased fluorescence intensity of skin *in vivo*, in all experiments. *In vitro* results were consistent with *in vivo* measurements.

The primary goal of the Chapter 6 is the fabrication, biocompatibility testing, and measured release of a marker dye (Na Fluorescein) from a micro-patterned drug delivery device using an ophthalmic Nd:YAG laser. The device can be implanted in the sub-conjunctival space or sub-scleral space. The results established that the drug delivery device retained its fluidic content intact until it was released. We can measure the half-

life of the dye in the eye for more than two weeks after the dye is released. Histology study showed minimal immune response such as inflammation after implantation of the drug delivery device.

In chapter 7, signal variation of the fluorescent emission spectra between the anterior and posterior chamber of *in vivo* rabbit and *ex vivo* enucleated pig eyes is discussed. This chapter verifies and supports the conclusion of chamber 6 that the released dye in fact measured from the posterior chamber of the rabbit eye.

In chapter 8, the future direction has described along with the questions that are not focused in the studies done in this dissertation.

The final chapter in this dissertation summarizes work presented in preceding chapters and gives conclusions about the value of the technique presented in medical optics.

CHAPTER 2: BACKGROUND

2.1. OVERVIEW

The main emphasis of this dissertation is use tissue clearing hyperosmotic agent such as 100% anhydrous glycerol to various situation that will increase the penetration depth of the turbid tissue to which light can travel easily, principally for the purpose of improving the imaging and therapeutic medical techniques. The penetration depth of a ray of light into tissue is often very shallow due to scattering that causes quick diffusion of the light. This inability to maintain a collimated beam of light limits the effectiveness of many light-based medical applications. This research addresses the problem and utilizes the modification of the optical properties of tissue by application of hyperosmotic chemical agents. Also, in this dissertation hyperosmotic agent was applied to (i) skin blood vessels to change the blood perfusion, (ii) increase visibility of various eye layers by altering the tissue properties to create optical window, and (iii) to release the content from the implantable drug delivery devices by light-activation. Variation in auto-fluorescence of eye tissue due to temperature change was also examined. Some general concepts are discussed before the ultimate motivation of this PhD research is described.

2.1.1. Hyperosmotic agents: optical clearing

Osmotically active agents have been used in ophthalmology for years to temporarily reduce scattering in the eye tissue such as cornea, sclera. Much of the work investigating the use of these agents on sclera has been done by Tuchin *et al*.[1-4] When agents such as glucose solution, Trazograph, and polyethylene glycol are applied to turbid sclera, it becomes a highly transparent media. Conversely, exposure of the cornea to hypotonic bathing solutions such as a NaCl bath causes swelling, and a transformation from being a transparent media to a turbid one.[5] Chance *et al.* have shown changes in scattering of lipid and cell suspensions when the concentration of solutes such as glucose and electrolytes is altered.[6] Liu *et al.* have used Rayleigh-Gans and Mie theory to evaluate the effect of refractive index and osmolarity changes on overall scattering of cell suspensions.[7] The chemical agents used in various studies were (i) glycerol, (ii) dimethyl sulfoxide (DMSO), (iii) glucose, (iv) sucrose, (v) polyethylene glycol, and (vi) sodium chloride. Glycerol is a sugar-alcohol used in medicine and cosmetics and is found in the body. In medicine it is used as an ophthalmic diagnostic aid.[8] These hyperosmotic agents could be used to improve the penetration depth of light in the turbid medium shown in Figure 2.1.

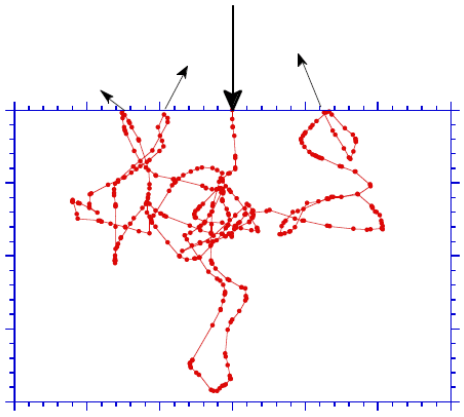

Figure 2.1. Light interaction with turbid tissue medium.

2.1.2. Fluorescence

Fluorescence occurs when a molecule in its ground state absorbs energy and is excited to an electronically excited state. From there, the molecule undergoes vibrational relaxation and/or internal conversion in which energy is generally emitted as heat. Then, from the lowest vibrational level in an excited electronic state, the molecule returns to its ground state by emitting a photon. Since the molecule has undergone a non-radiative decay (heat generation), the emitted photon has less energy than the incident photon. This is known as a Stokes shift. Thus, fluorescence is only present at longer wavelengths than the excitation, or incident, light. A diagram of fluorescence in terms of energy levels is displayed in Figure 2.2, known as a Jablonski diagram. As can be seen in the Jablonski diagram, fluorescence is not the only phenomenon possible when photon is absorbed. Other path includes elastic scattering, inelastic scattering, phosphofluorescence, and non-radiative decay (vibrational relaxation).

The time scale of fluorescence depends on the exact substance and incident energy, but is much longer than the absorption time course. The time course of absorption is on the order of 10^{-15} seconds, while the fluorescent lifetime is on the order of 10^{-8} seconds. The short lifetime of absorption, according to the Franck-Condon principle, does not allow for any molecular interaction during the process, while the longer relative lifetime of fluorescence emission allows for a variety of other interactions.[9]

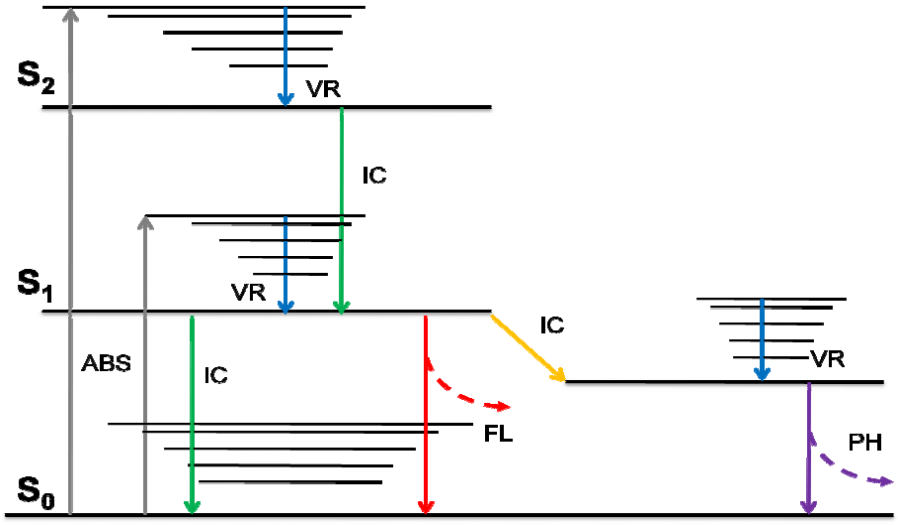

Figure 2.2. Jablonski diagram/ Fluorescence occurs when a photon is absorbed, exciting a molecule to an excited electronic state. After a non-radiative decay to the lowest vibrational level of an electronic state. The molecule returns to its ground state by emitting a fluorescent photon. ABS: absorption; IC: internal conversion, VR: vibrational relaxation; FL: fluorescence emission; IC: intersystem crossing; PH: phosphorescence.

2.1.3. Optical properties

When light interacts with tissue, a variety of events can occur. It is useful to define light as a particle, or photon, for most tissue optics applications. When a photon is incident upon a piece of tissue it can reflect off the surface, known as specular reflectance, or enter into the tissue. Whether a photon is specularly reflected or enters into the tissue is governed by Fresnel's laws, which depend on the incident angle, incident index of refraction, tissue index of refraction, and the polarization state of the incident light. If the photon enters the tissue, it can be absorbed, elastically scattered, inelastically scattered, or transmitted.

Due to the relatively complex molecular nature of tissue, these events are best understood on a probabilistic and empirical level. The probability of a photon being absorbed while traveling over an infinitesimal distance, dz (cm), is described by the product of the absorption coefficient, μ_a (cm^{-1}), and the distance, dz (cm). The absorption coefficient is related to light irradiance in a non-scattering medium through Beer's Law:

$$E(z) = E_0 e^{-\mu_a(\lambda)z} \qquad (1)$$

Where E_0 is the incident irradiance (W/m^2), μ_a is the wavelength dependent absorption coefficient (cm^{-1}), z is the depth in the medium (cm), and E(z) is the irradiance at that depth (W/m^2). Similarly, the probability of a photon being scattered while traveling over an infinitesimal distance, dz (cm), is described by the product of the scattering coefficient, μ_s (cm^{-1}), and the distance, dz (cm). The angle at which the scattering occurs is described by the anisotropy factor, g. The anisotropy represents the

average cosine of the scattering angle, where -1 represents total backscattering, 0 represents isotropic scattering, and 1 represents total forward scattering. Tissue is highly forward scattering, with g values between 0.7-0.99. The anisotropy and scattering coefficient can be described by a single term known as the reduced scattering coefficient, and is defined as:

$$\mu_s' = \mu_s(1-g) \qquad (2)$$

This is often used if the exact values of μ_s and g are coupled, and their individual values are not known.

2.2. MOTIVATION

Most common causes of blindness in the United State are (i) Macular degeneration, (ii) Diabetic retinopathy, (iii) Glaucoma, and (iv) Cataract. Annual cost of treating blindness for the US Government is about 4 billion dollars a year. Furthermore, more than 1.75 million individuals are diagnosed with Age-related macular degeneration (ARMD) in the USA who are 40 years of age or older. This number is going to further rise to 3 million by year 2020.

ARMD is a degenerative condition of the macula. It is the most common cause of vision loss in the United States of America for those 60 years or older. Its prevalence increases with age. ARMD is caused by the hardening of the arteries that nourish the retina. This deprives the sensitive retinal tissue of oxygen and nutrients that it needs to function and thrive. As a result, the central vision deteriorates. In the worst cases, it

causes a complete loss of central vision, making reading or driving impossible. ARMD is classified as either wet (neovascular) or dry (non-neovascular). In wet ARMD, new vessels form to improve the blood supply to oxygen-deprived retinal tissue. However, the new vessels are very delicate and break easily, causing bleeding and damage to surrounding tissue.

The current treatment for the ARMD involves with (i) coagulation/ablation with Argon laser (ii) intra-vitreal injection of anti-angiogenic drugs. The treatment with photocoagulation further worsens vision loss in treated patient. In a study showed that about 20% chances of severe vision loss within 3 months in the treated group vs. 11% controlled group. There are multiple side effects with the intra-vitreal injection. The primary treatment for wet ARMD is periodic injection of a drug such as Lucentis® (ranibizumab), in the eye which is painful and causes multiple risks of endophthalmitis. The chances of having endophthalmitis are 0.16% and 0.05% per intra-vitreal injection. Also it can cause lens trauma (0.7%), retinal detachment (0.6%), and systemic VEGF-A inhibition predispose to excess thrombo-embolic complications in the first year of follow-up. Figure 2.3 depicts some of the problems associated with the current treatments.

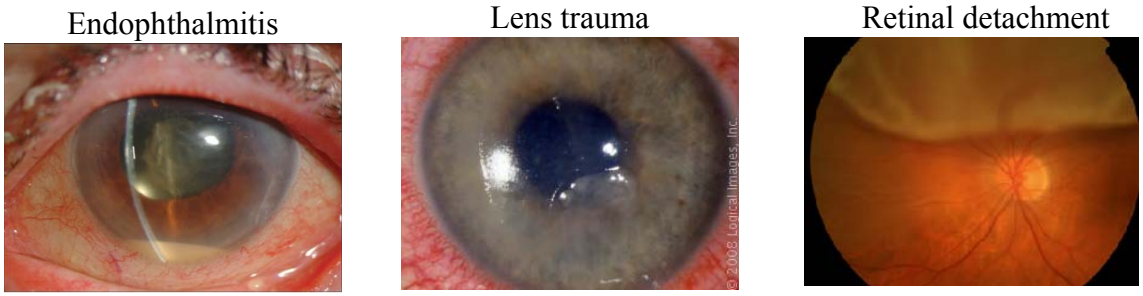

Figure 2.3. Side effects of current treatment using intra-vitreal injection to eye

Thus, there is a great need for an improved drug delivery device. The therapeutic efficacy of a drug depends on how the drug is delivered. The limitation of any conventional drug delivery systems such as implants or oral delivery systems is a sharp initial increase in drug concentration to a peak above the therapeutic range, followed by a fast decrease in concentration to a level below the therapeutic range. The time spent in the optimum concentration range for therapeutic effect is therefore very short.

Therefore, the primary goal of my proposed Ph.D. dissertation research is to investigate the biocompatibility of a drug delivery device in super-scleral and sub-conjunctival space of *in vivo* rabbit eye. The proposed drug delivery package will provide precise and repeatable dosing of medication to patients based on their need by optically clearing the sclera with hyper-osmotic agent such as 100% anhydrous glycerol and a pulsed Nd-YAG clinical laser to release the drug.

Our hypothesis is that the concentration of fluorescence dye in the eye tissue is directly correlated to the concentration of drug that will be released from the drug delivery device.

2.3. BACKGROUND AND SIGNIFICANCE

2.3.1. Current approaches to ARMD treatment

ARMD is the leading cause of blindness and visual disability in patients aged ≥60 years in North America and Europe.[10] Worldwide, ARMD is the third leading cause of blindness, behind cataract and glaucoma, causing 8.7% of all legal blindness.[11] The

clinical spectrum of ARMD encompasses drusen, hyper-plasia of the retinal pigment epithelium (RPE), geographic atrophy and choroidal neo-vascularization (CNV). These changes affect the macula of the retina and subsequently may affect central or reading visual acuity.

ARMD has been classified in one of the two ways. It can be divided into two broad clinical categories depending on whether there is a presence of abnormal neo-vascularization: neo-vascular (synonymous with exudative or wet) and dry ARMD. A second classification is used depending on the extent of visual impairment; late ARMD, which includes neo-vascular ARMD and an advanced dry form called geographic atrophy and early ARMD that includes all other forms (Figure 2.4). Early (dry) ARMD is more prevalent than neo-vascular ARMD in the USA. However, patients with neo-vascular or wet ARMD account for about 75% of cases of severe visual impairment secondary to ARMD.[12]

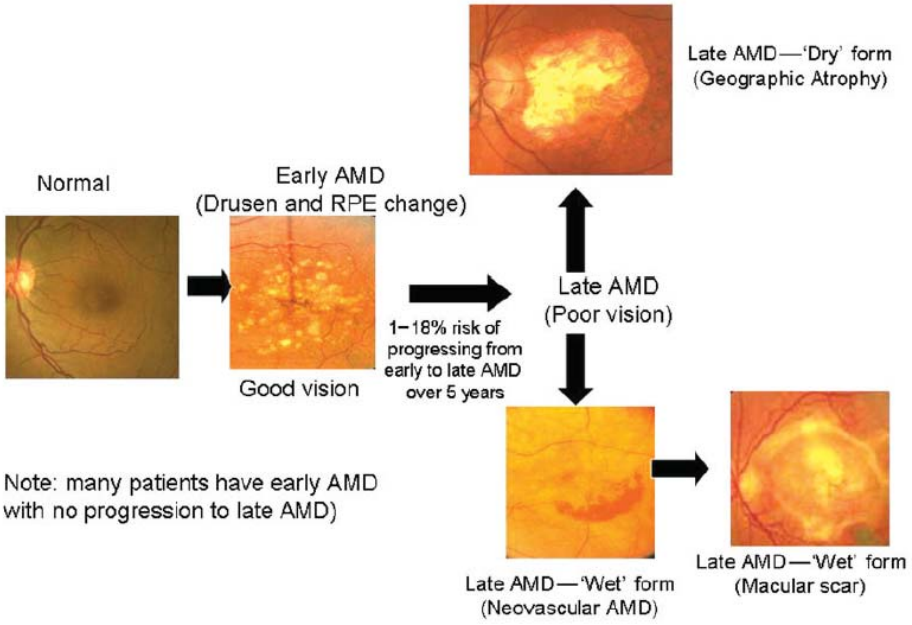

Figure 2.4. Classification of age related macular degeneration (ARMD)[11]

Patients with early (dry) ARMD consisting of drusen and hyperplasia of the RPE may have no visual difficulties (Figure 2.5a). A minority of patients with early (dry) ARMD may progress to geographic atrophy. Geographic atrophy is gradually progressive, and may involve the center of the fovea causing central visual loss (Figure 2.5b). Geographic atrophy accounts for about 25% of patients with severe visual loss secondary to ARMD.[12]

It is believed that the changes in Bruch's membrane and RPE that occur in dry ARMD may give rise to a state where blood vessels may sprout off existing choriocapillaris (pro-angiogenic state). These vessels then break through the normal level of Bruch's membrane into the sub-RPE or sub-retinal spaces. Neo-vascular ARMD is defined by the development of CNV. The patient will often report a sudden worsening of

their central vision, often with distortion. Clinically, the CNV produces hemorrhage, exudative retinal detachment or serious or hemorrhagic pigment epithelial detachments (Figure 2.5c). In end-stage disease, this results in a fibro-vascular or atrophic macular scar and subsequent permanent damage to the central vision.

(a) (b) (c)

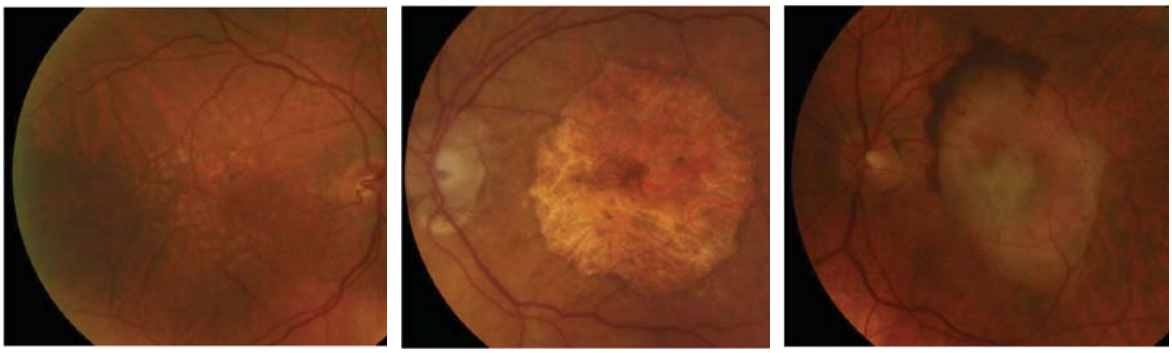

Figure 2.5. Fundus photograph showing an eye with (a) drusen and RPE hyperplasia (b) advanced geographic atrophy (dry ARMD) (c) neovascular age-related macular degeneration.[11]

2.3.2. Prevalence/demographics

Friedman *et al*.[13] found that ARMD occurs in patients over the age of 55 years. Prevalence increases substantially with increasing age. They also estimated that ARMD affects >1.75 million individuals aged ≥40 years in the USA. Owing to the rapidly ageing population, this figure is projected to rise to almost 3 million by 2020. Furthermore, about 10–15% of patients with ARMD have severe loss of central vision. The prevalence

of ARMD varies between racial groups with higher prevalence in European-descended populations. Pooled data from three large epidemiological studies showed that drusen were strongly age-related in the black population, and that sight-threatening ARMD was less prevalent than in a white population.[13] Hispanic and Latin American populations seem to have a lower incidence of advanced and neo-vascular ARMD than European-descended white populations.[10,14] There is little data available on other population groups.

2.4. CURRENT TREATMENTS FOR ARMD

2.4.1. Conventional laser treatment

Argon laser photocoagulation can be used to ablate the area of active CNV in patients with neo-vascular ARMD. The Macular Photocoagulation study established that laser photocoagulation prevented severe loss of vision (loss of six or more lines of visual acuity) in extra-foveal CNV secondary to ARMD.[15] This randomized, controlled trial (RCT) terminated recruitment to the extra-foveal arm at 18 months as 60% of untreated eyes but only 25% of treated eyes had severe visual loss.[15] A 5-year follow-up data showed that 64% of untreated eyes developed severe visual loss compared with 46% of treated eyes at 5 years.[16] However, there is a 54% recurrence rate at 5 years after treatment. Approximately 75% of recurrences occur within the first year.

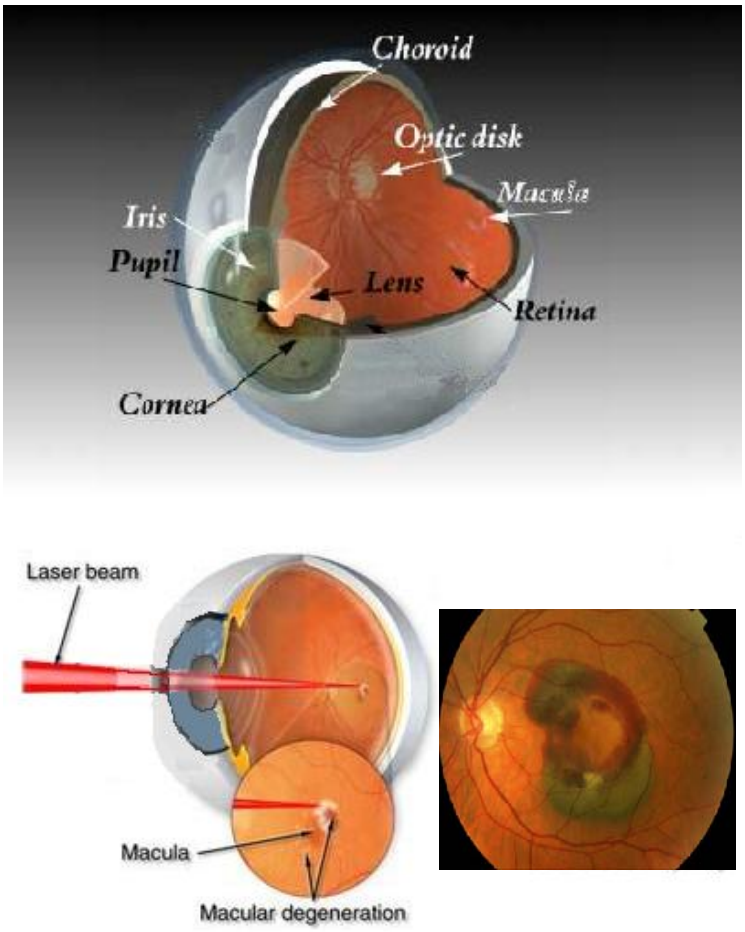

Figure 2.6. Current treatment of coagulation/ablation using Argon laser

2.4.2. Intra-vitreal injection treatment: anti-angiogenic drugs

There is currently extensive research on modulating the angiogenic response with anti-vascular endothelial growth factor (anti-VEGF) to treat ARMD. There is extensive *in vitro* and *in vivo* evidence that VEGF is implicated in retinal angiogenesis and vascular permeability. There has been intense laboratory and clinical research in this area, and

researchers have developed agents that block VEGF activity some of which are already in clinical use:

2.4.2.1. Pegaptanib sodium (Macugen®)

Pegaptanib (Macugen®, Eyetech Pharmaceuticals, NY, USA) is a selective anti-VEGF oligonucleotide conjugated with a polyethylene glycol that binds to the major human soluble VEGF isoform (VEGF165). A phase III RCT comparing intra-vitreal doses of 0.3, 1.0 and 3.0 mg and sham injection showed that with six weekly injections over a 48-week period there was a significant reduction in moderate visual loss (<15 letters lost) at 54 weeks follow-up. In the 0.3 mg treatment group, there was a statistically significant increase in the proportion of patients with stable vision with 70% losing <15 letters versus 55% in the sham treatment group (P, 0.001).[16]

2.4.2.2. Ranibizumab (Lucentis®)

A recombinant anti-VEGF monoclonal antibody fragment that binds to all iso-forms of VEGF-A (Ranibizumab, Lucentis®; Genentech, CA, USA) has been developed. Recent published Phase III data show a benefit from treatment for all lesion types and sizes with ranibizumab with repeated four weekly intra-vitreal injections. The ANCHOR study[17] randomized 423 patients with predominantly classic neo-vascular or wet ARMD to monthly injections of Lucentis® at two different doses or to conventional treatment with verteporfin PDT. The 12-month results showed 94.3% of patients treated with 0.3 mg Lucentis® and 96.4% treated with 0.5 mg lost <15 letters on visual acuity testing

compared with 64.3% in the PDT-treated group. In addition, visual acuity improved by ≥15 letters in 35.7% of the 0.3 mg Lucentis®-treated group and 40.3% of the 0.5 mg-treated group with only 5.6% of PDT-treated patients improving vision. The average visual acuity change was a gain of 8.5 letters in the 0.3-mg group and 11.3 letters in the 0.5-mg group compared with a decrease of 9.5 letters in the PDT-treated group at 12 months.

The MARINA study[18] randomized 716 patients with minimally classic or occult neo-vascular ARMD to monthly injections of Lucentis® at two different doses or to sham treatment. The 24-month results showed 92% of patients treated with 0.3 mg Lucentis® and 90% treated with 0.5 mg lost fewer than 15 letters on visual acuity testing compared with 52.9% in the sham-treated group. In addition, visual acuity improved by ≥15 letters in 26.1% of the 0.3 mg Lucentis®-treated group and 33.3% of the 0.5-mg treated group compared with only 3.8% of sham injection group. The average visual acuity change was a gain of 5.4 letters in the 0.3-mg group and 6.6 letters in the 0.5-mg group compared with a decrease of 14.9 letters in the sham injection group at 24 months.

The PIER study[19] was a prospective, multi-center, randomized, controlled trial of 184 patients with sub-foveal CNV due to ARMD received either ranibizumab (0.3 or 0.5 mg) or sham treatment once a month for 3 months and followed by doses every once every 3 months for a total of 24 months in a 1:1:1 ratio. At the 12 months, patients with quarterly treatment gained a mean of 2.9 ETDRS letters (0.3 mg group) or 4.3 letters (0.5 mg group) compared with a mean loss of 8.7 letters for the sham group with 12% (0.3 mg

group) and 13% (0.5 mg group) gaining 15 letters or more. This study suggests that the efficacy of ranibizumab is reduced if given as a quarterly treatment.

The results from the Fung *et al.*[20] which was a prospective open-label interventional case series of neo-vascular ARMD patients with sub-foveal CNV treated with three consecutive monthly intra-vitreal injections of ranibizumab (0.5 mg) with further injections if clinically indicated, support this treatment strategy. At month 12, the mean visual acuity improved by 9.3 letters (P value = 0.001) and the mean OCT central retinal thickness decreased by 178 mm (P value = 0.001). Visual acuity improved 15 or more letters in 35% of patients. These visual acuity and OCT outcomes were achieved with an average of 5.6 injections over 12 months. This small study suggests visual acuity outcomes similar to the Phase III clinical studies, may be achieved with fewer intra-vitreal injections.

2.4.2.3. Bevacizumab (Avastin®)

Initially developed for use in oncology (licensed for use in colorectal cancer), bevacizumab (Avastin®) has been increasingly used as an intra-vitreal injection to treat neo-vascular or wet ARMD. Bevacizumab is a full-length, humanized, monoclonal antibody binding all forms of VEGF-A. Several published case series have suggested efficacy similar to that of Lucentis®, but as yet there have been no prospective, randomized, controlled trials published. The largest retrospective case series of 266 eyes with follow-up of 2 months (data available for 222 eyes) showed visual acuity improvement in 31.1% with a statistically significant reduction in mean central macular

thickness.[21] The evidence for the efficacy of intra-vitreal bevacizumab in treating neo-vascular ARMD is from interventional case series with no reports from multi-center, randomized, controlled trials. However, despite the availability of a licensed alternative treatment (ranibizumab), there is widespread, worldwide 'off-label' use of bevacizumab for this indication as Lucentis, is significantly more expensive than Avastin and as Avastin was available prior to the licensing of Lucentis. This has given rise to the highly unusual situation of a drug (Avastin®) used for an unlicensed indication despite robust clinical trials supporting the safety and efficacy of a licensed alternative (Lucentis®) in treating wet ARMD.

2.5. PROBLEM WITH CURRENT TREATMENT FOR WET ARMD

2.5.1. Conventional laser treatment

Patients with juxta-foveal CNV fared less well than extra-foveal CNV. At 5-year follow-up, 55% of treated patients with laser had experienced severe visual loss compared with 65% controls.[22] A subgroup analysis found that classic CNV without an occult component benefited from treatment and that juxta-foveal lesions with an occult component did not benefit from laser photocoagulation. Patients with treated sub-foveal CNV were less likely to have severe visual loss at 4-year follow-up than untreated eyes (23 versus 45%).[23] However, this treatment is rarely performed as there is a significant risk of immediate worsening of vision in treated patients (20% chance of severe visual loss within 3 months in the treated group versus 11% of controls).

2.5.2. Conventional intra-vitreal drug delivery

Side-effects of the intra-vitreal drug delivery include endophthalmitis (0.16%), lens trauma (0.7%) and retinal detachment (0.6%).[24,25] The risk of endophthalmitis in the two studies ANCHOR and MARINA was 1.4% over 2 years (0.05% per intra-vitreal injection). Even though it is possible to achieve the efficacy of the drug using a fewer intra-vitreal injection, the risk of endophthalmitis is always exits.

Intra-vitreal VEGF inhibitors appear to be relatively free from systemic side-effects and complications although systemic VEGF-A inhibition may predispose to thrombo-embolic complications and an excess risk of thrombo-embolic complications was reported in the first year of follow-up in the ranubizumab (Lucentis®) randomized, controlled trials which diminished in the second year of follow-up. The SAILOR (Safety Assessment of Intra-vitreal Lucentis® for ARMD) study is an ongoing phase IIIb study with patients randomized to 0.3 or 0.5 mg of Lucentis. A planned interim safety analysis from this study reported a higher risk of cerebro-vascular accidents in the 0.5 mg group (1.2%) compared with the 0.3 mg group (0.3%). Therefore, there is a greater need for a safer drug delivery system to treat wet ARMD.

2.6. NOVEL APPROACH FOR TREATING WET ARMD

We are proposing a novel approach to deliver these anti-angiogenic drugs using a light-activated drug delivery system combined with a hyper-osmotic agent such as 100% anhydrous glycerol to optically clear the sclera to get a direct access to the drug delivery

device as needed. Before introducing the experimental deign of this device the efficacy of the hyper-osmotic agent is explored in the following section.

2.7. REFERENCES

1. Bakutkin VV, Maksimova IL, Semyonova TN, Tuchin VV, Kon IL. Controlling of optical properties of sclera. SPIE Proceedings, 1995; 2393:137−141.

2. Tuchin VV, Maksimova IL, Zimnyahkov DA, Kon IL, Mavlutov AK, Mishin AA. Light propagation in tissues with controlled optical properties. *Proceedings SPIE*, 1996; 2925:118−142.

3. Tuchin VV, Maksimova IL, Zimnyakov DA., Kon IL, Mavlutov AH, Mishin AA. Light Propagation in tissues with controlled optical properties. *Journal of Biomedical Optics*, 1997; 2(4):401−417.

4. Zimnyakov DA, Tuchin VV, Mishin AA, Kon IL, Serov AN, In-vitrohuman sclera structure analysis using tissue optical immersion effect. Proceedings SPIE, 1996; 2673:233–247.

5. Stevenson R, Vaja N, Jackson J. Corneal transparency changes resulting from osmotic stress. *Ophthalmic Physiol. Opt.*, 1983; 3(1):33–39.

6. Chance B, Liu H, Kitai T, Zhang Y. Effects of solutes on optical properties of biological materials: models, cells, and tissues. Analytical Biochemistry, 1995; 227:351–362.

7. Liu H, Beauvoit B, Kimura M, Chance B. Dependence of tissue optical properties on solute-induced changes in refractive index and osmolarity. *Journal of Biomedical Optics*, 1996; 1(2):200–211.

8. *The Merck Index*, 12th Edition, Budavari S, O'Neil MJ, Smith A, Heckelman PE, Kinneary JF, editors, Merck Research Laboratories : Merck & Co., Inc., Whitehouse Station, NJ, 1996.

9. Keller MD, Majumder SK, and Mahadevan-Jansen A. Spatially offset Raman spectroscopy of layered soft tissues. Optics Letter. 2009; 34(7): 926-8.

10. Klein R, Klein BE, Jensen SC, Mares-Perlman JA, Cruickshanks KJ, Palta M. Age-related maculopathy in a multiracial United States population: the National Health and Nutrition Examination Survey III. Ophthalmology, 1999; 106:1056–1065.

11. Resnikoff S, Pascolini D, Etya'ale D et al. Global data on visual impairment in the year 2002. Bull World Health Organ, 2004; 82:844–851.

12. Klein R, Klein BE, Jensen SC, Meuer SM. The five-year incidence and progression of age-related maculopathy: the Beaver Dam Eye Study. Ophthalmology, 1997; 104:7–21.

13. Friedman DS, O'Colmain BJ, Munoz B et al. Prevalence of age-related macular degeneration in the United States. Arch Ophthalmology, 2004; 122: 564–572.

14. Varma R, Fraser-Bell S, Tan S, Klein R, Azen SP. Prevalence of age-related macular degeneration in Latinos: the Los Angeles Latino eye study. Ophthalmology, 2004; 111:1288–1297.

15. Anonymous Argon laser photocoagulation for senile macular degeneration. Results of a randomized clinical trial. Arch Ophthalmology, 1982; 100:912–918.

16. Gragoudas ES, Adamis AP, Cunningham ET Jr, Feinsod M, Guyer DR. Pegaptanib for neovascular age-related macular degeneration. New England Journal of Medicine, 2004; 351:2805–2816.

17. Brown DM, Kaiser PK, Michels M et al. Ranibizumab versus verteporfin for neovascular age-related macular degeneration. New England Journal of Medicine, 2006; 355:1432–1444.

18. Rosenfeld PJ, Brown DM, Heier JS et al. Ranibizumab for neovascular age-related macular degeneration. New England Journal of Medicine, 2006; 355:1419–1431.

19. Brown DM PIER study data. Retinal Physician 2006 Symposium, 2007.

20. Fung AE, Lalwani GA, Rosenfeld PJ et al. An optical coherence tomography-guided, variable dosing regimen with intravitreal ranibizumab (Lucentis) for neovascular age-related macular degeneration. American Journal of Ophthalmology, 2007;143:566–583.

21. Spaide RF, Laud K, Fine HF et al. Intravitreal bevacizumab treatment of choroidal neovascularization secondary to age-related macular degeneration. Retina, 2006; 26:383–390.

22. Macular Photocoagulation Study Group Laser photocoagulation for juxtafoveal choroidal neovascularization. Five-year results from randomized clinical trials. Arch Ophthalmology, 1994; 112:500–509.

23. Macular Photocoagulation Study Group Laser photocoagulation of subfoveal neovascular lesions of age-related macular degeneration. Updated findings from two clinical trials. Arch Ophthalmology, 1993; 111: 1200–1209.

24. Gragoudas ES, Adamis AP, Cunningham ET Jr, Feinsod M, Guyer DR. Pegaptanib for neovascular age-related macular degeneration. New England Journal of Medicine, 2004; 351, 2805–2816.

25. D'Amico DJ, Masonson HN, Patel M et al. Pegaptanib sodium for neovascular age-related macular degeneration: two-year safety results of the two prospective, multicenter, controlled clinical trials. Ophthalmology, 2006; 113:992–1001.

CHAPTER 3: PERFUSION IN HAMSTER SKIN TREATED WITH GLYCEROL[1]

3.1. ABSTRACT

The objective of this chapter is to quantify the effect of hyper-osmotic agent (glycerol) on blood velocity in hamster skin blood vessels measured with a dynamic imaging technique, laser speckle contrast imaging (LSCI). A dorsal skin-flap window was implanted on the hamster skin. The hyper-osmotic drug i.e. glycerol was delivered to the skin through the open dermal end of the window model. A two-dimensional map of blood flow of skin blood vessels was obtained from the speckle contrast (SC) images. Preliminary studies demonstrated that hyper-osmotic agents such as glycerol not only make tissue temporarily transparent, but also reduce blood flow. The blood perfusion was measured every 3 minutes for 36−66 minutes after diffusion of anhydrous glycerol. Blood flow in small capillaries was found to be reduced significantly within 3−9 minutes. Blood flow in larger blood vessels (i.e. all arteries and veins) decreased over time and some veins had significantly reduced blood flow within 36 minutes. At 24 hours, there was a further reduction in capillary blood perfusion whereas larger blood vessels regained flow compared to an hour after initial application of glycerol. Blood velocity and vessel

[1]The experiments contained in this chapter were published in a peer-reviewed journal: Raiyan T. Zaman, Ashwin B. Parthasarathy, Gracie Vargas, Bo Chen, Andrew K. Dunn, Henry G. Rylander Iliad Ashley J. Welch, Perfusion in Hamster Skin Treated With Glycerol, *Lasers in Surgery and Medicine,* 41:492–503 (2009)

diameter of the micro-vasculatures of hamster skin was reduced by the application of 100% anhydrous glycerol. At 24 hours, capillary perfusion remained depressed.

3.2. INTRODUCTION

The diffusion of hyper-osmotic agents such as glycerol in skin reduces light scattering which increases the penetration depth of light. The increase in penetration depth is due to a reduction of refractive index mismatch among the cellular contents, structural components (such as collagen and elastin fibers), and extra-cellular fluid.[1] In addition, a hyper-osmotic agent such as glycerol increases the local concentration of scattering particles as a result of tissue dehydration.[2] The increase in penetration depth should enhance diagnostic (optical coherence tomography) and therapeutic (coagulation of blood vessels) procedures.[3] One side effect for some hyper-osmotic agents and particularly glycerol is the reduction in blood vessel diameter and flow velocity.[1, 4–7] It is this dynamic change in tissue perfusion that is the subject of this paper.

In a previous study, Vargas *et al*. measured flow velocity of *in vivo* hamster skin blood vessels using Doppler Optical Coherence Tomography (DOCT) before and after 100% anhydrous glycerol application.[3] Veins with inner diameters of 500 μm or less were completely closed with no blood flow at 50 minutes after treating the sub-dermal skin with glycerol. Although blood flow through arteries decreased, some flow remained through the treatment with glycerol. The Doppler image also identified that glycerol induced a decrease in optical thickness of the connective tissue overlaying the blood

vessels on the sub-dermal side and conformed to the shape of the blood vessels. Although, the DOCT study provided absolute blood flow velocity and morphological changes induced by glycerol for up to 50 minutes, the velocity and associated morphology were measured for only a single pair of blood vessels such as an artery and a vein. Choi *et al.* demonstrated the application of laser speckle imaging (LSI) to an i*n vivo* rodent dorsal skinfold model and showed LSI's potential as a wide-field microvasculature imaging modality.[8] In this hemodynamic study, blood flow velocity was measured for up to 16 minutes after glycerol application and showed an heterogeneous decrease in blood flow with an initial decrease in venular flow and a delayed decrease in arteriolar flow of the microvasculature network of the rodent dorsal skin-fold chamber. A study by Zhu *et al.* showed the changes in morphology of vessels and blood flow velocity of chick chorioallantoic membrane after application of hyper-osmotic agents such as glycerol and glucose.[9] In their study, measurements were made up to 31.5 minutes and one additional measurement at 48 hours after the application of hyper-osmotic agents such as glycerol and glucose. Both agents reduced local blood flow velocity and at 48 hours there was some recovery. However, the hemodynamics of hamster skin blood vessels and their morphological changes as a function of vessel type and size after application of a hyper-osmotic agent such as glycerol from 0 to 66 minutes and at 24 hours has not been investigated in the hamster model using laser speckle contrast imaging (LSCI) technique. Our research extends LCSI measurements of dynamics in morphology and blood flow velocity of the hamster skin microvasculature

such as arteries, veins, and capillaries over short term (0−66 minutes) and the long term (24 hours) after application of glycerol and both natural and saline induced recovery.

To investigate the transport of hyper-osmotic agents across skin and microcirculation on a full thickness of skin from both the epidermal and sub-dermal side of skin, a series of *in vivo* experiments were performed using a hamster dorsal skin-flap window model. LSCI provided a two-dimensional (2-D) map of blood flow in skin blood vessels during and after the diffusion of glycerol in the skin. The blood flow map was obtained using a dynamic imaging technique—LSCI.[10−11]

3.3. SPECKLE CONTRAST (SC) IMAGING

Laser speckle is a random interference pattern caused by coherent addition of scattered laser light. Motion of the scattering particles causes blurring or de-correlation of the speckle pattern. Quantification of the extent of blurring provides a measure of speed of the moving scatterers. This measurement is done by calculating speckle contrast (SC). The local SC is defined as the ratio of the standard deviation, σ_s, to the mean intensity of the back scattered light from the surface of the sample, $<I>$, in a small region of the image,[10]

$$SC = \frac{\sigma_s}{< I >} \qquad (1)$$

To ensure accurate determination of σ_s and $<I>$, the size of the region over which the SC is computed must be large enough to contain a sufficient number of pixels: however, not so large that significant spatial resolution is lost. SC values range between 0

and 1 and are inversely related to blood flow.[12] A SC of 1 indicates that there is no blurring of the speckle pattern and, therefore, no motion, whereas, a SC of 0 means that the scatterers are moving fast enough to average out all of the speckles. However, in practice it is never possible to get absolute 0 and speckle averaging effects prevent obtaining a SC of 1 for a completely static sample.

To quantify blood flow the SC values can be converted to intensity correlation decay times, τ_c, using

$$SC = \frac{\sigma_s}{\langle I \rangle} = \left[\frac{\tau_c}{2T} \{1 - \exp(-2T/\tau_c)\} \right]^{1/2} \qquad (2)$$

Yuan *et al.* suggest that an integration time (T) of 5 milliseconds is appropriate for physiological flow measurements.[13]

3.4. MATERIALS AND METHODS

3.4.1. Animal preparation

Male Golden Syrian hamsters (n = 13) weighing 120 to 150 g obtained from Harlan Sprague-Dawley, were used for the experiments. Six out of thirteen hamsters were used in the control group study. All experimental procedures were conducted according to protocols approved by the Animal Care Committee of The University of Texas at Austin. Hamsters were anesthetized with IP 200 mg/kg Ketaset and 10 mg/kg Xylazine. The depth of the aesthesia was monitored throughout the procedure by checking heart rate, breathing, and toe pinch and by supplements of one half of the initial dose of Ketaset

every one hour. Body temperature was kept constant at 37°C with a heating pad designed for small animal experiments. All hamsters were held on the heating pad with two pieces of surgical tape (one at the thoracic area and other at the pelvic area) to minimize any movement. In addition, two velcro straps held the heating pad at a fixed position on a lab jack and the lab jack on an optical table. These constraints fixed the animal position each time a LCSI measurement was performed.

3.4.2. Surgical procedure

The *in vivo* experiments described in this study were performed on the hamster dorsal skin-flap window preparation which isolated a section of skin from the body while maintaining hydration and function. Papenfuss *et al*. first developed the model for the simultaneous observation of the sub-dermal and epidermal sides of skin.[14] This allowed a direct *in vivo* view of dermal blood vessels while having access to the epidermal side of the skin. Prior to surgery the dorsal area of a hamster was shaved and epilated. The dorsal skin was raised from the mid-section of the body and sutured to a C-clamp to hold the skin away from the body. A circular section was cut from one section of skin, leaving the facing section exposed on its sub-dermal side. An aluminum chamber was sutured to both sides of the skin. The final preparation viewed from the epidermal (left) and sub-dermal side (right) is shown in Figure 3.1. Before LCSI measurements, the window (on the sub-dermal side) was filled with either phosphate buffer saline (PBS) for control experiments or 100% anhydrous glycerol for the experimental group. The total volume of fluid was

approximately 0.7 mL and 0.2 mL was replenished every 10 minutes until 36, 60, or 66 minutes. All experiments began 5−10 minutes after the completion of surgery.

Figure 3.1. Hamster dorsal skin flap window preparation showing a single thickness of hamster skin. (a) Shown from the epidermal side. (b) Shown from the exposed sub-dermal side. In this particular window preparation direct visualization of blood vessels is allowed.

3.4.3. Experimental procedure

3.4.3.1. Control group study

In the control group study, hamsters (n = 6) were divided into two groups based on different end points. After applying PBS solution, hamsters from C1 (n = 3) were observed for up to 60 minutes and group C2 (n = 3) was observed for 60 minutes and then at 24 hours. The PBS solution was not removed from the window before the glass was placed after the initial measurements (60 minutes) and no additional solution was

added for the 24 hour experiment. All hamsters from the experimental and control groups were euthanized according to an approved protocol.

3.4.3.2. Experimental group study

Blood flow velocity measurements were taken every 3 minutes for 36, 60, or 66 minutes using the LSCI technique. An additional 24 hours measurement was made on some of the animals. Three measurements were taken to allow a statistical analysis on the 24 hours group. For both experimental and control group studies, we started the experiment with the lowest observation time and then increased gradually. Thus, the hamsters (n = 7) in the experimental group were divided into three groups—E1, E2, and E3 based on three different end points. LSCI measurements every 3 minutes were made for 36 minutes in group E1 (n = 2), for 66 minutes in group E2 (n = 2), and for 60 minutes in Group E3 (n = 3). An additional 24 hours measurement was made for Group E3. For E3, after the initial measurements (60 minutes), a round thin glass was placed into the window over the cutout section of the skin to prevent the tissue from dehydrating. While animals were kept overnight at Animal Resource Center at the University of Texas the anhydrous glycerol was not removed from the window before the glass was placed. The thin glass was removed but no glycerol was added for the 24 hours LSCI measurement. A new bottle of glycerol was opened after each experimental group to prevent absorption of water from the atmosphere. All experiments for a given group were completed with in a week after opening a bottle of glycerol.

3.4.3.3. Speckle imaging system

The instrument (see Figure 3.2) for the LCSI measurements used in this experiment was developed by Dunn *et al*.[15] A diode laser beam (Sharp DL7140; λ = 780 nm, 30 mW; Thorlabs, Newton, NJ, U.S.A.) was collimated (collimating lens C240-TM; Thorlabs) and directed toward the sample. The lens was positioned approximately 10 cm above the area of interest and the lens was adjusted to provide even illumination of 1 cm diameter window on the sub-dermal side of the hamster skin. The illuminated area was imaged onto a CCD camera (Basler 602F, Basler Vision Technologies, Ahrensburg, Germany) through a zoom lens. Conversion of raw speckle images into a 2 dimensional (2-D) pseudo blood flow SC map (see Figures 3c−3d and 4a−4h) was constructed by custom written software based on Equation 1. Equation 2 was used to obtain τ_c of flow. 5 milliseconds interval was used for the exposure duration of the camera. The blood flow velocity in microvasculature was assumed to be inversely proportional to τ_c. The velocity of the blood vessels was normalized with the velocity at 0 minute (immediately after the application of glycerol or PBS).

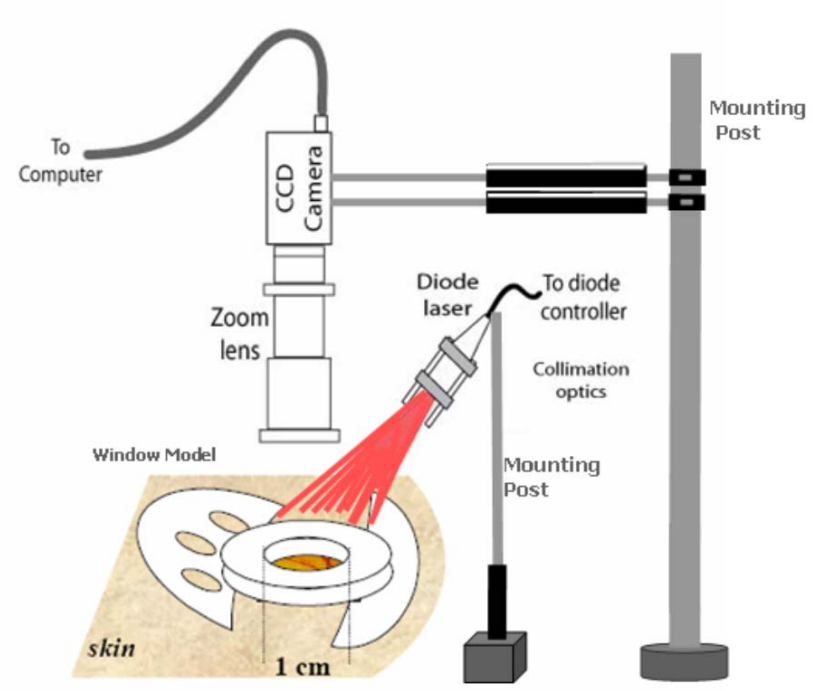

Figure 3.2. Schematic illustration of the instrumentation setup for speckle imaging of skin blood flow. A laser diode beam is expanded to illuminate a 1 cm diameter window on the sub-dermal skin, which is imaged onto the CCD camera. The computer acquires raw speckle images and computes relative skin blood flow maps.

3.4.3.4. Photography of hamster dorsal skin treated with glycerol or PBS solution

With the window in the horizontal plane, an EOS digital SLR camera (Digital Rebel XT Canon Japan) attached to a surgical microscope (Topcon OMS75, NJ, U.S.A.) was used to photograph the skin in the dorsal skin flap window preparation from the sub-dermal side. The epidermal side was imaged with a special lens (FUJINON-TV 1:1.8/75, Fuji Photo Optical Co., Japan) connected with an Olympus CAMADIA C-3040ZOOM digital camera (Olympus Optical Co., LTD, Tokyo, Japan). The camera shutter was

triggered using software (DSLR Remote Pro version 1.3.2, Breeze Systems). To enhance images a single layer of damp white gauze was placed on the sub-dermal side for epidermal photographs and vies versa. Photographs from the epidermal and sub-dermal sides of the native *in vivo* and treated skin with glycerol or saline solution were captured every 3 minutes (at the same time of LSCI measurements). Photographs (see Figures 3a) provide a measure of vessel diameter and along with sub-dermal visualization of the skin allowed identification if a vessel was an artery, vein, or capillary.

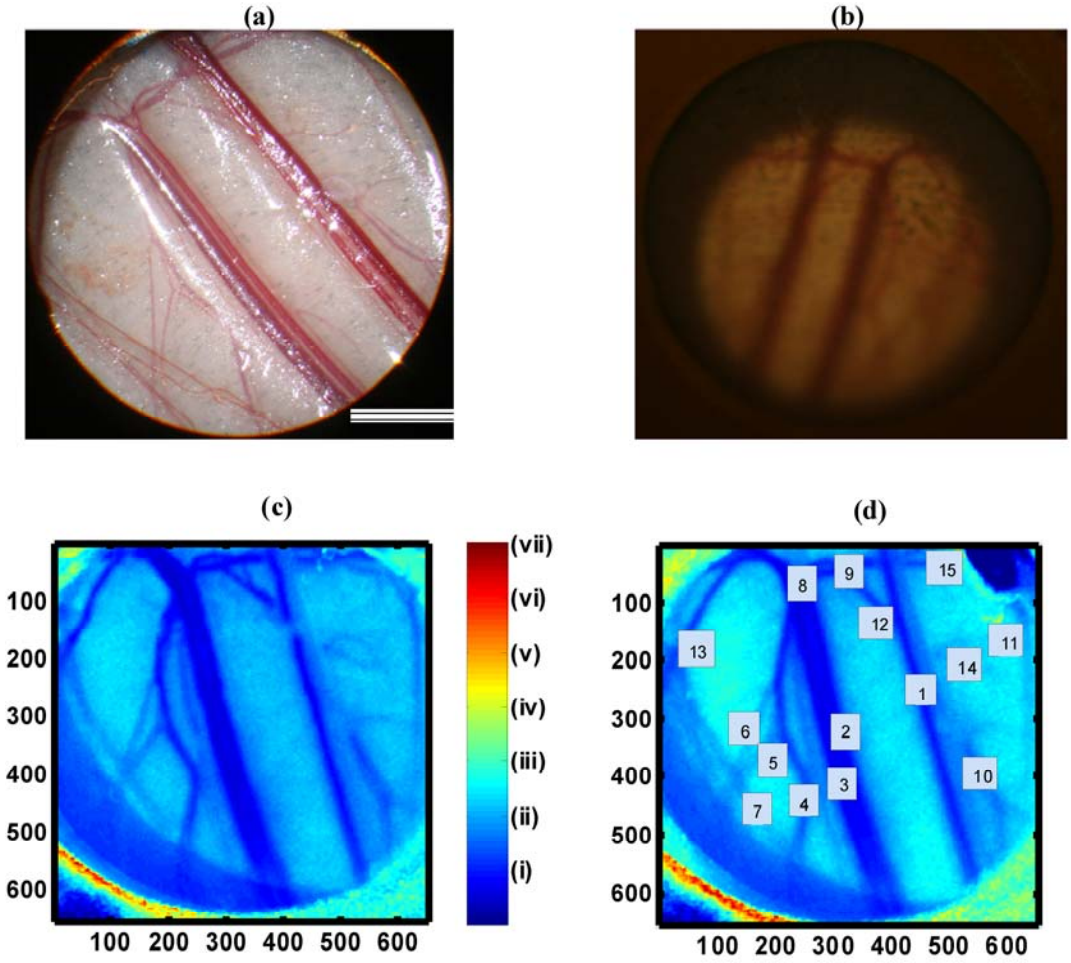

Figure 3.3. Photographs of a dorsal skin flap window preparation from one of the hamster from the experimental Group 1 (E1) (scale bar: 0.25 cm) showing the (a) sub-dermal (b) epidermal side of the window (c) SC images represent (i) fastest blood velocity or lowest SC (ii) slower blood velocity (iii) no blood flow (iv)-(vii) outside the window model (d) numbered microvasculature for identification and analysis. The darker area of the SC image represents blood vessels by black = 1 and white = 0 for speckle contrast.

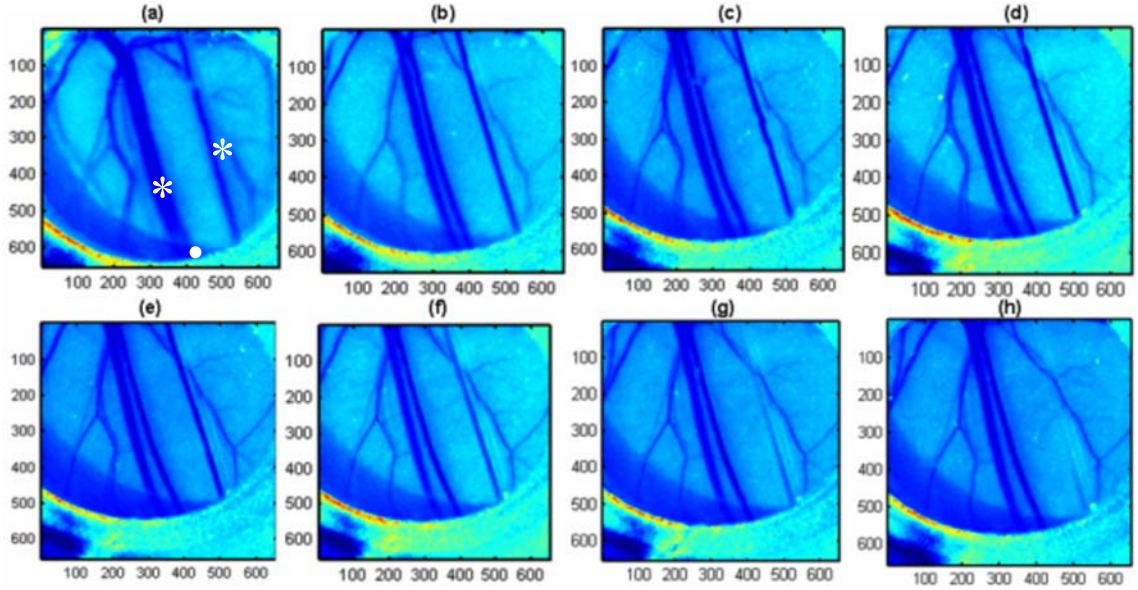

Figure 3.4. SC images of the sub-dermal blood vessels of one of the hamsters from the experimental Group 1 (E1) after application of anhydrous glycerol: (a) 0 minute (b) 3 minutes (c) 9 minutes (d) 15 minutes (e) 24 minutes (f) 27 minutes (g) 30 minutes (h) 36 minutes. Positions 1 and 3 of Figure 3.3d are veins highlighted with asterisk and position 2 of Figure 3.3d is an artery highlighted with a solid circle. Same color bar from Figure 3.3 applies to Figure 3.4. The darker area of the SC image represents blood vessels by black = 1 and white = 0 for speckle contrast.

3.4.3.5. Diameter measurement of blood vessels

Blood vessel's outer diameter was measured from the sub-dermal photograph using custom written software. The vessel diameter was measured at each position where the blood flow velocity was measured using the LSCI technique. The diameter was measured in small segments where the blood vessels are in a straight line. An edge detection Randon function was implemented in a form of Hough[16] transformation to detect the diameter of these small straight segments of the microvasculature. The

motivation for using the Hough transformation was to detect the edge of the blood vessels which could be in arbitrary shape. The average diameter of the arteries and veins of all seven hamsters was calculated by taking the average diameter of these small segments. The arteries and veins were identified as small or large based on their vessel diameter. Thus, individual standard deviation was calculated for these arteries and veins.

3.4.3.6. Blood flow velocity measurement of blood vessels

Blood flow velocity was measured from approximately two arteries, two veins, and four capillaries from each hamster model. However, these numbers varied slightly due to the individual hamster's physical modality. Only one position was selected for each microvasculature to measure the blood flow using LSCI technique. To calculate the blood flow velocity within the microvasculature (see Figure 3.5), a 5 × 5 square pixel subset from the entire pixels was chosen that fit entirely inside larger vessels (arteries and veins) from the 2-D map of the SC values that correspond to 76 × 76 μm^2 area. The area of 76 × 76 μm^2 was chosen to measure the blood velocity at the central part of arteries and veins as most of the larger microvasculature were much larger than this chosen area. However, when the diameter of the blood vessels decreased and become smaller than this selected area due to vasoconstriction from glycerol application, a 45.6 × 45.6 μm^2 area (3 × 3 square area) within the selected 5 × 5 square area of pixels was chosen in the 2-D map. Thus, only 35% of the original selected area of the 2-D map corresponded to the velocity-induced SC changes when the larger blood vessel diameter decreased due to glycerol application. This measuring technique was adopted to avoid capturing any SC

values from the surrounding areas which did not represent flow within the selected arteries or veins. To calculate the blood flow velocity within the capillaries a 2×2 square area of pixels was considered. However, for capillaries with vessel diameters less than 30.4 μm, a subset of 1×1 square area of pixel size was selected to calculate blood flow velocity. For a 1×1 square area of pixel from the SC image, blood flow velocity was not a statistically significant measure since the measurement was based on a single value. Therefore, measurement variance was not reduced by average. These selected subsets of pixels were always inside the vessel diameter.

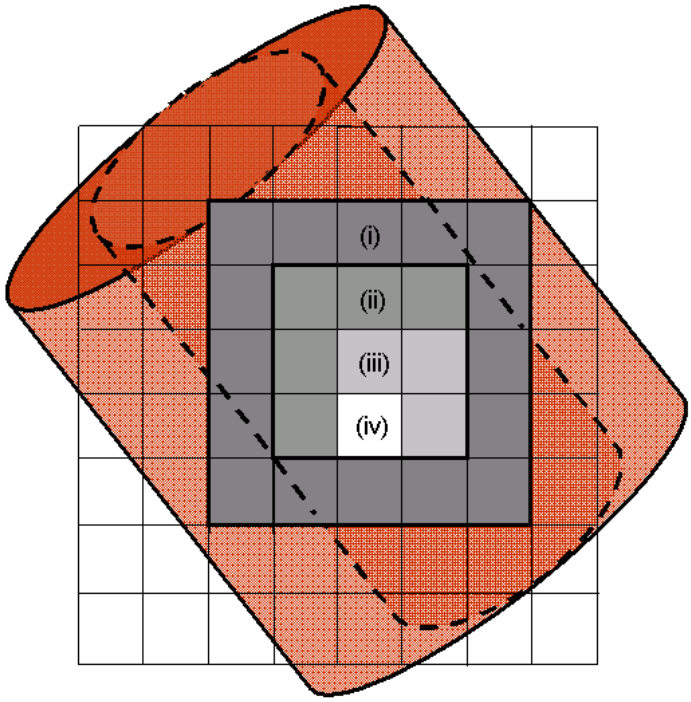

Figure 3.5. A subset of 8×8 pixels are shown from a 656×656 area of pixels of a SC image. Selection of subset of pixel size (i) 5×5 represents 76×76 μm^2 area inside larger blood vessels such as arteries and veins (ii) 3×3 represents 45.6×45.6 μm^2 area inside larger blood vessels with diameter < 76 μm (iii) 2×2 represents 30.4×30.4 μm^2 area inside capillaries (iv) 1×1 represents 15.2×15.2 μm^2 area inside capillaries to calculate blood flow velocity measurements as a function of vessel size.

3.4.3.7. Field-of-view (FOV) co-registration image

The position of imager and animal were fixed for 60 or 66 minutes. Animals were housed overnight at the Animal Resource Center and returned to our laboratory for 24 hours measurements. The field-of-view (FOV) registration was obtained by optical alignment of the SC images at 0 minutes and 24 hours for both experimental and control groups[17–19] to prevent erroneous 24 hours measurements. Specific points in the major arteries and veins of the SC images from 24 hours measurement were co-registered with the SC images from 0 minute. The technique of registering image is illustrated in Figure 3.6. If the SC images from these two observation points were not optically aligned, the registered image would appear distorted. For the capillaries once the alignment was done, a particular pixel (i, j) was selected from the SC image of 60 or 66 minutes which was also valid for 24 hours. For all hamsters, the registered images were found to be optically aligned after the spatial transformation (Figure 3.7).

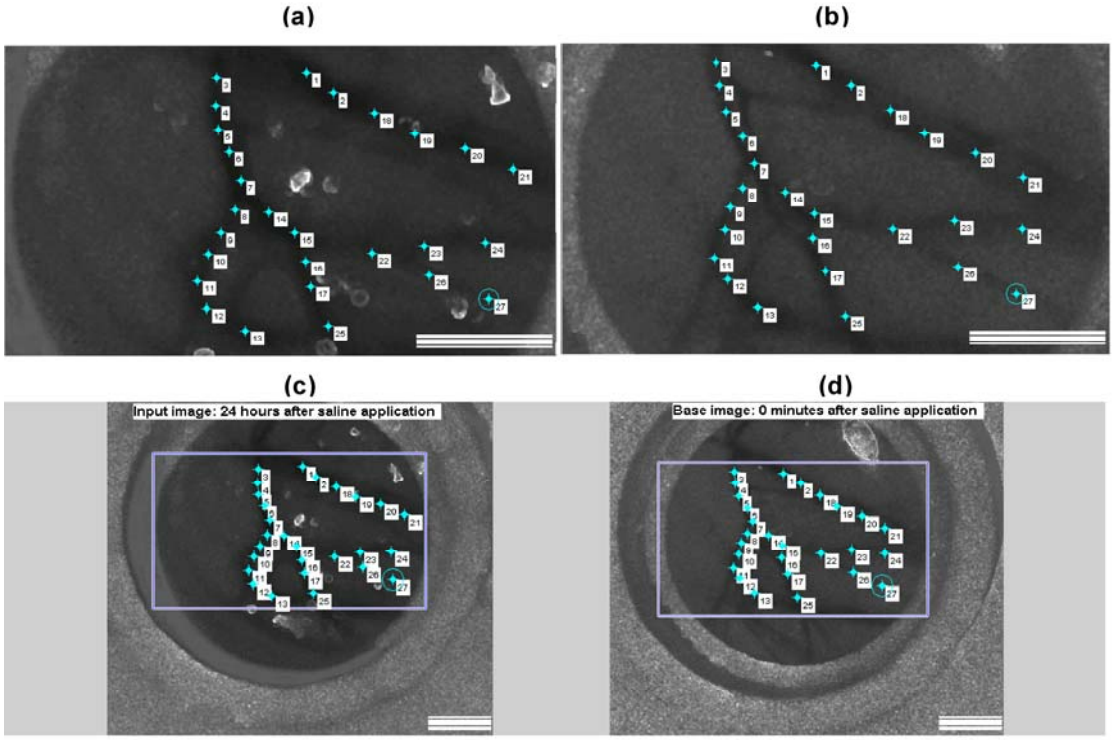

Figure 3.6. Registering a SC image at 24 hours as input (c) with base image or 0 minutes after saline application (d). (a) and (b) are magnified images of input and base SC images, respectively. The control point pairs the input and base images are highlighted in blue stars and identified with numbers. To get a better resolution minimum of 27 control point pairs was selected in the input and base SC images. The scale bar: 0.25 cm for all four images.

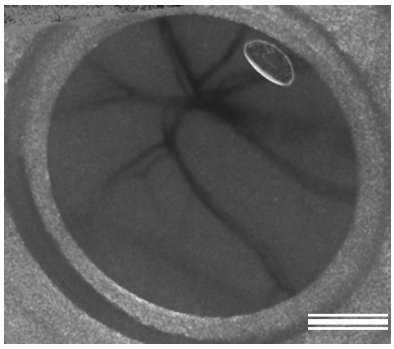

Figure 3.7. Registered input and base images after spatial transformation showed an optical alignment between speckle images at 0 minutes and 24 hours after saline application. The scale bar: 0.25 cm.

3.4.4. Statistical analysis

After PBS or glycerol application, averages were taken for the control (n = 6) and experimental (n = 7) groups to identify significant changes in blood flow velocity. Variance was calculated by performing standard deviation between all animals at each observation time point for the control and experimental groups. A Bonferroni correction was applied in which a pair-wise comparison was performed for all three separate areas (i.e. artery, vein, and capillary) at each time point.

3.5. RESULTS

3.5.1. Effect of 100% anhydrous glycerol on SC imaging

Photographs from the sub-dermal and epidermal skin of hamster after flap window implantation are shown in Figure 3.3a and Figure 3.3b, respectively. The epidermal side of the skin optically cleared within 3 minutes after treatment with glycerol. The skin remains transparent for at least 66 minutes. The skin was not transparent at 24 hours. Figures 4 and 8−12 illustrate the effect of 100% anhydrous glycerol on blood vessels of hamster's sub-dermal skin. The SC image consisting of 656 × 656 areas of pixels (1 pixel = 15.2 μm), was computed directly from the raw speckle images using Equation 1 (Figures 3c−3d, 4a−4h). The darker areas in the SC image indicate blood flow in the microvasculature.

One hamster was selected from each experimental group to show typical results on the changes in blood flow velocity (see Figures 8−10) due to glycerol application. The

average changes in blood flow velocity of all seven hamsters of the experimental group with standard deviations are illustrated in Figure 3.11. Each velocity response is normalized with respect to velocity at 0 minutes. Table 3.1 illustrates the changes in vessel diameter and blood flow velocity of sub-dermal blood vessels due to glycerol application in all seven hamsters of the experimental group. The arteries and veins are both divided in to small and large vessels based on their diameter. The change in diameter is illustrated in Figure 3.12.

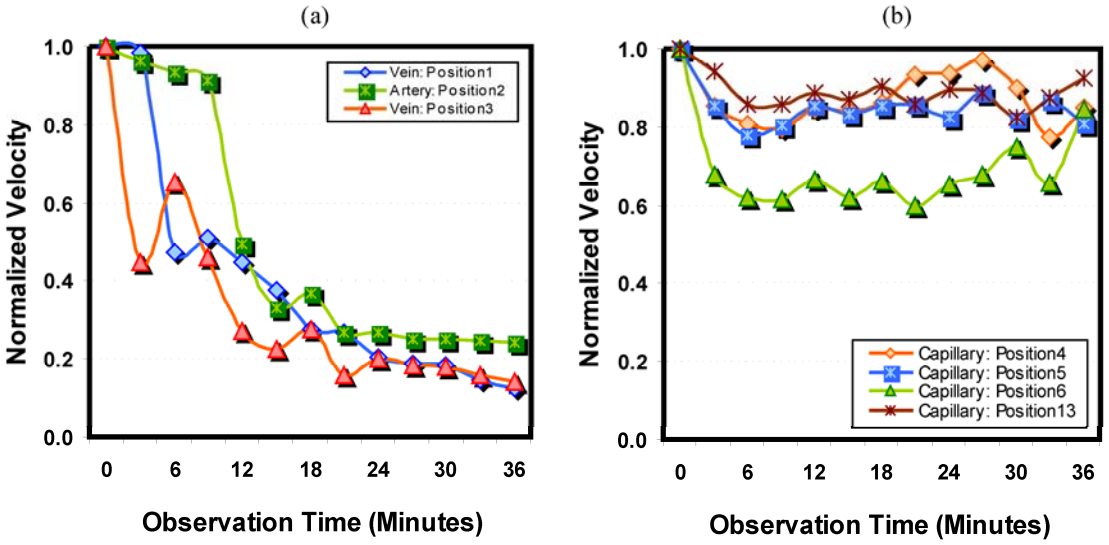

Figure 3.8. Normalized velocity of blood perfusion in arteries, veins, and capillaries of one of the two hamster's sub-dermal skin from Group E1 treated with glycerol. Diameter of the artery (position 2) and two veins (positions 1 and 3) are small. The SC images of this hamster are shown in Figure 3.4. Observation time: 36 minutes.

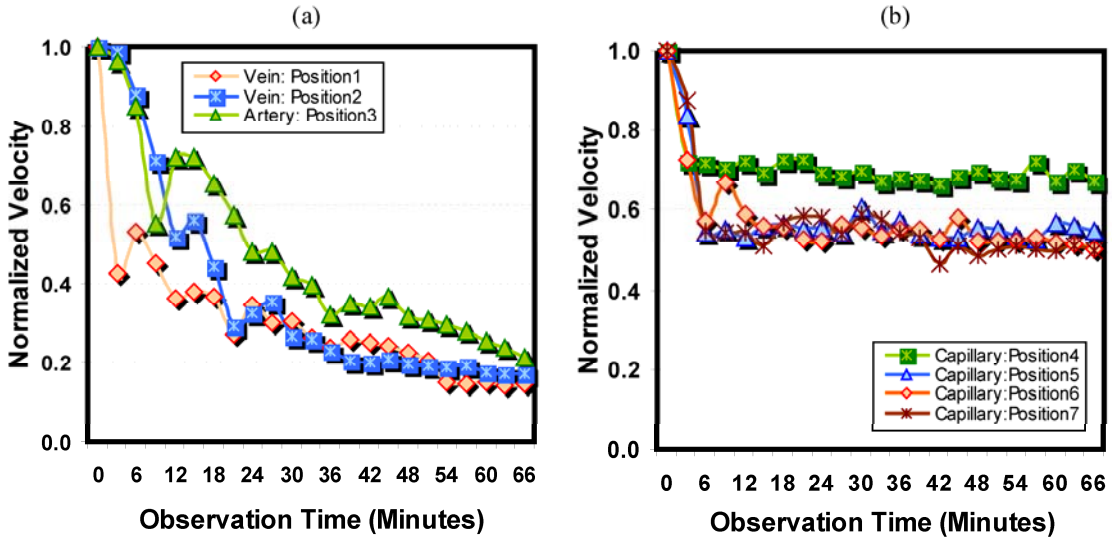

Figure 3.9. Normalized velocity of blood perfusion in microvalsculatures of one of the two hamster's sub-dermal skin from Group E2 treated with glycerol. The diameter of the artery (position 3) and both veins (positions 1 and 2) are small and large, respectively. Observation time: 66 minutes.

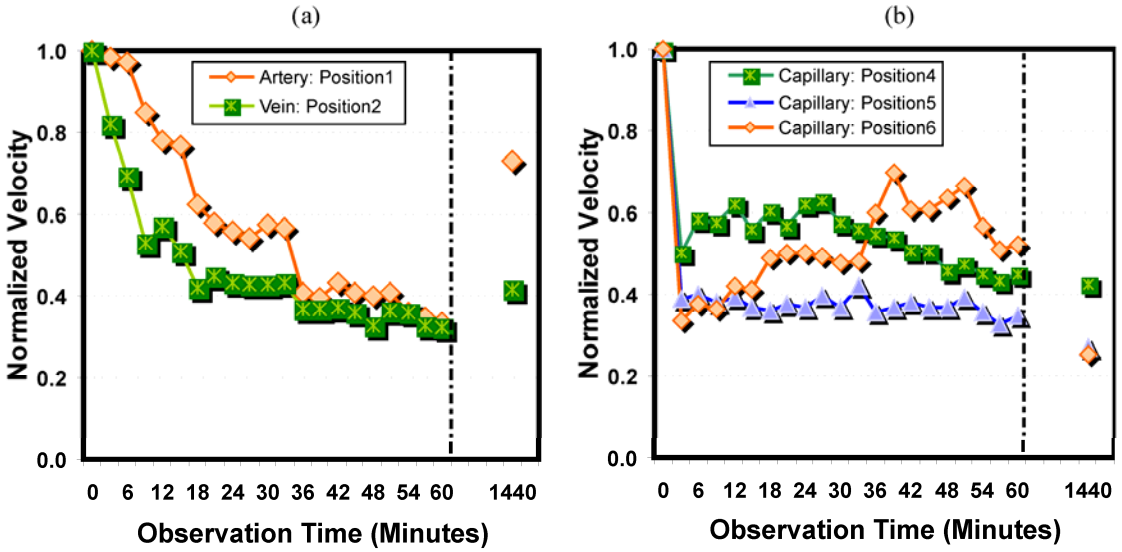

Figure 3.10. Normalized velocity of blood perfusion in arteries, veins, and capillaries of one of the three hamster's sub-dermal skin from Group E3 treated with glycerol. The artery (position 1) and vein (position 2) are large in diameter. Observation time: 60 minutes and one measurement at 24 hours.

Table 3.1. Average changes in diameter of blood vessels and normalized blood flow velocity due to hyper-osmotic agent with standard deviation.

	Arteries (n = 14)				Veins (n = 11)			
	Small: 144−267 µm (n = 8)		Large: 321−336 µm (n = 6)		Small: 249−354 µm (n = 5)		Large: 471-600 µm (n = 6)	
Time min	Diameter	Normalized Velocity	Diameter	Normalized Velocity	Diameter	Normalized Velocity	Diameter	Normalized Velocity
0	211 ± 8	1.00±0.00	328 ± 2	1.00±0.00	298 ± 6	1.00±0.00	540 ± 9	1.00±0.00
3	308 ± 6	0.92±0.02	455 ± 25	0.96±0.02	301 ± 15	0.79±0.03	519 ± 8	0.82±0.04
6	349 ± 8	0.90±0.01	483 ± 25	0.91±0.03	273 ± 16	0.67±0.02	537 ± 12	0.75±0.02
9	376 ± 6	0.74±0.04	493 ± 12	0.84±0.01	252 ± 14	0.58±0.03	533 ± 5	0.63±0.02
12	367 ± 13	0.65±0.03	504 ± 15	0.82±0.01	267 ± 23	0.49±0.03	512 ± 10	0.55±0.02
15	343 ± 11	0.64±0.06	429 ± 9	0.87±0.02	236 ± 12	0.45±0.03	492 ± 17	0.65±0.04
18	336 ± 16	0.62±0.05	398 ± 12	0.75±0.02	311 ± 22	0.40±0.03	522 ± 23	0.56±0.03
21	288 ± 25	0.49±0.04	334 ± 15	0.74±0.03	319 ± 19	0.36±0.02	576 ± 40	0.41±0.03
24	274 ± 27	0.45±0.03	311 ± 14	0.81±0.06	328 ± 24	0.36±0.03	574 ± 24	0.50±0.03
27	255 ± 29	0.45±0.04	252 ± 4	0.79±0.05	331 ± 37	0.36±0.04	468 ± 17	0.50±0.03
30	244 ± 27	0.40±0.03	214 ± 4	0.73±0.04	259 ± 27	0.32±0.03	448 ± 34	0.55±0.06
33	225 ± 24	0.39±0.03	206 ± 7	0.68±0.02	221 ± 47	0.34±0.03	423 ± 31	0.48±0.03
36	210 ± 23	0.38±0.04	199 ± 8	0.65±0.03	190 ± 49[*2]	0.32±0.03	382 ± 27	0.45±0.03
39	212 ± 8	0.38±0.01	197 ± 8	0.58±0.03	175 ± 34[*2]	0.32±0.03	372 ± 21	0.36±0.02
42	218 ± 7	0.37±0.01	187 ± 9	0.58±0.03	164 ± 24[*2]	0.32±0.03	356 ± 20	0.32±0.01
45	246 ± 18	0.40±0.01	170 ± 11	0.55±0.03	157 ± 20[*2]	0.32±0.03	338 ± 22	0.33±0.01
48	241 ± 19	0.35±0.01	232 ± 8	0.54±0.03	252 ± 32[*2]	0.31±0.03	357 ± 15	0.31±0.01
51	221 ± 10	0.31±0.00	219 ± 12	0.56±0.04	318 ± 32[*2]	0.31±0.03	407 ± 19	0.30±0.01
54	230 ± 15	0.32±0.01	258 ± 10	0.55±0.03	334 ± 41[*2]	0.30±0.03	404 ± 8	0.30±0.01
57	206 ± 14[*1]	0.31±0.01	254 ± 5	0.52±0.03	294 ± 35[*2]	0.29±0.02	406 ± 5	0.30±0.01
60	225 ± 12[*1]	0.25±0.01	239 ± 11	0.53±0.03	246 ± 28[*2]	0.29±0.03	418 ± 7	0.29±0.01
63	267 ± 7[*1]	0.22±0.01	233 ± 15	0.52±0.04	200 ± 29[*2]	0.25±0.03	193 ± 37	0.29±0.02
66	253 ± 20[*1]	0.20±0.00	233 ± 11	0.51±0.04	181 ± 26[*2]	0.21±0.03	200 ± 38	0.27±0.02
1440	228 ± 4	0.82±0.00	291 ± 6	0.99±0.03	221 ± 19	0.51±0.02	462 ± 20	0.61±0.02

n is the total number of blood vessels, which were chosen in each experimental group to calculate blood flow velocity. n is not same for each observation time for arteries (n_a) and veins (n_v): (i) between 0−36 minutes n_a=14 (S:8, L:6) and n_v=11 (S:5, L:6); (ii) between 36−60 minutes n_a=11 (S:5, L:6) and n_v= 8 (S:4, L:4); (iii) at 24 hours n_a= 7 (S:1, L:6) and n_v= 4 (S:2, L:2) where S and L represent the number of small and large blood vessels, respectively. Table 3.2 listed the total n for each experimental group.

[*1]Three hamsters in the experimental group had complete blood vessel occlusion in the small arteries.

[*2] Four hamsters in the experimental group had complete blood vessel occlusion in the small veins.

The diameter of both small (144−267 µm) and large (321−336 µm) arteries increased immediately after glycerol application, and then decreased after 12 minutes. The rate of occlusion in small arteries was found to be much higher than for the large

arteries. Complete blood flow stoppage was observed in three out of five small arteries between 57−66 minutes after the glycerol application in three hamsters in groups E2 and E3. At 24 hours, small arteries were still slightly dilated and large arteries regained 89% of their baseline diameter. The diameter of both small and large veins varied (see Figure 3.12). After the glycerol application, blood flow ceased in all four small veins among four hamsters between 36−66 minutes. At 24 hours, the small and large veins regained 74 % and 86% of their baseline diameter, respectively.

The blood flow velocity reduced faster in small arteries compared to the large arteries during minutes 9 to 57. Three out of five small arteries were occluded during 57−66 minutes and the blood flow ceased. No occlusions were identified among large arteries. Although, the average blood flow velocity in the arteries decreased for all seven hamsters after applying hyper osmotic agent (Figure 3.11), at 24 hours, the velocity regained 97% of its original flow.

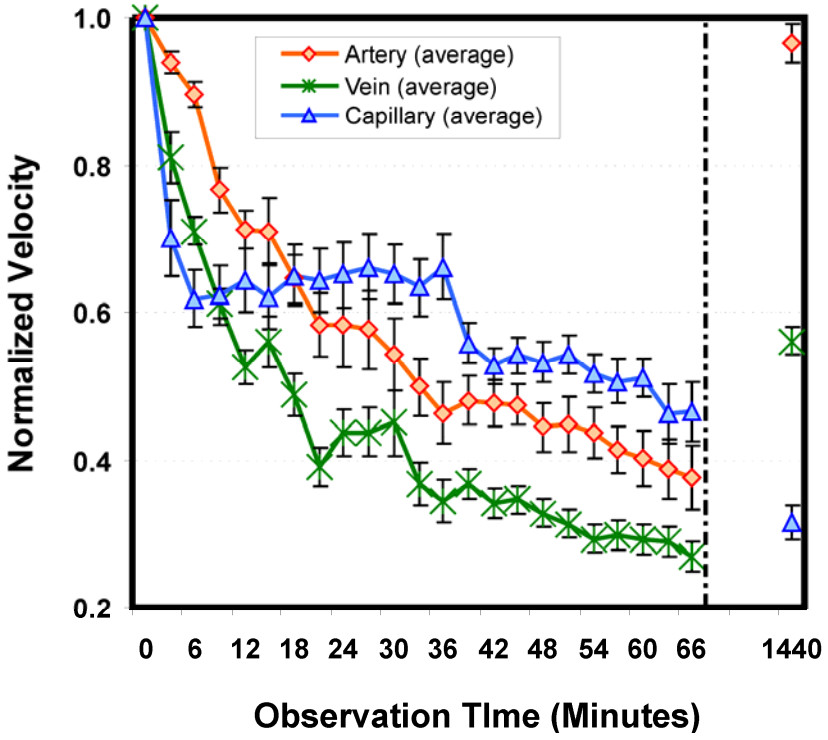

Figure 3.11. Average changes in blood flow velocity of all arteries, veins, and capillaries due to glycerol application to the sub-dermal skin of 7 hamsters from the experimental group. The average value standard deviations of arteries, veins, and capillaries are ±0−0.06, ±0−0.05, and ±0−0.05, respectively. Each response is normalized with respect to its value at t = 0.

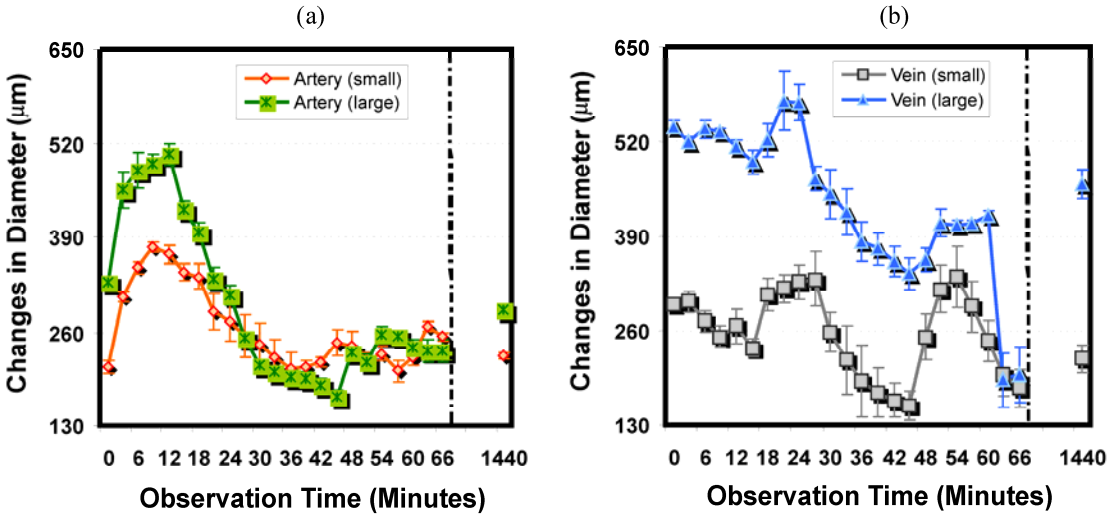

Figure 3.12. After applying glycerol the average changes in diameter of the hamster skin blood vessels were measured for arteries and veins. The arteries and vein were classified based on their diameter at baseline. The baseline diameter of arteries was much smaller than veins. The diameters of the small and large arteries ranged between 144−267 µm and 321−336 µm, respectively. The baseline diameters of the small and large veins were 249−354 µm and 471−600 µm, respectively. A standard deviation was calculated among small and larger arteries of the hamsters from the experimental group.

All four small veins with diameter between 249−354 µm from four hamsters in the experimental group had a significant reduction in blood flow velocity from 36 to 66 minutes. For example, the dark area corresponding to the position 1 in Figure 3.4g completely disappeared within 36 minutes in the SC image. Blood flow velocity of veins was further reduced up to 66 minutes compared to 30 minute measurements (Figures 3.9a−3.10a). Large veins with diameter 471−600 µm did show some reduction in blood flow velocity without any occlusion. All veins showed a similar reduction in blood velocity as arteries for all 7 hamsters after glycerol application (Figure 3.11). At 24 hours, blood flow velocity of all veins regained 56% compared to baseline velocity.

Any blood vessels with diameter within 15.2−30.4 μm were considered as capillaries. The blood flow in the capillaries decreased after applying hyper osmotic agent which is illustrated in Figures 3.8b, 3.9b, and 3.10b. An immediate reduction in blood velocity was observed within the first six minutes after initial glycerol application and stayed unchanged up to 30 minutes. The blood flow velocity in some capillaries continued to decrease at 24 hours compared to 1 hour (Figures 3.10b and 3.11). Table 3.2 lists the normalized blood flow velocities of arteries, veins, and capillaries which are categorized into experimental groups after skin was treated with glycerol. Each measured blood flow velocity was compared with respect to its baseline velocity at t=0. After normalization, the baseline blood flow velocity was specified as a unity (1.0). Standard deviations in Table 3.2 were with respect to normalized values.

Table 3.2. Relative blood flow velocity of the microvasculatures in the experimental group hamster's sub-dermal skin due to 100% anhydrous glycerol application.

Observation Time	3-minute	½ hour	1 hour	24 hours
		Arteries		
		(Average ± Standard deviation **)**		
E1 (n = 3)	0.962 ± 0.016	0.254 ± 0.023	—	—
E2 (n = 4)	0.961 ± 0.001	0.416 ± 0.022	0.254 ± 0.012	—
E3 (n = 7)	0.916 ± 0.018	0.739 ± 0.037	0.486 ± 0.039	0.966 ± 0.034*
All Groups	0.938± 0.016	0.543 ± 0.046	0.402 ± 0.038	—
		Veins		
		(Average ± Standard deviation **)**		
E1 (n = 3)	0.714 ± 0.047	0.183 ± 0.002	—	—
E2 (n = 4)	0.706 ± 0.049	0.286 ± 0.003	0.161 ± 0.003	—
E3 (n = 4)	0.984 ± 0.036	0.813 ± 0.049	0.424 ± 0.013	0.561 ± 0.019
All Groups	0.809 ± 0.034	0.449 ± 0.045	0.292 ± 0.019	—
		Capillaries		
		(Average ± Standard deviation **)**		
E1 (n = 8)	0.832 ± 0.027	0.825 ± 0.015	—	—
E2 (n = 7)	0.790 ± 0.019	0.612 ± 0.015	0.564 ± 0.019	—
E3 (n = 10)	0.618 ± 0.021	0.550 ± 0.003	0.473 ± 0.022	0.316 ± 0.023
All Groups	0.701 ± 0.052	0.651± 0.041	0.510 ± 0.025	—

n is the total number of blood vessels that were chosen in each experimental group to calculate blood flow velocity.
* Not a significant change ($p<0.05$) based on ANOVA t-test.

3.5.2. Effect of PBS solution on SC imaging

The average change in blood flow velocity of the blood vessels of all six hamsters from control groups C1 and C2 due to application of PBS solution is illustrated in Figure 3.13. Unlike 100% anhydrous glycerol, the PBS solution slightly increased blood flow velocity of the hamster's sub-dermal microvasculature. In both control groups, the average arterial blood velocity of four out of six hamsters at 3 minutes after applying PBS solution showed an increase (compared to baseline) similar to veins. Unlike veins,

the arterial blood velocity exhibited a steady trend that was close to the baseline velocity. A slight decrease in arterial blood velocity was observed between 18 and 33 minutes followed by a gradual increase up to 60 minutes after the initial PBS application. However, the blood flow velocity of arteries, veins, or capillaries did not increase significantly. At 24 hours, all three hamsters from the C2 group demonstrated a slight increase in blood flow velocity among arteries, veins, and capillaries compared to the baseline. However, the increase in the blood flow velocity at any given time was not statistically significant. These statistically non-significant changes in blood flow velocity after applying PBS solution may have been due to some bias caused by surgical trauma or anesthesia.

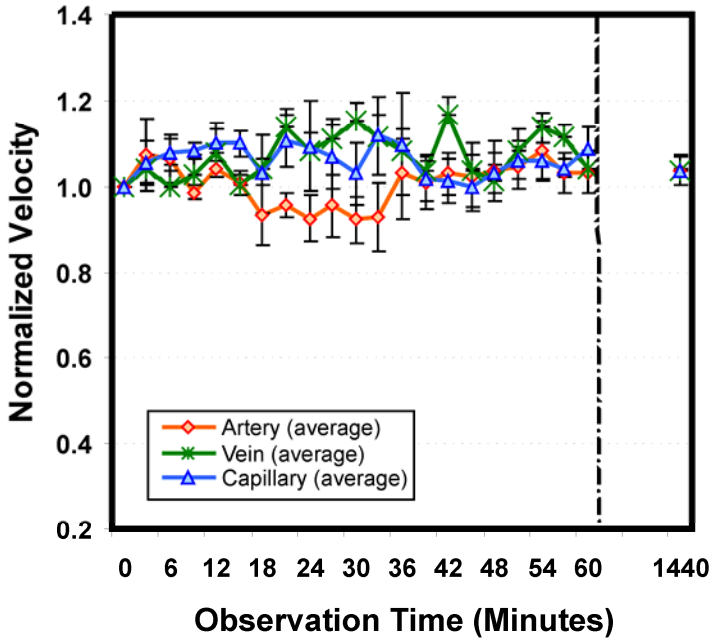

Figure 3.13. Normalized average blood velocity of all six hamster's sub-dermal skin blood vessels after saline application. Variance of blood flow velocity was calculated by standard deviation of all hamsters of individual groups for each observation time. Observation time: 60 minutes and one measurement at 24 hours.

3.6. DISCUSSION

Although the SC values of the initial native skin (pre-glycerol treatment) blood flow varied among the hamsters, the ratio between the velocity calculated based on correlation time (τ_c) at two different observation time points of the microvasculature was consistent among all seven hamsters of the experimental group over time.

The blood flow velocity of arteries in all seven hamsters decreased at 30 minutes after the initial application of 100% anhydrous glycerol. In this LSCI study, after glycerol application the average diameter of small and large arteries increased up to 9 and 12 minutes, respectively, followed by a decrease. Both of these findings are closely correlated with the findings of a previous DOCT studies by Vargas *et al.* and Barton *et al.*[3, 20–21] In the DOCT study, the arterial diameter increased up to 10 minutes.

Our results illustrate that the blood velocity of veins was reduced faster and more significantly than arteries. The velocity decreased in small veins to such an extent that the dark area due to blood flow, disappeared completely within 36 minutes after applying 100% anhydrous glycerol. We also observed small arteries occluded along with cessation of blood flow velocity at 57 minutes from initial glycerol application. This occlusion was due to small vein's thin vessel wall compared to artery's lumen diameter. Thus, the chemical diffusion dynamics occurred faster in veins than arteries. This finding verified results from the DOCT study, where Doppler images showed glycerol enhanced trans-dermal visualization of blood vessels along with cessation of blood flow in veins and sometimes in arteries.[3]

The decrease in blood flow induced by glycerol could be due to an inflammatory response by the tissue in response to osmotic equilibrium deviations. In an acute inflammatory response, blood vessels are subjected to increased permeability and plasma exits into the extra-vascular network.[22–23] Moreover, in native blood vessels, the majority of blood cells are concentrated in the center of the stream, with an increased concentration of plasma near the lumen wall.[22] This characteristic is important in keeping the viscosity near the lumen wall at a minimum so that peripheral resistance is lower than it would be if the cells were uniformly distributed. If plasma is lost to the extra-vascular network due to osmotic pressure incurred by 100% anhydrous glycerol, this property is lost and the flow in the blood vessels is reduced because there is greater drag on the lumen walls.[22]

The diameter of small arteries and veins decreased along with reduction in blood flow velocity. Thus, the change in diameter and reduction in blood velocity may have a direct correlation. For example, in Figure 3.3d, Position 1 (diameter 144 μm) and position 3 (diameter 567 μm) are both veins, only position 1 has a significant reduction in blood velocity (see the gradual changes of dark area in Figure 3.4a to Figure 3.4h). The dark area representing position 1 disappears completely in Figure 3.4h. This effect may be caused by an increased clearing of the tissue overlying the vessels and could also occur with vasoconstriction.

Some of the small arteries and veins with 2.3−2.4× smaller diameter compared to large microvasculature showed a major reduction in blood flow velocity with complete cession. At 30 minutes after glycerol application, the average velocity of the small

arteries decreased 60.0% compared to the large arteries whose velocity reduced only 27.0%. Three out of five small arteries completely occluded between 57−66 minutes. At 30 minutes, the average blood flow velocity of small veins reduced 68% compared to 45% in large veins. Blood flow in majority of small veins (4 out of 5) ceased at 36 minutes which was much earlier than small arteries. At 24 hours, the arteries and veins respectively regained 97% and 56% of their original blood velocity. A t-test with 95% confidence interval showed that the regained velocity of arteries compared to baseline is not statistically significant. However, the blood flow velocity of veins at 24 hours is significant. These results established that arteries can completely reverse the effect of a hyper-osmotic agent without any sub-dermal skin hydration with 0.9% saline.

The reason for this recovery of blood flow velocity in arteries and veins without saline may due to one side of the epidermal skin being intact during the experiment. The *in vivo* skin of hamsters can rapidly hydrate this microvasculature. Wang and Tuchin reported optical clearing by topical sub-dermal application of glycerol was reversible and under certain conditions may not damage skin once the tissue was hydrated.[24] At 24 hours, we observed some hamster's sub-dermal tissue dehydrated even after the sub-dermal side of the skin was covered with a round piece of glass. To avoid tissue dehydration it was necessary to apply saline to the tissue.

These observed morphological effects of glycerol will likely aid to permanent laser destruction of blood vessels of cutaneous vascular lesions. Specifically, decreased peripheral blood flow velocity induced by glycerol will facilitate permanent destruction of blood vessels using laser irradiation, particularly in those situations where high

velocity of blood flow compromises the effectiveness of laser irradiation. Previous studies have shown that complete flow cessation in blood vessels before irradiation significantly reduces the fluence rate [W/cm^2], which is required to destroy the vessel permanently.[25]

This study further showed that the blood flow velocity in capillaries of treated sub-dermal skin reduced faster than in either an artery or a vein. This effect was due to capillary's thinnest vessel wall compared to arteries and veins. In a capillary, the effect was more significant since only 1−2 red blood cells can pass through the vessel at a given time. 100% anhydrous glycerol increased viscosity and had a long term effect with less recovery.[3, 20] Within 3 minutes after initial glycerol application, the blood flow velocity in all capillaries decreased by 30%. Unlike arteries and veins, capillaries velocity continuously decreased up to 24 hours.

One possible hypothesis for this phenomenon is that the local blood velocity in capillaries is mediated by nitric oxide (NO), whereas flow in arteries and veins is at least partially regulated by the autonomic nervous system (ANS). Thus, the ANS can override the effect of topical application of glycerol on blood velocity of arteries and veins. Another possible hypothesis is that the much smaller cross-sectional area of capillaries is very quickly and easily affected by the hyper-osmotic agent. Burek *et al.* states that the reduction of blood flow velocity in the microvasculature such as arteries is due to an inhibition of NO biosynthesis.[26] The study further showed that NO is important for functional hyperemia (vasodilatation) of the cat optic nerve head (ONH) microcirculation during increased neural activity with flickering light stimuli to the eye.[25] Wang *et al*.

agrees that NO clearly plays a role in regulating blood flow to the dog ophthalmic arteries.[27] Thus, the changes in blood flow velocity and diameter of the microvasculature may have direct correlation with the inhibition of NO biosynthesis after the hamster's sub-dermal skin is treated with 100% anhydrous glycerol. In the LCSI study, blood vessels dilated in the beginning of the glycerol treatment, which could be due to the availability of NO to the microvasculature. However, while time progressed the NO biosynthesis is inhibited and the microvasculature is forced to constrict along with reduction in blood flow velocity. In a previous study, Bertuglia *et al.* measurements on dynamic arteriolar diameter changes from skeletal muscle in conscious hamsters demonstrate that NO is not required for vasomotion in the skeletal muscle of conscious animals.[28] Bertuglia's study further validates the findings of this LSCI study that the NO definitely plays a role in vasomotion or regulating the diameter of the microvasculatures of the hamster's sub-dermal skin when the hamsters are under deep anesthetic and completely unconscious. Further investigation is needed to confirm either of these hypotheses.

A statistical analysis was performed for all blood flow velocity data collected from the seven hamsters of the experimental group. The Bonferroni correction was applied to the interaction decomposition in which a pair wise comparison is performed for all three separate areas (i.e. artery, vein, and capillary) at each time point.[29–31] A statistical significance ($p<0.05$) was observed in the difference in blood velocity between an artery and a capillary, and a vein and a capillary at 12 minutes after the initial application of glycerol. However, the changes in blood flow velocity of arteries and veins

of all seven hamsters showed no significance during 0−66 minutes except for at 24 hours. At 24 hours, arteries normalized average blood flow velocity was not significant with respect to baseline unlike veins.

The accuracy of these relative changes in blood flow velocity and blood vessel diameter may have impacted by surgical trauma and effects of anesthesia. The FOV co-register and LSCI sampling error may also introduce uncertainty. In all likelihood, the changes that are observed in this study are probably due to a combination of multiple physiological processes induced by glycerol application.

3.7. CONCLUSION

Glycerol was found to decrease the blood flow velocity of veins and to some degree of arteries within 1 hour after the initial application of glycerol. Although, at 24 hours recovery of blood flow velocity was observed without hydrating the glycerol treated skin with PBS or 0.9% saline, unlike arteries veins did not regained normal velocity. Also, capillaries did not return to normal flow compared to pre-glycerol treatment. A further study on capillary treated with glycerol can be done using a 2-photon microscope that could validate and quantify the absolute blood flow velocity at 24 hours. The glycerol application also caused an immediate increase in blood vessel diameter followed by a reduction in diameter within 1 hour. At 24 hours, arteries and veins regained their original vessel diameter. Further studies are required to evaluate the two hypothesis presented in this study to identify the underline causes for blood flow velocity

to reduce along with decrease in vessel diameter after application of 100% anhydrous glycerol.

3.8. ACKNOWLEDGEMENTS

This research has been supported by the National Science Foundation (UTA06−688) and Caster Foundation. Raiyan Zaman was a recipient of the Air Force Academy Travel Grant to attend ASLMS conference, 2008. Special thanks to Dr. Gracie Vargas for teaching Raiyan the technique for implanting the window model on hamster.

3.9. REFERENCES

1. Vargas G, Chan EK, Barton JK, Rylander III HG, Welch AJ. Use of an agent to reduce scattering in skin. Lasers Surgery and Medicine, 1999; 24:133–141.

2. Ghosn MG, Tuchin VV, and Larin KV. Depth-resolved monitoring of glucose diffusion in tissues by using optical coherence tomography. Optics Letters 2006; 31(15): 2314−2316.

3. Vargas G, Readinger A, Dozier SS, Welch AJ. Morphological changes in blood vessels produced by hyper osmotic agents and measured by optical coherence tomography. Photochemistry and Photobiology 2003; 77(5): 541–549.

4. Bakutkin VV, Maksimova IL, Semyonova TN, Tuchin VV, Kon IL. Controlling of optical properties of sclera. Proc. SPIE 2393 1995; 137–141.

5. Tuchin VV, Maksimova IL, Zimnyahkov DA, Kon IL, Mavlutov AK, Mishin AA. Light propagation in tissues with controlled optical properties. Proc. SPIE 2925, 1996; 118–142.

6. Tuchin VV, Maksimova IL, Zimnyakov DA, Kon IL, Mavlutov AK, Mishin AA. Light propagation in tissues with controlled optical properties. Journal of Biomedical Optics 1997; 2: 401–417.

7. Vargas G, Chan KF, Thomsen SL, Welch AJ. Use of osmotically active agents to alter optical properties of tissue: effects on the detected fluorescence signal measured through skin. Lasers Surg.Med.2001; 29:213–220.

8. Choi B, Ramirez-San-Juan JC, Lotfi j, Nelson JS, Linear response range charactization and *in vivo* application of laser speckle imaging of blood flow dynamics. Journal of Biomedical Optics 2006; 11(4):041129.

9. Zhu D, Zhang J, Cui H, Mao Z, Li P, Luo Q. Short-term and long-term effects of optical clearing agents on blood vessels in chick chorioallantoic membrane. Journal of Biomedical Optics 2008; 13(2):021106.

10. Briers JD, Webster S. Laser speckle contrast analysis (LASCA): a nonscanning, full-field technique for monitoring capillary blood flow. Journal of Biomedical Optics 1996; 1:174–179.

11. Dunn AK, Bolay H, Moskowitz MA, Boas DA. Dynamic imaging of cerebral blood flow using laser speckle. Journal of Cerebral Blood Flow and Metabolism 2001; 21:195–201.

12. Fercher A, Briers J. Flow visualization by means of single exposure speckle photography. Opt. Commun. 1981; 37:326–329.

13. Yuan S, Devor A, Boas DA, Dunn AK. Determination of optical exposure time for imaging of blood flow changes with laser speckle contrast imaging. Applied Optics 2005; 44(10): 1823−1830.

14. Papenfuss HD, Gross JF, Intaglietta M, Treese FA. A transparent access chamber for the rat dorsal skin flap. Microvascular Research 1979; 18:311–318.

15. Dunn AK, Bolay H, Moskowitz MA, Boas DA. Dynamic imaging of cerebral blood flow using laser speckle. Journal of Cerebral Blood Flow and Metabolism 2001; 21:195–201.

16. Boyle R, and Thomas R. *Computer Vision:A First Course*, Blackwell Scientific Publications 1988; Chap. 5.

17. Shams R, Barnes N, and Harley R. Image registration in Hough space using gradient of images. IEEE Xplore on Digital Image Computing Techniques and Applications 2007; 226−232.

18. Chunhavittayatera S, Chitsobhuk O, and Tongprasert K. Image registration using Hough transform and phase correlation. International Conference on Advanced Communication Technology (ICACT) 2006; 973–977.

19. Cole-Rhodes A, Johnson K, LeMoigne J, and Zavorin I. Multiresolution registration of remote sensing imagery by optimization of mutual information using a stochastic gradient. IEEE Trans. on Image Processing 2003; 12(12):1495–1511.

20. Vargas G. Reduction of light scattering in biological tissue: implications for optical diagnostics and therapeutics. Doctoral Dissertation 2001; The University of Texas at Austin.

21. Barton JK. Predicting dosimetry for laser coagulation of *in vivo* cutaneous blood vessels. Doctoral Dissertation 1998; The University of Texas at Austin.

22. Wahl LM, Wahl SM. Inflammation. In Wound Healing, Biochemical and Clinical Aspects (Edited by I. K. Cohen, R. F. Diegelmann, and W. J. Lindblad), pp. 40–53. W. B. Saunders Co.,Philadelphia, 1992; [Chapter 3].

23. Walter JB, Israel MS. The inflammatory reaction. In General Pathology, 4th ed., (Edited by J. B. Walter) pp. 69–83. Churchill Livingston, London 1974; [Chapter 6].

24. Wang RK, Tuchin VV. Tissue clearing as a tool to enhance imaging capability for optical coherence tomography. Proc.SPIE 4619 2002; 22–25.

25. Boergen KP, Birngruber R, Gabel VP, and Hillenkamp F. Experimental studies on controlled closure of small vessels by laserirradiation. Proc. Lasers Surg. Med. Biol. Munich 1977; 5: 15.

26. Burek DG, Riva CE. Vasomotion and spontaneous low-frequency oscillations in blood flow and nitric oxide in cat optic nerve head. Microvascular Research 1998; 55: 103−112.

27. Wang Y, Okamura T, and Toda N. Mechanism of acetyl-choline-induced relaxation in dog external and internal ophthalmic arteries. Exp. Eye Res 1993; 57: 275−282.

28. Bertuglia S, Colantuoni A, and Dunn R Jr. Effect of L-NMMA and indomethacin on arteriolar vasomotion in skeletal muscle microcirculation of conscious and anesthetized hamsters. Microcirc. Res. 1994; 48: 68−84.

29. Abdi H. The Bonferonni and Sidak corrections for multiple comparisons. N.J. Salkind (ed.) Thousand Oaks, CA: Sage, *Encyclopedia of Measurement and Statistics 2007.*

30. Miller RG, Jr. Simultaneous Statistical Inference. NewYork: Springer. Verlog, 1991.

31. Shaffer JP. Multiple Hypothesis Testing. *Ann. Rev. Psych.* 9951; 46: 561−584.

CHAPTER 4: CHANGES IN MORPHOLOGY AND OPTICAL PROPERTIES OF SCLERA AND CHOROIDAL LAYERS DUE TO HYPER-OSMOTIC AGENT[2]

4.1. ABSTRACT

Light scattering in the normally white sclera prevents diagnostic imaging or delivery of a focused laser beam to target in the under lying choroid layer. In this chapter, we examine changes in optical properties and dynamics of blood owing to the application of the glycerol to the sclera of rabbits. Recovery dynamics are monitored after the application of saline. These measurements provide an estimate of the diffusion time of glycerol through the sclera and examine the hypothesis that glycerol reduces blood flow. The speed of clearing for injection delivery is compared to the direct application of glycerol through an incision in the conjunctiva. Although, the same volume of glycerol was applied through the two different methods, the sclera cleared much faster (5−10 seconds) with the topical application of glycerol compared to the injection method (3 minutes). In addition, the direct topical application of glycerol spreads over a larger area in the sclera than the later method. A Diffuse Optical Spectroscopy (DOS) system provided spectral analysis of the remitted light every two minutes. Comparison of

[2]The experiments contained in this chapter were accepted for publication in a peer-reviewed journal: Raiyan T. Zaman, Rajaram, Narasimhan, Nichols, Brandon S., Rylander, Henry G. III, Wang, Tianyi, Tunnell, James W., Welch, Ashley J., Changes in Morphology and Optical Properties of Sclera and Choroidal Layers due to Hyper-osmotic Agent, The Journal of Biomedical Optics 2010

measurements to those obtained from phantoms with various absorptions and scattering properties provided estimates of the absorption coefficient and reduced scattering coefficient of rabbit eye tissue.

4.2. INTRODUCTION

Light scattering in the normally white sclera prevents diagnostic imaging or delivery of a focused laser beam to targets in the under lying choroid layer. Methods to optically clear the sclera include localized pressure which removes local water and dehydrates the volume under the pressure or delivery of a hyper-osmotic agent that dehydrates and provides index matching of collagen fibers.

Hyper-osmotic agents such as 100% anhydrous glycerol, substantially increase the penetration depth of light in sclera[1–10] increased by reducing light scattering in tissue.[11–13] A potential benefit of the optical clearing technique is the improvement of laser therapeutic techniques that rely on sufficient light penetration to targets embedded in sub-scleral or super-choroidal spaces. Combining optical clearing with laser irradiation could reduce the fluence for therapeutic applications and prevent excessive damage.[14] However, glycerol causes a decrease in blood flow when this agent is used in skin.[15] Thus, these experiments are designed to examine the dynamics of blood flow in the conjunctiva and choroid after the application of glycerol.

A number of researchers have demonstrated the ability of diffuse optical spectroscopy (DOS) to non-invasively monitor optical properties and hence physiology

of tissue. Light is delivered and collected with an optical fiber probe that is placed in contact with the tissue surface. Weak light pulses sample the tissue beneath the probe without causing damage and provide valuable information regarding the scattering and absorption properties of tissue. The scattering from tissue can be correlated to tissue micro-architecture and is due to cells in the epithelial layer and collagen in the stroma. Tissue absorption is caused primarily by hemoglobin confined to blood vessels and melanin. Thus, in this study, diffuse remitted light is measured using DOS where by an optical fiber probe delivers and collects light from the tissue surface. The measured diffuse reflectance spectra are analyzed to determine blood volume fraction, blood oxygen saturation, blood vessel diameter, melanin concentration, and level of scattering. The development and validation of the DOS model has been described in detail earlier by Rajaram *et al*.[16] Analysis of the remitted light assumes a negative power law dependence of scattering on wavelength.[17] Because hemoglobin is not homogeneously distributed in tissue, Beer's law cannot be used to suitably describe the absorption and hence recover the hemoglobin concentration from sampled tissue. The algorithm to account for the inhomogeneous distribution of hemoglobin (confined to blood vessels) assumes confined distributions of absorbers that have been validated using tissue phantoms and Monte Carlo simulations.[18–20] By fitting the collected diffuse reflectance with a set of equations, oxygen saturation, mean vessel diameter, blood volume fraction, and scatter density can be estimated. Blood volume fraction and mean vessel diameter refer to total amount of blood sampled by the probe and the area to which it is confined, respectively. A brief

description of DOS and the equations used to spectrally constrain the absorption and scattering are described in Sections 2.8 and 2.9.

Previous studies have documented a decrease in blood flow and even closure of blood vessels[15, 21] followed by vessel recovery as the concentration of hyper-osmotic agent dissipates. These studies have proposed that the dehydration and hydration of the sclera and choroidal layers are primarily responsible for improvement observed by optical clearing. However, in this study we sought to examine the relationship between the optical properties such as reduced scattering coefficient, absorption coefficient, and the various morphological features of the tissue—melanin concentration, blood volume fraction, oxygen saturation, and blood vessel diameter.

This study examines the dynamics of changes in optical properties and the affect glycerol has on the local vascular system. By injecting glycerol through the conjunctiva and making time series measurements with DOS it is possible to follow dynamic changes in optical properties and the vascular system of the choroid and conjunctiva. DOS measurements continuously monitor blood oxygen saturation, blood vessel size, blood volume fraction, and scattering changes owing to the infusion of glycerol and subsequent rehydration of the system. By measuring these relationships we intend to determine whether there is a correlation between the morphological properties and the optical properties of the sclera after exposure to the optical clearing agent. As glycerol induced clearing induces large changes in tissue scattering and absorption that may exceed the bounds of validity of typical DOS algorithms, the possibility of errors must be considered. Two additional points are (1) the rate of clearing of the injection method of

glycerol delivery compared to direct application through an incision in the conjunctiva and (2) visualization of the choroid after application to glycerol.

4.3. METHODOLOGY

4.3.1. Animal preparation

Female SPF Dutch Belted (n = 8) rabbits weighing 4 to 5 lbs were used to identify changes in morphology and optical properties of sclera and choroidal layers after application of 100% glycerol. All experimental procedures were conducted at the Animal Resource Center according to protocols approved by the Animal Care Committee of The University of Texas at Austin. Prior to the experiment, the rabbits were anesthetized with Glycopyrrolate 0.02mg/kg intramuscularly (IM) followed by 5mg/kg Xylazine and 40mg/kg Ketamine hydrochloride (Rompun-Ketaset) in the proportions: 60% of 20 mg/ml Rompun to 40% of 100 mg/ml Ketaset by volume. Anesthesia was maintained with isoflurane (1.5−3%) inhalant during the experiment. Isoflurane was supplemented by acepromazine (0.25−1.0 mg/kg) administered intramuscularly as needed for individual rabbits demonstrating a high intolerance to isoflurane. One hour prior to termination of isoflurane, buprenorphine 0.01−0.05 mg/kg was administered IM for any pain or discomfort.

Rabbits were positioned in the ventral recumbent position. Oxygen saturation and pulse, heart and respiration rate were monitored every 15 minutes throughout the study using a vet/ox G2 Digital pulse oxymeter (Heska Corp. Loveland, CO, USA). This

monitor was connected via a shaved area of the feet or the ear depending on the best contact for recording. Animals were kept warm with warm water blankets. The anesthetic and monitoring procedures were performed by a skilled technician from the Animal Resource Center of the University of Texas at Austin.

4.3.2. Dehydration/hydration cycle

Glycerol and saline were used to create "dehydration" and "hydration" cycles, by altering the osmotic pressure of the sclera. Glycerol removed water (dehydration) and a decrease in glycerol concentration was accomplished by flooding with saline or natural diffusion (hydration). Glycerol introduces morphological changes to the tissue owing to changes in optical properties.[21] During the dehydration cycle, 100% anhydrous glycerol was applied to the sclera by injection through the conjunctiva and deposited on top of sclera. A single volume of 0.1 mL glycerol was injected one time prior to spectroscopy measurements. The first measurement time 0^{+} was within 15 seconds of the completion of the injection which required 2 minutes. The morphological changes were captured using a slit lamp connected with an EOS Digital SLR Canon camera every 2 minutes up to 26 minutes during the dehydration cycle. Morphological changes became constant after 18 minutes and as well as the optical properties (measured with DOS). Therefore, only the first 18 minutes of measurements are presented. The dehydrated tissue was then hydrated by applying 0.9% saline solution. These dehydration and hydration cycles were repeated 4 times for the same duration of time. The optical properties were measured for

12 minutes during the hydration cycle due to no identifiable changes after this time of reference.

4.3.3. *In vivo* eye model

In this study, we are interested in three layers of the *in vivo* eye model: (i) bulbur conjunctiva, (ii) sclera, and (iii) choroid. The bulbar conjunctiva is a thin (54.7±1.9 μm) clear outermost epithelium membrane that covers the sclera.[22–24] The naturally white sclera is just beneath the conjunctiva, which is opaque due to its normal level of hydration. Collagen accounts for 90% of the dry weight of all mammalian sclera. In addition, some fine blood vessel arcades exist on both the surface of conjunctiva and sclera; however, sclera is mostly avascular and is anatomically similar to dura mater of brain. The thickness of the sclera varies from 1000 μm at the posterior pole to 300 μm just behind the rectus muscle insertions. It is continuous with the dura mater and the cornea, and provides an attachment for the extra ocular muscle insertions. The choroid lies between the sclera and retinal pigment epithelium (RPE) and consists of four layers (i) Haller's layer (outermost layer), (ii) Sattler's layer, (iii) Choriocapillaris, and (iv) Bruch's membrane (innermost layer). Haller's and Sattler's layers consist of large and medium diameter blood vessels, respectively; Choriocapillaris layer has capillaries.[25] Melanin, a darkly colored chromophore synthesized by melanocytes, occurs throughout the choroidal layer helps limit uncontrolled reflection within the eye and increases vision.[26] The RPE is the pigmented cell layer just outside the neuro-sensory retina that

nourishes retinal visual cells, and is firmly attached to the underlying choroid and overlying retinal visual cells.

The optical model is illustrated in Figure 4.1a depicts the light interaction with the three layers of eye tissue. We assumed three different cases (i) at baseline (before 100% anhydrous glycerol application) light scattered from the DOS light beam undergoes multiple refractions and propagations in the sclera; (ii) after glycerol application, light penetration depth increases leading to higher absorption in the choroidal layer (iii) as the sclera rehydrates, it becomes less transparent which increases backscattering. Figures 4.1b−4.1d illustrate these hypothesized scenarios that were implemented in the eye model.

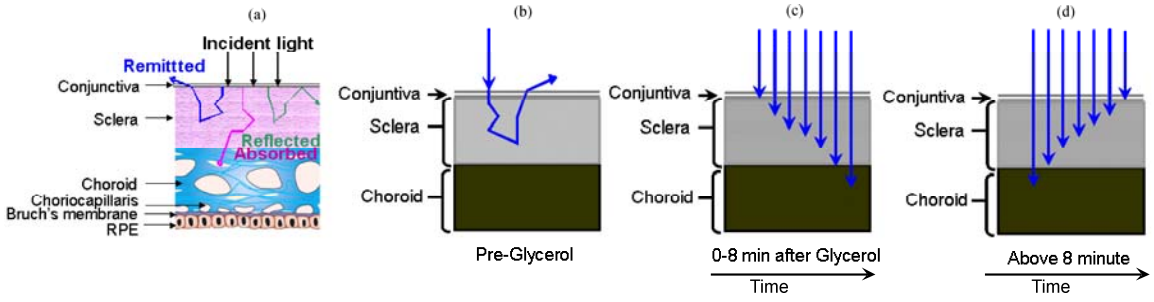

Figure 4.1. Morphological and optical property change of the eye associated with optical clearing: (a) Anatomy and light propagation in eye model, (b−d) light propagation in normal (baseline), dehydrated, and hydrated tissue.

4.3.4. Surgical procedure

A wire eye speculum was placed in the eye to hold the eyelid at a fixed position. The position of the eye was stabilized with a suture placed in the limbus. The suture helped to lower the eye that provided access to the sclera for delivering the hyper-osmotic agent. Injection sites were superficial to Tenon's capsule. We introduced glycerol close to the limbus area where the sclera was the thinnest, 300 μm. Glycerol was delivered to sclera in two methods (i) injecting through bulbar conjunctiva (using a 27G ½ hypodermic needle from Beckton Dickinson, NJ, USA), (ii) direct topical application after 0.3 cm incision at the conjunctiva. The glycerol was injected very slowly due to the high viscosity of the 100% anhydrous glycerol. The glycerol was poured from the original container into smaller airtight screw cap bottle for each experiment to prevent the glycerol from absorbing any moisture from the air due to its hygroscopic nature. The rest of the glycerol after each experiment was discarded to prevent contamination.

4.3.5. Photography of sclera treated with glycerol and saline

An EOS digital SLR Canon camera (Digital Rebel XT, Japan) attached to a slit lamp (Topcon SL-6E) captured the morphological changes of the sclera and choroidal layers during the dehydration and hydration cycles. The camera shutter was triggered by digital single-lens reflex (DSLR) software using a computer. A photograph was taken of the *in vivo* sclera at baseline (pre-glycerol application), immediately after glycerol

application (0^+ minute), every 2 minutes up to 26 minutes, and after hydrating the sclera with 0.9% saline.

4.3.6. Diffuse Optical Spectroscopy (DOS) system

The system used to collect the diffuse reflectance has been described in detail by Zaman *et al*.[27] Briefly, the DOS system consists of three main components: (i) a tungsten halogen lamp to shine white light (LS-1, Ocean Optics), (ii) a custom-designed fiber-optic probe (core diameter = 200 μm; NA = 0.22; FiberTech Optica), and (iii) a spectrometer (USB4000, Ocean Optics) (Figure 4.2). The fiber-optic probe consists of 2 individual fibers, separated by 370 μm, that are terminated with SMA connectors. The source and detector fibers were connected to the lamp and spectrometer, respectively. The analysis model is unique to the probe geometry used in this study.

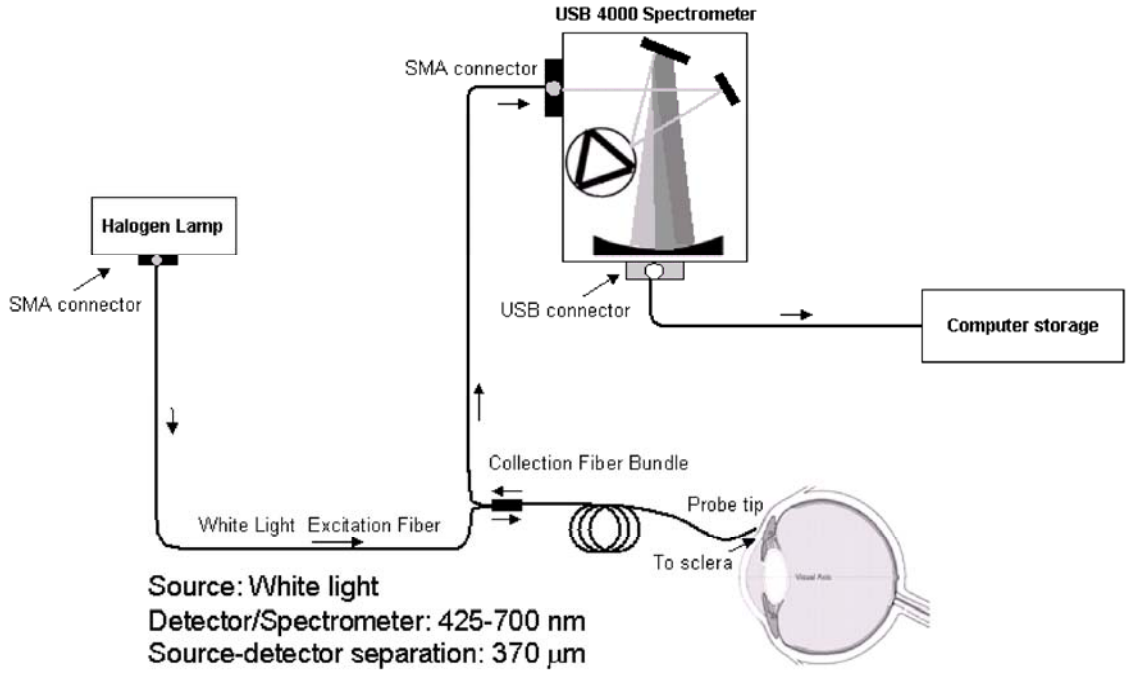

Figure 4.2. Schematic illustration of the instrumentation setup for DOS system.

We measured the diffuse reflectance spectrum from tissue over a wavelength range of 425−700 nm that includes most of the Soret band. The fiber-optic probe was placed in contact with the surface of the bulbar conjunctiva, and the average was taken from 3 measurements of white light spectra (Figure 4.3: average of all eight rabbits) at each time point that was reflected from eye tissue. Each reflectance spectra was collected within 100 milliseconds. Reflectance spectrum from the bulbar conjunctiva and sclera were collected at the same location of the glycerol injection prior to injection (baseline), immediately after glycerol application (0^+ minute), and every two minutes up to 18 minutes. Another set of reflectance spectrum was collected immediate after hydrating (0^+ minute) the sclera with 0.9% saline and every 2 minutes up to 12 minutes. Prior to

spectral analysis, recorded signals were corrected for system response. We subtracted the detector dark current and normalized the sample reflectance by the reflectance of a Lambertian reflector (Spectralon, Labsphere Inc.; 40% reflectance standard).

Analysis of data revealed that some results were affected by the time of day of the experiments: morning (AM) or afternoon (PM). Therefore some results were grouped as AM or PM.

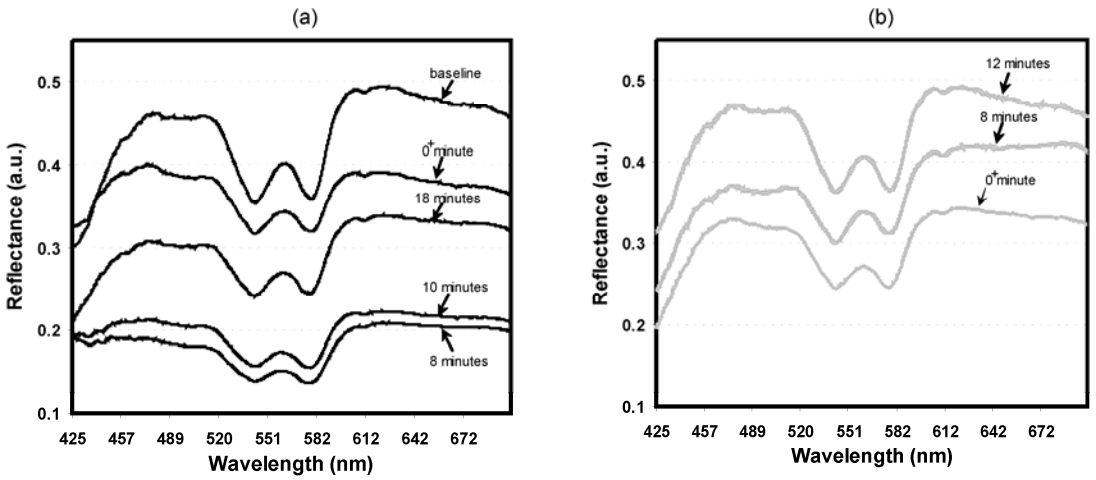

Figure 4.3. Reflection spectrum of rabbit sclera measured using DOS system. (a) Dehydration cycle: plot of average reflection spectrum of sclera at baseline, 0^+, 8, 10, and 18 minutes post-clearing. (b) Hydration cycle: plot average reflection spectrum of sclera at 0^+, 8, 10, and 18 minutes after saline injection. The mean spectrum was calculated from 8 samples.

4.3.7. Sampling depth measurement

The sampling depth of optical fibers is a function of the source-detector separation distance and the optical properties of the tissue. Determination of the sampling

depth assumes importance due to the multilayered nature of eye tissue. It is possible to approximate the reflected light as a volume average; however, as the hyper-osmotic agent optically clears the sclera it is important to know if the probe can sample reflectance from the choroid. Therefore, knowledge of sampling depth is necessary as we report changes of these properties.

Estimates of the changes in sampling depth were obtained using a container (base painted with non-reflective black paint), which was filled with 10% diluted intralipid (10% intralipid:water with 1:9 ratio) solution to mimic the scattering of the natural sclera. The reduced scattering coefficient (μ_s') of the diluted intralipid solution at 630 nm was 1.0–5.0 mm^{-1}, which falls within the physiological range of μ_s' for *in vitro* bovine and porcine sclera (3.58−10.09 mm^{-1}).[28] A LabVIEW interface (SD Instrument, MC2000 controller) controlled the position of the fiber optic probe of the Diffuse Optical Spectroscopy (DOS) system. The fiber-optic probe was initially placed at the base of the phantom. The reflectance intensity measured was close to zero due to the non-reflective black paint. Subsequently, the probe was moved in the z-direction and the reflectance intensity was recorded at each step (50 μm). The experiment was continued until the reflectance intensity reached a constant value. The slope of the curve provided a measure of this particular probe's sampling depth. Based on our experiments, the average sampling depths were identified between 379–525 μm for the simulated white sclera. Table 4.1 illustrates various μ_s' values of the intralipid solutions and its associated sampling depth.

Table 4.1. Measured sampling depth for various μ_s' at 630 nm

μ_s' of Diluted Intralipid Solution (mm^{-1})	Sampling Depth (μm)
1.0	532
1.5	511
2.0	487
2.5	466
3.0	441
3.5	418
4.0	398
4.5	385
5.0	379

4.3.8. Tissue phantoms—LUT based DOS inverse model

The diffusion approximation is a traditional method for determining optical properties from diffuse reflectance measurements as described by Farrell *et al*.[29] or a modified form according to Kienle *et al*.[30] However, a drawback of these models is their lack of accuracy at close source-detector separations (less than one mean free path) and low albedo [$\mu_s'/(\mu_s' + \mu_a) < 0.9$]. We used a lookup table (LUT)-based DOS inverse algorithm to determine the optical properties from the diffuse reflectance measurements. Briefly, the DOS inverse model is a database of experimental measurements of calibration standards of known optical properties and is unique to the fiber geometry. The DOS inverse model is valid for probe geometries with close source-detector separations and in tissue with low albedo. The development and validation of the LUT-based DOS inverse model has been described in detail previously by Rajaram *et al*.[16] Recently, the

LUT model was validated for extracting blood vessel diameter using micro-fluidic devices in a scattering medium (μ_s' of 1.0 mm^{-1} at 630 nm).[31] Thus, spectroscopy estimates these physiological changes during variable sampling volume for the course of these experiments. The LUT-based DOS inverse model estimates the absorption (μ_a) and μ_s' over a wide range of absorption and scattering values with associated errors of ±11.6% and ±5.9%, respectively.

We constructed LUT using calibration standards of known optical properties. These calibration standards were made with polystyrene microspheres (diameter = 1.0 μm; Poly-sciences) and 10% India ink (Salis International) dissolved in water to simulate scattering and absorption, respectively. The physical thickness of the tissue phantom was 3.0 mm. Optically the tissue phantom was considered as semi-infinite for the wavelengths of interest. The optical properties of the polystyrene microspheres and India ink were calculated using Mie theory and a UV-Vis spectrophotometer, respectively.

The LUT matrix (6×10) was constructed using reflectance measurements from 60 tissue phantoms with varying scattering [$\mu_s'(\lambda)$ = 0.25−4 mm^{-1}] and absorption parameters [$\mu_a(\lambda)$ = 0−6.41 mm^{-1}] that encompassed the range of optical properties found in tissue previously illustrated by Welch *et al.*[32] These 60 phantoms covered the entire range of the LUT matrix. The LUT of reflectance as a function of $\mu_s'(\lambda)$ and $\mu_a(\lambda)$ is illustrated in Figure 4.4. A single reflectance spectrum at different observation times similar to Figure 4.3 (illustrated the average reflectance trend from all eight rabbits) from *in vivo* rabbit eye tissue was statically compared to the LUT to estimate the optical

properties of the sclera and choroidal layers during baseline, dehydration, and hydration cycles.

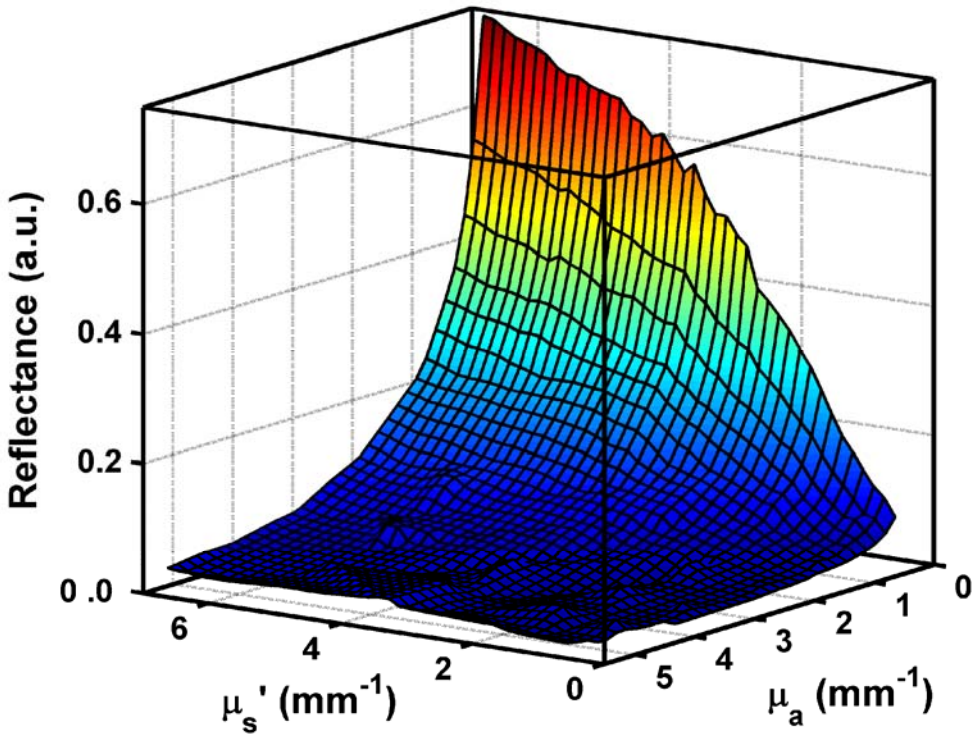

Figure 4.4. Resulting LUT-based DOS inverse model consists of known optical properties of tissue phantom made from polystyrene bead with various concentration of India ink (10% concentration). The spectral dependence of reflectance spectra (R) results from the wavelength-dependent optical properties of reduced scattering $\mu_s'(\lambda)$ and absorption $\mu_a(\lambda)$. By constraining the scattering and absorption coefficients, optical properties such as scatterer size and density, melanin concentration, blood volume fraction, oxygen saturation, and blood vessel diameter are extracted. These optical properties are extracted from a single reflectance spectrum at different observation time similar to Figure 4.3 that depicted the average of all 8 rabbits.

4.3.9. Data analysis

The optical properties of the sclera and choroidal layers are extracted from spectrally resolved diffuse reflectance spectra (*R*) fit to the unique LUT-based DOS inverse model (Figure 4.4). The spectral dependence of R results from the wavelength-dependent optical properties of $\mu_s^{'}(\lambda)$ and $\mu_a(\lambda)$. By constraining the scattering and absorption coefficients, optical properties such as scatterer size and density, melanin concentration, blood volume fraction, oxygen saturation, and blood vessel diameter are extracted. These optical properties are extracted from a single reflectance spectrum at different observation times. A nonlinear optimizing routine (average fit time 5−10 seconds) statically adjusts the spectrally resolved diffuse reflectance spectra to extract the optical properties. The reduced scattering coefficient is constrained to the form

$$\mu_s^{'}(\lambda) = \mu_s^{'}(\lambda_0).\left[\frac{\lambda}{\lambda_0}\right]^{-B} \qquad [\text{mm}^{-1}] \qquad (1)$$

where λ_0 = 630 nm. Mourant *et al.* have shown that a power law dependence on wavelength is an ideal approximation of scattering in bulk tissue.[17] Here, scattering magnitude and scatterer size are represented by $\mu_s^{'}(\lambda_0)$ and *B*, respectively. We assume that absorption in the visible range is due to melanin, oxy- and deoxy-hemoglobin and calculate the absorption coefficient as a linear combination of absorbers:

$$\mu_a^{total}(\lambda) = \mu_a^{Hb}(\lambda) + \mu_a^{mel}(\lambda) \qquad [\text{mm}^{-1}] \qquad (2)$$

The absorption coefficient of melanin is modeled as $\mu_a(\lambda) = [mel].\varepsilon_{mel}(\lambda)$ where *[mel]* represents melanin concentration (mg/mL) and $\varepsilon_{mel}(\lambda)$, the wavelength-dependent extinction coefficient of melanin [mm^{-1}/(mg/mL)].

A correction factor accounts for the inhomogeneous distribution of blood in tissue, as described by van Veen *et al.*[19] This correction factor modifies the absorption coefficient of hemoglobin to account for the confined distribution of hemoglobin in blood vessels. The absorption coefficient of hemoglobin and the correction factor are represented by the following equations:

$$\mu_a^{Hb}(\lambda) = C_{corr}.cHb.\mu_a(\lambda) \qquad [mm^{-1}] \qquad (3)$$

$$C_{corr} = \left[\frac{1-\exp(-\mu_a(\lambda).d)}{\mu_a(\lambda).d}\right] \qquad (4)$$

where *cHb* represents the blood volume fraction, $\mu_a(\lambda)$ is the absorption coefficient of whole blood assuming a hemoglobin concentration of 150 g/L, and *d* is the mean vessel diameter (mm). The absorption coefficient of blood is calculated as:

$$\mu_a(\lambda) = \alpha.\mu_{aHbO_2}^{blood}(\lambda) + (1-\alpha).\mu_{aHb}^{blood}(\lambda) \qquad [mm^{-1}] \qquad (5)$$

where α is the oxygen saturation of blood, $\mu_{aHbO_2}^{blood}(\lambda)$ and μ_{aHb}^{blood} respectively represent the absorption coefficients of fully oxygenated and fully deoxygenated blood. The extinction coefficients for oxy- and deoxy-hemoglobin have been documented in the literature of Prahl previously.[33] Based on the constraining equations described above, a Levenberg-Marquadt nonlinear optimization fits the diffuse reflectance spectra to the LUT-based DOS model. The fit parameters— $\mu_s'(\lambda_0)$, *B*, *[mel]*, *cHb*, *d*, and α are constrained to vary

within a physiologically relevant ranges of 0.55–3.2 mm^{-1}, 0.9–1.2, 0.001–0.05 mg/mL, 0.3–4.5%, 10–120 μm, and 0–1, respectively.[16] All these fit parameters are calculated simultaneously once the reflectance spectra is fit to the LUT.

4.3.10. Statistical analysis: Quadratic Mixed Regression Model (QMRM)

We analyzed data using a quadratic mixed regression model[34] (QMRM) with observation nested with rabbit. Independent variables in all models included time and hydration status. In addition, time square was included to investigate a possible quadratic effect. Four separate QMRMs were run with the above independence for each dependent variable.

4.4. RESULTS

4.4.1. Sclera and choroidal layers: change in morphology

Photographs of the morphological changes in sclera and choroidal layers due to 100% anhydrous glycerol are shown in Figure 4.5. Glycerol injection through conjunctiva and deposition on sub-conjunctiva optically cleared the sclera in 3 minutes, whereas the direct topical application after incision of the conjunctiva caused the sclera to become transparent within 10 seconds. For the glycerol injection method, we found that the sclera became transparent in 8 minutes and stayed clear for 10−15 minutes. The clear

sclera became less transparent over next 11 minutes and completely opaque once saline was applied.

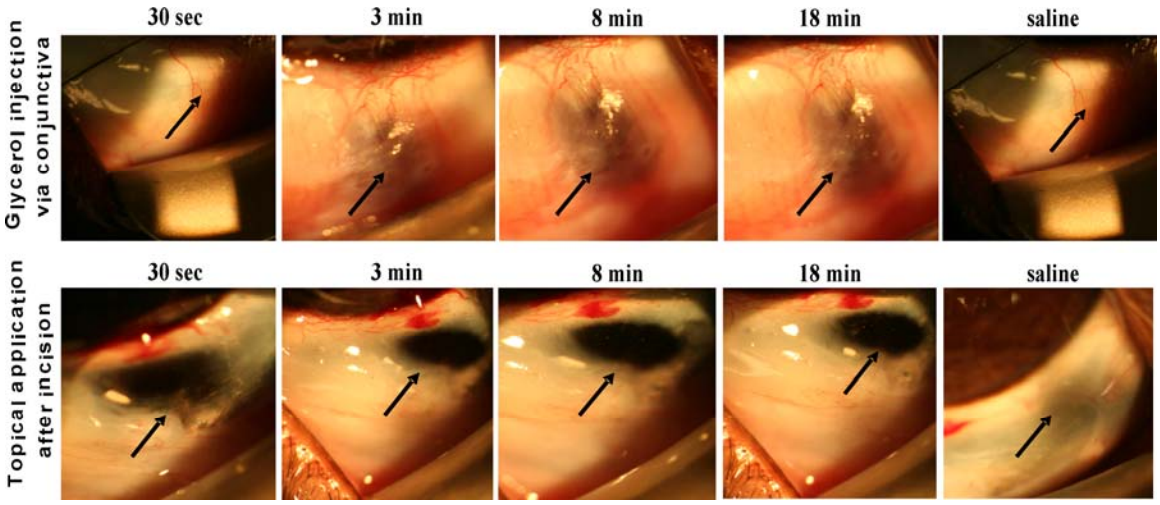

Figure 4.5. Macroscopic time-lapse images of rabbit eye model before, during and after optical clearing. The time-lapse is indicated above each image.

Spectroscopic measurements were obtained only with the injection method of glycerol application. Measurements were made through the clearing process and after addition of saline at the 18-minute mark.

4.4.2. Diffuse Optical Spectroscopy (DOS)

Measurements prior to the injection of glycerol were expected to represent average optical properties of the conjunctiva and sclera owing to the limited penetration depth and increased scattering of the DOS light source. The low values of $\mu_a(\lambda)$ at the baseline measurement in Figures 4.7c−4.7f confirm this hypothesis. Once the hyper-

osmotic agent was introduced light penetration depth increased and measurements were affected by the choroidal layer. All experimental conditions were kept constant throughout the experiment for each animal except for the starting time of the experiments for three rabbits. The separation of the rabbit data is post-hoc due to the observation of two different ranges of diameter of blood vessels. Therefore, the optical properties for rabbits were separated into two subgroups for n = 5 (AM) and n = 3 (PM) to identify any minor changes that may be the contributing factor of physiologic changes in the rabbit eye. Data from five rabbits were collected during morning between 7:00−9:30 AM and remaining three rabbits were collected in the afternoon between 12:30−4:00 PM.

4.4.2.1. Reduced scattering coefficient (μ_s')

The μ_s' at 630 nm decreased immediately after glycerol injection that is indicated as 0^+ minutes in Figures 6a−6b. The maximum reduction of 57% in scattering occurred at 8 minutes during the dehydration cycle at afternoon measurement, and was followed by a gradual increase. After hydrating the tissue, scattering increased linearly with respect to time and returned to baseline at 12 minutes after the saline application. Baseline μ_s' at the afternoon was slightly higher compared to the morning measurement.

4.4.2.2. Absorption coefficient (μ_a)

Estimation of μ_a was based on (i) melanin concentration (mg/mL), (ii) blood volume fraction (%), (iii) oxygen (O_2) saturation (%), and (iv) mean blood vessel

diameter (μm). These values were extracted from the inverse solution of the measured reflectance over the wavelength band from 425 to 700 nm. Absorption as a function of wavelength prior to injection of glycerol (baseline) is shown in Figure 4.7a. Absorption coefficient spectrum in Figure 4.7a showed a distinctive absorption peak between 525−600 nm wavelengths due to the presence of blood volume at the bulbar conjunctiva, the site of glycerol injection as shown in Figure 4.7b. The variations of μ_a in sclera and choroidal layers during the dehydration and hydration cycles for the 542 nm wavelength consisted of a distinctive blood absorption peak and provided identifiable changes caused by the hyper-osmotic agent (Figures 4.7c). The variation of μ_a at 650 nm wavelength that minimized the effect from blood absorption was presented in Figure 4.7d. The μ_a of the dehydrated sclera and choroidal layers returned to baseline at 12 minutes after applying saline to the eye tissue.

Different patterns of the μ_a were noted in the AM and PM sub groups as shown in Figures 4.7e and 4.7f, respectively. Although, the maximum optical clearing occurred at 8 minutes, the highest absorption peak during morning measurements for 650 nm wavelengths was observed at 4 minutes unlike afternoon measurements. Also, the peak μ_a during the afternoon was slightly higher than the morning.

4.4.3. Melanin, blood volume concentration, and oxygen saturation

Although, the conjunctiva and sclera layers did not contain any melanocytes, a trace amount of melanin concentration was indicated at baseline (Figures 4.8a−4.8b) due

to the lower bound of melanin concentration in the diffusion inverse model. The lower bound was set to an extremely small non-zero number of 0.001 mg/mL for smooth execution of the model. When the sclera started to become optically clear during the dehydration cycle, the DOS system detected a high concentration of melanin from the choroidal layer. Thus, the highest amount of melanin concentration was detected from rabbit's choroidal layer at 8 minutes followed by a gradual decrease. The melanin concentration returned to baseline measurement at 12 minutes after hydrating the tissue. The detected melanin concentration was slightly lower during the afternoon measurements for the three rabbits compared to morning measurements. However, statistically the difference between the morning and afternoon measurements was not significant.

The initial baseline and zero minute measurements of blood volume fraction represented the values from the anterior eye such as conjunctiva and part of sclera. The blood volume fraction assumed to have a concentration of 150 g/L. The computed blood volume fraction in all eight rabbits increased 3.7× at 8 minutes during the dehydration cycle. The blood volume fraction for the afternoon measurement showed an initial decrease at immediate after the glycerol application compared to the morning measurements. Most of the physiological absorption parameters such as melanin concentration, and blood volume fraction returned to the baseline at the end of the hydration cycle.

At baseline, detected O_2 saturations for AM and PM sub groups were 82% and 86%, respectively (Figures 4.8e−4.8f). Immediately after glycerol application at 0^+

minute, the O_2 saturation increased up to 92% and 98% respectively during morning and afternoon due to the detection of O_2 saturation and decreased thereafter. During the dehydration cycle, the lowest amount of O_2 saturation (27%−37%) was detected at 6 minutes followed by a gradual increase. At the end of the dehydration cycle or at 18 minutes, the O_2 saturation reached its highest saturation level of 99%−100%. The pattern in O_2 saturation was very different between the morning and afternoon measurements during the hydration cycle. For the morning measurements, the O_2 saturation gradually increased unlike the afternoon measurements where the saturation decreased first and then followed by an increase. For both morning and afternoon measurements, an increase of O_2 saturation of 99%−100% or hyperoxia was observed at end of hydrating cycle compared to baseline.

The diffusion inverse model computed a mean blood vessel diameter for each measurement (Figures 4.9a−4.9b). Thus, a total of eight mean blood vessel diameters at each observation time point were collected from the eight rabbits. After analyzing data of the mean blood vessel diameter the eight rabbits fell into two sub groups: small and large microvasculatures. At baseline, the diameter of blood vessels from conjunctiva and scleral layers for the PM group were smaller in size with diameters of 10−36 μm with respect to vessel diameters of the AM group which were 91−120 μm. In addition to the physiological condition, the dynamics of the blood vessel diameter is not constant over time.[35] The small and large blood vessel groups for rabbits showed different dilation patterns upon glycerol application. The smaller blood vessels had a delayed increase in diameter during the dehydration cycle (Figure 4.9b). These vessels dilated and diameter

increased to a maximum of 3.4× or 64±10 μm at 12 minutes. A slight decrease in diameter followed after 12 minutes without any outside hydration. After hydrating the sclera, an immediate enlargement of diameter was observed. The larger blood vessels in rabbit conjunctiva, sclera, and choroidal layers showed a similar trend (Figure 4.9a). The larger blood vessels dilated slightly compared to the smaller vessels and started to constrict 4 minutes after the initial glycerol application. The larger blood vessel returned to baseline diameter at the end of hydration cycle.

A QMRM with random effect was used for statistical analysis. We used 95% confidence interval ($p<0.05$). In the QMRM, all data from the rabbits were combined for the analysis. The μ_s' and μ_a were significant for both the dehydration and hydration cycles. The detected melanin concentration, blood volume fraction, O_2 saturation, and change in blood vessel diameter were significant for both dehydration and hydration cycles. In addition, the time and quadratic time in the QMRM were significant for μ_s', μ_a, melanin concentration, blood volume fraction, and change in blood vessels diameter. However, the O_2 saturation did not have any significant effect of time as a linear function; but, the quadratic effect of time was significant.

4.5. DISCUSSION

4.5.1. Summary

Methods that reduce water content of sclera can also alter collagen spacing and size to optically clear the tissue. Hyper-osmotic agents such as 100% anhydrous glycerol

can clear the sclera and has known to affect the local vascular system. The goal of this study is to measure the dynamics of the vascular system that comes in contact with glycerol as related to changes in optical properties. Is there a closure of blood vessels as reported when glycerol contacts *in vivo* rat and hamster dermis? Another goal of this study is to test a method for rapid clearing of the sclera. Although, we did not anticipate any unexpected results, we have identified a significant difference in blood vessel diameter between AM and PM measurements. All of these issues are discussed in the following paragraphs.

4.5.2. Optical clearing methods

Although, the same volume of glycerol was applied through the two different optical clearing methods, the rate of optical clearing of sclera varied greatly. The sclera cleared much faster (initial clearing 5−10 seconds) with the topical application of glycerol after opening the conjunctiva than with the injection method (first sign of clearing at 3 minutes after the injection time of 2 minutes). Moreover, the direct topical application of glycerol spread through larger area in the sclera than the later method. Observation suggested that the injection method of glycerol held the volume of glycerol in a blister form in the sub Tenon's area (an extremely thin layer between the bulbar conjunctive and sclera that provides extra protection to sclera) and restricted the spread of glycerol to areas surrounding the injection site.

4.5.3. Morphological changes

Clearing the sclera with glycerol improves visualization of the *in vivo* choroid space. Rapid clearing of a circular pattern with 1.5 cm diameter of the sclera is achieved by making an incision in the conjunctiva and directly applying a large volume (0.1 mL) of glycerol directly to the sclera. The reduction in light scattering is quantified using the injection method of application which slowed to clearing process so DOS measurements could be made. Moreover, the injection method is less invasive compared to incision method. As in previous studies reported in the literature, the direct application of saline reverses the clearing processing within seconds by hydrating the tissue. Although, tissue restoration or reversal of the morphological change during hydration cycle is rapid (5 seconds), the time required for optical properties to reach the baseline measurement are relatively slow (12 minutes). Specifically, the detected melanin concentration decreased gradually as the water defuses into the dehydrated sclera. However, 10 minutes after applying saline, water increased collagen spacing and size to its native level making the sclera opaque. Thus, our study associates the morphological change with the optical properties after implementing the clearing technique using 100% anhydrous glycerol.

4.5.4. DOS inverse and *in vivo* eye models

Light penetration depth increased as glycerol replaced water in the sclera. We hypothesis that there are three different scenarios that govern the data of this research: (i) at baseline, sclera was highly scattering; collimated light penetrated a few μm through

conjunctiva and anterior sclera; (ii) during glycerol induced dehydration, the sclera optically cleared and the light penetration depth increased and the collimated beam reached the choroidal layer where most of the light was absorbed due to the high concentration of melanin; (iii) as the sclera become less transparent at 8 minutes as water returned to the sclera and the light penetration depth decreased and scattering increased in the sclera as illustrated in Figures 4.6−4.7.

The DOS system provides a unique opportunity to compute optical properties and blood dynamics from the remitted spectrum during application of a hyper-osmotic agent. The technology is typically applied to skin which is a multi layered tissue not that dissimilar to the eye. The LUT-based DOS inverse model estimated baseline μ_s' = 2.8 mm^{-1} at 630 nm, μ_a = 0.3 mm^{-1} at 542 nm and 0.005 at 650 nm which are slightly lower than the physiological range of μ_s' (4.3 mm^{-1} at 630 nm) and μ_a (0.55 mm^{-1} at 542 nm and 0.4 mm^{-1} at 650 nm) respectively for porcine *in vitro* sclera study measured with an integrating sphere.[28] The main difference is the white sclera that quenches the source beam until glycerol induced clearing becomes significant. The highest observed value of μ_s' in our study is 3.1 mm^{-1}, that is slightly lower than the *in vitro* value reported by Chan *et al*. [28] This may be due to higher absorption by chromophores such as red blood cell (RBC) and melonocytes in *in vivo* tissue. O_2 absorption levels for *in vitro* and *in vivo* blood are also significantly different.

4.5.5. Changes in optical properties

The dynamic changes in DOS data attest to the diffusion time of the hyper-osmotic agent through the sclera using the injection method of delivery for the glycerol. This diffusion time is clearly dependent upon the method of applying the glycerol. Injection as performed in this experiment reduces the volume of glycerol reaching the sclera relative to the direct application method. Clearly DOS results are initially governed by the highly scattering sclera and then shift to properties of the choroidal layer as the sclera becomes optically clear. The clearing of a 300 μm thick sclera in rabbit sclera takes approximately 8 minutes. The reduced scattering curve of Figure 4.6 suggests a time constant of approximately 2.5 minutes.

The accuracy of the absolute magnitude of computed optical properties was impacted by assumptions associated with the inverse problem. During experiments the hyper-osmotic agent caused a rapid increase in optical depth of the sclera as μ_s' decreased. While tissue-simulating phantoms had a constant thickness, the physical thickness of the sclera decreased as the clearing agent dehydrated the sclera.[36]

Nevertheless, the results paint a remarkable picture of the dynamic changes taking place in the sclera and choroidal layers. The technique provides a tool for comparing the dynamic response of different agents and methods for delivery of the clearing agents upon optical properties.

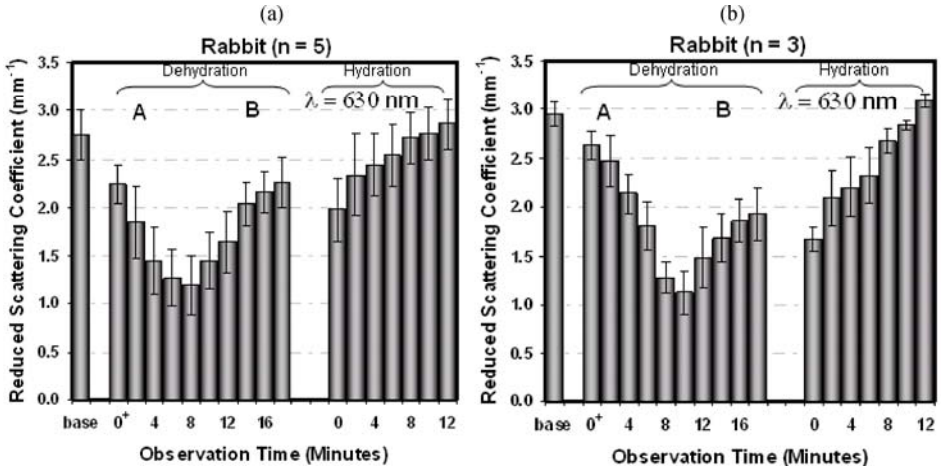

Figure 4.6. μ_s' of rabbit eye sclera and choroid for (a) morning (AM) measurement n = 5 and (b) afternoon (PM) measurement n = 3 at baseline, after dehydration by injecting 100% anhydrous glycerol and hydration with 0.9%. Region A and B represent increase and decrease of optical clearing of sclera, respectively. All values are statistically significant ($p<0.05$) for both the dehydration and hydration cycles (quadratic mixed regression model). Error bars in terms of standard deviation are computed for all averaged μ_s'.

The optical property changes observed in the sclera and choroidal layers are clearly due to the morphological changes induced by glycerol. Perhaps glycerol triggers an inflammatory response owing to osmotic equilibrium deviations. In an acute inflammatory response, water leaves the inflammatory region and it becomes dehydrated which reduces μ_s' and increases penetration depth as the sclera clears. Since penetration depth increases from its minimum value of 330 μm as μ_s' in the sclera decreases, the DOS system is able to detect melanin and blood volume fraction from the highly vascular choroidal layer.

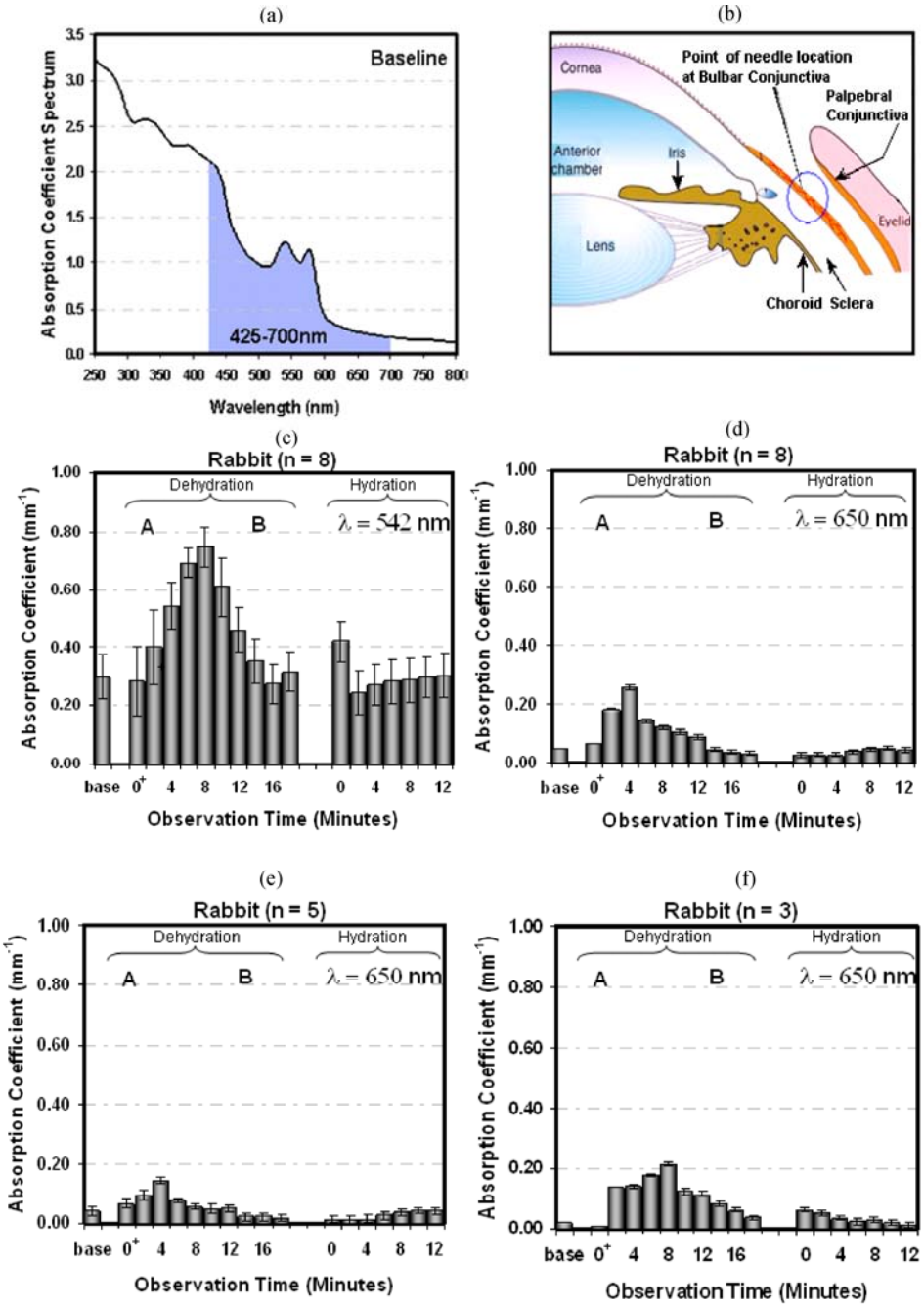

Figure 4.7. Absorption spectrum of sclera collected (a) at baseline between 425–700 nm wavelength (b) at bulbar conjunctiva, the location of the glycerol injection that has some superficial blood vessels; absorption coefficients (μa) are calculated at (c) 542 nm and (d) 650 nm wavelength respectively, to capture the strong blood absorption between 525–600 nm wavelength and no blood absorption between 630–700 nm wavelength of rabbits conjunctiva and part of sclera (mostly avascular) at baseline, and sclera and choroid at

dehydration cycle by injecting 100% anhydrous glycerol and hydration cycle with 0.9% saline. Rabbit absorption coefficient is separated into two sub groups for (e) n = 5 at morning and (f) n = 3 at afternoon observation time. Region A and B represent increase and decrease of optical clearing of sclera, respectively. All values are statistically significant ($p<0.05$) for both cycles (quadratic mixed regression model). Error bars in terms of standard deviation are computed for all averaged μ_a.

4.5.5.1. Blood dynamics

The simple hypothesis that the glycerol would reduce blood flow became complicated, considering the data from Figures 4.8−4.9. First, there was the dichotomy in the computed diameter of blood vessels for AM and PM experiments (Figure 4.9) and values of μ_a (Figures 4.7c−4.7d). Small blood vessels diameters (PM n = 3) were associated with afternoon experiments while larger diameters occurred during morning experiments (AM n = 5).

In this study, we have shown that the μ_a for rabbits is governed by the presence of blood and melnocytes. The μ_a intensity varies slightly between the morning and afternoon measurements. The slightly higher μ_a during the afternoon may be due to the dilation of the blood vessels which causes an increase in blood flow as opposed to the morning measurements where blood vessel diameter decreased during the dehydration cycle. The blood flow in the sclera is primarily modulated by the local tissue O_2 saturation and carbon dioxide (CO_2). Nitric oxide (NO) also regulates retinal circulation during induction of hyperoxia in rabbits.[37] Vessel diameter and blood velocity along with wall shear rate decreased transiently during artificially induced hyperoxia with 100% O_2 saturation.[37] Previous studies revealed that endothelin (ET)-1, a protein plays a major role

in hyperoxia-induced vasoconstriction via binding to ET type A (ETA) receptor of smooth muscle in humans[38] and animals such as rabbits and newborn pigs.[39–41] There is a biphasic response to exogenous endothelin (ET)-1 on choroidal vessels of rabbit, suggesting that endogenous ET-1 preferentially elicits vasodilation via binding to ET type B (ETB) receptor of vascular endothelium, most likely by stimulating endothelial NO release.[42] During the afternoon measurements (n = 3) small blood vessels that increased in diameter when O_2 saturation reached a hyperoxia level or 99−100% saturation during the dehydration cycle. The presence of NO may stimulate dilation in the smaller blood vessels unlike morning measurements where larger blood vessels experience vasoconstriction. The difference in dilation pattern between the morning and afternoon measurements among the smaller and larger blood vessel size may be explained by Brubaker.[43] Blood vessel diameter in the eye is not constant throughout the day due to the water dynamics. The aqueous humor production and filtration rate in ciliary body varies diurnally: it is normally 3.0 μL/min in the morning, 2.4 μL/min in the afternoon, and further drops to 1.5 μL/min at night.[43] It is possible that during the morning hours the aqueous humor production masked the effect of NO on the choridal blood vessels and decreased blood vessels diameter. Therefore, it is hypothesized that a local transmitter for regulation of blood vessel of rabbit conjunctiva and choroidal layer is NO.

In our study, we have identified two different ranges of computed blood vessel diameters (91−120 μm and 10−36 μm) in rabbit eye. These different ranges of blood vessels could be explained by Ninomiya *et al*. who has used scanning electron

microscopy (SEM) to investigate the micro-vascular architecture of choroid and the anterior segment of the Yorkshire pig eye.[44] Capillaries at bulbar conjunctiva have sparse capillary network with 16.0 μm diameters and well developed venous network ranges between 33.3−99.0 μm. Capillaries at choroid are flattened with luminal diameter of 8.9−13.9 μm. Arteries and veins at choroidal layer are 93 μm and 120−138 μm in diameter, respectively. The detected blood vessel diameters during morning and afternoon measurements with the DOS system are within this physiological range. Thus, it is possible that during the morning measurement we are able to identify more arteries and veins from bulbar conjunctiva and choroidal layers respectively due to rested eye unlike afternoon measurement. In another words, the microvasculature found in this study illustrates a complex architecture of blood vessels diameter of rabbit eye.

Although, we initially hypothesized that blood flow in microvasculature of eye tissue decreased during dehydration cycle, our study showed different diameter size blood vessels changed in diameter differently in the presence of glycerol. These changes in diameter could lead to an alteration in blood flow velocity of these microvasculatures. According to our study, smaller blood vessels during afternoon dilated and led to an increase in blood flow velocity unlike larger blood vessels. During the morning measurements, the larger blood vessels may lead to vasoconstriction as the diameter reduced to one third of its original diameter after dehydrating the tissue. These differences in vessel diameter and their reduction in blood flow velocity in the presence of hyper-osmotic agent may be physiological phenomenon such as inflammation. Inflammation can cause vasodilation and increase in blood flow velocity. In our study,

the larger blood vessels showed slight vasodilation followed by vasoconstriction during the dehydration cycle. It could be that the larger blood vessels are less affected by glycerol and lead to minor inflammation compared to smaller blood vessels.

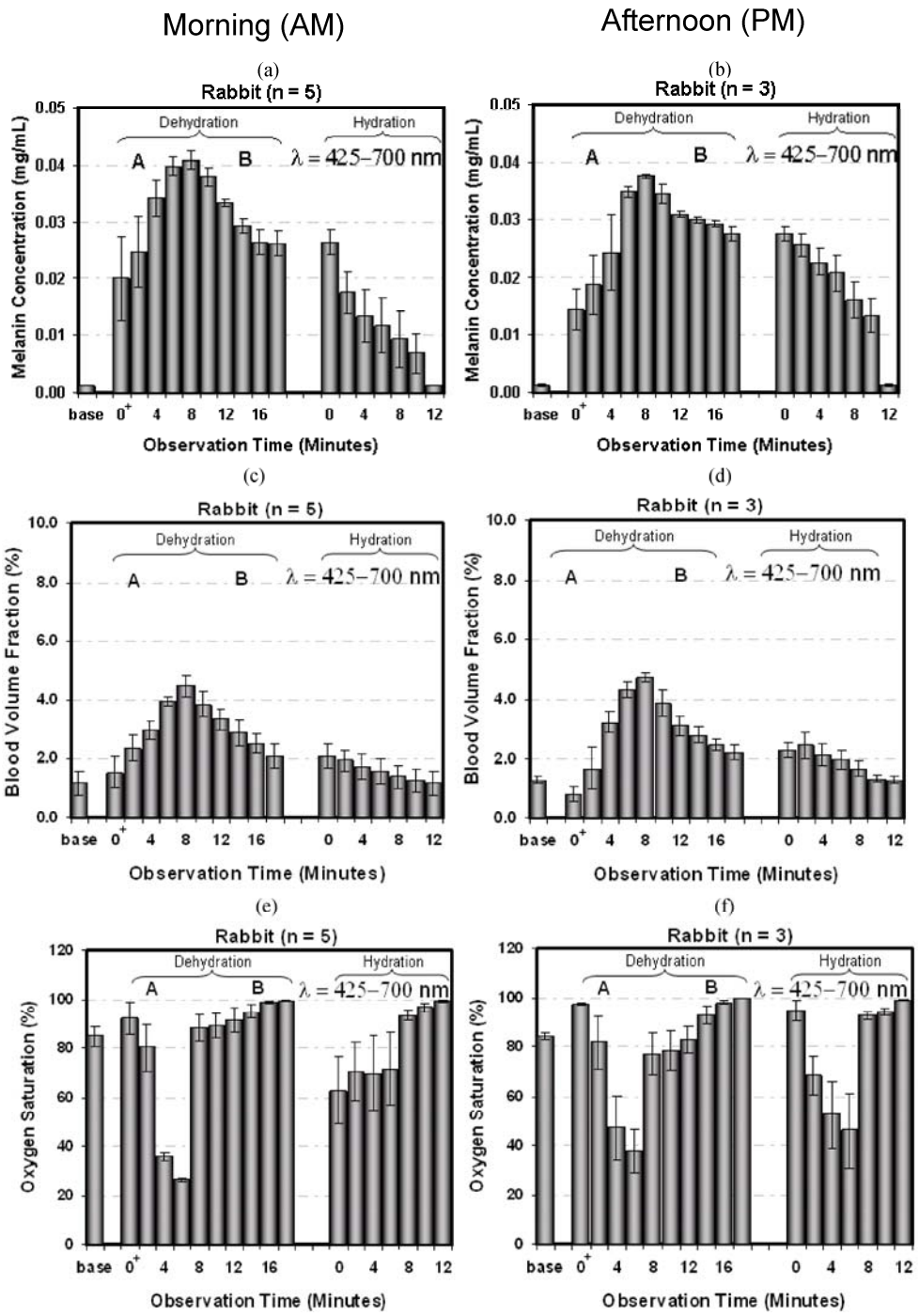

Figure 4.8. Detected melanin concentration from rabbits conjunctiva and sclera (a) n = 5 in the morning and (b) n = 3 in the afternoon during baseline show a trace amount of melanin (conjunctiva and sclera do not have any melanocyte that could produce melanin) due to the setting of the lower boundary of the inverse model (0.001 mg/ml) for smooth execution of the inverse model.

Blood volume fraction of two sub groups of rabbits (c−d) conjunctiva and sclera at baseline; dehydration leads to optical clearing of sclera and increases visibility of choroidal layer causes more blood volume detection. Oxygen saturation of two sub groups of rabbits (e−f) conjunctiva and sclera at baseline; dehydration leads to acute inflammatory response causes blood vessel dilation and slower blood flow and decrease O2 saturation. The hydration cycle starts with the application of 0.9% saline that decreases optical clearing of eye. Region A and B represent increase and decrease of optical clearing of sclera, respectively. Based on a quadratic mixed regression model blood volume fraction, and oxygen saturation are statistically significant ($p<0.05$) for both dehydration and hydration cycles. However, the detection of melanin concentration is only significant for the hydration cycle. Error bars in terms of standard deviation are computed for all averaged optical properties.

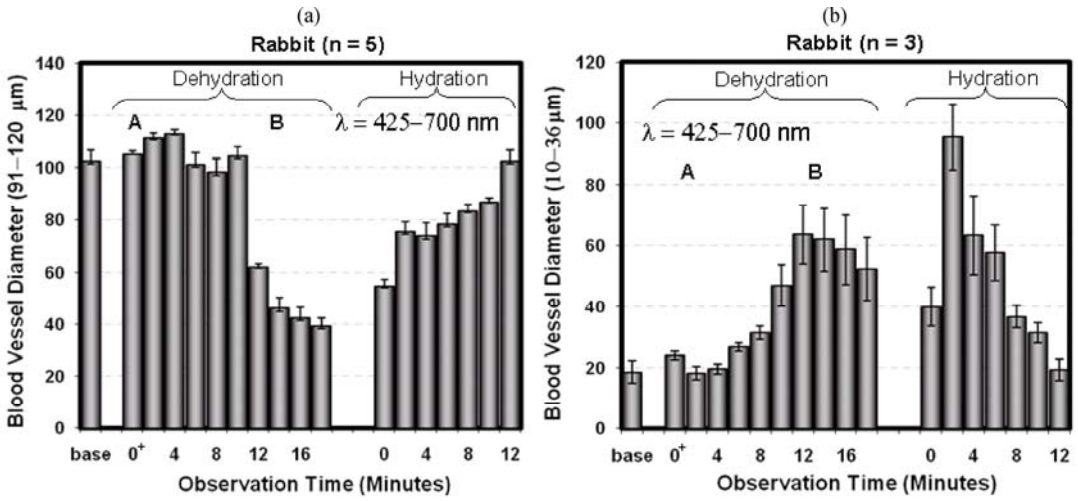

Figure 4.9. Blood vessel diameter of (a) rabbit (n = 5) with 91−120 μm and (b) rabbit (n = 3) with 10-36 μm in conjunctiva and may be sclera (mostly avascular) at baseline; after dehydration by injecting 100% anhydrous glycerol leads acute inflammatory response causes smaller (10−36 μm) blood vessel dilation leads to slower blood flow and decreases O2 saturation; however, larger blood vessels (91−120 μm) dilates much slower than the smaller blood vessel and followed by a gradual decrease in diameter; and hydration with 0.9% lead to decrease optical clearing of sclera leads to baseline measurement. Region A and B represent increase and decrease of optical clearing of sclera, respectively. All values are statistically significant ($p<0.05$) for both cycles (quadratic mixed regression model). Error bars in terms of standard deviation are computed for all averaged blood vessels diameter.

4.5.5.2. O2 saturation

O_2 saturation increases immediately after glycerol application at 0^+ minute, followed by a nonlinear decrease as sclera dehydrates and reflectance is obtained form the deeper layers. At the end of the dehydration and hydration cycles O_2 saturation reached hyperoxic level. The 99−100% saturation in O_2 level could be due to an acute inflammatory response where blood vessels are subjected to increase permeability and plasma exits into the extra vascular network.[45−47] In the native (pre-glycerol) blood vessels, the majority of blood cells are concentrated in the center of the stream, with an increased concentration of plasma near the walls.[45] This characteristic is important keeping the viscosity near the walls at a minimum so that peripheral resistance is lower than it would be if the cells were uniformly distributed. When blood plasma escapes into the extra-vascular network, this property is lost and flow in the blood vessels is reduced and may influence the O_2 saturation because there is greater drag on the walls.[46]

Aside from simply inducing an osmotic imbalance that results in water loss, it is also possible that glycerol enters the lumen of the blood vessels by diffusion. The main issue of concern if 100% anhydrous glycerol enters the vessels is the osmotic shift in red blood cells. The application of glycerol to red blood cells leads to an initial shrinking of the cells as intracellular water leaves rapidly, followed by swelling when intracellular water reenters the cells; glycerol continues to enter the cells by facilitated diffusion.[45] This phenomenon ultimately leads to an increase in O_2 saturation which was observed in this study.

4.6. CONCLUSION

This study provides evidence supporting the use of optical clearing agent such as 100% anhydrous glycerol for improved visualization of choroidal layer by creating an optical window in the sclera. Rapid clearing is achieved by delivery of the hyper-osmotic agent through an incision in the conjunctiva. Only seconds were required whereas 8 minutes were required to clear the sclera using the injection method. Four minutes after injection glycerol caused an inflammatory response as supported by the fact that blood vessels were dilated and low saturation levels were computed.

The DOS method provided a method for not only addressing optical properties, but physical properties that govern these properties. It was unexpected to find the significant differences in properties associated with morning and afternoon measurements. This is one more variable to complicate analysis of the process. This study promises a novel way of accessing various layers of eye for treating ocular diseases without any invasive surgery.

4.7. ACKNOWLEDGEMENTS

This research has been supported by the National Science Foundation BES-0529340. Special thanks to Kathryn Starr at the Animal Resource Center (ARC) who helped with the anesthetic part of the animal experiment.

4.8. REFERENCES

1. Bakutkin VV, Maksimova IL, Semyonova TN, Tuchin VV, Kon IL. Controlling of optical properties of sclera. Proc. SPIE 2393, 1995;137–141.

2. Tuchin VV, Maksimova IL, Zimnyahkov DA, Kon IL, Mavlutov AK, Mishin AA. Light propagation in tissues with controlled optical properties. Proc. SPIE 1996; 2925: 118–142.

3. Tuchin VV, Maksimova IL, Zimnyakov DA, Kon IL, Mavlutov AK, Mishin AA. Light propagation in tissues with controlled optical properties. Journal of Biomedical Optics, 1997; 2:401–417.

4. Tuchin VV, Optical Clearing of Tissues and Blood, PM 154, SPIE Press, Bellingham, WA, 2006 (Chapter 2, pp. 23−58 and subsection 8.3, pp. 188−191).

5. Bashkatov AN, Tuchin VV, Genina EA, Sinichkin YP, Lakodina NA, Kochubey VI. The Human Sclera Dynamic Spectra: *In Vitro* and *In Vivo* Measurements. Proc SPIE 1999; 3591: 311−319.

6. Tuchin VV, Culver J, Cheung C, Tatarkova SA, DellaVecchia MA, Zimnyakov D, Chaussky A, Yodh AG, Chance B. Refractive Index Matching of Tissue Components as a New Technology for Correlation and Diffusing-Photon Spectroscopy and Imaging. Proc. SPIE 1999; 3598: 111−120.

7. Tuchin VV. Coherent Optical Techniques for the Analysis of Tissue Structure and Dynamics. Journal of Biomedical Optics 1999; 4(1): 106−124.

8. Sacks ZS, Kurtz RM, Juhasz T, Mourau GA. High Precision Subsurface Photodisruption in Human Sclera. Journal of Biomedical Optics 2002; 7(3): 442−450.

9. Genina EA, Bashkatov AN, Sinichkin YP, Tuchin VV. Optical clearing of the eye sclera *in vivo* caused by glucose. Quantum Electronics 2006; 36 (12): 1119−1124.

10. Ghosn MG, Carbajal EF, Befrui N, Tuchin VV, Larin KV. Differential Permeability Rate and Percent Clearing of Glucose in Different Regions in Rabbit Sclera. Journal of Biomedical Optics 2008;13: 021110-1−021110-6.

11. Vargas G, Chan EK, Barton JK, Rylander III HG, Welch AJ. Use of an agent to reduce scattering in skin. Lasers Surgery and Medicine 1999; 24:133–141.

12. Vargas G, Chan KF, Thomsen SL, Welch AJ. Use of osmotically active agents to alter optical properties of tissue: effects on the detected fluorescence signal measured through skin. Lasers Surgery and Medicine 2001; 29: 213–220.

13. Vargas G. Reduction of Light Scattering in Biological Tissue: Implications for Optical Diagnostics and Therapeutics. Doctoral Dissertation 2001; The University of Texas at Austin.

14. Boergen KP, Birngruber R, Gabel VP, Hillenkamp F. Experimental studies on controlled closure of small vessels by laser irradiation. Proc. Lasers Surg. Med Biol. Munich 1977; 5: 15.

15. Zaman RT, Parthasarathy AB, Vargas G, Chen B, Dunn AK, Rylander III HG, Welch AJ. Perfusion in hamster skin treated with glycerol," Lasers in Surgery and Medicine, 2009; 41:492−503.

16. Rajaram N, Nguyen TH, Tunnell JW. Lookup table-based inverse model for determining optical properties of turbid media. Journal of Biomedical Optics Letters 2008; 13(5): 050501.

17. Mourant JR, Fuselier T, Boyer J, Johnson TM, Bigio IJ. Predictions and measurements of scattering and absorption over broad wavelength ranges in tissue phantoms. Applied Optics 1997; 36(4), 949−957.

18. Finlay JC, Foster TH. Effect of pigment packaging on diffuse reflectance spectroscopy of samples containing red blood cells. Optics Letter. 2004; 29(9): 965−967.

19. Van Veen RL, Verkruysse W, Sterenborg HJ. Diffuse-reflectance spectroscopy from 500 to 1060 nm by correction for inhomogeneously distributed absorbers. Optics Letter 2002; 27(4): 246−248.

20. Svaasand L, Fiskerstrand E, Kopstad G, Norvang L, Svaasand E, Nelson J, Berns M. Therapeutic response during pulsed laser treatment of port-wine stains: Dependence on vessel diameter and depth in dermis. Lasers Medical. Science 1995; 10(4): 235−243.

21. Vargas G, Readinger A, Dozier SS, Welch AJ. Morphological changes in blood vessels produced by hyper osmotic agents and measured by optical coherence tomography. Photochemistry and Photobiology 2003; 77(5): 541−549.

22. Stephenson RW. *Anatomy, Physiology and Optics of the Eye: A Textbook for Orthoptic Students*, Kimpton Publishers, 1973.

23. Nemeth SC. *Ocular Anatomy and Physiology*, Slack Incorporated Publishers, 2007.

24. Feng Y, Simpson TL. Corneal, limbal, and conjunctival epithelial thickness from optical coherence tomography. Optometry and Vision Science 2008; 85(9): 880−883.

25. Hayreh SS. Segmental nature of the choroidal vasculature. British Journal of Ophthalmology 1975; 59(11): 631−48.

26. Young AR. Chromophores in human skin. Phys. Med. Biol. 1997; 42:789−802.

27. Zaman RT, Diagaradjane P, Wang JC, Swartz J, Rajaram N**,** Gill-Sharp KL, Cho SH, Rylander HG, Payne DJ, Krishnan S, Tunnell JW. *In vivo* detection of gold nanoshells in tumors using diffuse optical spectroscopy. IEEE Journal of Selected Topics in Quantum Electronics, 2007; 13(6): 1715–1720.

28. Chan EK, Sorg B, Protsenko D, O'Neil M, Motamedi M, Welch AJ. Effects on compression on soft tissue optical properties. IEEE Journal of Selected Topics in Quantum Elcetronics, 1996; 2 (4): 940–950.

29. Farrell TJ, Patterson MS, Wilson B. A diffusion theory model of spatially resolved, steady-state diffuse reflectance for the noninvasive determination of tissue optical properties *in vivo*. Med. Phys. 1992; 19: 879−888.

30. Kienle A, Patterson MS. Improved solutions of the steady-state and the time-resolved diffusion equations for reflectance from a semi-infinite turbid medium. J. Opt. Soc. Am. A. 1997; 14: 246−254.

31. Rajaram N, Gopal A, Zhang XJ, Tunnell JW. Experimental validation of the effects of microvasculature pigment packaging on *in vivo* diffuse reflectance spectroscopy. Journal of Lasers in Surgery and Medicine, 2010; 42(7): 680–688.

32. Welch AJ, Gemert MJ. Appendix to Chap. 8 in *Optical-Thermal Response of Laser-Irradiated Tissue*, Plenum, New York, 1995.

33. Prahl S. Tabulated molar extinction coefficient for hemoglobin in water. http://omlc.ogi.edu/spectra/hemoglobin/index.html. Accessed 7/24/09.

34. West BT, Welch KB, Galecki AT. Linear mixed models: a practical guide using statistical software, Chapman & Hall/CRC, 2007.

35. Ethier CR, Johnson M, Ruberti J. Ocular Biomechanics and Biotransport. Annual Revision Biomedical Engineering, 2004; (6): 249−273.

36. Ghosn MG, Tuchin VV, Larin KV. Depth-resolved monitoring of glucose diffusion in tissues by using optical coherence tomography. Optics Letters, 2006; 31(15): 2314−2316.
37. Kiel JW. Endothelin modulation of choroidal blood flow in the rabbit. *Exp Eye Res*. 2000; 71:543–550.

38. Dallinger S, Dorner GT, Wenzel R, et al. Endothelin-1 contributes to hyperoxia-induced vasoconstriction in the human retina. *Invest Ophthalmol Vis Sci*. 2000; 41:864–869.

39. Zhu Y, Park TS, Gidday JM. Mechanisms of hyperoxia-induced reductions in retinal blood flow in newborn pig. *Exp Eye Res*., 1998; 67:357–369.

40. Takagi C, King GL, Takagi H, Lin YW, Clermont AC, Bursell SE. Endothelin-1 action via endothelin receptors is a primary mechanism modulating retinal circulatory response to hyperoxia. *Invest Ophthalmol Vis Sci*., 1996; 37:2099–2109.

41. Nishimura K, Riva CE, Harino S, Reinach P, Cranstoun SD, Mita S. Effects of endothelin-1 on optic nerve head blood flow in cats. *J Ocul Pharmacol Ther*. 1996; 12:75–83.

42. Kiel JW. Endothelin modulation of choroidal blood flow in the rabbit. Exp Eye Res., 2000; 71:543–550.

43. Brubaker RF. Measurement of aqueous flow by fluorophotometry. The Glaucomas. St. Louis, MO: C.V. Mosbey Co., 1989; 337−344.

44. Ninomiya H, Inomata T. Mirovascular anatomy of the pig eye: scanning electron microscopy of vascular corrosion casts. Journal of Veterinarian Medical Science, 2006; 68(11): 1149−1154.

45. Verkruyssa W, Khan M, Choi B, Svaasand LO, Nelson SJ. Measuring the effects of topically applied skin optical clearing agents and modeling the effects and consequences for laser therapies. Proc. SPIE, 2005; 5695: 278−287.

46. Walter JB, Israel MS. Chapter 6 in *The Inflammatory Reaction In General Pathology*, Churchill Livingston, London, 1974.

47. Wahl LM, Wahl SM. *Inflammation in wound healing. Biochemical and Clinical Aspects*, W. B. Saunders Co., Philadelphia, 1992; 40–53.

CHAPTER 5: VARIATION OF FLUORESCENCE IN TISSUE WITH TEMPERATURE[3]

5.1. ABSTRACT

Previous studies demonstrated a decrease in fluorescence intensity as tissue temperature increased. *In vitro* samples were increased from room temperature and *in vivo* canine liver from body temperature. This study investigated variations in fluorescence intensity with temperatures starting at 14°C and compared *in vivo* and *in vitro* results for consistency. A fiber optic based noninvasive system was used to characterize the temperature effect on tissue fluorescence in hamster dorsal skin *in vivo*, and in sclera and cornea of enucleated pig eyes *in vitro*. As tissue was allowed to progress through the temperature range of 14°C to 42°C over 30-40 minutes, the spectra of auto-fluorescence with respect to temperature was sampled every 1–2 minutes to yield each samples. A pulsed nitrogen laser was used to excite fluorescence through a fiber optic probe with a source-detector aperture separation of 370 μm. Fluorescence intensity decreased as temperature increased from 14°C to 42°C in a phantom containing Rhodamine B dye. Results from both *in vivo* and *in vitro* tissue followed the same trend of decreasing intensity as tissue temperature increased from 14°C. Spectral intensity

[3]The experiments contained in this chapter were in press for publication in a peer-reviewed journal: Raiyan T. Zaman, Narasimhan Rajaram, Alex Walsh, Jeffrey Oliver, Henry G. Rylander III, James W. Tunnell, Ashley J. Welch, Anita Mahadevan-Jansen, *Lasers in Surgery and Medicine January 2011*

lineshape changed around 450 nm due to absorption from tissue. Cooling a tissue increased fluorescence intensity of skin *in vivo*, in all experiments. In *vitro* results were consistent with *in vivo* measurements.

5.2. INTRODUCTION

Most of our interpretation of fluorescence data is based upon *in vitro* and *in vivo* measurements at either room temperature or body temperature, respectively. A considerable volume of research examines changes in tissue optical properties for frozen and heated tissue.[1] Since detected fluorescence is dependent upon tissue optical properties, several groups have extended these studies to determine the relationship between tissue temperature and measured fluorescence. [1, 2]

In a previous study, Romano *et al.* measured relative fluorescence yield of thin gelatin films doped with Rhodamine B as a function of temperature from 35°C to 150°C.[2] Results from Romano's study clearly demonstrated that the fluorescence decreased as temperature increased in these films. Similar results starting at room temperature and extending to 75°C were obtained by Mahadevan-Jansen in *in vitro* bovine cornea (unpublished results). Fluorescence was also measured in *in vivo* canine liver tissue in a study by Buttemere *et al*.[3] Diffuse reflectance spectroscopy and fluorescence assessed the local thermal damage caused by radio-frequency ablation. The major spectral alternations associated with thermal coagulation were a red shift in fluorescence emission peak at 480 nm, a decrease in the overall fluorescence intensity, and an increase in the diffuse reflectance from 450 to 750 nm for temperature from normal body temperature up to

maximum ablation temperature of 110°C. These authors demonstrated that the fluorescence signal decreased in phantom, *in vitro*, and *in vivo* situations as temperature was increased from about 32°C or room temperature.

Our research expands these studies by extending the lower range of temperature to 14°C. Measurements are made in a phantom, *in vitro* cornea and sclera of a pig eye, and *in vivo* measurements from hamster skin.

5.3. MATERIALS AND METHODS

5.3.1. Fluorescence Spectrometer System

A fluorescence spectrometer system developed by the BioPhotonics Laboratory at the University of Texas at Austin was used to measure fluorescence in this study.[4] The system measured the fluorescence excited from collagen and NADH in cornea, sclera of enucleated pig eyes, and in *vivo* hamster dorsal skin. The fluorescence spectrometer system used a probe with a single source fiber and single detector fiber separated by 370 μm. A pulsed nitrogen laser (NL-100, Stanford Research Systems, Mountain View, CA) delivered an excitation wavelength at 337 nm to excite collagen and NADH fluorophores during the fluorescence measurements. The fluorescence spectrometer system measured the emission spectrum over 345−700 nm wavelengths. A representation of the spectral experimental system is shown in Figure 5.1.

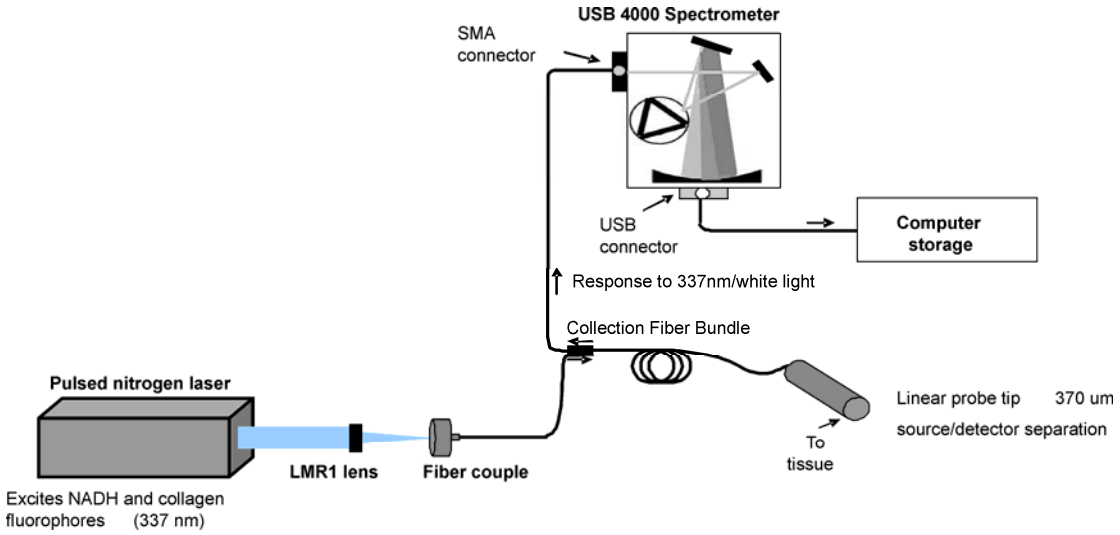

Figure 5.1. A schematic illustration of the instrumentation setup for the spectral diagnostic system.

5.3.2. Temperature measurement

Temperature was measured every two minutes with a thermal imaging infrared (IR) camera (Thermo Vision SC4000, Flir Systems, Inc., Billerica, MA) until temperature reached about 42°C. The IR camera was set to a frame size of 320×256 pixel. The temporal plot was collected with 800 frames per second for each observation time point. The temperature resolution of the thermal camera was 1°C. Like other thermal cameras the IR camera was sensitive to water content of samples. For the biological samples such as hamster tissue or enucleated pig eyes, the surface temperature was measured due to the relatively shallow penetration depth (high absorption and emissivity of the tissue surface) of the water in the operational bandwidth of the camera (3−5 μm for our experiment). A

strict measurement procedure was followed to minimize variations in temperature owing to water content.

5.3.3. Experimental procedures

Fluorescence measurements as a function of temperature were performed using (1) a phantom of Rhodamine B fluorescent dye, (2) cornea and sclera of enucleated pig eyes, (3) *in vivo* hamster dorsal skin.

5.3.3.1. Phantom study: Rhodamine B dye

Rhodamine B dye was diluted with deionized water and placed in a four-sided clear methacrylate cuvette (Fisherbrand Disposable Cuvets with spectral range from 340–750nm and accuracy UV/VIS range 285–750nm). The cuvette was stored in a refrigerator for an hour to reduce the temperature to about 14°C. A beaker filled with tap water was placed on top of a hot plate, and 1.0 cm of the cuvette was submerged in the water bath until the water bath reached approximately 45°C (Corning 4x5 inch top PC-220 Hot Plate/Stirrer, USA). As temperature of the dye in the cuvette increased, the temperature was measured with an IR camera placed 15.0 cm from the cuvette and focused at the surface of the dye in the cuvette. The temperature profile of the dye was collected every two minutes up to 20 minutes as the dye temperature increased from 14°C up to 42°C. The Rhodamine B dye inside the cuvette was stirred with a wood skewer every one minute to uniformly distribute the temperature. Due to the corrosive nature of Rhodamine B dye, the fiber optic probe of the fluorescence spectrometer system was placed at the

outside wall of the cuvette. Fluorescence intensity was measured immediately after the temperature measurement to prevent any effect of nitrogen laser on the temperature profile.

5.3.3.2. *In vitro* study: enucleated pig eye

Eight frozen enucleated pig eyes (n = 3 for sclera and n = 5 for cornea) provided by the Air Force Research Laboratory at Brooks City-Base were used based on under an IACUC approved tissue sharing protocol. The eyes were harvested and stored in antibiotic and phospho-buffer solution (PBS) immediately after enucleation. Storage containers holding the eyes were placed in ice to minimize sample degradation during transport. Eyes were placed in a freezer for one night. The next day, eyes were removed and measurements began when the eyes reached between 14°C−15°C. The time between enucleation of the eyes and experimental studies was 16 hours. These measures were taken to avoid excessive tissue degradation. The pig eyes were placed on a Styrofoam holder and a heat lamp (12.0 cm from the specimen) was used to increase the temperature. The IR camera fit with 25.0 mm lens was placed 60.0 inches from the enucleated eye. The probe of the fluorescence spectrometer system was gently placed in contact with the *in vitro* eye tissue and fluorescence spectra were measured. Temperature followed by fluorescence was measured every two minutes up to 36 minutes from 14°C to 42°C.

5.3.3.3. *In vivo* study: hamster

Three male Golden Syrian hamsters (weighing 120 to 150 g) obtained from Harlan Sprague Dawley, were used for the *in vivo* experiments. All experimental procedures were conducted according to protocols approved by the Animal Care Committee of The University of Texas at Austin (IACUC: 06060801). Hamsters were anesthetized with IP 200 mg/kg Ketamine and 10 mg/kg Xylazine. The depth of the anesthesia was monitored throughout the procedure by checking heart rate, breathing, and toe pinch. Supplements of one half of the initial dose of Ketamine were injected every one hour. The core body temperature was kept constant at 37°C with a heating pad designed for small animal experiments that was placed under the animal.

The dorsal area of a hamster was shaved and epilated before an ice pack was placed on the skin for three minutes to cool the surface of the skin. Once the ice pack was removed, the IR camera was used to identify the initial temperature. Temperature and fluorescence were measured every two minutes thereafter as the skin passively returned to normal temperature. This process was repeated three times for each hamster for repeatability.

5.3.3.4. Fluorescence lineshape

It was important to determine the fluorescence lineshape dependence upon temperature. Any changes in lineshape would depict the conformational change in tertiary protein structure of the tissue after the changes in temperature. Thus, each fluorescence spectrum for every observation time (wavelength 345−700 nm) was

normalized with the highest fluorescence intensity of that particular spectrum. Normalization compensates for subject to subject variation in fluorescence intensity and measurement system variation.

5.4. RESULTS

5.4.1. Phantom study: Rhodamine B dye

A 3-dimentional representation of the fluorescence intensity in Rhodamine B dye with respect to temperature and observation time is presented in Figure 5.2a. Figure 5.2b is the 2-dimentional depiction of Figure 5.2a for clear illustration of the changes in fluorescence intensity dependent on temperature. The peak fluorescence intensity (a.u.) from Rhodamine B decreased monotonically as temperature increased from 14°C to 42°C. A sharp decrease in fluorescence intensity occurred at about 34°C.

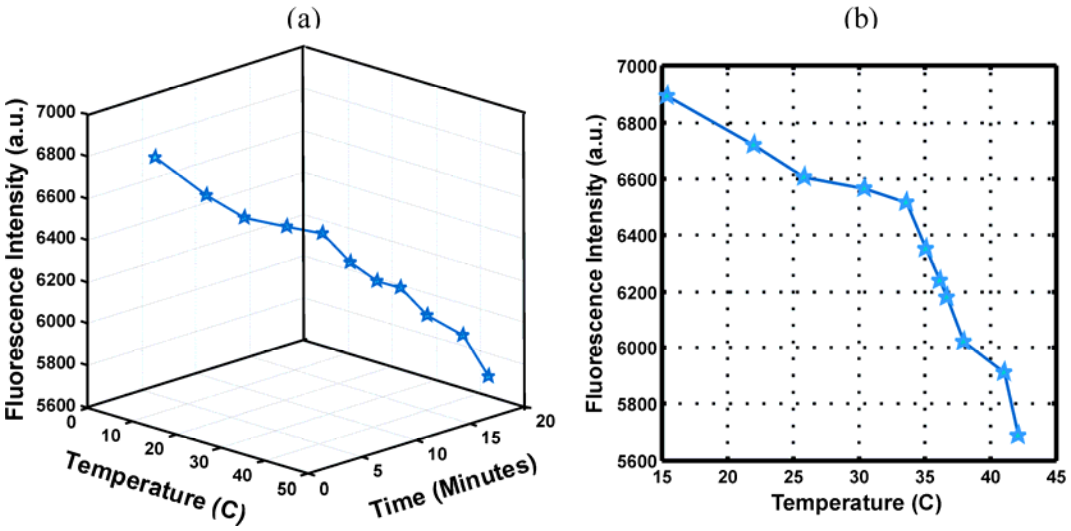

Figure 5.2. Active temperature change of phantom made of Rhodamine B dye solution using hot water bath represented in (a) 3-dimension with fluorescence intensity, temperature, and time (b) 2-dimension. Fluorescence intensity is measured between 345–700 nm. However, the depicted intensity in the fluorescence vs. temperature diagram is at 590 nm.

5.4.2. *In vitro* study

In the *in vitro* study, fluorescence decreased as temperature increased from 14°C to 42°C. A 3-dimentional representation of the fluorescence intensity calibrated each day with respect to temperature (°C) and observation time (minutes) is illustrated in Figure 5.3. The baseline fluorescence intensity of sclera of an enucleated pig eye showed 2 times the intensity compared to cornea. The change in normalized fluorescence intensity of all sclera (n = 3) and cornea (n = 5) due to temperature increase are illustrated in Figures 5.4a−5.4b. The average normalized fluorescence intensity of *in vitro* sclera and cornea decreased as a result of heating to 44% and 22%, respectively. The change in

fluorescence intensity in sclera and cornea was significantly different statistically ($p < 0.1$) based on the Tukey–Kramer multi-comparison test. The fluorescence of all eight enucleated pig eyes decreased as temperature was increased with the heat lamp. Sharp decreases in fluorescence are depicted in Figure 5.4 for both sclera and cornea. The temperature associated with these decreases varied from sample to sample.

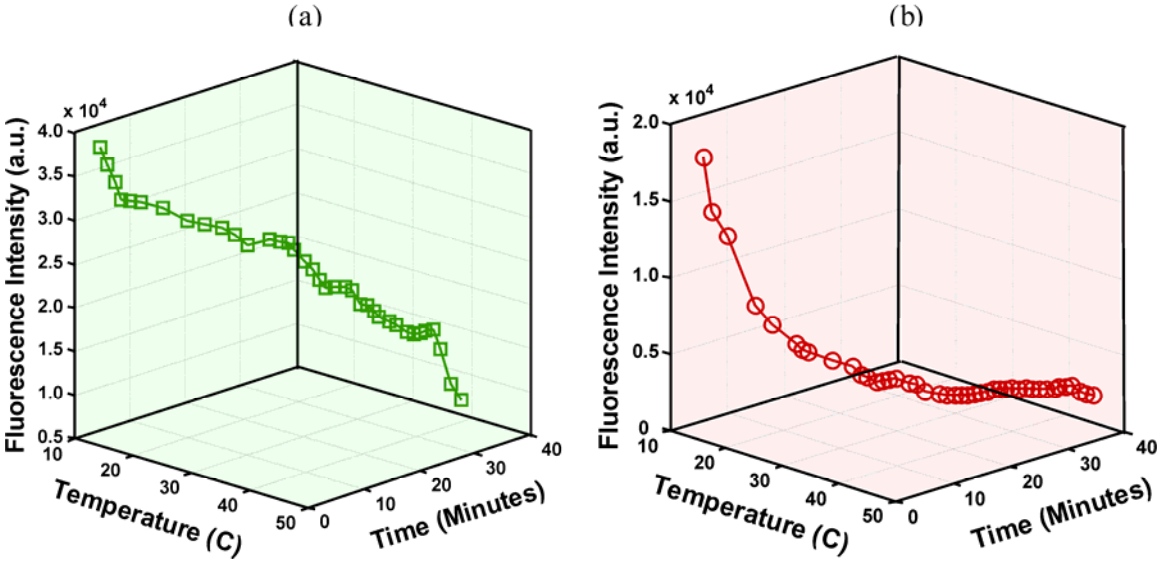

Figure 5.3. Active temperature change in *in vitro* enucleated pig eye tissue with heat lamp (a) sclera (n = 1) (b) cornea (n = 1). Fluorescence intensity is measured between 345–700 nm. However, the depicted intensity in the fluorescence vs. temperature diagram is at 434 nm.

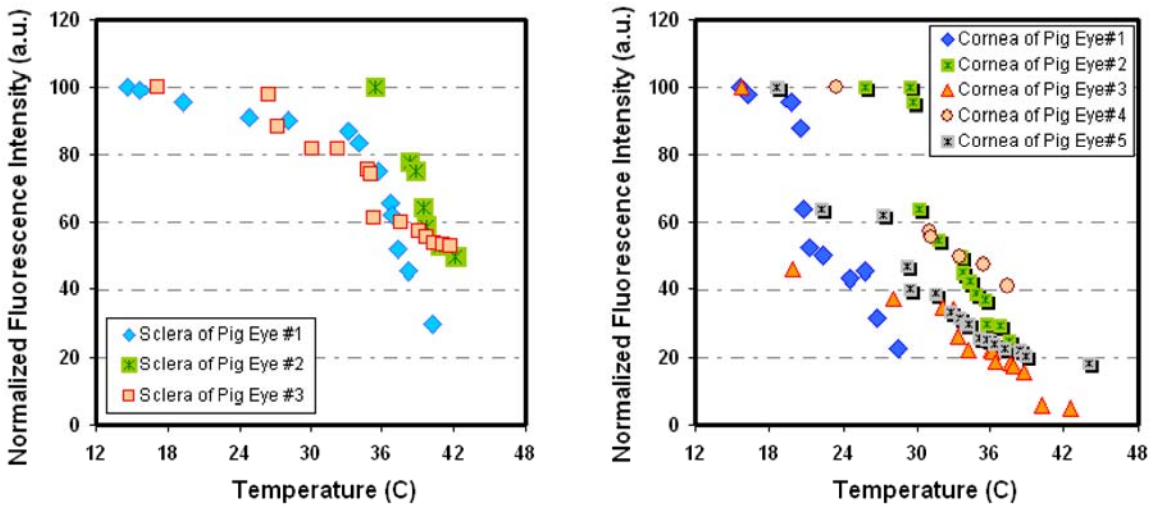

Figure 5.4. Change in normalized fluorescence intensity with respect to pre-heat baseline temperature (fraction is multiplied with 100). Active temperature change in *in vitro* enucleated pig eye tissue with heat lamp (a) sclera (n = 3) (b) cornea (n = 5). Fluorescence intensity is measured between 345–700 nm. However, the depicted intensity in the fluorescence vs. temperature diagram is at 434 nm.

5.4.3. *In vivo* study

The change in normalized fluorescence intensity of hamsters (n = 3) skin is illustrated in Figures 5.5. Each animal was subjected to three cooling cycles and the data in Figure 5.5 is the average of the three cycles. The changes in average fluorescence intensity with respect to temperature follow a similar trend in each cooling cycle. Fluorescence intensities of hamster skin decreased to by about 20% as temperature increased. Note that the temperature increase in the *in vivo* study was passive in that it resulted from the hamster's own metabolic processes (i.e. no active heating was

employed). Therefore, the maximum temperature for these experiments was the natural skin temperature of around 32°C.

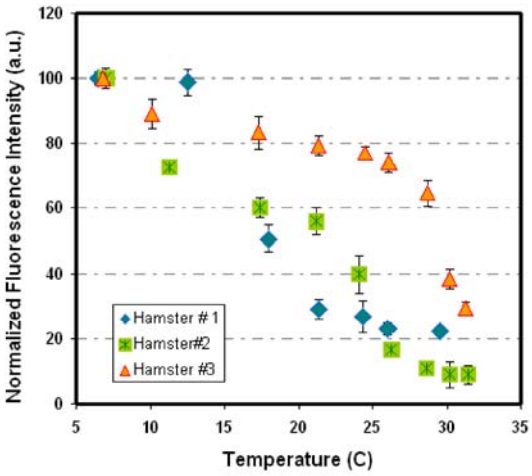

Figure 5.5. Change in normalized fluorescence intensity of *in vivo* skin with respect to temperature at immediate after removing cold-pack (fraction is multiplied with 100). Passive temperature change in *in vivo* hamster dorsal skin (n = 3) with standard deviation of ±1–6. Fluorescence intensity is measured between 345–700 nm. However, the depicted intensity in the fluorescence vs. temperature diagram is at 434 nm.

The normalized fluorescence spectra indicate slight changes in lineshape for wavelengths lower than the peak intensity wavelength. This observation implies that there are spectral lineshape changes in the fluorophores such as collagen and NADH due to change in absorption when temperature increases. Figure 5.6a illustrates fluorescence spectra at all the observation times and the normalized spectra are shown in Figure 5.6b.

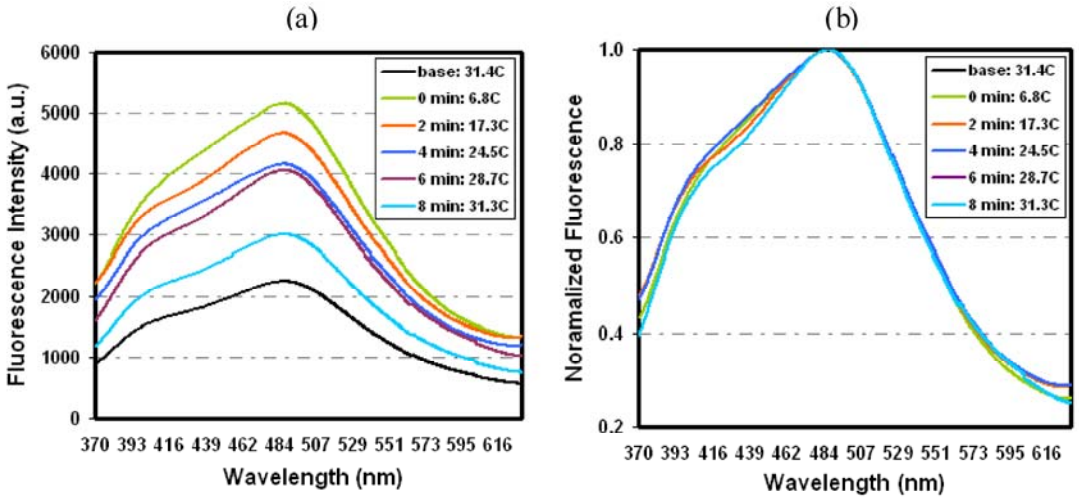

Figure 5.6. Change in (a) fluorescence intensity counts (b) normalized fluorescence with the highest fluorescence intensity in hamster skin with respect to temperature.

For the *in vivo* study, lowering the body temperature with an ice pack produced the same intensity-temperature response as starting with a frozen sample and heating it.

5.5. DISCUSSION

Our results verify the previous studies and extend the range of measurements to temperatures below normal body temperature. In the previous study by Buttemere and Mahadevan-Jansen *et al.*,[3] a radio frequency (RF) probe with a temperature sensor was used to asses the thermal damage in *in vivo* liver tissue. Fluorescence and diffuse reflectance were measured from native or room temperature to 75°C. These tissues denature within 100 seconds. After 100 seconds fluorescence intensity leveled off which

implied cell necrosis. Current RF treatment typically extends 150 seconds more than the measured atrophy time.

The Buttemere study also shows that the shape of fluorescence spectra changes between 42°C −57°C. Cell mitochondrial death occurs at 42°C and at 57°C protein starts to denature. Thus, scattering increases due to overt necrosis after these threshold temperatures. Numerous other published studies[6–10] indicate that the dominant change in tissue optical properties upon thermal coagulation increases in reduced scattering coefficient (μ_s'). The increase in μ_s' reflects changes occurring on a cellular and intracellular level. Protein denaturation, hyalinization of collagen, cytoskeleton collapse, and cell membrane rupture, are known to occur at onset temperatures between 45 and 90°C.[11] These thermally induced structural changes affect the size and distribution of scattering particles in the tissue and, consequently light distribution. The exact correlation between these morphological changes and alternations in tissue optical characteristics has not yet been determined.

The upper limit 42°C for our study (according to approved protocol) should not cause any obvious structural change in tissue as suggested in other studies. However, it is possible that even the lower temperatures cause changes such as water concentration and/or tissue density that affect the optical properties of tissue which in turn could affect the fluorescence. This could also be due to change in pH and certain enzymatic activity.

The active and passive methods of tissue heating both illustrated a sharp change in fluorescence drop after a certain temperature increase. A sharp change in fluorescence intensity was seen for both sclera and cornea of the enucleated pig eye. The sharp change

in fluorescence in sclera occurred while the tissue temperature reached about 26°C unlike cornea which happened much earlier at 19°C. For the hamster skin the change occurred between 17–27°C. These sharp changes might be due to the change in water concentration of the tissue while the temperature increased. However, the variability observed may be attributed to biological variability between specimens. In other words, the initial water content varied for each specimen; thus, fluorescence properties may have changed at different rates for each specimen as a function of initial water content. Also, the tissues have different types and structure of collagen.

The magnitude of the baseline fluorescence intensity between sclera and cornea also differ. The possible explanation for the intensity difference may be due to the amount of excitation light absorbed by collagen. The cornea is relatively clear; thus, most of the light absorbed by collagen is collimated. Whereas, the sclera scatters collimated light; so, both collimated and scattered light reaches the collagen. Therefore, the fluence of the excitation light in the sclera near the surface is much higher than the fluence at a comparable collection depth in the cornea.

The phantom study with Rhodamine B dye showed a similar trend in decreased fluorescence intensity with increased temperature as found in a previous study by Romano *et al*.[5] There were no obvious changes in the optical properties of Rhodamine B.

We hypothesize that the decrease in observed fluorescence as a function of temperature is likely due to a combination of changes in tissue optical properties as well as fluorescence quantum yield. Potential causes affecting fluorescence emission include changes in tissue microenvironment and early changes in chemical bonds. Other changes

include shrinkage or expansion of the tissue that could affect the probability of photon interaction. Further studies that can isolate the effects of optical properties from any fluorescence changes, both experimental as well as modeling studies, would be required to improve our understanding of the basis for the observed decrease.

The variation in fluorescence quantum yield may be due to multiple tryptophan residues which are present in most proteins.[12–15] These tryptophan residues contribute to the total emission.[12–15] The emission spectra of the tryptophan reflect the average environment of tryptophan. As tryptophan residue becomes hydrogen bonded or exposed to water its emission spectra and quantum yield is changed. There are several factors that determine the emission from tryptophan residues of protein molecules such as (1) quenching by proton transfer from nearby charged amino groups, (2) quenching by electron acceptors such as protonated carboxyl groups, (3) electron transfer quenching by disulfides and amides (4) electron transfer quenching by peptide bonds in the protein backbone, and (5) resonance energy transfer among the tryptophan residues.[16–21] Additionally, a protein may exist in more than a single conformation, with each displaying a different quantum yield. The variability in the quantum yields of proteins is due to a number of interactions, all of which depend on the details of the protein structure. The effect of temperature on tryptophan and its fluorescence intensity is discussed in the following paragraph.

The effect of heat on the conformation of bovine ß-lactoglobulin B had been studied using intrinsic fluorescence spectroscopy by Mills.[22] This study investigated the effect of temperature on tryptophan fluorescence of ß-Lactoglobulin B. After each change

in temperature, the protein was excited at 295 nm (a wavelength at which only tryptophan absorbs) and the emission spectrum was recorded. The peak fluorescence intensity (F_{max}) of the emission spectra decreased when temperature was increased from 20 to 90°C degree. Protein concentration also decreased with increased temperature (1.5-70°C degree). There was an increase in F_{max} at low temperature which was thought to result from disulphide bond reduction by $Na_2S_2O_3$.[23] These results support the findings in our study.

The enhanced fluorescence at temperatures below normal *in vivo* temperature provided an interesting point for speculation. Would cooling enhance the signal to noise ratio of diagnostic fluorescence measurements? Once again, additional work is needed to make this determination.

5.6. CONCLUSION

In this study we have shown that fluorescence intensity decreased in phantom, *in vitro* and *in vivo* tissues as temperature increased. This change in fluorescence did not depend on the method of temperature increase such as either actively or passively. Temperatures below 37°C (37°C to 14°C) produced a monotonic increase in fluorescence intensity down to our end point of 14°C.

5.7. ACKNOWLEDGEMENTS

This research has been supported by the National Science Foundation (UTA06−688) and Caster Foundation. Raiyan Zaman was a recipient of the ASLMS Travel Grant to attend and present at the Annual Conference of American Society for Lasers in Medicine and Surgery, 2009.

5.8. REFERENCES

1. Ramanujam N, Richards-Kortum R, Thomsen S, Mahadevan-Jansen A, Follen M, Chance B. Low temperature fluorescence imaging of freezetrapped human cervical tissues. Optics Express, 2001; 8(6):335−343.

2. Romano V, Greber CM, Frenz M, Forrer M, Weber HP. Measurement of temperature distributions after pulsed IR-radiation impact in biological tissue models with fluorescent thing films. SPIE Proceeding paper, Laser Tissue Interaction II, 1991; (1427):16−26.

3. Buttemere CR, Chari RS, Anderson CD, Washington MK, Mahadevan-Jansen A, Lin W-C. *In vivo* assessment of thermal damage in the liver using optical spectroscopy. Journal of Biomedical Optics, 2004; 9(5):1018−1027.

4. Rajaram N, Kovacic D, Migden MF, Reichenberg JS, Nguyen TH, Tunnell JW. *In vivo* determination of optical properties and fluorophore characteristics of non-melanoma skin cancer. Proceedings of SPIE, 2009; 7161: 1021−1029.

5. Romano V, Zweig AD, Frenz M, Weber HP. Time-resolved thermal microscopy with fluorescent thin films. Applied Physics, 1989; 49:527−533.

6. Lin WC, Toms SA, Motamedi M, Jansen ED, Mahadevan-Jansen A. Brain tumor demarcation using optical spectroscopy; an *in vitro* study. Journal of Biomedical Optics, 2000; 5:214–220.

7. Ritz JP, Roggan A, Isbert C, Muller G, Buhr HJ, Germer CT. Optical properties of native and coagulated porcine liver tissue between 400 and 2400 nm. Lasers in Surgery and Medicine, 2001*;* 29: 205–212.

8. Ritz JP, Roggan A, Germer CT, Isbert C, Muller G, Buhr HJ. Continuous changes in the optical properties of liver tissue during laser-induced interstitial thermotherapy. Lasers in Surgery and Medicine, 2001; 28: 307–312.

9. Pickering JW, Posthumus P, and Gemert MJ van. Continuous measurement of the heat-induced changes in the optical properties (at 1,064 nm) of rat liver. Lasers in Surgery and Medicine, 1994; 15:200–205.

10. Germer CT, Roggan A, Ritz JP, Isbert C, Albrecht D, Muller G, Buhr HJ. Optical properties of native and coagulated human liver tissue and liver metastases in the near infrared range. Lasers in Surgery and Medicine, 1998; 23:194–203.

11. Pearce J, Thomsen S. Rate process analysis of thermal damage in *Optical-Thermal Response of Laser-Irradiated Tissue*, A. J. Welch and M. J. C. van Gemert, Eds., pp. 561–606, Plenum Press, New York, 1995.

12. Burstein EA, Abornev SM, Reshetnyak YK. Deconposition of protein tryptophan fluorescence spectra into log-normal components, I: decomposition algorithms. Biophysics Journal, 2001; 81:1699–1709.

13. Reshetnyak YK, Burstein EA. Decomposition of protein tryptophan fluorescence spectra into log-normal components, II: the statistical proof of discreteness of tryptophan classes in protein. Biophysics Journal 2001; 81:1710–1734.

14. Reshetnyak YK, Koshenvik Y, Burstein EA. Decomposition of protein tryptophan fluorescence spectra into log-normal components, III: correlation between fluorescence and micro environment parameters of individual tryptophan residues. Biophysics Journal 2001; 81:1735–1758.

15. Eftink MR. Fluorescence techniques for studying protein structure. Methods Biochemical Anal, 1990; 35:117–129.

16. Callis FR, Liu T. Quantitative prediction of fluorescence quantum yields for tryptophan in proteins. Journal of Physical chemistry B, 2004; 108:4248–4259.

17. Callis PR, Vivian JT. Understanding the variable fluorescence quantum yield of tryptophan in proteins using QM-MM simulations: quenching by charge transfer to the peptide backbone. *Chem Phys Lett*, 2003; 369:409–414.

18. Ababou A, Bombarda E. On the involvement of electron transfer reactions in the fluorescence decay kinetics heterogeneity of proteins. Protein Science 2001; 10: 2102–2113.

19. Adams PD, Chen Y, Ma K, Zagorski M, Sonnichsen FD, McLaughlin ML, Barkley MD. Intrmodelcular quenching of tryptophan fluorescence by the peptide bond in cyclic hexapeptides. Journal of American Chem Society, 2002; 124: 9278–9286.

20. Chen Y, Barkley MD. Toward understanding tryptophan fluorescence in proteins. Biochemistry, 1998; 37: 9976–9982.

21. Chen Y, Liu B, Yu H-T, Barkley MD. The peptide bond quenches indole fluorescence. Journal of American Chem. Society, 1996; 118: 9271–9278.

22. Mills, OE. Effect of temperature on tryptophan fluorescence of ß-Lactoglobulin B. *Biochimica et Biophysica Acta,* 1976; 434: 324–332.

23. Mills OE, Creamer LK. Biochim. Biophys. Acta, 1975; 379: 681–626.

CHAPTER 6: LIGHT ACTIVATED MICRO-PATTERNED DRUG DELIVERY DEVICE IN *IN VIVO* RABBIT EYE—FABRICATION, BIOCOMPATIBILITY, AND RELEASE MEASUREMENT[4]

6.1. ABSTRACT

The primary goal of this study is the fabrication, biocompatibility testing, and measured release of a marker dye (Na Fluorescein) from a micro-patterned drug delivery device using two different methods—(i) generating mechanical pressure (ii) light activated using an ophthalmic Nd:YAG laser. The device can be implanted in the sub-conjunctival space or sub-scleral space. We have developed a drug delivery device with 3×6×1.5 mm^3 dimensions (width × length × depth) that is fabricated (Zhang Research Group) from ultraviolet (UV) cured biocompatible polyurethane, a form of poly-methyl methacrylate (PMMA), under sterile condition. The device has a 82 μm thick clear cap made from a transparent bio-compatible polymer. The device consists of two 2.6 mm diameter reservoirs containing 10% Na fluorescence USP sterile dye. Once the reservoirs are filled with the dye, the cap is bonded to the device using UV and NOA68 optical glue. After the device is tested for leaks, it is then implanted in the rabbit's eye (n =2) where the cap of the device is facing toward the exterior of the eye. The rabbits are placed under

[4]The experiments contained in this chapter were submitted for publication in a peer-reviewed journal: Raiyan T. Zaman, MSE, Ashwini Gopal, MSE, Xiaojing Zhang, PhD, James W. Tunnell, PhD, Ashley J. Welch, PhD, Henry G. Rylander III, MD, *Lasers in Surgery and Medicine 2010*

observation in the Animal Resource Center (ARC) facility for 2 weeks until the eyes completely recovered from the implant surgery. To check for leaks, the pupil of the rabbits is dilated with 3 drops of 1% tropicamide every 1 and 1/2 minutes for 5 minutes. Once the pupil is dilated, a fiber optic probe and a fluorescence spectrophotometer system are used to measure the intensity of 10% Na fluorescence in the aqueous and vitreous humor. Once the animals recovered from the surgery, 100% anhydrous glycerol is topically applied to the eye tissue where the drug delivery device is implanted to decrease light scattering in the conjunctiva and sclera. An ophthalmic Nd:YAG laser is used to ablate the membrane of the device to deliver the fluorescence dye. Measurements of fluorescence intensity are collected until the measurements return to baseline. Once the experiments are completed the animals are euthanized according to an approved protocol and the eye tissues are collected for histology. We found that none of the devices leaked after implantation. The ablation threshold of the drug delivery device before implantation was found to be at 6.5 mJ of power to release the fluorescence dye from the reservoirs. However, implanted device required 10 mJ of power to create a 100 μm hole in the membrane. The half-life measurement of the dye in the posterior chamber or vitreous humor was found to be 13 days. Histology study showed minimal immune response such as inflammation. This study established that the drug delivery device retained its fluidic content intact until it was released. We can measure the concentration of the dye in the aqueous and vitreous for more than two weeks after the dye is released.

6.2. INTRODUCTION

The method by which a drug is delivered can have a significant effect on the drug's therapeutic efficacy.[1, 2] Conventional drug delivery systems such as tablets[3-5], pumps[6-8], implants[9, 10], injectable microspheres (such as Luprom Depot[11]), and patches[12] often produces a sharp initial increase in concentration to a peak above the therapeutic range, followed by a fast decrease in concentration to a level below the therapeutic range. Many polymeric implants achieve pulsatile release of a chemical via triggering by specific stimuli (changes in pH[13-15]) or temperature[16-18], exposure to ultrasound[19, 20], enzymes[21], photochemical[22], or change in electric[23-27] or magnetic[19, 28] fields or molecules present in the human body, such as antigens[29] or water). However, these devices are seldom used in combination with tissue clearing using hyperosmotic agent (100% anhydrous glycerol) and photo activation.

The conventional treatment for ocular disease is particularly difficult due to several factors including physiological barriers, space limitations within and surrounding the eye, and trauma to eye from invasive therapies. For example, treatment methods for wet age-related macular degeneration (ARMD) require coagulation/ablation by Argon laser, intra-vitreal drug delivery or periodic injection of anti-angiogenic drugs such as Lucentis (ranibizumab) through the sclera. Photocoagulation with Argon laser may worsen the vision in treated patients with disciform ARMD. There is about a 20% chance of vision loss within 3 months in the treated group versus 11% of controls.[30] Other side-effects occur from intra-vitreal injection such as causing pain and multiple risks of endophthalmitis (0.16%) or 0.05% per injection, lens trauma (0.7%), retinal detachment

(0.6%), and systemic VEGF-A inhibition predisposes patients to excess thrombo-embolic complications in the first year of follow-up.[31, 32]

Also, therapeutic efficacy of a drug delivery via these conventional treatment methods are not always optimum due to the fact that efficacy depends on how the drug is delivered. The time spent in the optimum concentration range for therapeutic effect is therefore very short for conventional drug delivery such as intra-vitreal injection or oral delivery. Also, non-invasive drug delivery to the anterior and posterior chambers of the eye is severely impeded by physiological barriers. For example, eye drops and oral medications must permeate through the modified mucosal membrane of the cornea or the blood-retina barrier, respectively. A study by Geroski and Edelhauser reported that only 5% of the dispensed eye drops may reach the anterior intraocular tissues through the cornea.[33] Furthermore, drug is diluted by lacrimation, tear drainage, and turnover limits the drug contact time with the cornea. On the other hand, according to Fraunfelder oral medications require larger doses to reach therapeutic levels due to presence of the blood-retina barrier. This may result in serious systemic side effects.[34-38] Therefore, there is a need for an improved method of drug delivery to treat ocular diseases.

The primary goal of this study is to investigate a novel drug delivery device implanted between the super-scleral and sub-conjunctival space by making an incision in the conjunctiva. Important aspects of the study include the biocompatibility of the device and the half-life comparison between the two methods of dye release by (i) mechanical pressure and (ii) light activation with an ophthalmic Nd:YAG laser. The duration of action of a drug is known as its half life. This is the period of time required for the

concentration or amount of drug in the body to be reduced by one-half of the maximum amount. We have considered the half life of the 10% Na fluorescence dye in relation to the amount of the dye present in the vitreous humor of the posterior chamber.

Another important findings of this study is the difference in threshold power of the pulsed Nd:YAG laser to release the content from the reservoir by ablating the membrane while the drug delivery device is implanted in the eye and when it is not. Release the dye from the device that is implanted in the eye needs optical clearing of the conjunctiva using hyper-osmotic agents such as 100% anhydrous glycerol.

6.3. MATERIALS AND METHODS

6.3.1. Animal preparation

Female SPF Dutch Belted (n = 2) rabbits weighing 4 to 5 lbs were used for the implant surgery. All experimental procedures were conducted according to protocols approved by the Institutional Animal Care and Use Committee (IACUC) of the University of Texas at Austin (AUP-2009-00061). Prior to the experiment, the rabbits were anesthetized with 35mg/kg Ketamine, 5 mg/kg Xylazine, and 0.75 mg/kg Acepromazine. One hour prior to termination of the surgery, Buprenorphine 0.01−0.05 mg/kg was administered IM for any pain or discomfort.

Rabbits were positioned in the ventral recumbent position. Oxygen saturation, pulse, and respiration rate were monitored every 15 minutes throughout the study using a vet/ox G2 Digital pulse oxymeter (Heska Corp. Loveland, CO, USA). This monitor was

connected via a shaved area of the feet or the ear depending on the best contact for recording. Animals were kept warm with warm water blankets. The anesthetic and monitoring procedures were performed by a skilled technician from the Animal Resources Center (ARC) of the University of Texas at Austin.

6.3.2. *In vivo* eye model

In this study, we are interested in anterior (aqueous humor) and posterior (vitreous humor) chambers of the *in vivo* eye. The anterior chamber is the space in the eye that is behind the cornea and in front of the iris. The anterior chamber is filled with a watery fluid known as the aqueous humor or aqueous which is produced by a structure alongside the lens called the ciliary body. The aqueous passes first into the posterior chamber (between the lens and iris) and then flows forward through the pupil into the anterior chamber of the eye. Posterior chamber (vitreous chamber is called as posterior chamber) is the space in the eye behind the iris and the lens and it is filled with vitreous humor. Vitreous humor consists of 99% water and remainder is a mixture of collagen, proteins, salts, and sugars. Although, the vitreous humor is mostly made of water, it has a jellylike consistency, and this viscosity helps the eye hold its shape. The vitreous humor has no vascularization, so once a drug gets into this part of the eye it will diffuse out slowly.

We are also interested in the three layers of the *in vivo* eye: (i) bulbur conjunctiva, (ii) sclera, and (iii) choroid. The bulbar conjunctiva is a thin (54.7±1.9 μm) clear outermost epithelium membrane that covers the sclera.[39–41] The naturally white sclera is just beneath the conjunctiva, which is opaque due to its normal level of hydration.

Collagen accounts for 90% of the dry weight of all mammalian sclera. In addition, some fine blood vessel arcades exist on both the surface of conjunctiva and sclera; however, sclera is mostly avascular and is anatomically similar to dura mater of brain. The thickness of the sclera varies from 1000 μm at the posterior pole to 300 μm just behind the rectus muscle insertions. It is continuous with the dura mater and the cornea, and provides an attachment for the extra ocular muscle insertions. The choroid lies between the sclera and retinal pigment epithelium (RPE) and consists of four layers (i) Haller's layer (outermost layer), (ii) Sattler's layer, (iii) Choriocapillaris, and (iv) Bruch's membrane (innermost layer). Haller's and Sattler's layers consist of large and medium diameter blood vessels, respectively; Choriocapillaris layer has capillaries.[41] Melanin, a darkly colored chromophore synthesized by melanocytes, occurs throughout the choroidal layer and helps limit uncontrolled reflection within the eye.[42] Figure 6.1 depicts the anatomy of the cross-sectioned eye model.

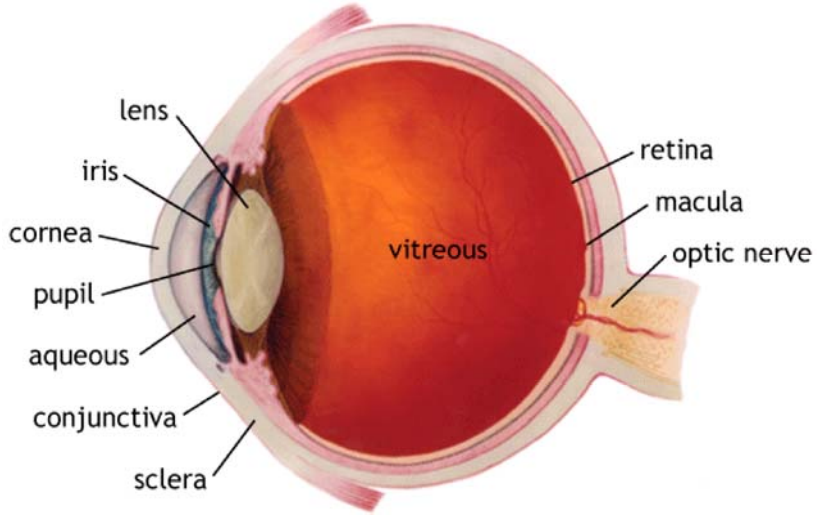

Figure 6.1. Cross-sectional view of an adult eye.

6.3.3. Micro-patterned drug delivery device fabrication

We developed two different generations (first and second) of drug delivery devices. The important differences between the first and the second generation drug delivery devices were the shape of the four corners and bottom of the device. The second generation device had smoother edges and with boat shaped bottom for easier insertion. Also, the bonding between the membrane and the device was much stronger for the second generation device due to a different optical adhesive. General description of the fabrication process is described in the following paragraphs.

A drug delivery device with 3×6×1.5 mm^3 dimensions (width × length × depth) is fabricated (Zhang Research Group) from ultraviolet (UV) cured biocompatible polyurethane, a form of poly-methyl methacrylate (PMMA), under sterile condition. The device has 82.0 μm thick clear cap or device membrane made from a transparent bio-compatible polymer. The device consists of two 2.6 mm of diameter reservoirs containing 10% Na fluorescence USP sterile dye. Once the reservoirs are filled with the dye, the cap is bonded to the device with optical adhesive using ultra violet (UV) light.

Initial step of the device fabrication started with making of mold from Polydimethylsiloxane (PDMS). PDMS was fabricated using conventional rapid prototyping.[43–45] Figure 6.2 illustrated a schematic diagram of the implantable drug delivery device created in UV curable polymer (polyurethane precursor). The PDMS was replicated from SU8 masters created on silicon wafers. SU8 photo-resist was patterned on silicon using conventional photolithographic process (Microchem Corporation).[43] Molds for PDMS with feature size of 2.6 mm diameter reservoirs and 1.5 mm depth were

created on SU8 master molds (Figure 6.3a). The PDMS with curing agent (1:10 mixture ratio) was poured on the master mold and cured at 70°C for 30 minutes. The cured PDMS was then peeled off the mold to create the template for creation of the drug delivery devices. The UV curable polymer is then poured onto the PDMS mold to create the reservoirs in the devices and cured under a UV lamp (Figure 6.3b). The devices were peeled carefully from the PDMS mold (Figure 6.3c) and 5.0 µL of the 10% Na fluorescein dye was pipetted into each reservoir. The first and second generation devices were then bonded to a thin layer of plastic film (82 µm) using UV curing Norland Optic Adhesive NOA65 and NOA68 (Thorlabs, Inc. Newton, NJ, USA), respectively, under a UV lamp for 10 minutes. Once the devices were cured, they were washed with water to remove any unwanted debris and checked for leak. The devices were then placed under the UV lamp for additional 20 minutes for sterilization. Photograph and schematic cross section of the device are depicted in Figures 6.4a and 6.4b.

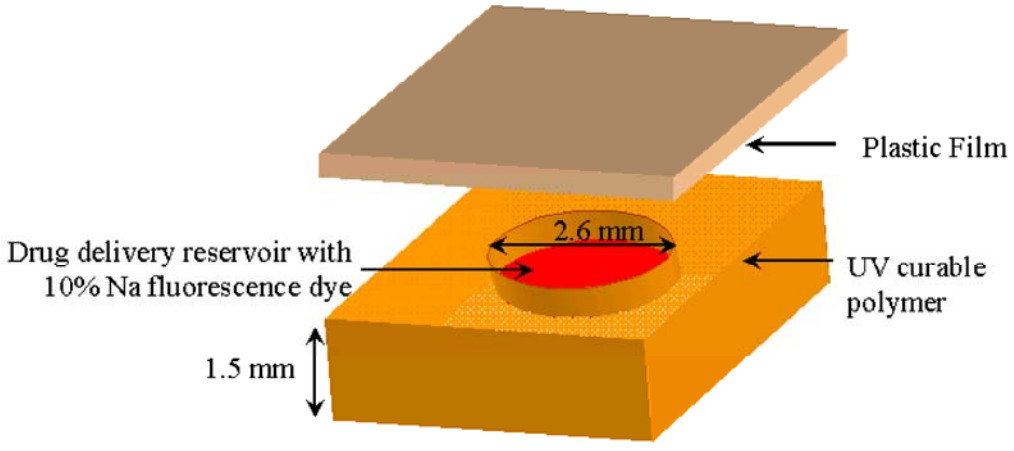

Figure 6.2. A schematic illustration of the implantable drug delivery device.

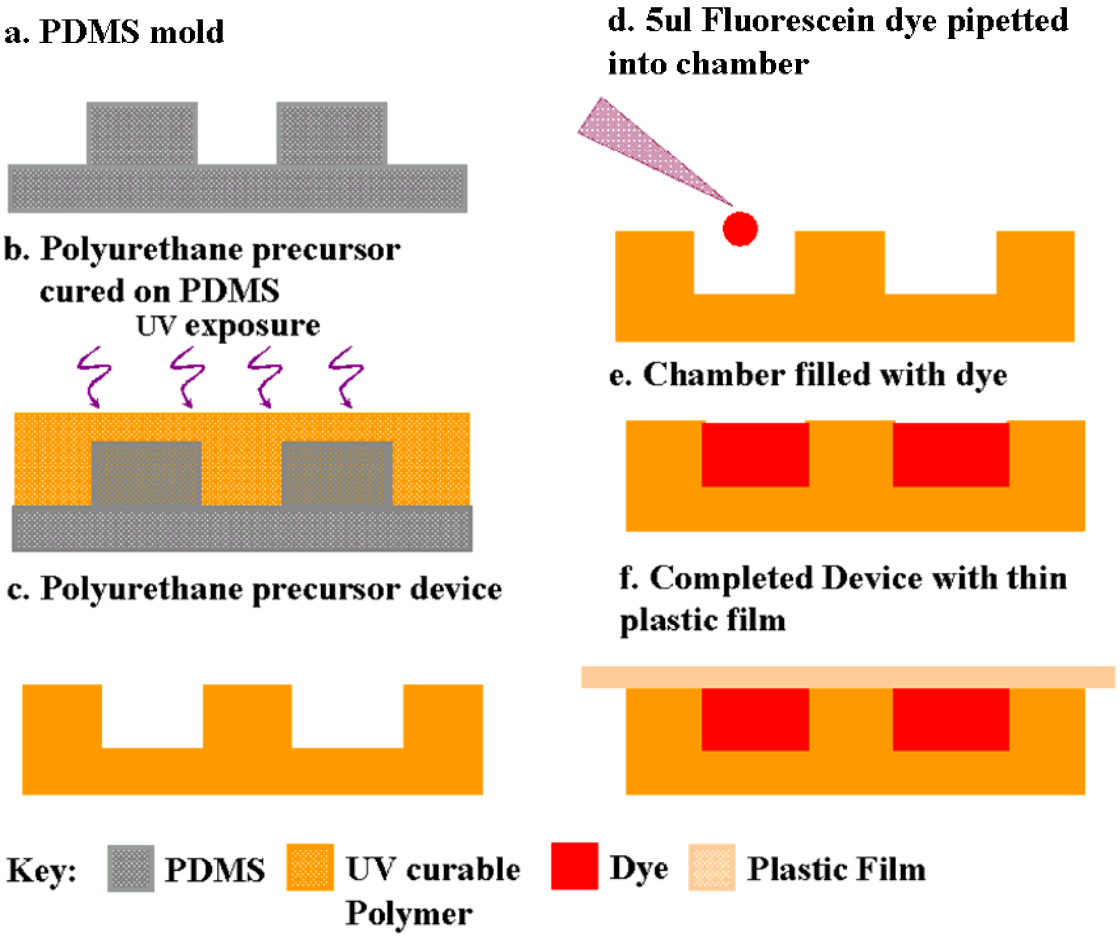

Figure 6.3. Schematic illustration of the fabrication processes of the implantable drug delivery device.

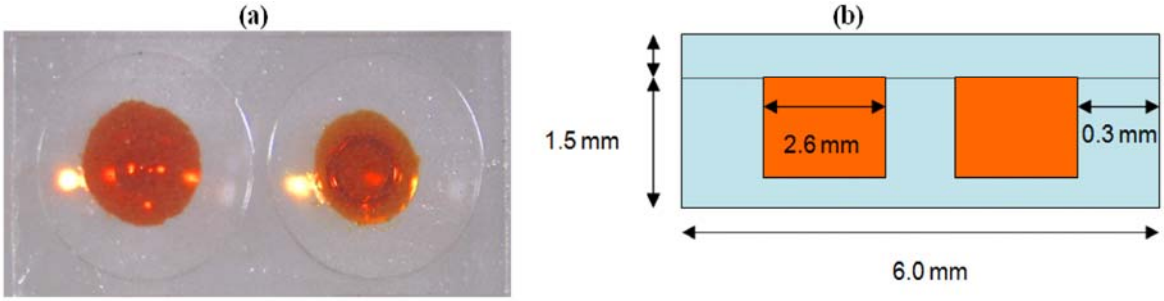

Figure 6.4. (a) Photograph of the drug delivery device from the top (b) schematic: side-view cross section of the device.

6.3.4. Device stability testing

The long term stability of the drug delivery device was tested by submerging the device under water filled glass bottle and observed for any leak. The glass bottles with the device were shaken every day vigorously to generate maximum wear and tear to identify the breaking point where the device would leak.

6.3.5. Fluorescence Spectrophotometer (FS) system

The fluorescence spectrophotometer (FS) system consists of four main components: (i) a tungsten halogen lamp to shine white light (LS-1, Ocean Optics), (ii) a low pass filter with transmission between 390–480 nm with cutoff at 505±15 nm wavelength (FD1B, an additive dichroic color filter, blue, Thorlabs, Inc. Newton, NJ, USA) (iii) a custom-designed fiber-optic probe (core diameter = 200 μm; NA = 0.22; FiberTech Optica), and (iv) a spectrometer (USB4000, Ocean Optics). The fiber-optic probe consists of 2 individual fibers with core to core separation of 370 μm that are terminated with SMA connectors. The source and detector fibers were connected to the lamp and spectrometer, respectively. The low pass filter is placed between the light source and the fiber-optic probe. A built-in 74-VIS collimated lens is used in the LS-1 light source before termination with the fiber-optic probe. Figure 6.5 is the schematic illustration of the FS system.

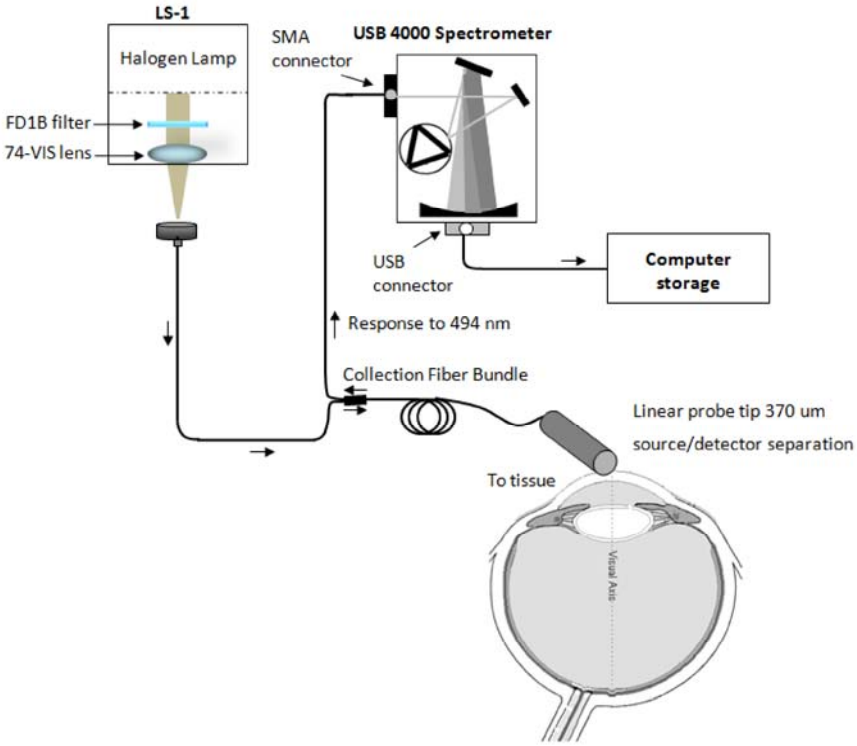

Figure 6.5. Schematic illustration of the instrumentation setup for Fluorescence Spectrophotometer (FS) system.

We collected the 10% Na fluorescence emission spectrum from the eye tissue over a wavelength range of 450−700 nm. The fiber-optic probe was placed in contact with the surface of the cornea, and the average was taken from 5 measurements of blue light spectra at each time point. Each fluorescence spectra was collected within 500 milliseconds. Fluorescence spectra from the cornea were collected at the same location during baseline (before implant), immediately after implant, and once every week until the membrane of the device is ablated either mechanically or using ophthalmic Nd:YAG laser. After the release of the dye, fluorescence emission spectrum was collected twice a

week until the intensity returned to its baseline measurement. Prior to spectral analysis, recorded signals were corrected for system response by subtracted the detector dark current and with respect to the fluorescence intensity of Rhodamin B fluorophores.

6.3.6. Sampling depth measurement

The sampling depth of optical fibers is a function of the source-detector separation distance and the optical properties of the tissue. Determination of the sampling depth assumes importance due to the location of the dye in the eye. It is important to know if the probe can sample fluorescence emission spectrum from the aqueous humor (anterior chamber) or from the vitreous humor (posterior chamber). Therefore, knowledge of sampling depth is necessary as we report the path of the dye upon release from the device.

Estimates of the changes in sampling depth were obtained using a container (base painted with non-reflective black paint), which was filled with 3.0 μL 10% Na fluorescein dye in 6.0 mL water (dye:water with 5:1000 ratio) solution to mimic the fluorescence after the maximum release from the drug delivery device, and measured through the rabbit's dilated pupil. A LabVIEW interface (SD Instrument, MC2000 controller) controlled the position of the fiber optic probe of the FS system. The fiber-optic probe was initially placed at the base of the phantom. The fluorescence intensity measured was close to zero due to the non-reflective black paint. Subsequently, the probe was moved in the z-direction and the fluorescence intensity was recorded at each step (50 μm). The experiment was continued until the fluorescence intensity reached a constant

value. The slope of the curve provided a measure of this particular probe's sampling depth. The slope was calculated by differentiating the fluorescence intensity of the diluted 10% Na fluorescein dye and depth in z-direction. After the differentiation, a ratio was calculated between the differentiated values that depicted the highest peak of the intensity at a specific sampling depth. After this peak sampling depth, the fluorescence intensity started to decline. Based on our experiments, the maximum sampling depth was identified to be 17.6 mm for the case of dilated pupil (Figure 6.6).

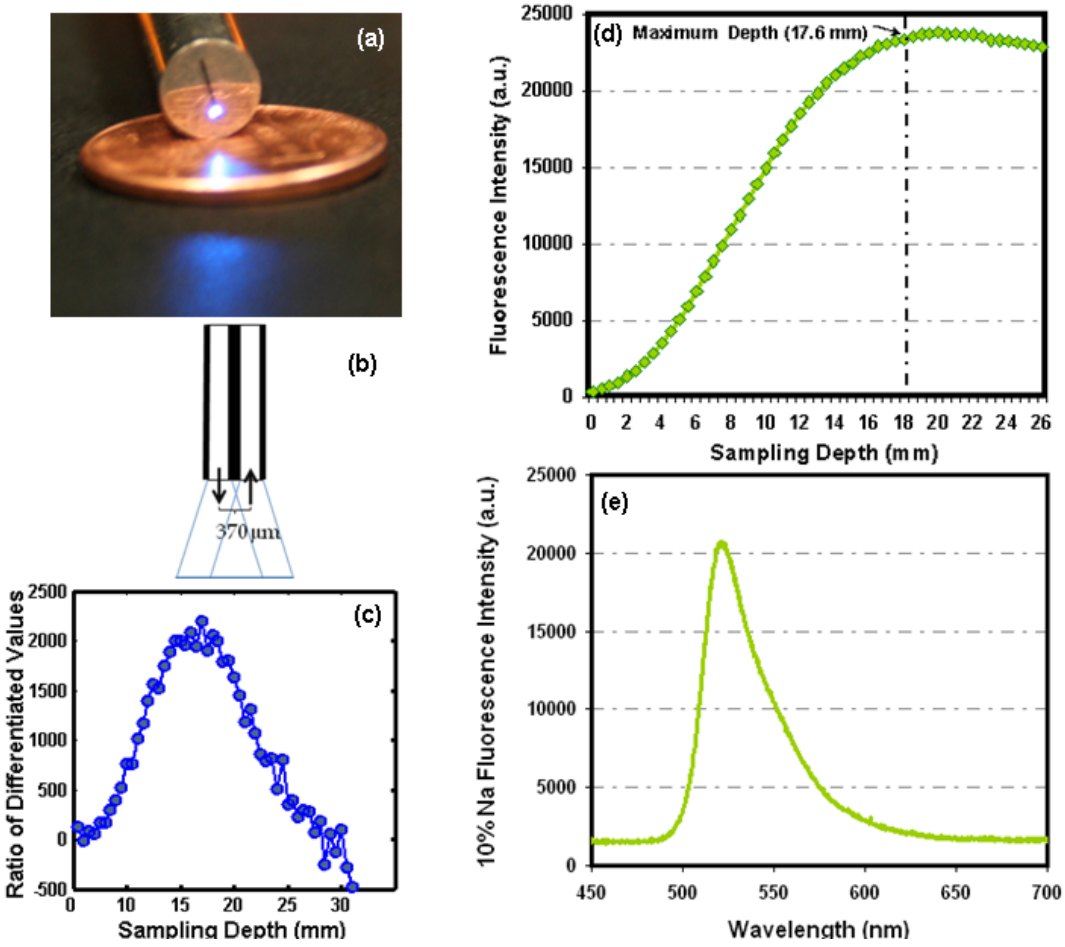

Figure 6.6. (a) Photograph of the custom-made fiber optic probe (b) probe geometry (c) differentiated values (d) sampling depth of the probe (e) Emission spectrum of 10% Na fluorescein dye with maximum peak at 520 nm.

6.3.7. Power measurement

It was important to know how much power was required to ablate the membrane of the drug delivery device before we could implant the device in the *in vivo* rabbit eye. Also, this value must be within the physiological range (0–15 mJ) that can be used in humans safely. Thus, before any implant surgeries, the device was placed vertically on a beaker filled with water where the membrane was facing towards the laser beam. An ophthalmic Nd:YAG laser was used starting from zero until the threshold power was reached at which the membrane was ablated. The threshold power was recorded as it would be the starting point for the membrane ablation of the implanted drug delivery device in the *in vivo* rabbit eye.

6.3.8. Surgical implant procedures

A wire eye speculum was placed in the rabbit eye to hold the eyelid at a fixed position. The position of the eye was stabilized with a suture placed in the limbus using a 6-0 prolene (0.10–0.14 mm diameter). The suture helped to position the eye to gain access to the superior temporal sclera. The device was implanted by making a 6.5 mm incision in the conjunctiva so that the device could be aligned with the cornea horizontally. However, the implant surgery in the two rabbits was slightly varied to identify the best method for delivering the content of the device. For one of the rabbit we made a 2.0 mm scleral flap to create a direct access for the content of the device to reach the blood vessels of the highly vascularized choroidal layer, and for the second implant

no scleral flap was made. For simplicity, the rabbits with scleral flap and without scleral flap are called rabbit 1 and rabbit 2, respectively. For both cases the drug delivery device was placed between the sub-conjunctival and super-scleral space of rabbit's eye that was 0.5 mm away from the corneal limbus. Although, the implant was placed at the same location for the both rabbits, for rabbit 1 and rabbit 2 the incisions were fornix based (incision at the limbus) and limbus based flaps (incision at the superior temporal sclera), respectively. The membrane of the device was facing outward, away from the eye. Surgical sutures, 6-0 prolene and 6-0 fast absorbing plain gut (Ethicon, Inc), were used to close the incision at the conjunctiva for rabbit 1 and rabbit 2, respectively. During the surgery, 0.5% Proparacaine Hydrocholoride Ophthalmic sterile solution USP (Falcon Pharmaceuticals) was used to anesthetized the eye. At the end of the implant surgery Bacitracin Zinc and Polymyxin B Sulfate Ophthalmic Ointment USP (Bausch & Lomb) was used to prevent any post-operative infection. Figure 6.7 illustrated the surgical procedure and the implant location. At the limbus, the implanted location, the sclera was the thinnest (300 μm).

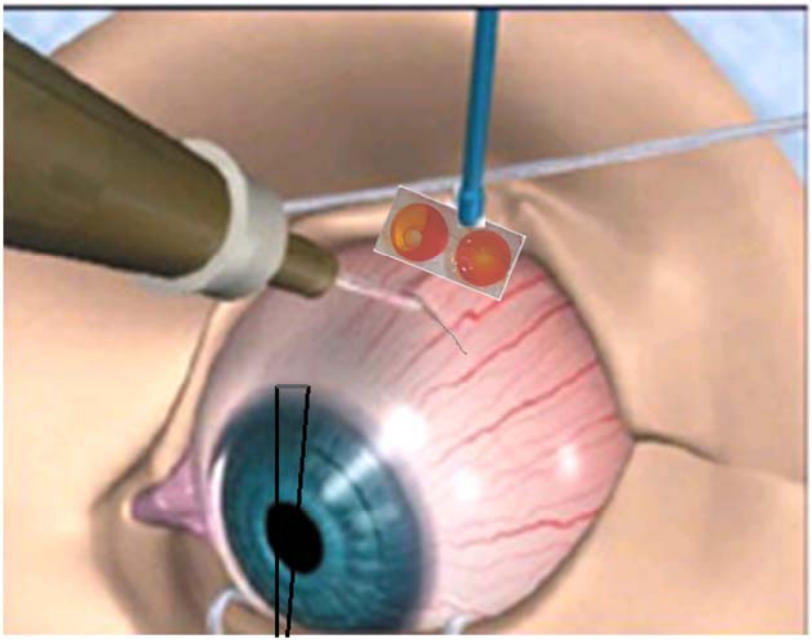

Figure 6.7. A schematic diagram of the implant surgical procedure. A suture, 6-0 prolene, was used to hold down the eye ball to create space for the implant. The drug delivery device was implanted horizontally with respect to the cornea. The drug delivery device was placed between the sub-conjunctival and super-scleral space of rabbit's eye that was 0.5 mm away from the cornea.

Once the drug delivery devices were implanted into the eye, the rabbits were placed under observation in the ARC facility for 2 weeks until the eyes completely recovered from the surgery. At this time, any leak from the device was checked by dilating the pupil of the implanted eye using 3 drops of 1% Tropicamide every 1 and 1/2 minutes for 5 minutes. Once the pupil dilated, a fiber optic probe with a noninvasive FS system (Section 2.4) was used to measure the intensity of 10% Na fluorescence from the aqueous (anterior chamber) and vitreous (posterior chamber) humors.

6.3.9. Two different methods of dye release

After complete recovery (two to three weeks) from the implant surgery, the conjunctiva was optically cleared with topical application of hyper-osmotic agent (100% anhydrous glycerol). The glycerol was poured from the original container into smaller airtight screw cap bottle for each experiment to prevent the glycerol from absorbing any moisture from the air due to its hygroscopic nature. The rest of the glycerol after each experiment was discarded to prevent contamination. Initial optical clearing process started at 3 minutes. However, to clear the conjunctiva and part of sclera completely took about 8 minutes. After 8 minutes the tissue started to become opaque again. Thus, multiple topical applications of glycerol may be needed to get best results. Once the eye tissue became optically clear, the drug delivery device became visible and the content of the drug delivery device was released in two different methods. During the first method the dye from the reservoir of the rabbit 1 was release by generating mechanical pressure using a 28G needle. In the second experiment, an ophthalmic Nd:YAG laser (ELLEX, LaserEX, SuperQ) was used to disrupt the membrane of the implanted device in rabbit 2.

6.3.10. Photography of eye after implant

Two different methods were applied to photograph the implanted device. For the rabbit 1 an EOS digital SLR Canon camera (Digital Rebel XT, Japan) attached to a slit lamp (Topcon SL-6E) was used to capture the condition of the implant. The camera shutter was triggered by digital single-lens reflex (DSLR) software using a computer. For

the rabbit 2 a CCD camera (HV-C20 Hitachi Denshi, Ltd.) attached to a surgical microscope (Topcon OMS75, NJ, U.S.A.) was used to capture the image. A photograph was taken of the *in vivo* conjunctiva immediately after implant and every time the fluorescence intensity was measured from the implanted eye.

6.3.11. Scaling factor

Five enucleated pig eyes were provided by the Air Force Research Laboratory at Brooks City-Base. The eyes were harvested and stored in antibiotic and buffer solution immediately after enucleation. The solution was made from 0.5 L 1X Hank's Balanced Salt Solution (HBSS) with Ca and Mg, 10 mM HEPES buffer, 100 I.U./mL Penicillin, 100 I.U./mL Streptomycin and 0.05 mg/mL Gentamicin. Storage containers holding the eyes were placed in ice to minimize sample degradation during transport. Eyes were placed in a 4° C refrigerator for one night. The time between enucleation of the eyes and experimental studies was 16 hours. These measures were taken to avoid excessive tissue degradation. The next day eyes were removed from the solution and held until temperature reached between 24°C−25°C (room temperature). Once the eye reached this specific temperature, 3.3 mL of vitreous humor was extracted from the posterior chamber of an enucleated pig eye using a 18G needle and fluorescence intensity was measured each time 1.0 µL of 10% Na fluorescein dye was added to the liquid. This process was repeated 5 times for each addition of 1.0 µL dye to find the correlation between the fluorescence intensity of the dye associated with a specific volume of the dye. However,

volume of rabbit vitreous humor (1.67 mL) is about one and half times smaller than the porcine. This information was used to correct the scaling factor for the *in vivo* rabbit fluorescence measurements to calculate the amount of dye present in the rabbit eye after the release from the drug delivery device.

6.4. RESULTS

6.4.1. *In vitro* study

The yield of the drug delivery device was found to be 46% for the first generation drug delivery device. In another words, 46% of the devices did not leak during the stability testing. However, the second generation device had a 100% yield. This increase yield in the second generation drug delivery device was due to the higher adhesion strength of the optical glue, NOA68. This UV cured glue can bond glass to plastic. Thus, it was much stronger adhesion force between plastic to plastic bonding for the drug delivery device. Both generation devices were submerged under water and stayed intact for 83 (first generation) and 365 (second generation) days of the observation. The membrane stayed intact and no leak was found in the second generation devices.

The threshold power of the ophthalmic Nd:YAG laser to ablate the membrane of the *ex vivo* drug delivery device was measured at 6.5 mJ to create a 100.0 μm diameter hole, unlike the implanted device which was measured at 10.0 mJ. Photograph (Figure 6.8a) of the ablated membrane captured using a fluorescence microscope (Olympus BX51, Leeds Instruments, Inc. TX) and the same device was imaged (Figure 6.8b) using

the Spectral Domain Polarization Sensitive Optical Coherent Tomography (SD-PSOCT) to measure the thickness of the membrane.

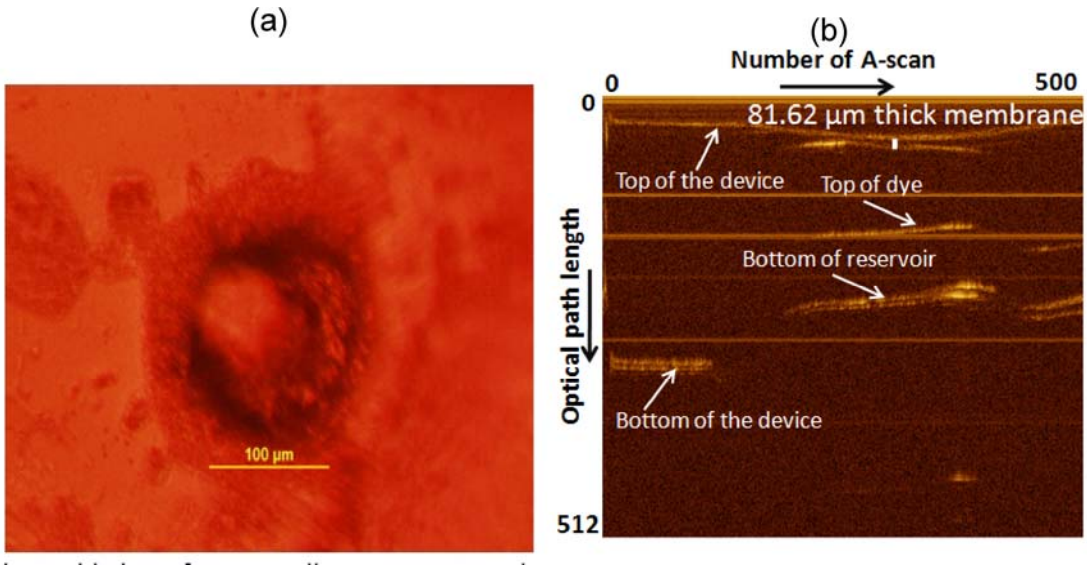

Figure 6.8. (a) Fluorescence microscope (Olympus BX51) image of a 100 µm diameter hole in the reservoir membrane of the drug delivery device created by the Nd:YAG laser ablation (b) same drug delivery device was photographed using the Spectral Domain Polarization-Sensitive Optical Coherent Tomography (SD-PSOCT) to measure the thickness of the membrane.

Figure 6.9 illustrated the scaling factor of the fluorescence intensity vs. volume of 10% Na fluorescein dye in the vitreous humor that was extracted from posterior chamber of the enucleated pig eye. It depicted a linear relationship with the volume of the dye and its associated fluorescence intensity.

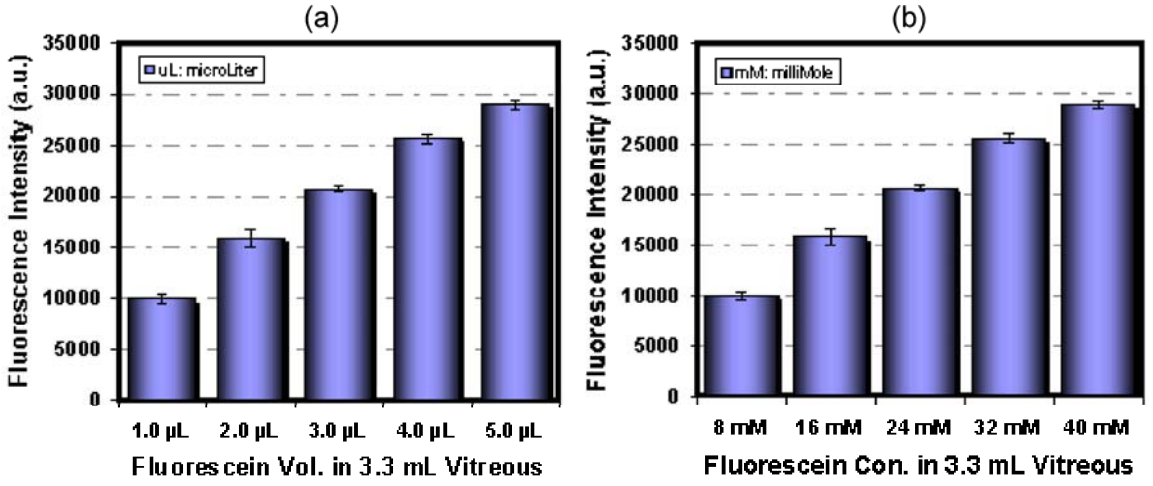

Figure 6.9. Scaling factor calculation using 10% Na Fluorescein dye in the 3.3 mL vitreous humor from the posterior chamber enucleated pig eye (n = 5) and measured 5 times for each additional 1.0 µL of dye. The fluorescnce intensity is depicted with respect to (a) volume (b) concentration.

6.4.2. *In vivo* study

Only one of the two reservoirs was ablated mechanically for rabbit 1 to find out the stability of the membrane of the intact reservoir. For rabbit 2, membrane of only one of the reservoirs was ablated using ophthalmic Nd:YAG laser. Photographs were taken up to the end of the experiment where the fluorescence intensity returned to baseline measurement. Figures 6.10 and 6.11 verified that the device did not leak from the intact reservoir of the both rabbits during the entire duration of the experiments. At the end of the study, the implanted device was extracted from the rabbit 1. However, for rabbit 2, the implanted device extruded from the surrounding tissue one day after the last measurement (day 20 since the dye release). Thus, only the surrounding tissue with the device from the rabbit 1 was collected for histology (Figure 6.12a) unlike the rabbit 2

where only device was analyzed for the laser ablation pattern on the membrane (Figure 6.12b). Figures 12c and 12d are the enlargement of the holes shown in Figure 6.12b.

Figures 6.13a and 6.13b showed the half-life of the 10% Na Fluorescein dye in the posterior chamber of the rabbit 1 and rabbit 2, respectively. The normalized fluorescence intensity showed no fluorescence activity before the content was released by ablating the membrane. At 21 days since the first implant, the membrane was ablated mechanically for the rabbit 1. However, two weeks were found to be adequate for recovery from the implant surgery based on the information collected from the rabbit 1. Thus, at 14 days the membrane was ablated for the implanted device in the rabbit 2 using an ophthalmic Nd:YAG laser with a threshold power of 10 mJ. About 17 minutes after the release of the dye the fluorescence intensity peaked. That measurement corresponded to a volume of 3.82±0.7 μL and 3.4±0.4 μL for rabbit 1 and rabbit 2, respectively. In other words, the concentration of the 10% Na fluorescein dye in the vitreous humor of rabbit 1 and rabbit 2 was 60.84±11.15 and 54.15±6.37 milli-mole per 1.67 milli-liter of rabbit vitreous humor, respectively at 17 minutes post ablation.

The measured half-life of 10% Na fluorescein dye from the posterior chamber from the both rabbits was 13 days. During this time the fluorescence intensity reduced to half of the original intensity. At 19 days from the dye release, the fluorescence intensity reached its baseline measurement for both rabbits. Thus, at 21 days since the release, the rabbits were euthanized after the extraction of the implanted device with or without the surrounding eye tissue. The second generation device in the rabbit 2 extruded at 19 days after the dye release due to the boat shape curvature of the device and the semi-circle

shape of the limbus. The half-life measurement of the 10% Na fluorescein dye was not effected as the intensity already reached to base-line measurement.

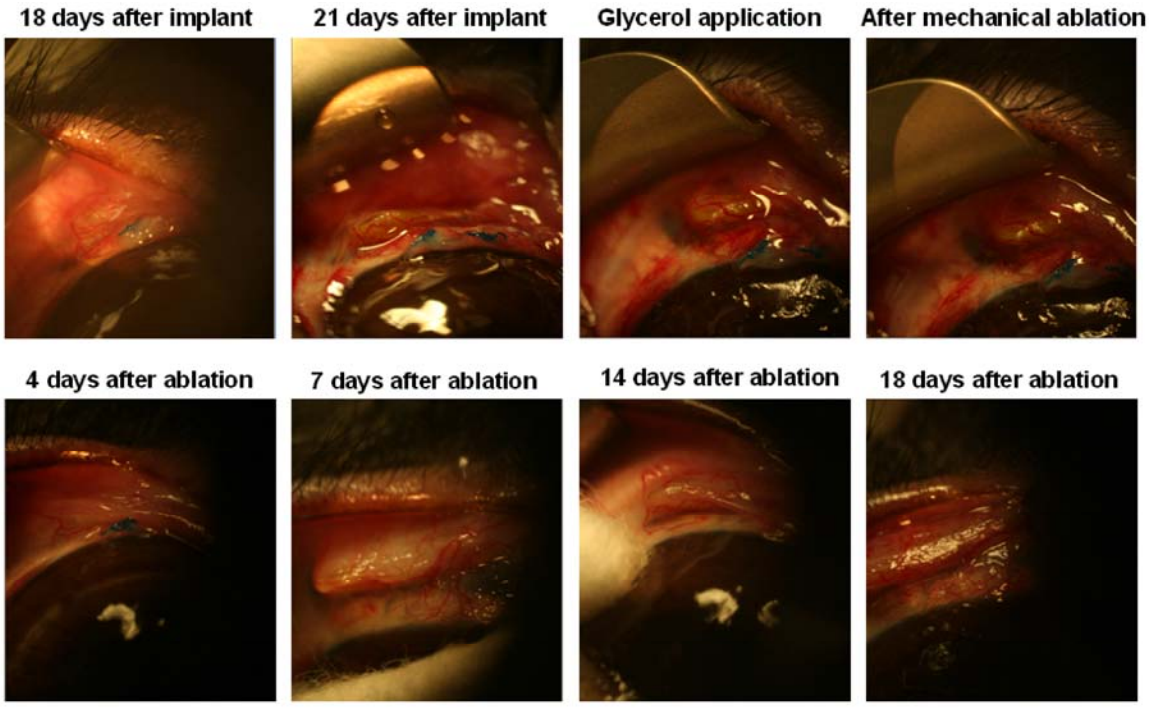

Figure 6.10. Photograph with an EOS digital SLR Canon camera attached to a slit lamp captured the condition of the site of the implant of the drug delivery device. At 21 days after the implant 100% anhydrous glycerol was topically applied to optically clear the eye tissue that lead to clearing of conjunctiva and sclera. This is highlighted with an arrow including the site of incision where the 6-0 prolene suture was used to close the incision. After the optical clearing, the membrane of the device was ablated mechanically using a 28G needle.

The results of the histology study are shown in Figures 6.14a–6.14d. Histology study showed encapsulation of the device by the eye tissue with minimal immune response such as inflammation.

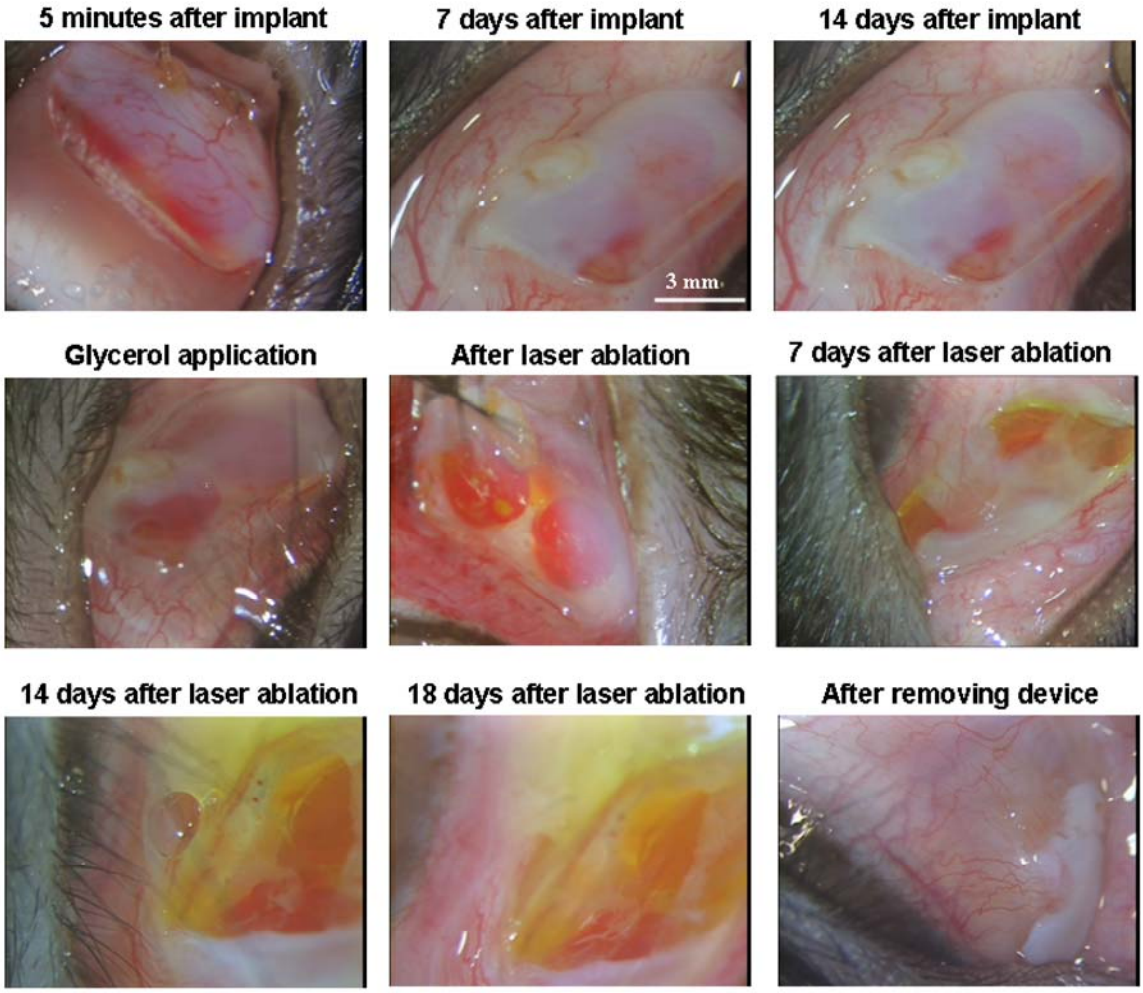

Figure 6.11. Photograph with a CCD camera (HV-C20 Hitachi Denshi, LtD) attached to a surgical microscope (Topcon OMS75, NJ, U.S.A.) captured the condition of the site of the implanted device. At 14 days after the implant 100% anhydrous glycerol was topically applied to optically clear the eye tissue that lead to clearing of conjunctiva and sclera. After the optical clearing, the membrane of the left reservoir (yellow spots) was ablated using an ophthalmic Nd:YAG laser with 10 mJ power.

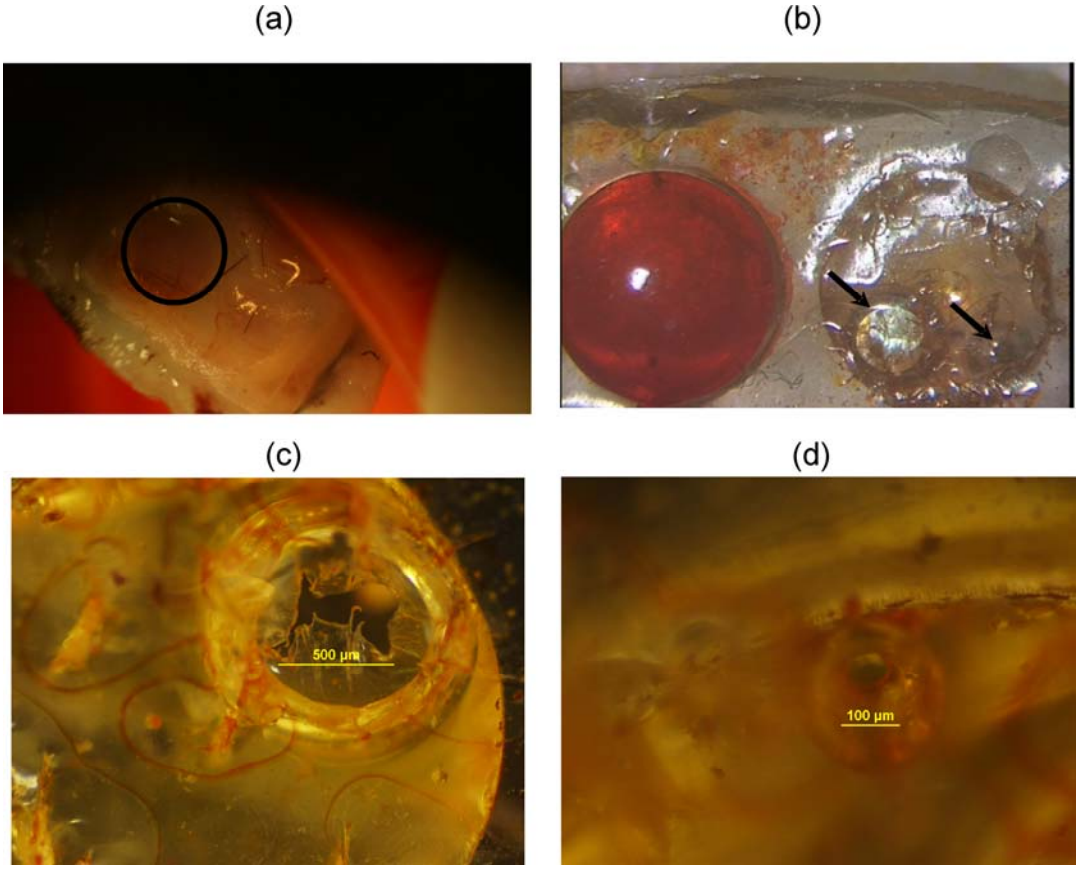

Figure 6.12. (a) Photograph (EOS digital SLR Canon camera attached to a slit lamp) of the implanted device extracted with surrounding eye tissue from the rabbit 1 for histology at 39 days after the implant. The intact reservoir with dye is highlighted with a circle and empty reservoir (no trace of dye) shown at the bottom; (b) Photograph (CCD camera attached to a surgical microscope) of the implanted device that was extracted from the rabbit 2 at end of the experiment (fluorescence intensity reached at baseline) to observe the effect of laser ablation on the membrane of the reservoir. Two different holes are identified on the membrane of the device highlighted with arrow. (c)-(d) Fluorescence microscope (Olympus BX51) images of the ablations shown in Figure (b). The size of the holes is about 500 µm and a dark ring presents surrounding the hole due to disintegration of the membrane due to laser. There is also a small penetration of about 100 µm. The round depression on the top figure (b) is an air bubble.

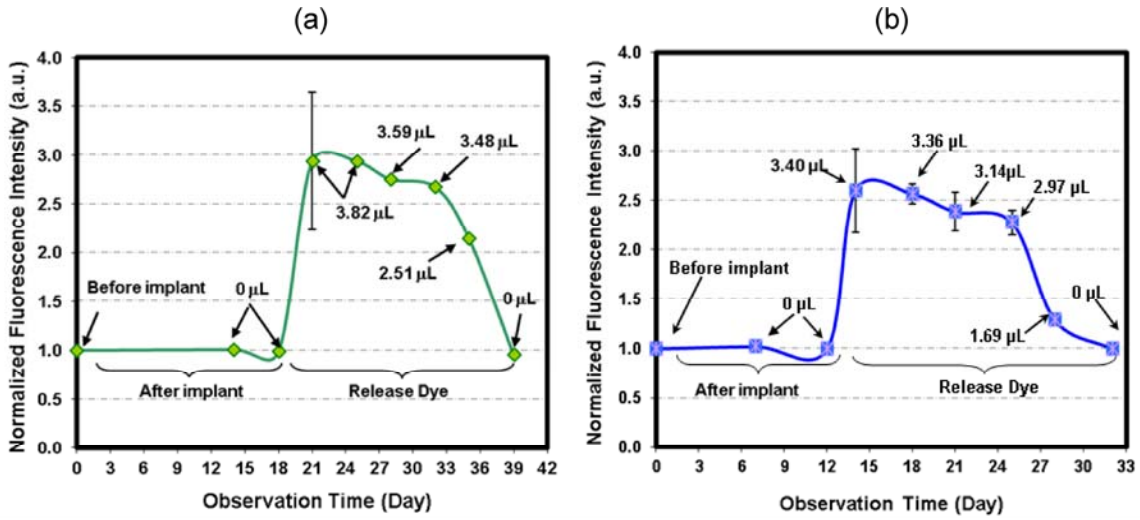

Figure 6.13. Fluorescence intensity associated with the volume of the 10% Na Fluorescein dye in the vitreous and humor of the posterior chamber of *in vivo* rabbit. Half-life of the dye in both rabbits (rabbit 1 and rabbit 2) is found to be 13 days despite the different release methods. Membrane of the device was ablated (a) mechanically using a 271/2G needle for rabbit 1 (b) light activated using an ophthalmic Nd:YAG laser for rabbit 2.

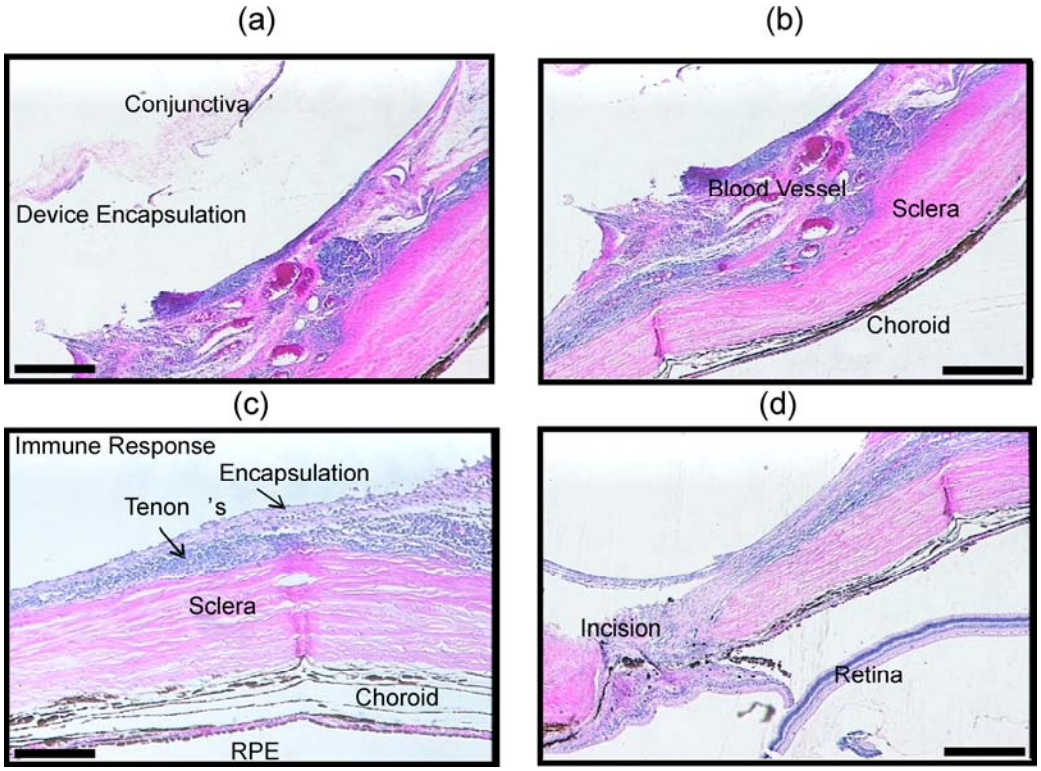

Figure 6.14. Results of the histology study of the collected eye tissue from the rabbit 1. The sample is 5 µm thick. (a) Device encapsulation can be observed (b) small micro-vasculatures are shown between the sub-conjunctiva and super-scleral layers (c) minimal immune response and inflammation (d) incision through sclera to choroid is observed in the eye with scleral flap. Scale bar: 300 µm.

6.5. DISCUSSION

One of the unique advantages of this drug delivery system is that it allows separation of the components (reservoirs) that control device performance from those that affect drug stability. The formulation that controls the drug release (the reservoir membranes) is to a first approximation independent of any formulation that may be included in the reservoir to control the drug stability. This is vastly different from other

drug delivery systems that have been developed.[46-47] A passive MEMS drug delivery device with mechanically controlled pump was described by *Lo* et al.[47]

Our drug delivery device was fabricated using PMMA which is not only bio-compatible but also can be implanted in the eye for long time. A study by Lo *et al.* showed that a form of PMMA which is PDMS was used to build their refillable implant device for eye.[46-47] Due to the refillable nature the device, it can be implanted for 2-3 years. However, they showed only in *in vitro* study on enucleated porcine eye. There are other studies which reported that cyclosporine implant fabricated from PMMA can be implanted for 3-5 years. Therefore, the PDMS is very stable and reliable for these types of implant method in drug delivery. Also, PMMA is used for ophthalmic intraocular lens in the eye when the original lens has been removed in the treatment of cataract. In orthopedics, PMMA bone cement is used to affix implants and to remodel lost bone. In cosmetic surgery, tiny PMMA microspheres suspended in some biological fluid are injected under the skin to reduce wrinkles or scars permanently. Therefore, PMMA is very stable and safe to use for long term use for treating any ocular diseases.

The required energy level (6–10 mJ) to ablate the membrane of the drug delivery device was within the safe range of 0–15mJ for eye surgery. The implanted device extruded from the rabbit 2 showed multiple ablations (diameters between 100–500 μm) on the membrane without destroying the other reservoir. Thus, the content of the drug delivery device could safely be released from one chamber without inadvertently rupturing the second chamber to provide controlled dosing.

The results of the histology study of the extracted tissue with implanted device from the rabbit 1 showed biocompatibility with no harmful side effect to the tissue. It showed no necrosis and minimal inflammation.

The first implanted drug delivery device in the rabbit 1 had shown about 2.0 mm shift from the original implanted location and settled in the cul-de-sacs. This is thought to be due to the shape of the device and as well the horizontal incision (with respect to cornea) at the limbus. Thus, we changed the design of the second generation device to give a more stationary feature by creating a boat like bottom and the four corners of the device were angled to remove any sharp edges. Also, the limbus based flap with horizontal incision away from the limbus creates a natural physical barrier for the device from moving away from the implant area. For the rabbit 2, a second generation device was implanted with a combination of a new incision method to hold the device in the original position. No shift was observed. This device stayed at the limbus area (sclera with thinnest thickness of 300 μm) and provided an additional advantage of fast tissue clearing effect from 100% anhydrous glycerol. For the rabbit 2, the tissue clearing took only 3 minutes to clear completely unlike the rabbit 1 that took about 8 minutes. The shape of implant 2 was not matched to the curvature of the sclera and that mismatch contributed to the extrusion. Ideally, the implant should be curved to match the curvature of the sclera and the device should be implanted with the long axis perpendicular to the limbus.

Due to the large sampling depth of 17.6 mm, the probe with specific geometry could sample posterior chamber that is just underneath the crystalline lens with a mean

depth of 11.2 mm from the cornea of rabbit.[48,49] For a specific drug used for treating ocular diseases, identifying the concentration of the specific drug at different locations within the eye is important. The location of the drug conjugated with fluorescent dye may be achieved by spectral analysis of the emission signal. The fluorescence spectra that were collected in this study showed a maximum emission peak at 520 nm wavelength unlike the emission spectra from cornea, anterior chamber, and lens reported by McLaren and Brubaker where the maximum emission occurred at 530 nm.[50] They used a scanning ocular spectrofluorometer to measure fluorescence in a two-dimensional cross-section through the cornea, anterior chamber, and crystalline lens. In this spectrofluorometer, a xenon arc lamp was filtered by a diffraction grating monochromator with bandpass of 4 nm and a range of 400–800 nm. They measured excitation and emission spectra of fluorescein, fluorescein glucuronide, and Rhodamin B in these three layers of *in vivo* pigmented rabbit's eye (n = 3) after topical administration. In the three rabbits, the emission spectra of fluorescein dye (typical peaks at 520 nm) in the cornea were shifted toward longer wavelength by 6–10 nm and 1–3 nm in the anterior chamber. Similar red shift was also identified from the crystalline lens. This 'red shift' is presumed to result from the fluorescein being bound by the protein in the cornea.[51] As the maximum fluorescence emission spectra collected form the two *in vivo* rabbits in our study did not peak at 530 nm wavelength, the location of the fluorescein dye cannot be from either cornea, anterior chamber, or crystalline lens. Therefore, the dye must have diffused into the posterior chamber of the eye.

Although, the knowledge of half-life of a drug or substance is an important aspect for treating any ocular diseases, no other study has ever investigated the half-life of a fluorescent marker that is provided to the eye in controlled incremental dosages. In our study, the measured half-life for both release techniques was found to be 13 days, but the volume or concentration of the dye present in the posterior chamber differed. The rabbit 1 showed larger dye volume present in the posterior chamber. This difference may due to direct diffusion through the scleral flap. Half-life is related with not only the rate of diffusion of the substance but also the inverse relationship to the molecular weight (MW) of that substance. Thus, one may assume that based on MW the 10% Na fluorescence dye (MW 332.3 Dalton) would have a much shorter half-life compared to other ocular drugs such as Ranibizumab (MW 48 KDalton). However, the half-life for the dye was found to be much longer than that of Ranibizumab (delivered in a traditional method of intra-vitreal injection). Gaudreault *et al.* evaluated the pharmacokinetic (PK) and serum bioavailability of ranibizumab after a single intra-vitreal (ITV) or intra-venous (IV) dose in cynomolgus monkeys.[49] Ranibizumab cleared in parallel from all ocular compartments, with a terminal half-life of approximately 3 days. It distributed rapidly to the retina (6–24 hours), and concentrations were approximately one third that in the vitreous and humor. After ITV injection, bioavailability (F) was 50% to 60%. Serum concentrations were very low, reflecting wider distribution and faster clearance when ranibizumab reached the serum. After IV administration, the terminal half-life was even lower, approximately only 0.5 day. The longer half-life from the implanted drug delivery method compared to the traditional method could be due to the complex

pharmacokinetics of the dye over weeks following a complex route to the posterior chamber unlike direct injection to the vitreous humor.

6.6. CONCLUSION

In this study, we have shown that the material for the drug delivery device is bio-compatible and can be implanted in either the sub-scleral or sub-conjunctival space. The device membrane can be ablated with an ophthalmic Nd:YAG laser after tissue clearing to maintain a controlled release of the content without disrupting the other chamber. A device built as an array with many chambers is feasible. The study also showed that small molecules such as 10% Na fluorescein dye can get into the posterior chamber. Thus, the half-life or drug availability of 13 days is higher than other similar molecule in the eye most likely due to complex pharmacokinetics from the implant once the membrane is ablated. Based on our observation, the device needs to be implanted with the long axis parallel to the limbus with incision away from the cornea for creating natural barrier. However, a better option for implant would be long axis perpendicular to the limbus. Thus, in future the size of the device needs to be reduced by at least one half of the current dimension with more smooth and rounded edges. In addition, the device should be curved such that it fits the radial curvature of the sclera (radius, r = 12 mm). Although, this preliminary study was only done for two rabbits, the findings could be a mile stone for an alternative method for treating ocular diseases.

6.7. ACKNOWLEDGEMENTS

Raiyan Zaman was a recipient of the ASLMS Travel Grant to attend and present at the Annual Conference of American Society for Laser Medicine and Surgery, 2010. Special thanks to Dr. Welch and Dr. Otto to provide financial support for this project.

6.8. REFERENCES

1. Bakken EE, Heruth K. Temporal control of drugs, an engineering perspective. Ann. New York Acad. Sci., 1991; 618: 422–412.

2. Kost AJ, Langer R. Responsive polymeric delivery systems. Adv. Drug Delivery Revision, 1991; 6: 19–50.

3. Wu BM, Borland SW, Giordano RA, Cima LG, Sachs EM, Cima MJ. Solid free-form fabrication of drug delivery devices. J. Control Release, 1996; 40:77–87.

4. Katstra WE, Palazzolo RD, Rowe CW, Giritlioglu B, Teung P, Cima MJ. Oral dosage forms fabricated by Three Dimensional Printing. J Control Release, 2000; 66: 1–9.

5. Rowe CW, Katstra WE, Palazzolo RD, Giritlioglu B, Teung P, Cima MJ. Multimechanism oral dosage forms fabricated by three dimensional printing. J. Control Release, 2000; 66: 11–17.

6. Santoro N. Efficacy and safety of intravenous pulsatile gonadotropin-releasing hormone: Lutrepulse for injection. *Am J. Obstet. Gynecol*, 1990; 163: 1759–1764.

7. Creasy GW, Jaffe ME. Pulsatile delivery systems. *Ann. Ny Acad. Sci*, 1991; 618:548–557.

8. Creasy GW, Jaffe ME. Endocrine/reproductive pulsatile delivery systems. Adv. Drug Delivery Rev, 1991; 6: 51–56.

9. Sampath P, Brem H. Implantable slow-release chemotherapeutic polymers for the treatment of malignant brain tumors. Journal of the Moffitt Cancer, 1998; Center 5: 130–137.

10. Physician's Desk Reference (Ed,: R. Arky), Medical Economics Company, Montvale, NJ, USA, 1998; 2587–2589.

11. Physician's Desk Reference (Ed,: R. Arky), Medical Economics Company, Montvale, NJ, USA, 1998; 3139–3150.

12. Brown L, Langer R. Transdermal delivery of drugs. *Ann Rev. Med.*, 1988; 39: 221–229.

13. Siegel RA, Falamarzian M, Firestone BA, Moxley BC, pH-cobtrolled release from hydrophobic/polyelectrolyte copolymer hydrogels. J. Controlled Release, 1988; 8:179–182.

14. Kim JH, Kim JY, Lee YM, Kim KYJ. Controlled release of riboflavin and insulin through crosslinked poly (vinyl alcohol)/chitosan blend membrane. *Appl. Polym. Sci*., 1992; 44: 1923–1828.

15. Gutowska A, Bark JS, Kwon IC, Bae YH, Cha y, Kim SW. Squeezing hydrogels for controlled oral drug delivery. *J. Controlled Release*, 1997; 48: 141–148.

16. Bae YH, Okano T, Hsu R, Kim SW. Thermo-sensitive polymers as on-off switched for drug release. *Makromol. Chem. Rapid Commun.*, 1987; 8: 481–485.

17. Hoffman AS, Afrassiabi A, Dong LC. Thermally reversible hydrogels: II. Delivery and selective removal of substances from aqueous solutions. *J. Controlled Release*, 1986; 4: 213–222.

18. Okano T, Bae YH, Kim SW. Pulsed and Self-Regulated Drug Delivery, Ed.: J. Kost, CRC Press, Boca Raton, FL, USA 17–45, 1990.

19. Kost J, Lander R. Pulsed and Self-Regulated Drug Delivery, Ed.: J. Kost, CRC Press, Boca Raton, FL, USA 3–16, 1990.

20. Kost J, Leong K, Lander R. Ultrasound-enhanced polymer degradation and release of incorporated substances. *Proc. Natl. Acad. Sci.*,1989; 86: 7663–7666.

21. Fischel-Ghodsian F, Brown L, Mathiowitz E, Brandenburn D, Lander R. Enzymatically controlled drug delivery. *Proc. Natl. Acad. Sci.* 1988; 85: 2403–2406.

22. Mathiowitz E, Cohen MD. Polyamide microcapsules for controlled release vs. photochemical release. *J. Membr. Sci.,* 1989; 40: 67–86.

23. Kwon IC, Bae YH, Kim SW. Electrically erodible polymer gel for controlled release of drugs. *Nature*, 1991; 354: 291–293.

24. Bae YH, Kwon IC, Kim SW, in Polymeric Drugs and Drug Administration, Ed:, R. M. Ottenbrite, American Chemical Society, Washington, DC, USA, 98–110, 1994.

25. Milner LL. Electrochemically controlled release of drug ions from conducting polymers. *Mol. Cryst. Liq. Cryst.,* 1998; 160: 297–301.

26. Hepel M, Fijalek Z. in Polymetric Drugs and Drug Administration, Ed.: R.M. Ottenbrite, American Chemical Society, Washington, DC, USA, 79–97, 1994.

27. Schwendeman SF, Amidon GL, Levy RJ. Determinants of the modulated release of antiarrhythmic drugs by iontophoresis through polymer membranes. Macromolecules, 1993; 26: 2264–2272.

28. Edelman ER, Kost J, Bobeck H, Langer R. Regulation of drug release from polemer matrices by oscillating magnetic fields. *J. Biomed. Matter. Res.,* 1985; 19: 67–83.

29. Suzuki Y, Tanihara M, Nishimuru Y, Suzuki K, Kakimaru Y, Shimizu Y. A new drug delivery system with controlled release of antibiotic only in the presence of infection. *J. Appl. Biomat.,* 1998; 42:112–116.

30. Macular Photocoagulation Study Group Laser photocoagulation of subfoveal neovascular lesions of age-related macular degeneration. Updated findings from two clinical trials. Arch Ophthalmol, 1993; 111: 1200–1209.

31. Gragoudas ES, Adamis AP, Cunningham ET Jr, Feinsod M, Guyer DR. Pegaptanib for neovascular age-related macular degeneration. N Engl J Med, 2004; 351: 2805–2816.

32. D'Amico DJ, Masonson HN, Patel M et al. Pegaptanib sodium for neovascular age-related macular degeneration: two-year safety results of the two prospective. multicenter, controlled clinical trials. Ophthalmology, 2006; 113: 992–1001.

33. Geroski DH, Edelhauser HF, Invest. Ophthalmol. Vis. Sci., 2000**;** 41: 5.

34. Fraunfelder FT, JAMA, 1977; 237: 5 doi:10.1001/jama.237.5.446b

35. Fraunfelder FT, Ophthalmology, 1979; 86: 1.

36. Fraunfelder FT, Ophthalmology, 1980; 87: 2.

37. Fraunfelder FT, J. Am. Ophthalmol, 1990; 110: 4.

38. Stephenson RW. *Anatomy, Physiology and Optics of the Eye: A Textbook for Orthoptic Students*, Kimpton Publishers, 1973.

39. Nemeth SC. *Ocular Anatomy and Physiology*, Slack Incorporated Publishers, 2007.

40. Feng Y, Simpson TL. Corneal, limbal, and conjunctival epithelial thickness from optical coherence tomography. Optometry and Vision Science, 2008; 85(9): 880−883.

41. Hayreh SS. Segmental nature of the choroidal vasculature. British Journal of Ophthalmology, 1975; 59(11): 631−48.

42. Young AR, “Chromophores in human skin,” Phys. Med. Biol., 1997; (42): 789−802.

43. Anderson J, Chiu D, Jackman R, Cherniavskaya O, McDonald J, Wu H, Whitesides S, and Whitesides G. Fabrication of Topologically Complex Three-Dimensional Microfluidic Systems in PDMS by Rapid Prototyping. Science, 1993; 261: 895.

44. McDonald J, Duffy D, Anderson J, Chiu D, Wu H, Schueller O, Whitesides G. Fabrication of microfluidic systems in poly (dimethylsiloxane). Electrophoresis, 2000; 21(1): 27–40.

45. http://www.microchem.com/products/su_eight.htm

46. Lo R, Li Po-Ying, Saati S., Agrawal RN, Humayun MS, Meng E. A passive MEMS drug delivery pump for treatment of ocular diseases. Biomed Microdevices, 2009; 11: 959–970.

47. Lo R, Kuwahara K, Li Po-Ying, Agrawal R, Humayun MS, Ellis Meng. A Passive Refillable Intraocular MEMS Drug Delivery Device. Proceedings of 2006 International Conference on Microtechnologies in Medicine and Biology Okinawa, Japan 9–12 May 2006.

48. Lavanya R, Teo L, Friedman DS, Aung HT, Baskaran M, Gao H, Alfred T, Seah SK, Kashiwagi K, Foster PJ, Aung T. Comparison of anterior chamber depth measurements using the IOLMaster, scanning peripheral anterior chamber depth analyser, and anterior segment optical coherence tomography. Journal of Ophthalmology, 2007; 91:1023–1026.

49. Gaudreault J, Fei D, Rusit J, Suboc P, Shiu V. Preclinical Pharmacokinetics of Ranibizumab (rhuFabV2) after a Single Intravitreal Administration. *Investigative Ophthalmology and Visual Science*, 2005; 46: 726–733.

50. McLaren JW, Brubaker RF. A Scanning Ocular Spectrofluorophotometer. Investigative Ophthalmology & Visual Science, 1988; 29(8).

51. Delori FC, Castany MA, Webb RH. Fluorescence characteristics of sodium fluorescein in plasma and whole blood. Exp Eye Res, 1978; 27:417.

CHAPTER 7: SIGNAL VARIATION OF FLUORESCEIN DYE IN ANTERIOR AND POSTERIOR CHAMBERS OF EYE[5]

7.1. ABSTRACT

Identifying the location of a fluorescent tagged drug for treating ocular disease is an important aspect for any drug delivery system. Thus, we have tested a hypothesis where signal of a fluorescein dye may vary either because of the presence of natural occurring fluorophores of the eye tissue or the dye itself based on the location of the dye in the eye. The overarching goal is to be able to measure the concentration of a fluorescent tagged drug in both the anterior and posterior chambers of the eye. In this study, we have identified a unique phenomenon in signal variation of fluorescence emission spectra based on the location of the fluorescein dye in the eye. We have developed a fluorescence spectrophotometer (FS) system to identify the emission spectra at 520 nm from the 10% Na fluorescein USP sterile dye. The FS system consists of four main components: (i) a tungsten halogen lamp to shine white light with 130 mW power (LS-1, Ocean Optics), (ii) a low pass filter with transmission between 390–480 nm with cutoff at 505±15 nm wavelength (FD1B, an additive dichroic color filter, blue, Thorlabs, Inc. Newton, NJ,

[5]The experiments contained in this chapter had accepted in December for publication in a peer-reviewed ASLMS Conference, April 2011 and awarded a Travel Grant to attend the conference: Raiyan T. Zaman, Henry G. Rylander III

USA) (iii) a custom-designed fiber-optic probe (core diameter = 200 μm; NA = 0.22; FiberTech Optica), and (iv) a spectrometer (USB4000, Ocean Optics). The fiber-optic probe consists of 2 individual fibers with core to core separation of 370 μm that are terminated with SMA connectors. For both *in vitro* and *in vivo* experiments we have injected 5 μL dye diluted in 25 μL of 0.9% saline in either the anterior or posterior chamber (not both) of an enucleated pig (n = 16) and *in vivo* rabbit eyes (n = 10), respectively. Then, fluorescence emission spectra were collected every 3 minutes up to 30 minutes using the FS system. However, for the *in vivo* experiment the emission spectra was only collected after the pupil was dilated using 3 drops of 1% tropicamide every 1 and 1/2 minutes for 5 minutes (the dilation completes within 10 minutes). The results showed signal variation between the anterior and posterior chambers of the eye. The emission peak of the fluorescence signal from the anterior chamber red shifted to the longer wavelength unlike the posterior chamber. Also, the line shape of the emission signal was distinctive for the posterior chamber. We eliminated the possibility of this signal difference (by further experiment) due to the constituents of the aqueous and vitreous humors from the anterior and posterior chambers, respectively. Thus, the most likely reason for this red shift to the longer wavelength may be due to the presence of intrinsic fluorescence of protein in the cornea of the enucleated pig and *in vivo* rabbit eyes. Also, change in pH can cause the change in fluorescence emission spectra. These results clearly identify the variability in fluorescence emission spectra of the 10% Na fluorescein dye based on the location of the dye in the eye. This unique phenomenon

could help determine the location of a fluorescently tagged molecule within the eye and deserves further investigation.

7.2. INTRODUCTION

Identifying the location of a drug tagged with fluorescent molecules for treating ocular disease is an important aspect for any drug delivery system. Information about the distribution of a drug in the eye is important for bio-availability analysis at the target tissue. There are many studies done on the interaction of fluorescein in the aqueous humor. However, there is no study being done where a distinction may be drawn between the fluorescence emission signal based on location of the eye such as anterior and posterior chamber. Thus, we have tested a hypothesis that emission signal of a dye may vary based on the location of the dye. If the signal variation exists, the cause needs to be identified. In this study, we have identified a unique phenomenon in signal variation of fluorescence emission spectra based on the variation in the location such as anterior and posterior chambers of the eye.

Many of the properties of 10% Na fluorescein dye (molecular formula $C_{20}\ H_{10}\ 0_5$ •Na2) make it an ideal tracer for use in ophthalmic research.[1] The lack of toxicity, the lack of binding except loose reversible binding to albumin, and the apparent lack of local metabolism by the eye are all important properties that make fluorescein dye useful as a quantitative tracer. Thus, in our study we have used 10% Na fluorescein dye to generate the emission spectra from the anterior and posterior chamber of the *in vivo* rabbit and *ex vivo* enucleated pig eyes for signal variation analysis. Fluorescence emission intensity is

primarily a function of the concentration of a certain fluorophore, the excitation wavelength, and the emission wavelength.

7.3. MATERIALS AND METHODS

7.3.1. Fluorescence Spectrophotometer (FS) system

The fluorescence spectrophotometer (FS) system consists of four main components: (i) a tungsten halogen lamp to shine white light (LS-1, Ocean Optics), (ii) a low pass filter with transmission between 390–480 nm with cutoff at 505±15 nm wavelength (FD1B, an additive dichroic color filter, blue, Thorlabs, Inc. Newton, NJ, USA) (iii) a custom-designed fiber-optic probe (core diameter = 200 μm; NA = 0.22; FiberTech Optica), and (iv) a spectrometer (USB4000, Ocean Optics). The fiber-optic probe consists of 2 individual fibers with core to core separation of 370 μm that are terminated with SMA connectors. The source and detector fibers were connected to the lamp and spectrometer, respectively. The low pass filter is placed in between the light source and the fiber-optic probe. A built-in 74-VIS collimated lens is used in the LS-1 light source before terminate with the fiber-optic probe. Blue light of the LS-1 lamp with 140 mW power was measured at 494 nm excitation wavelength using an EPM 2000e Laser Energy/Power meter (Molectron Detector, Inc.). However, the light that was conducted through the fiber optic probe to illuminate the *in vivo* and *ex vivo* eye tissue and excite the emission spectra from 10% Na fluorescein dye was measured to be 130 mW. The schematic illustration of the FS system is shown in Chapter 6, Figure 6.4.

We collected the 10% Na fluorescence emission spectrum from the eye tissue over a wavelength range of 450−700 nm. The fiber-optic probe was placed in contact with the surface of the cornea, and the average was taken from 5 measurements of blue light spectra at each time point. Each fluorescence spectra was collected within 500 milliseconds. Fluorescence spectra from the cornea were collected at the same location during baseline (before injecting the dye), immediately after injection, and until the fluorescence emission intensity starts to decrease. Prior to spectral analysis, recorded signals were corrected for system response by subtracting the detector dark current and with respect to the fluorescence intensity of Rhodamin B fluorophores.

7.3.2. *In vivo* eye model

The eye contains three different chambers: anterior, posterior, and vitreous. However, in this study we are interested in the aqueous humor of the anterior chamber and vitreous humor of the vitreous chamber *in vivo* eye. The anterior chamber is the space in the eye that is behind the cornea and in front of the iris. The anterior chamber is filled with a watery fluid known as the aqueous humor or aqueous which is produced by a structure alongside the lens called the ciliary body. The aqueous passes first into the posterior chamber (between the lens and iris) and then flows forward through the pupil into the anterior chamber of the eye. Vitreous humor is a transparent, colorless, gelatinous mass that consists of 99% water and remainder is a mixture of collagen, proteins, salts, and sugars. Although, the vitreous humor is mostly made of water, it has a firm, jellylike consistency, and this helps the eye hold its shape. Vitreous is produced by

the ciliary body and certain retinal cells. It is of rather similar composition to the aqueous, but contains very few cells (mostly phagocytes which remove unwanted cellular debris in the visual field, as well as the hyalocytes of Balazs of the surface of the vitreous, which reprocess the hyaluronic acid), no blood vessels, and 98-99% of its volume is water (as opposed to 75% in the aqueous) with salts, sugars, vitrosin, a type of collagen, a network of collagen type II fibers with the glycosaminoglycan hyaluronic acid, and also a wide array of proteins in micro amounts. Figure 7.1 illustrates the cross-sectional view of eye.

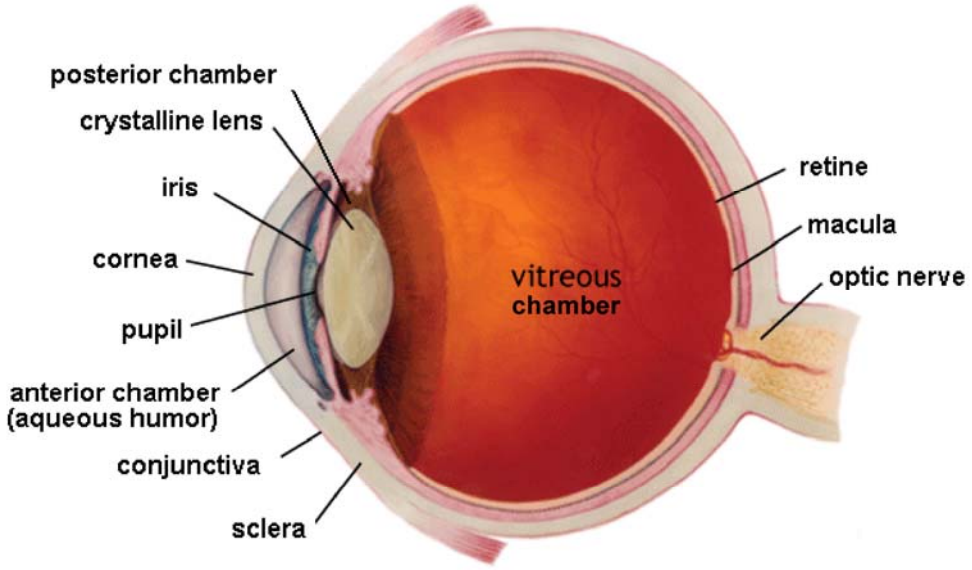

Figure 7.1. Cross-sectional view of an adult eye. In this study the vitreous chamber is called as the posterior chamber.

7.3.3. Experimental procedures: *in vivo*

Female SPF Dutch Belted (n = 5) rabbits weighing 4 to 5 lbs were used for this experiment. All experimental procedures were conducted according to protocols approved by the Institutional Animal Care and Use Committee (IACUC) of the University of Texas at Austin (AUP-2009-00061). Prior to the experiment, the rabbits were anesthetized with 35mg/kg ketamine, 5 mg/kg xylazine, and 0.75 mg/kg acepromazine.

Rabbits were positioned in the ventral recumbent position. Oxygen saturation and pulse, heart and respiration rate were monitored every 15 minutes throughout the study using a vet/ox G2 Digital pulse oxymeter (Heska Corp. Loveland, CO, USA). This monitor was connected via a shaved area of the feet or the ear depending on the best contact for recording. Animals were kept warm with warm water blankets. The anesthetic and monitoring procedures were performed by a skilled technician from the Animal Resources Center (ARC) of the University of Texas at Austin.

5.0 µL 10% Na fluorescein dye was added with 25.0 µL of 0.9% blood bank saline to make a volume of 30.0 µL that could be drawn easily into a 1 CC syringe. While the animals were under anesthetic this volume was injected to the either anterior or posterior chamber of the eye but not both for a single eye. The needle was kept horizontal with respect to the limbus area (the junction between the cornea and conjunctiva) for injecting the dye to the anterior chamber of the rabbit eye. However, for injecting the dye into the posterior chamber the needle was kept at a 45 degree angle. A 28G ½ inch needle was used for injecting the dye to both the anterior and posterior chambers. Figure 7.2

illustrates the injection methods to anterior and posterior chambers of the eye. Only ½ inches needle was safe enough length for these experiments. Before injection of any dye, the pupil of the injected eye was dilated using 3 drops of 1% tropicamide every 1 and 1/2 minutes for 5 minutes. Once the pupil dilated (after 10 minutes), a fiber optic probe with a noninvasive FS system was used to measure the intensity of 10% Na fluorescence from the aqueous (anterior chamber) and vitreous humors every 3 minutes up to 30 minutes (until the fluorescence intensity starts to decrease).

A small quantity (35.0 μL) of aqueous and vitreous humor from the anterior and the posterior chambers of the *in vivo* rabbit eye (n = 10) were extracted using a 28G ½ needle right before euthenization. These liquids were placed in a two separate four-sided clear methacrylate cuvette (Fisherbrand Disposable Cuvets with spectral range from 340–750 nm and accuracy UV/VIS range 285–750 nm). The FS system was used to measure the fluorescence intensity from the 10% Na fluorescein dye that are already mixed with the liquids from the eye. This experiment can eliminate any spectral differences in the anterior and posterior chambers due to the different sampling depth and also the effects of the cornea and the crystalline lens.

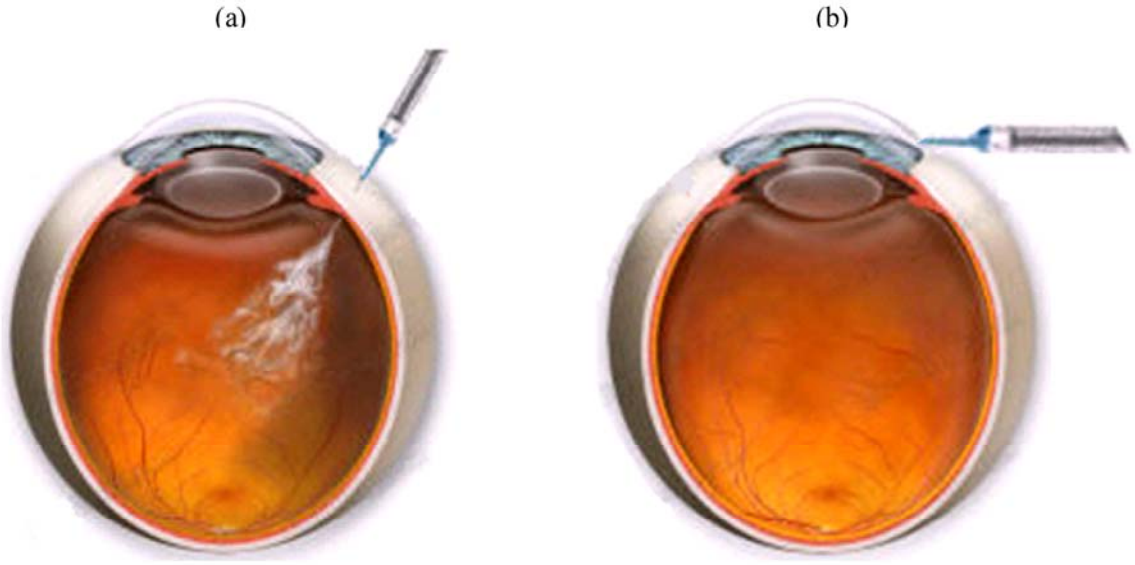

Figure 7.2. Schematic diagram of two different injection methods of 10% Na fluorescein dye (a) intra-vitreal injection at 45 degree angle (b) corneal injection horizontal to the pupil. The solution contains 5 µL dye mixed with 25µL of 0.9% blood bank saline.

7.3.4. Experimental procedures: *ex vivo*

We have a total of sixteen enucleated pig eyes from which eight of the eyes were used for anterior chamber and rest of them for the posterior chamber to measure fluorescence intensity. These eyes were provided by the Air Force Research Laboratory at Brooks City-Base and were used based on an IACUC approved tissue sharing protocol. The eyes were harvested and stored in antibiotic and buffer solution immediately after enucleation. The buffer solution was made from 0.5 L 1X Hank's Balanced Salt Solution (HBSS) with Ca and Mg, 10 mM HEPES buffer, 100 I.U./mL Penicillin, 100 I.U./mL Streptomycin and 0.05 mg/mL Gentamicin. Storage containers holding the eyes were

placed in ice to minimize sample degradation during transport. Eyes were placed in a 4° C refrigerator for one night. The time between enucleation of the eyes and experimental studies was 16 hours. These measures were taken to avoid excessive tissue degradation. The next day eyes were removed from the solution and let the eyes reached between 24°C−25°C (room temperature) in 45 minutes. Once the eye reached this specific temperature, the eyes were placed on a Styrofoam holder before injecting a total volume of 30.0 μL diluted dye (same as *in vivo* rabbit eye) into the enucleated pig eyes. After the injection, the probe of the FS system was gently placed in contact with the cornea of the *ex vivo* eye and fluorescence spectra were measured. Fluorescence intensity was measured every 3 minutes up to 30 minutes (until the fluorescence intensity start to decrease). Photographs were taken each time interval using a CCD camera (HV-C20 Hitachi Denshi, LtD) attached to a surgical microscope (Topcon OMS75, NJ, U.S.A.). Figure 7.3 depicts the enucleated eye before and after injection of dye.

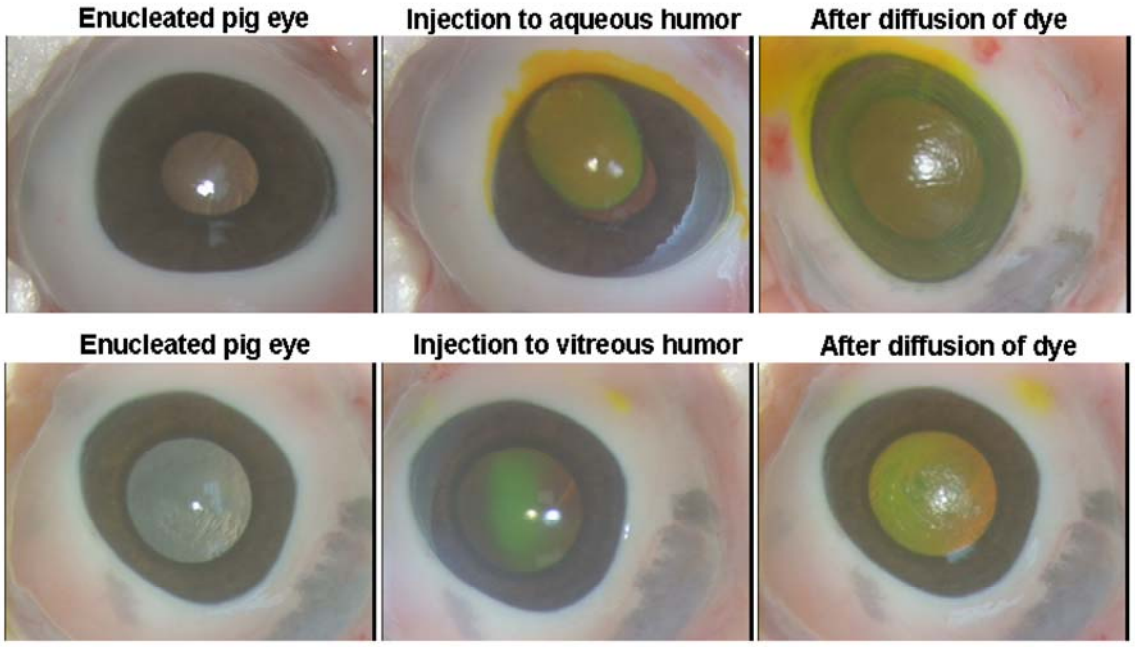

Figure 7.3. Photograph with a CCD camera (HV-C20 Hitachi Denshi, LtD) attached to a surgical microscope (Topcon OMS75, NJ, U.S.A.) captured the condition of the *ex vivo* enucleated pig eyes before and after the injection of fluorescein dye.

7.3.5. Monte Carlo modeling

A Monte Carlo model was developed to simulate any spectral variation that may occur due to the difference in optical properties of tissue layer and increase in penetration depth of the photon of the light source. The Monte Carlo method is a stochastic model that has been used to simulate problems that can be readily characterized by radiative transport theory such as light propagation in biological media. The method consists of a detailed bookkeeping of the scattering and absorption experiences of each individual photon as they propagate through a medium.

7.3.5.1. Monte Carlo: algorithm

The Monte Carlo program continuously scatters photons as they propagate through a medium until they are absorbed by a chromophore, reflected from, or transmitted through, the medium. The tissue is assumed to be infinitely wide and is characterized by its (a) thickness D (mm), (b) refractive index n, (c) absorption coefficient μ_a (cm^{-1}), (d) scattering coefficient μ_s (cm^{-1}), and (e) anisotropy factor g. Photons are launched normal to the air–tissue interface and distributed along a radial line of width equal to the beam radius 200 μm. The physical quantities of interest that are estimated with the Monte Carlo simulation is fluence rate $\Phi(\lambda_{ex}, r, z, \theta)$ (W/cm^2), and number of fluorescent emitted photon at various emission wavelength.

The path of each photon in the medium is characterized by steps of randomly varying lengths and an angle of deflection from the previous scattering site.[2] The step sizes and the angles are sampled from their respective probability distributions. Upon scattering, the directional cosines for the deflection angle cosθ are determined by the Henyey–Greenstein scattering function, which provides a good analytical representation of single scattering in tissue.[3]

The Monte Carlo simulation used in this study incorporates a variance reduction technique whereby a packet of photons, representing many photons, is propagated simultaneously through a particular path within the medium. Each photon packet starts with an assigned weight W that is set equal to 1. Photons can either be terminated by reflection or transmission out of the tissue or absorbed within the medium and creates fluorescence. To ensure conservation of energy, and to avoid a bias in the distribution of

photon deposition, a random termination technique known as the roulette is used. When the weight of a photon packet is reduced below a threshold value W_{th} (e.g., $W_{th} = 0.0001$), the roulette gives the photon bundle one chance in m (e.g., $m = 10$) of survival, with a weight of mW. Once the photon packet is terminated, its weight is set to zero, and this interaction marks the end of the photon's propagation within the medium. Given a pseudorandom number ξ, the roulette criterion for survival can be summarized as

$$W = \begin{cases} mW & if\ \xi \le 1/m \\ 0 & if\ \xi > 1/m \end{cases} \quad (1)$$

When the photon packet is fully absorbed (terminated), a new photon packet is launched into the tissue and the same recordkeeping procedure is followed.

7.3.5.2. Optical modeling of multi-layer rabbit eye tissue

Healthy tissues of the anterior rabbit eye chamber such as cornea and lens are highly transparent for visible light because of their ordered structure and the absence of strongly absorbing chromophores. Scattering is an important feature of light propagation in eye tissues. The size of the scatterers and the distance between them are smaller than or comparable to the wavelength of visible light, and the relative refractive index of the scattering matter is equally small (soft particles). Typical eye tissue models are long round dielectric cylinders for corneal collagen fibers and spherical particles for lens protein structure having a refractive index of n_s. They are regularly distributed in the isotropic base matter with a refractive index, $n_0 > n_s$.

To apply the Monte Carlo simulation to the particular tissue geometry involved in fluorescence emission from anterior and posterior chamber from 10% Na fluorescein dye, we developed a four-layered model of the tissues from cornea to vitreous humor. These layers, as illustrated schematically in Figure 7.4, are (i) cornea, (ii) aqueous humor (anterior chamber), (iii) crystalline lens, and (iv) vitreous humor (posterior chamber). The anterior interface is with air (n = 1.00) and the posterior interface is with the vitreous humor of the eye (n = 1.336).

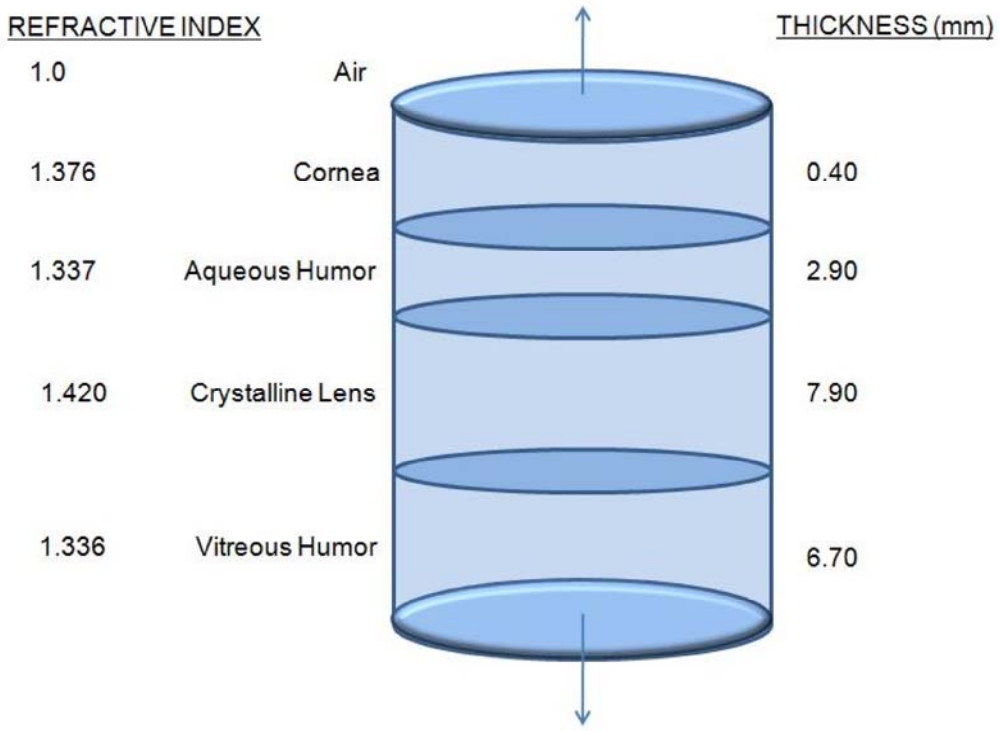

Figure 7.4. Multi-layered eye tissue structure used in generating fluorescence photons in the presence of the 10% Na fluorescein dye in the various layers. Visible blue was used as a light source to simulate the Monte Carlo model.

The contact fiber-optic probe has a diameter of 200 μm, and because the fiber was in contact with the eye tissue, a flat beam profile was chosen for the simulation. The 200 μm diameter of the fiber is considered the spot size of the incident beam on the corneal surface. The simulated response of the tissue to a flat-top beam of 200 μm radius, whose total energy was fixed at 65 mJ or 130mW for 500 millisecond integration time, was obtained with a total of 2,000,000 photons.

To model the fluorescence escape process, the transport parameters (μ_a, μ_s, g) for the eye at other wavelengths are also required. We compiled data of each eye layer at 21 different wavelengths from 450 to 650 nm in 10 nm intervals from using the data from the literature by Mahar.[4] A slab geometry, as required by the Monte Carlo simulation, is used for all layers, and the tissues are assumed to be of infinite lateral extent, which is a justified assumption for the wavelengths under study (494–530 nm). The optical properties for 495 nm wavelength are listed in Table 7.1 for the above eye layers.

Table 7.1. Four-layer eye optical model for rabbit (transport parameters μ_a, μ_s, g are for 495 nm only)

Layer	*D* (mm)	*n*	μ_a (cm^{-1})	μ_s (cm^{-1})	g
Air	—	1.0000	—	—	—
Cornea	0.4000	1.3760	2.2000	19.400	0.9
Aqueous humor	2.9000	1.3370	0.0462	17.070	0.9
Crystalline lens	7.9000	1.4200	0.2370	17.070	0.9
Vitreous humor	6.7000	1.3360	0.0537	17.070	0.9

7.3.5.3. Methodology of reconstruction

The following procedure was used to reconstruct the *in vivo* eye fluorescence spectrum using properties of eye tissue:

1. Calculating the excitation light distribution or fluence rate $\Phi(\lambda_{ex}, r, z, \theta)$ inside the model eye. The distribution of excitation light within the tissue must be specified. This was calculated using the Monte Carlo simulation, and is denoted as $\Phi(\lambda_{ex}, r, z, \theta)$ in units of W/cm^2. λ_{ex} is the excitation wavelength, while the r, z, θ represent local positions in cylindrical coordinates.
2. Obtaining the intrinsic fluorescence coefficient $\beta(\lambda_{ex}, \lambda_{em}, z)$.[5, 6] The intrinsic fluorescence coefficient β is defined as the product of the absorption coefficient due to the fluorephores, $\mu_{a_{fl}}$ (cm^{-1}), and the quantum yield Y (dimensionless) of fluorescence emission. Within a layer, β will be considered as a constant and therefore be denoted as a function of z, $\beta(\lambda_{ex}, \lambda_{em}, z)$. λ_{em} is the wavelength of emitted fluorescence light. The product of $\Phi \times \beta =$ photon absorption energy density $\rho(x, y, z)$ yields the density of fluorescence sources in units W/cm^3. Using experimental data, the relative β distribution is measured inside the tissue. The fluorophore density $\rho(z)$ is calculated from the fluorescence image obtained by the CCD camera. The intrinsic spectra of different eye tissue layers measured with the FS system are normalized to equivalent overall integral intensity (the areas from 450 nm to 650 nm under each normalized intrinsic spectral curve are

the same), and is denoted as $I_{norm}(\lambda_{ex},\lambda_{em},z)$, which is dimensionless. Then β was obtained using

$$\beta(\lambda_{ex},\lambda_{em},z)=\rho(z)\times I_{norm}(\lambda_{ex},\lambda_{em},z) \quad (2)$$

3. Calculating of Escape function $E(\lambda_{em},r,z)$. When a fluorophore emits a fluorescence photon, that photon must reach the surface and escape to be observed. The escape function $E(\lambda_{em},r,z)$ is the surface distribution as a function of radial position (r) of escaping photons from a point source of fluorescence at depth z and radial position $r=0$ within a tissue of thickness D. It can be calculated by Monte Carlo simulation. The unit of E is cm^{-2}. Simulations were conducted for a series of depths (z) inside the tissue, using the optical properties for the emission wavelengths of interest.
4. Calculating of the observed fluorescence, $F(\lambda_{ex},\lambda_{em},r)$. The observed flux rate of escaping fluorescence F in units of W/cm^2 at the tissue surface computed by the following convolution:[3,4]

$$F(\lambda_{em},\lambda_{em},r)=\int_0^D\int_0^{2\pi}\int_0^{\infty}\Phi(\lambda_{ex},r',z',\theta)\,\beta(\lambda_{ex},r',z') \times E(\lambda_{em},\sqrt{r^2+r'^2-2rr'\cos\theta'},z')r'dr'd\theta'dz' \quad (3)$$

The convolution in Equation (2) can be implemented numerically using discrete values for Φ and E that were generated by Monte Carlo simulation. A custom written Monte Carlo code in Matlab was developed to calculate the fluorescence escape function to simulate the light propagation process for an isotropic fluorescence point source buried at depth z inside the eye tissue. For a thin illumination beam in a clear medium with

negligible scattering, the fluorescence intensity will be the same in the tissue surface independent of radial position r. In Equation (3), the fluorescence escape function $E(\lambda_{em}, r, z)$ can be integrated with respect to *r* and θ:

$$\iiint E(\lambda_{em}, r, z) r dr d\theta = E(\lambda_{em}, z) \tag{4}$$

The contribution from a specific eye layer (from depth z_1 to depth z_2) to the observed *in vivo* fluorescence spectrum can be calculated as follows:

$$F_{layer:z_1 \to z_2}(\lambda_{ex}, \lambda_{em}) = \int_{z_1}^{z_2} \phi(z) \beta(\lambda_{ex}, \lambda_{em}, z) E(\lambda_{em}, z) dz \tag{5}$$

Within an eye layer, β is assumed to be independent of depth. In this study, the excitation wavelength λ_{em} is also fixed at 495 nm wavelength. Substituting λ_{em} with λ, Equation (5) becomes

$$F_{layer:z_1 \to z_2}(\lambda) = \beta(\lambda) \int_{z_1}^{z_2} \phi(z) E(\lambda, z) dz \tag{6}$$

The integral on the right side of the Equation (6) is the fluorescence detection efficiency,

$$\eta_{layer:z_1 \to z_2}(\lambda) = \int_{z_1}^{z_2} \phi(z) E(\lambda, z) dz \tag{7}$$

It is an integral of the product of the excitation light distribution inside the tissue and the fluorescence escape efficiency. The reconstructed eye *in vivo* spectrum is a linear combination of the product of intrinsic spectrum and the fluorescence detection efficiency of all the excited fluorescent fluorephores:

$$\begin{aligned} F(\lambda) = {} & \beta_{cornea}(\lambda)\eta_{cornea}(\lambda) + \beta_{aqueous\ humor}(\lambda)\eta_{queous\ humor}(\lambda) \\ & \beta_{lens}(\lambda)\eta_{lens}(\lambda) + \beta_{vitreous\ humor}(\lambda)\eta_{vitreous\ humor}(\lambda) \end{aligned} \tag{8}$$

7.4. RESULTS

7.4.1. *In vivo* study: rabbit eyes

For *in vivo* rabbit eye, fluorescence emission spectra varied between the anterior and posterior chambers. For the *in vivo* rabbit eye, the signal from the anterior chamber emission spectra peaked at 524 nm at 0 minute or immediate after injecting the dye. As time elapsed, the peak of the emission spectra started to shift to the longer wavelength and at 30 minutes the emission spectra peaked at 534 nm. On the other hand, the fluorescence emission spectra peaked at 505 nm wavelength immediate after the injection of the fluorescein dye into the posterior chamber and started to shift to the longer wavelength like anterior chamber. At 30 minutes, the emission spectra of the posterior chamber peaked at 520 nm wavelength. This phenomenon was identified as red shift. Also, there were intensity variations between the *in vivo* anterior and posterior chamber of the rabbit eye. Fluorescence intensity from the posterior chamber was 1.5 times higher than the anterior chamber. Emission signal from the posterior chamber reached maximum peak at 24 minutes unlike the anterior chamber (6 minutes after the injection). No line shape difference was observed between the emission signal from the anterior and posterior chamber of the *in vivo* rabbit eye. Figure 7.5 showed the average fluorescence intensity of the emission spectra of the anterior and posterior chambers of the *in vivo* rabbits.

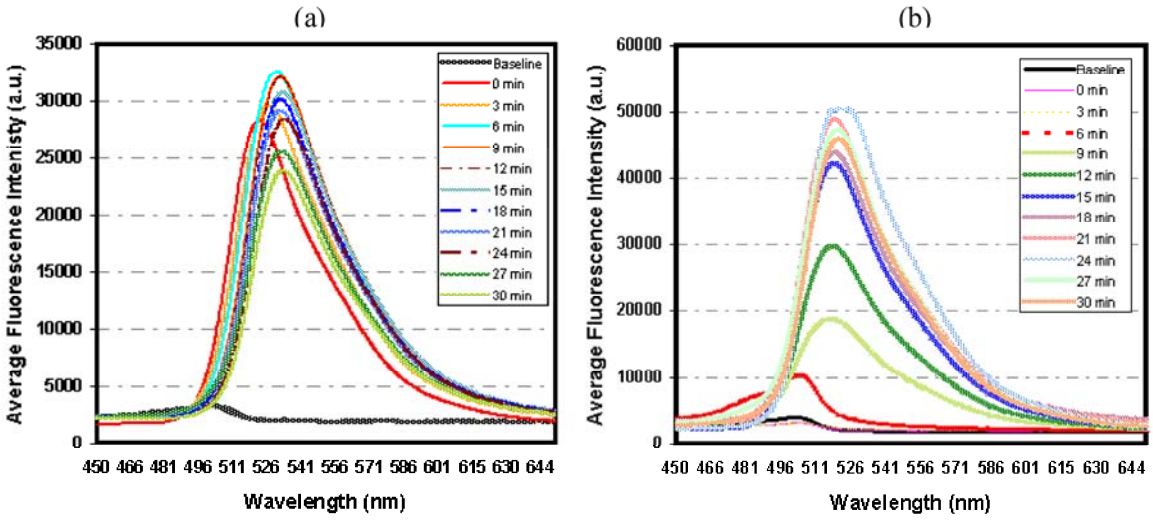

Figure 7.5. Average fluorescence intensity for 12 time intervals from five *in vivo* rabbit eyes before and after injecting 10% Na fluorescein dye in to (a) the anterior chamber (b) posterior chamber. The maximum fluorescence emission peaks for anterior and posterior chamber varied about 14 nm at 30 minutes observation point.

The results from the aqueous and vitreous humor that were collected from the anterior and posterior chamber of the *in vivo* rabbit eyes concurred with the findings discussed earlier. The maximum emission spectra from the aqueous and vitreous humor peaked at 534 nm and 520 nm, respectively. Figure 7.6 illustrated these results.

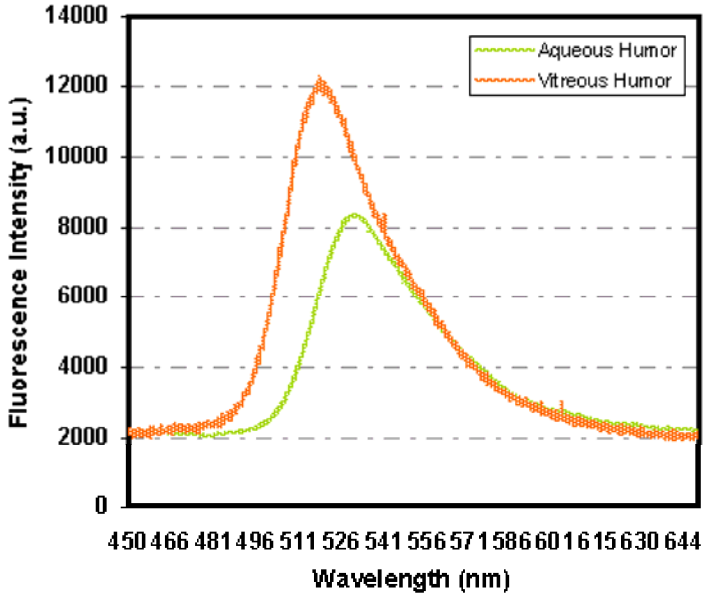

Figure 7.6. After the end of the *in vivo* rabbit experiment, 35.0 µL of aqueous and vitreous humor were collected from the anterior and the posterior chambers of the rabbit eye and fluorescence intensity was measured using the FS system. A red shift was identified in the emission spectra form the aqueous humor unlike the vitreous humor.

7.4.2. *Ex vivo* study: enucleated pig eyes

Two distinctive emission spectra were observed from the anterior and posterior chambers of the enucleated pig eyes. For the anterior chamber, the maximum fluorescence emission intensity peaked at 524 nm wavelength. No spectral shift was identified. The fluorescence intensity increased immediate after the injection of the dye. For the posterior chamber, the maximum fluorescence emission peak was observed at 502 nm. There was also a difference in line shape of the emission signal compared with anterior chamber. Absorption created a sharp decline in the emission spectra after 502 nm wavelength. Furthermore, the maximum fluorescence intensity from the anterior chamber

is almost 1.74 times larger than the posterior chamber. The highest fluorescence intensity peaked between 6–9 minutes for anterior and posterior chambers after the injection of the dye. After this time point, fluorescence intensity started to decrease gradually for the next couple of minutes. No red shift was observed for the enucleated pig eye. Figure 7.7 illustrated the average fluorescence intensity from the anterior and posterior chamber of the enucleated pig eyes.

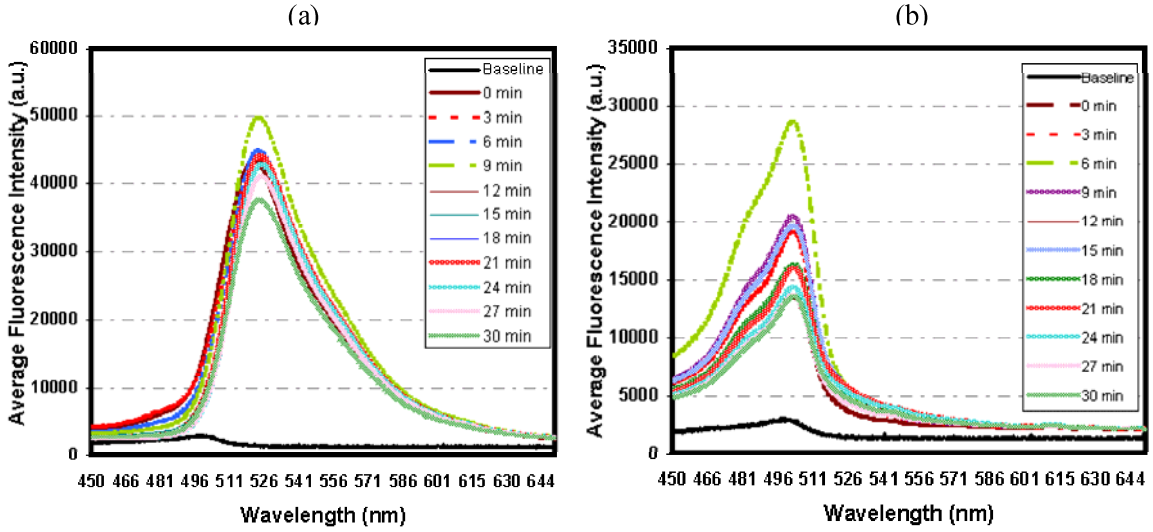

Figure 7.7. Average fluorescence intensity at 12 time intervals from sixteen *ex vivo* enucleated pig eyes before and after injecting 10% Na fluorescein dye into (a) the anterior chamber (b) posterior chamber. The maximum fluorescence emission peaks for anterior and posterior chamber varied about 20 nm. A blue shift has been observed in the fluorescence spectra from the posterior chamber.

7.4.3. Monte Carlo: rabbit eye model

Monte Carlo simulations were conducted to generate the fluence rate distribution inside the eye model for 495 nm excitation blue visible light and for the escape functions for the 40 different source depths and 21 different emission wavelengths from 450–650 nm. In this work, the *in vivo* fluorescence spectra were measured using a small beam illumination (200 μm diameter beam). Figure 7.8 shows the excitation light distribution as a function of tissue depth z (mm) and radial distance r (mm) for incident power density or fluence rate in W/mm^2. Fluence is very high in cornea, anterior chamber, and part of crystalline lens. Although, fluence rate is reduced in the posterior chamber, the incident power is still high enough to excite fluorophores in the posterior chamber. This fluence rate was further verified with MCML. Figure 7.9 (a) shows two experimental curves from *in vivo* rabbit's anterior and posterior chamber after injecting 5 μL fluorescein dye diluted with 25 μL of 0.9% blood bank saline. Each curve is normalized to have maximum intensity of 100 counts. Also, spectral shift is corrected. The theoretical curve fits quite close to the experimental curve. This suggests that the theoretical method employed in this study, the published eye optical properties and the fluorescence properties determined by the FS system measurements are correct. However, this model cannot show the spectral shift in the fluorescence emission spectrum.

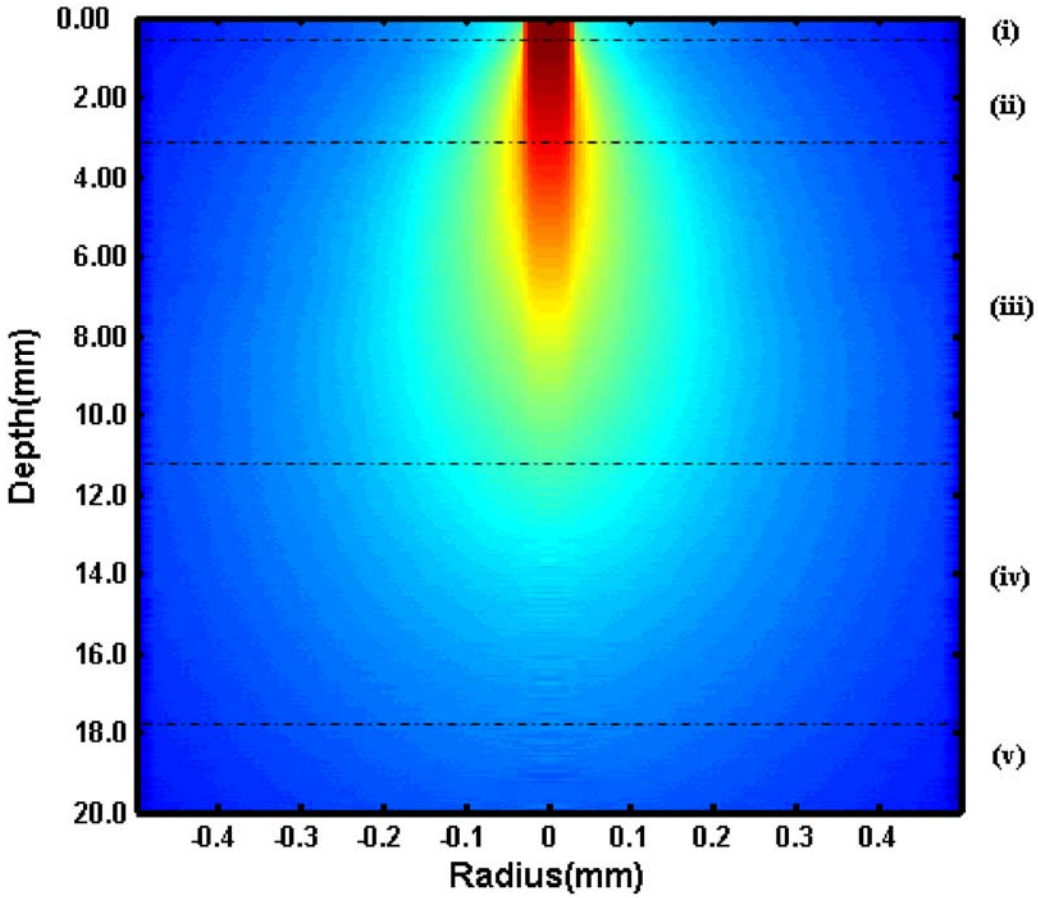

Figure 7.9. Fluence rate of light source with specific probe geometry (power: 65mJ and core diameter: 200 μm). The fluence rate was calculated by generating 2,000,000 photons per package for excitation wavelength of 495 nm. The roman numerical values represent (i) cornea, (ii) anterior chamber or aqueous humor, (iii) crystalline lens, (iv) posterior chamber or vitreous humor, (v) beyond posterior chamber of rabbit eye.

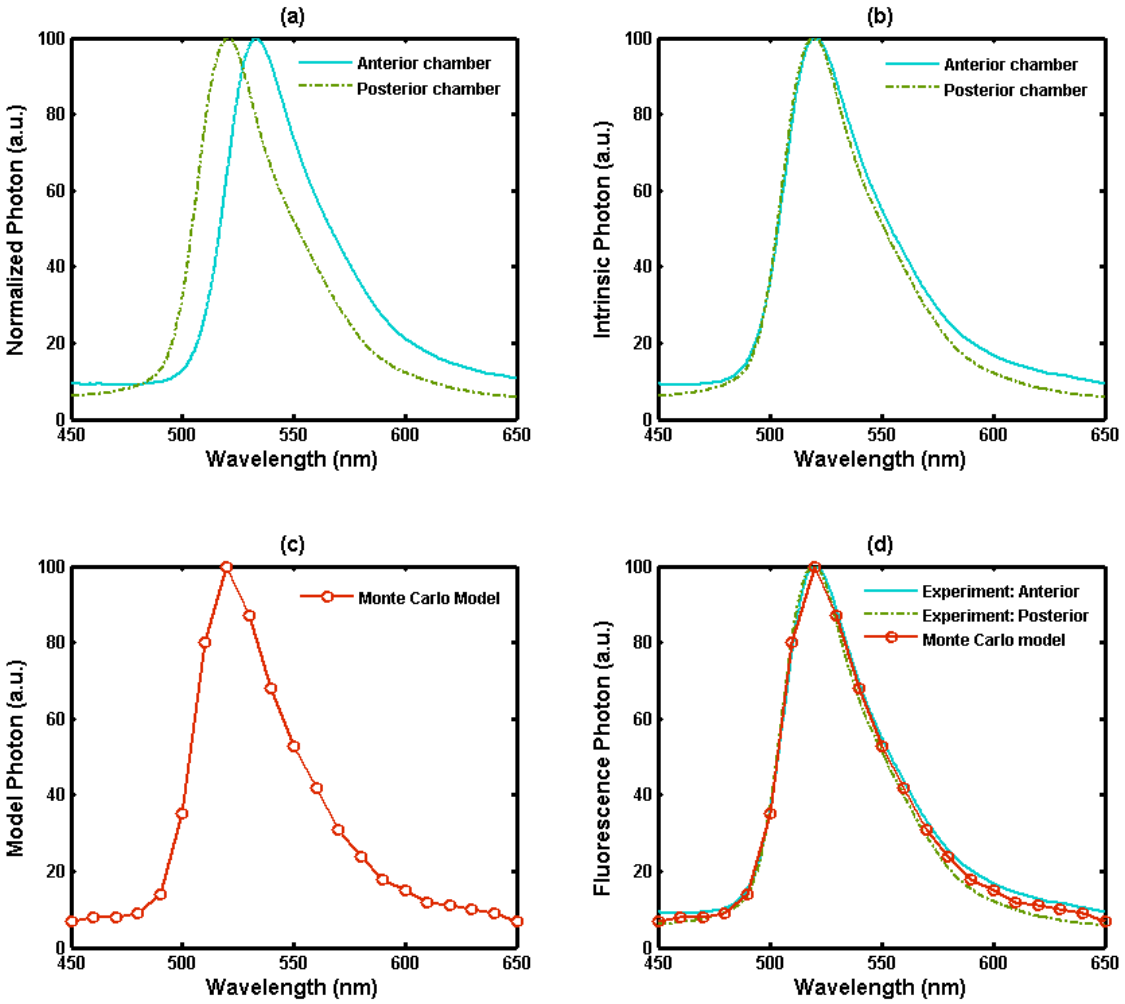

Figure 7.9. (a) The normalized fluorescence spectra (by maximum fluorescence intensity) of fluorescent fluorophores at different eye layers obtained by FS system measurements (b) intrinsic fluorescence spectra from anterior and posterior chamber (c) fluorescence spectra generated by Monte Carlo simulation (c) intrinsic fluorescence spectra from *in vivo* rabbit experiment vs. model.

7.5. DISCUSSION

Although, cornea and lens of eye have auto-fluorescence equivalent to 8×10^{-9} g/mL and 1.2×10^{-7} g/mL, their interference with fluorescence measurement after

injection to anterior and vitreous chambers are extremely low.[7] Thus, in our measurement of fluorescence spectra no correction was made for auto fluorescence. We have identified in this study that there were signal variations in the anterior and posterior chamber of the eye based on the location of the 10% Na fluorescein dye in the eye layer. These differences in emission spectra for the *in vivo* rabbit eye could be explained by McLaren and Brubaker.[7] They used a scanning ocular spectrofluorometer to measure fluorescence in a two-dimensional cross-section through the cornea, anterior chamber, and crystalline lens. In this spectrofluorometer a xenon arc lamp was filtered by a diffraction grating monochromator with bandpass of 4 nm and a range of 400–800 nm. They measured excitation and emission spectra of fluorescein, fluorescein glucuronide, and Rhodamin B in these three layers of *in vivo* pigmented rabbit's eye (n = 3) after topical administration. In the three rabbits, the emission spectra of fluorescein dye (typical peaks at 520 nm) in the cornea were shifted toward longer wavelength by 6–10 nm and 1–3 nm in the anterior chamber. Similar red shift was also identified from the crystalline lens. This 'red shift' is presumed to result from the fluorescein being bound by the protein in the cornea.[8]

The red shift in the emission spectra from the anterior chamber may be explained by corneal protein; however, the spectral shift in the emission signal from the aqueous humor need explanation. Aqueous humor of rabbit consists of 60 different proteins unlike blood plasma 6000.[9] Although, the protein concentration in aqueous humor is normally less than 1% of that in plasma, aqueous humor proteins may causes the red shift we observed in the aqueous humor collected from *in vivo* rabbit as well as the emission

signal from the anterior chamber. The red shift phenomenon and the lower intensity of the emission spectra from the anterior chamber compared to the posterior chamber can be explained by Romanchuk.[10] At high concentrations of fluorescein in solution (for our case, fluorescein concentration is high compared to the small volume of aqueous humor), quenching may occur because the fluorescein molecules collide among themselves and dissipate the previously absorbed energy without emission of light. This phenomenon is known as concentration quenching. At high concentrations of fluorescein, the intensity of the fluorescence may also be decreased because of dimmers and polymers which can absorb incoming light, but only feebly fluorescent or non fluorescent. Sometimes the dimmer or polymer emits fluorescent light at a longer wavelength than the monomers. This study validates, our finding that emission signal from the anterior chamber is much lower in intensity and red shifted.

For the *ex vivo* pig eye study, the emission spectra from the anterior and posterior chamber did not show any red shift. Rather, the signal from the posterior chamber showed blue shift. This phenomenon can be explained by the study by Mota *et al*.[11] The study showed that the change in pH level changes the absorption spectrum of the fluorescein dye. If pH level is lower than neutral pH of 7.4, the absorption spectra shifted to the shorter wavelength or blue shifted. The excitation spectra peaked at 440 nm wavelength (excitation peaked at 494 nm for pH 7.4) when pH for the sodium fluorescein aqueous solution was 3. The blue shift in absorption spectra also blue shifts the emission spectra. The reason for pH change in the eye is due to change in temperature. From the data obtained for the ocular temperature gradient,[12] it appears that at least a difference of

1° C exists across the anterior chamber. A study by Schwartz illustrated that it is to be expected that the aqueous humor at the posterior surface of the cornea will be at least 0.006 of a pH unit more than the aqueous humor bordering the anterior surface of the crystalline lens, assuming complete mixing of the anterior chamber contents. This represents a difference of 0.04×10^{-8} gram moles per liter of hydrogen ion or a 1.4% change. This ocular temperature gradient thus creates a hydrogen ion concentration gradient.[13]

We have seen absorption after 502 nm for the emission signal from the posterior chamber of the enucleated pig eyes. This absorption can be explained by the structure of the crystalline lens. Attenuation by the lens is partly dependent on lens thickness.[14] During *ex vivo* experiment the eyes were static and no dilation of pupil was possible. Thus, the crystalline lens was completely circular and largest thickness. In addition, the lens was observed to be opaque compared to the *in vivo* rabbit eye. The thickness of lens and opacity could be a factor for sharp decline in the emission spectra.

During the fluorescence measurement the angle of the probe is an important aspect for minimizing erroneous peak intensity. In this experiment we needed to consider the angle-dependency of the reflected and refracted light that is incident upon the tear-air interface. We have observed if the angle of the linear probe is not placed 90° angle respect to the cornea, the fluorescence signal was reduced in intensity. This finding can be verified by Brubakar.[15, 16] For angles of incidence less than approximately 65°, 90% or more of unpolarized light is refracted, but over 65°, a significant portion can be reflected. Thus, each measurement was taken with caution. We have also observed if the pupil of

the rabbit eyes were not dilated completely, the fluorescence signal from the fluorescein dye gets distorted in shape.

7.6. CONCLUSION

We have shown in this study that the spectral differentiation in fluorescence emission peak from the anterior and posterior chamber of the rabbit and pig eyes occurred based on the fluorescence interaction with the ocular tissue constituents. Fluorescence emission spectra from anterior and posteriors chambers are distinctive. Also, identifiable variations exist in the emission spectra between the *in vivo* and *ex vivo* eye. These spectral differences can be useful in identifying the distribution of fluorescent tagged drugs for treating ocular diseases.

7.7. ACKNOWLEDGEMENTS

Raiyan Zaman was a recipient of the ASLMS Travel Grant to attend and present at the Annual Conference of American Society for Laser Medicine and Surgery, 2011. I am thankful to Kathryn Starr for helping me with the experiment. Also, a special thanks to Dr. Jeff Oliver for providing fresh pig eyes for *ex vivo* experiments.

7.8. REFERENCES

1. The use of fluorescein in ophthalmological research. The Jonas S Friedenwald Memorial Lecture. Invest Ophthalmol, 1967; 6: 464–477.

2. Keijzer M, Jacques SL, Prahl SA, Welch AJ. Light distribution in artery tissue: Monte Carlo simulations for finite diameter laser beams. Lasers in Surgery and Medicine, 1989; 9: 148–154.

3. Jacques SL, Alter CA, Prahl SA. Angular dependence of HeNe laser light scattering by human dermis. Lasers Life Sci., 1987; 1: 309–333.

4. Maher EF. Transmission and absorption coefficients for the ocular media of the Rhesus monkey. SAM-TR-78-32, USAF School of Aerospace Medicine, 1978; 1–104.

5. Gardner CM, Jacques SL, Welch AJ. Fluorescence spectroscopy of tissue: recovery of intrinsic fluorescence from measured fluorescence. Applied Optics, 1996; 35(10): 1780–1792.

6. Keijzer M, Richard_Kortum R, Jacques SL, Feld MS. Fluorescence spectroscopy of turbid media: autofluorescence of the human aorta. Applied Optics, 1989; 28: 4286–4292.

7. McLaren JW, Brubaker RF. A Scanning Ocular Spectrofluorophotometer. Investigative Ophthalmology & Visual Science, 1988; 29(8).

8. Delori FC, Castany MA, Webb RH. Fluorescence characteristics of sodium fluorescein in plasma and whole blood. Exp Eye Res., 1978; 27:417–425.

9. Barsotti MF. The source of proteins in the aqueous humor in the eye. Doctoral thesis, Massachusetts Institute of Technology, 1990.

10. Romanchuk KG. Fluorescein. Physicochemical factors affecting its fluorescence. Diagnostic and surgical techniques, Survey of Ophthalmology, 1982; 26(5).

11. Mota MC, Carvalho P, Ramalho J, Leite E. Spectrophotometer analysis of sodium fluorescein aqueous solutions. Determination of molar absorption coefficient. International Ophthalmology, 1991; 15: 321–326.

12. Schwartz B, Feller MR. Temperature gradients in the rabbit eye, Investigative Ophthalmology, 1962; 1: 513.

13. Schwartz B. pH-temperature coefficient of rabbit anterior chamber aqueous humor. Division of Ophthalmology, Department of Surgery, State University of New York, Downstate Medical Center, Brooklyn, N. Y.

14. Lei B, Yao G. Spectral attenuation of the mouse, rat, pig, and human lenses from the wavelengths 360 nm to 1020 nm. Experimental Eye Research, 2006; 83: 610–614.

15. Brubaker RF. The flow of aqueous humor in the human eye.

16. Brubaker RF, Penniston JT, Grotte DA, et al. Measurement of fluorescein binding in human plasma using fluorescence polarization. Arch Ophthalmology, 1982; 100: 625–630.

CHAPTER 8: DISCUSSION AND FUTURE DIRECTION

8.1. DISCUSSION

A question remains about the complex pathway the fluorescence dye takes after released from the implanted device. Does it go to the anterior chamber at some point of time and get filtered by the cilliary body or does it go directly to the posterior chamber where it stays until it diffuses out. These questions we will not be answered until we could do measurement every one hour until the half-life is reached for the dye. Also, the scattering nature of skin and eye tissue treated with glycerol is in question. Question remains on what happens to the direction of scattering, namely the anisotropy factor. If the anisotropy factor changes rather than the scattering coefficient, in order to get a decrease in $\mu_s'(\lambda)$, an increase in forward scattering would have to occur. Thus, in this dissertation we sought to examine the relationship between the changes in optical properties due to the presence of hyperosmotic agent such as reduced scattering coefficient, absorption coefficient, and the various morphological features of the tissue such as melanin concentration, blood volume fraction, oxygen saturation, and blood vessel diameter. The challenge is the measurement of collimated transmittance, and thus the anisotropy factor, through a sample in multi-layers of tissue treated with glycerol. It is difficult to differentiate between truly collimated transmittance and highly forward scattered light. Investigation of these methods will aid in our understanding of tissue

optics and may be important to the development of new techniques in light-based medical applications.

8.2. FUTURE DIRECTION

The research studies in this dissertation are meant to serve as a proof-of concept of optically clearing tissues such as skin and eye by topical and injection method of applying a chemical agent such as 100% anhydrous glycerol. The optical clearing technique is combined with an implantable drug delivery device activated by laser light. Because it is among the first in this area, there are several directions that future research in this area can follow. I have attempted to offer some new avenues where the drug delivery device can be used to treat certain medical conditions. Also, I will propose a new design of a drug delivery device.

The probe that had used in the various experiments in this dissertation was designed and developed by me during my Masters program. Although, this probe had proven to be effective and able to sample various tissue constituents, it is not depth-resolved. Depth-resolved probe can be a very useful tool in medical diagnostic. For example, to diagnose dysplasia in cervical tissues, it is necessary to be in possession of a technique that is able to give depth information of the evolution of this disordered growth or measuring concentration of certain ocular drug that is tagged with fluorescent molecule in the different chamber of the eye. Fluorescence spectroscopy is one of the techniques that can give biochemical and structural information on the state of the probed tissue.[1-4] McLaren and Brubaker developed a depth-resolved scanning ocular spectroscopy system.[5] The challenge is to collect signal according to its emission depth.

The eye tissues are principally composed of four layers: cornea, aqueous humor of the anterior chamber, crystalline lens, and vitreous humor of the posterior chamber. Thus, to diagnose either dysplasia stage or any drug concentration in the eye tissue requires a reliable diagnostics tool to get the fluorescence spectra as a function of the signal depth.

8.2.1. New design: optical probe

Different methods have been used to get depth resolved measurements.[5-11] One way to alter the distance between the excitation and collection fibers is to increase the source-detector separation can sample deeper depth in the tissue. Another way the sample distance can be increased is by oblique illumination where a large angle illumination enables to one to get superficial signal and a small angle allows deeper collection.[12-14] A problem of this design is the probe size which may be too large as one increases this angle. Schwarz et al. proposed to use a ball lens positioned at the end of the probe to improve the depth resolution; indeed this enables an increase in the overlap of the collection and excitation light cones.[15] Following the similar idea but using two bevel excitation fibers with 200 μm and 500 μm core diameter and NA= 0.22 connected with a light source. The collection fiber core diameter is 500 μm. The probe has center-to-center source-detector separations of 500 and 750 μm. The angle at which the illumination paths intersect the collection region grows stepper with increasing source-detector separation. As shown in Figure 8.1, the new probe design with a ray traveling in air that enters the tissue has a total angular deviation β_1 and β_2 as it passes through the beveled excitation fiber and enters the tissue. The light needs to be shined to the sample through the angle fiber cores of the excitation fibers with fiber refractive index n_{f1} and n_{f2} and collected with an optical fiber in between the excitation fibers. The detection plane should be at

least 2 mm above the tissue plane. This will enhance the intensity of the collected photon due to larger collection region for the collection fiber. If $\theta_1 \leq 20^\circ$ and $\theta_2 \geq 35^\circ$ the excitation fiber will collect signal from two different depth. Because β_1 and β_2 will be two different excitation angles that will sample deeper and shallow tissue, respectively.

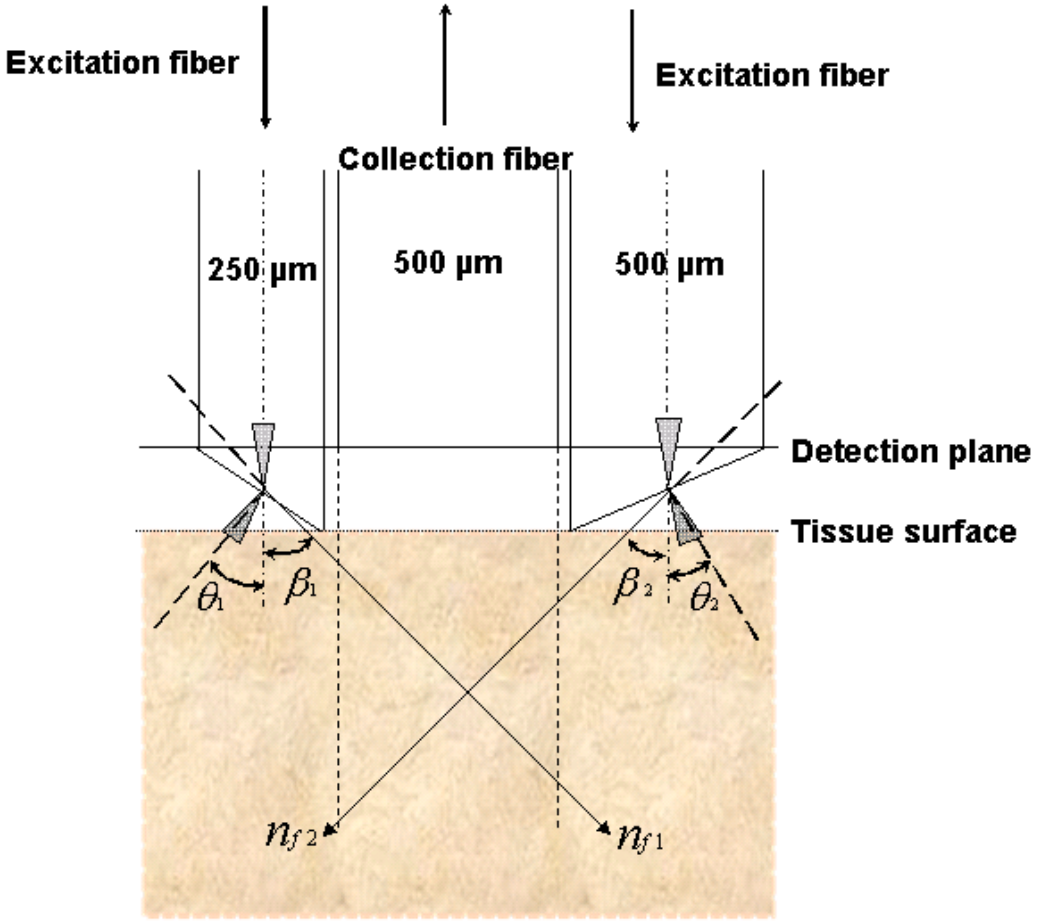

Figure 8.1 Schematic diagram of the new design with two beveled excitation fibers connected with light source showing illumination ray paths (solid lines) and collection fiber normal to the detection plane with collection region (dashed lines). Augmenting the angle results in tilting excitation cones away from the fiber axis denoted as θ and the relationship between θ and β is given by $\beta = \sin^{-1}(n_f \sin\theta) - \theta$ where n_f is the fiber refractive index.

8.2.2. New design: drug delivery device

The concept for the third generation device is shown in Figure 8.2 and will conform to the eye contours and integrate flow regulating components that will deliver specific and repeatable dose volumes. It will also incorporate geometrical changes suggested by ophthalmic surgeons to facilitate implantation. The shape of device will be rounded in order to distribute stress and minimize dead volume. Each reservoir can be activated with the laser by ablating the plug or valve made of materials that could be easily broken down. Each reservoir is connected with individual channels or capillaries that are connected to the main channel to delivery the drug to the tissue. Future versions will also explore pressure controlled pumping by creating pressure bubble using short-pulsed laser to achieve drug delivery.

The new deign of the drug delivery device could be a simple oval shape design with multiple reservoirs. This particular shape would be easy to insert through the incision created at the conjunctiva. One important aspect of this new design has to be the curvature that would be in sink with the radial shape of the sclera.

This implantable drug delivery device could be use for treating diabetes after complex pharmacokinetics after a one time implant. The device can be even placed in a circular manner in an implantable ocular lens after cataract surgery for treating patients who have ARMD. Thus, there are endless possibilities for the implantable drug delivery device for treating multiple diseases.

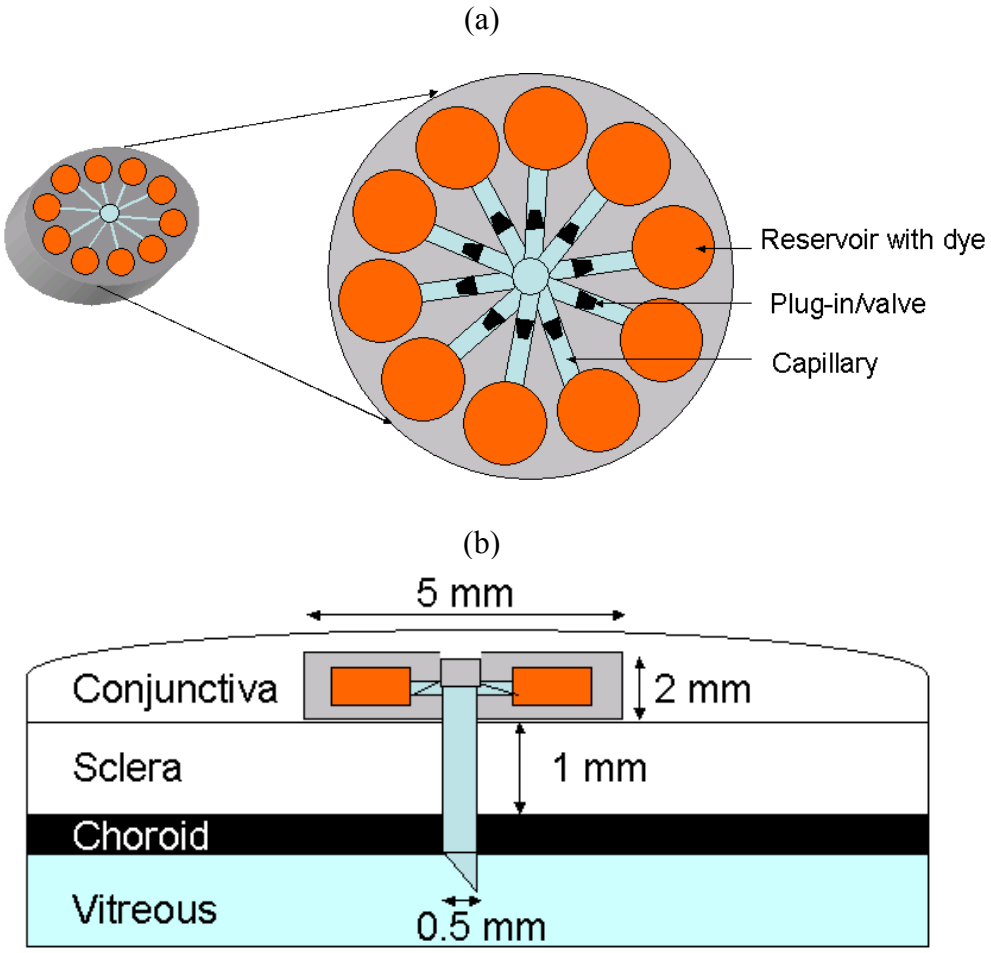

Figure 8.2. Figure design of the implantable drug delivery device with multiple reservoir (a) top view (b) cross-section.

8.2.3. New surgical method

In the current study, all the devices were implanted horizontal to the limbus. Thus, the implant surgery can be improved by placing the newly designed oval shape implant to the long axis perpendicular to the limbus. The horizontal incision will still work for this particular implant. However, the advantage of this vertical implant will be smaller incision compared to the current implant method. Figure 8.3 depicts the implant procedure schematically.

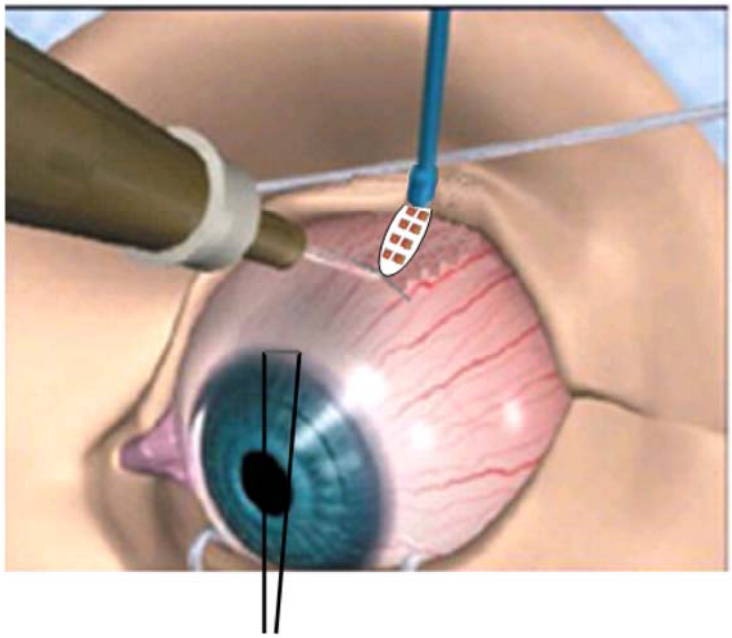

Figure 8.3. A new implant surgery with newly designed oval shape drug delivery device.

8.3. REFERENCES

1. Drezek R, Sokolov K, Utzinger U, Boiko I, Malpica A, Follen M, and Richards-Kortum R. J. Biomed. Opt., 2001; 6: 385–396.

2. Hung J, Lam S, LeRiche JC, Palcic B. Autofluorescnce of normal and malignant bronchial tissue. Lasers in Surgery and Medicine. 1991; 59: 930–933.

3. Holstein SV, Nilsson C, Andersson-Engels S, Willen R, Walther B, Svanberg K. Detection of adenocarcinoma in Barrett's oesophagus by means of laser induced fluorescence. Gut, 1996; 39: 711–716.

4. Huang Z, Zheng W, Xie S, Chen R, Zeng H, McLean DI, Lui H. Laser-induced autofluorescence microscopy of normal and tumor human colonic tissue. International Journal of Oncology, 2004; 24: 59–64.

5. McLaren JW, Brubaker RF. A scanning ocular spectrophotometer. Investigative ophthalmology and visual science, 1988; 29(8): 1284–1293.

6. Liu Q, Ramanujam N. Effect of fiber optic probe geometry on depth-resolved fluorescence measurements from epithelial tissues: a Monte Carlo simulation. Journal of Biomedical Optics, 2002; 27: 104–106.

7. Pfefer TJ, Schomacker KT, Ediger MN, Nishioka NS. Multiple-Fiber Probe Design for Fluorescence Spectroscopy in Tissue. Applied Optics, 2002; 41: 4712–4721.

8. Ghosh N, Majumder SK, Patel HS, Gupta PK. Depth-resolved fluorescence measurement in a layered turbid medium by polarized fluorescence spectroscopy Optics Letters, 2005; 30: 162–164.

9. Amelink A, Bard MPL, Burgers SA, and Sterenborg HJCM. Single-Scattering Spectroscopy for the Endoscopic Analysis of Particle Size in Superficial Layers of Turbid Media. Applied Optics, 2003; 42: 4095–4101.

10. Pfefer TJ, Matchette LS, Ross AM, Ediger MN. Selective detection of fluorophore layers in turbid media: the role of fiber-optic probe design. Optics. Letters, 2003; 28: 120–122.

11. Zhu CF, Liu Q, Ramanujam N. Sequential estimation of optical properties of a two-layered epithelial tissue model from depth-resolved ultraviolet-visible diffuse reflectance spectra. Journal of Biomedical Optics, 2003; 8: 237–247.

12. Utzinger U, Richards-Kortum R. Fiber optic probes for biomedical optical spectroscopy. Journal of Biomedical Optics, 2003; 8: 121–147.

13. Skala MC, Palmer GM, Zhu CF, Liu Q, Vrotsos KM, Marshek-Stone CL, Gendron-Fitzpatrick A, Ramanujam N. Investigation of fiber-optic probe designs for optical spectroscopic diagnosis of epithelial pre-cancers. Lasers in Surgery and Medicine, 2004; 34: 25–38.

14. Nieman L, Myakov A, Aaron J, Sokolov K. Compact beveled fiber optic probe design for enhanced depth discrimination in epithelial tissues. Applied Optics, 2004; 43: 1308–1319.

15. Q. Liu, and N. Ramanujam, *Opt. Letts*. 29, 2024–2026 (2004).

16. Schwarz RA, Arifler D, Chang SK, Pavlova I, Hussain IA, Mack V, Knight B, Richards-Kortum R, Gillenwater AM. Ball lens coupled fiber-optic probe for depth-resolved spectroscopy of epithelial tissue. Optics Letters, 2005; 30: 1159–1161.

CHAPTER 9: SUMMARY AND CONCLUSION

9.1. SUMMARY OF RESULTS

The research work contained in this dissertation centered around the development of a drug delivery device that could be implanted in the eye and release the content on demand using a hyper-osmotic agent to optically clear the tissue. However, before exploring this concept, changes in optical properties of tissue were identified by applying the 100% anhydrous glycerol to enhance the penetration depth of light. Scattering in most biological tissue greatly limits the depth to which tissue can be probed with light. This means that the depth to which information can be gathered with a light diagnostic system or the depth to which a chromophore can be treated in a therapeutic technique is minimal (generally, between tens of microns to a millimeter). The technique introduced in this dissertation greatly enhances the depth of light penetration in a specific highly scattering biological medium – such as hamster skin, rabbit conjunctiva, sclera, and choroid.

The technique of optical tissue clearing was first introduced in Chapter 3 where glycerol demonstrated that this hyper-osmotic not only make tissue temporarily transparent, but also reduce blood flow. Blood flow in larger blood vessels of hamster dorsal skin (i.e. all arteries and veins) decreased over time and some veins had significantly reduced blood flow. At 24 hours, there was a further reduction in capillary blood perfusion whereas larger blood vessels regained flow compared to an hour after

initial application of glycerol without hydrating the tissue with 0.9% saline. Both blood velocity and vessel diameter of the micro-vasculatures of hamster skin was reduced by the application of 100% anhydrous glycerol. At 24 hours, capillary perfusion remained depressed.

Chapter 4 experiments were designed to measure optical properties in eye tissue after the application of 100% anhydrous glycerol. This chapter examines the changes in optical properties and dynamics of blood owing to the application of the glycerol to the sclera of rabbits. Recovery dynamics are monitored after the application of saline. These measurements provide an estimate of the diffusion time of glycerol through the sclera and examine the hypothesis that glycerol reduces blood flow.

Chapter 5 investigated variations in fluorescence intensity with temperatures starting at 14°C and compared *in vivo* and *in vitro* results for consistency. A fiber optic based noninvasive system was used to characterize the temperature effect on tissue fluorescence in hamster dorsal skin *in vivo*, and in sclera and cornea of enucleated pig eyes *in vitro*. Fluorescence intensity decreased as temperature increased from 14°C to 42°C in a phantom containing Rhodamine B dye. Results from both *in vivo* and *in vitro* tissue followed the same trend of decreasing intensity as tissue temperature increased from 14°C. Spectral intensity lineshape changed around 450 nm due to absorption from tissue.

Since the ultimate goal of this research was to develop a technique that could someday be used clinically, one possible application for the technique was investigated. The optical clearing technique was used to increase the penetration depth of light to an

implanted drug delivery device between the sub-conjunctive and super-scleral space of *in vivo* rabbit eye (Chapter 6). A feasibility study was conducted to determine if the technique could be improved to deliver contents to the various layers of eye tissue without going through invasive surgery. In this study, we showed that the material for the drug delivery device was bio-compatible with minimum immune response and the device membrane can be ablated with an ophthalmic Nd:YAG laser after tissue clearing to maintain a controlled release of the content without disrupting the other chamber. The study also showed that small molecules such as 10% Na fluorescein dye can get into the posterior chamber. Thus, the half-life or drug availability at 13 days is higher than other delivery system in the eye most likely due to complex pharmacokinetics from the implant once the membrane is ablated. Although, the study was only done for two rabbits, the findings could be a mile stone for an alternative method for treating ocular diseases. The histological analysis conducted for this dissertation was helpful in determining the effect of implanted device on eye tissue along with glycerol application.

Chapter 7 illustrated the emission signal variation between the anterior and posterior chamber of the *in vivo* rabbit and *ex vivo* pig eyes. We have shown in this study that the spectral differentiation in fluorescence emission peak from the anterior and posterior chamber of the rabbit and pig eyes occurred based on the fluorescence interaction with the ocular tissue constituents. These spectral differences can be useful in identifying the path of drugs that may be fluorescently tagged for treating ocular diseases.

9.2. CONCLUSION

In this dissertation, a hyperosmotic agent was used in three out of five studies. This tissue clearing technique can alter the optical properties of biological tissue but can be easily reversible with saline and some time body can reverse the effect partially without any hydration. This tissue clearing agent was also used with light to activate an implantable drug delivery device in between sub-conjunctival and super-scleral space. It has been introduced by the work of this dissertation for the first time. The technique has been shown to be highly effective and has the potential for improving treatment for certain ocular diseases. While the studies contained in this dissertation cannot explore every physiological mechanisms involved in the process, or in fully exploring all of the potential medical applications, an attempt has been made to address the most crucial aspects necessary for future clinical research.

APPENDIX A: SWEPT SOURCE POLARIZATION-SENSITIVE OPTICAL COHERENCE TOMOGRAPHY (SS-PSOCT)

Optical coherence tomography (OCT) is a non-invasive imaging technique, capable of optical ranging within a highly scattering sample, such as biological tissue, with visualization of microstructures at a resolution approaching that of conventional histology. The technique, based on the optical scattering properties of tissue, is feasible because most biological tissues have a sufficient number of complex microscopic scattering elements to produce good contrast for OCT images. The development of polarization sensitive (PS) OCT has enabled OCT to sense the birefringence properties of biological tissue that are not provided by the conventional OCT. A number of medical applications for PSOCT have emerged over the last decade, for example burn assessment in skin, caries research in tooth, diagnostics of cornea and retina in ophthalmology, rheumatology, among the others. Recent report has shown the potential of PSOCT to detect ultra-structural changes in a muscle using the changes in the form birefringence related to dystrophy.

SS-PSOCT information presented in this section is adopted from the dissertation of Badr Elmaanaoul. The SS-PSOCT system (figure A.1) consists of a swept laser source and a fiber interferometer with source, reference, clock and trigger, sample, and detection paths. In single-mode fiber (SMF), core ellipticity, noncircular symmetry stresses, and

tight bends give rise to random birefringence that varies with wavelength. The two orthogonal polarization states, in the presence of PMD, travel through fiber at different speeds. This differential phase delay and differential group delay causes a broadening of the PSF. Higher orders of PMD can degrade performance of PSOCT systems.

The optical fiber signal interferometer was built with care to minimize PMD. Fiber length in the signal interferometer was kept as short as possible, and the whole fiber system was routed inside a 10 inch diameter polyvinyl chloride (PVC) open-top annulus tubing. Construction and packaging of the PS-OCT interferometer helped minimize PMD and allowed the acquisition of repeatable and accurate polarization sensitive measurements. Since PMD in the system was sufficiently reduced a calibration method to correct for PMD was not required. HI1060 FLEX fiber further reduces PMD compared to HI1060 fiber used; however, off the shelf optical components using the FLEX fiber were not readily available.

PS-OCT data typically consist of depth-resolved fringe amplitudes [$\Gamma_h(z)$ and $\Gamma_v(z)$] and relative phase [$\varphi_{v\text{-}h}(z)$] of detected interference signals in two orthogonal polarization modes (e.g., horizontal and vertical), where z is the penetration depth into the sample. $\Gamma_h(z)$, $\Gamma_v(z)$, and $\varphi_{v\text{-}h}(z)$ are determined by coherent demodulation or Hilbert transform techniques in time-domain PS-OCT or Fourier transform in spectral-domain PS-OCT. Analytical methods involving Jones-matrix analysis or geometrical methods involving Stokes vectors and the Poincaré sphere can then be used to estimate relevant specimen polarization properties [birefringence (Δn), biattenuance ($\Delta\chi$), or optic axis orientation (θ)].

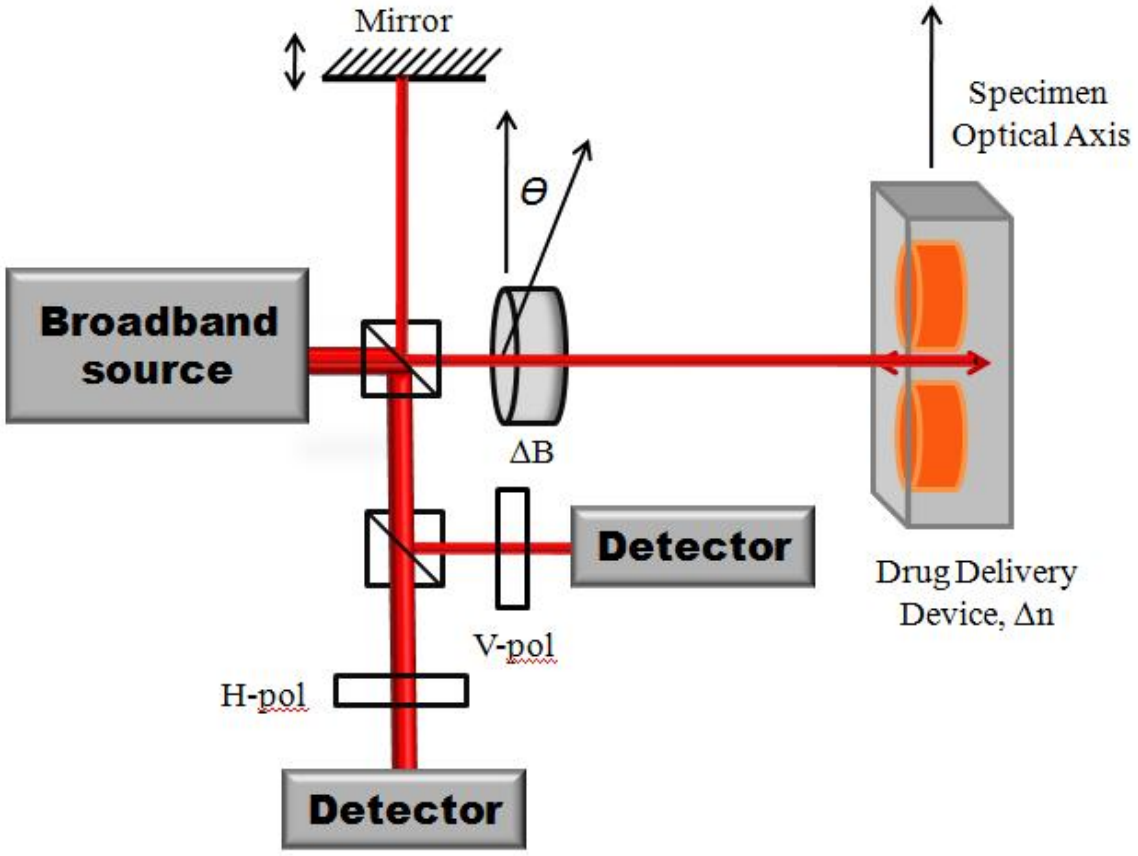

Figure A.1. Schematic representation of a PS-OCT system above ΔB is the strength of the internal birefringence (shown as waveplate), H-pol and v-pol are the linear polarizes.

APPENDIX B: DEPTH CALCULATION OF DEVICE MEMBRANE USING SD-PSOCT

Phase sensitive OCT: This is an image of one of the reservoir of the drug delivery device where the membrane thickness is 81.62μm. Each image is consisted of 500 A scans and 100 B scans with amplitude of 280 and 400 for x-axis (offset 624) and y-axis (offset 592), respectively. The scan pattern was raster with acquisition time of 1.482 seconds. The depth was calculated using the following equation:

Optical path length (OPL) = Depth × index of refraction

Where,

Optical path length = 2.6 mm

Index of refraction of 10% Na fluorescence dye = 1.29

Index of refraction of PDMS = 1.431

$$\text{The OPL of each pixel} = \frac{2..6\,mm}{512\,pixels} = 0.005078\,\frac{mm}{pixel}$$

The membrane consists of 23 pixels shown in the SC image shown in Figure B.1. calculated using Matlab code

Thus the OPL of the membrane

$$= 0.005078\,\frac{mm}{pixel} \times 23\ pixels$$

$$= 0.11679\ mm$$

$$\text{Membrane Depth} = \frac{OPL}{index\ of\ refraction\ of\ PDMS}$$

$$\text{Membrane Depth} = \frac{0.11679\ mm}{1.431}$$

Membrane Depth = 81.62 µm

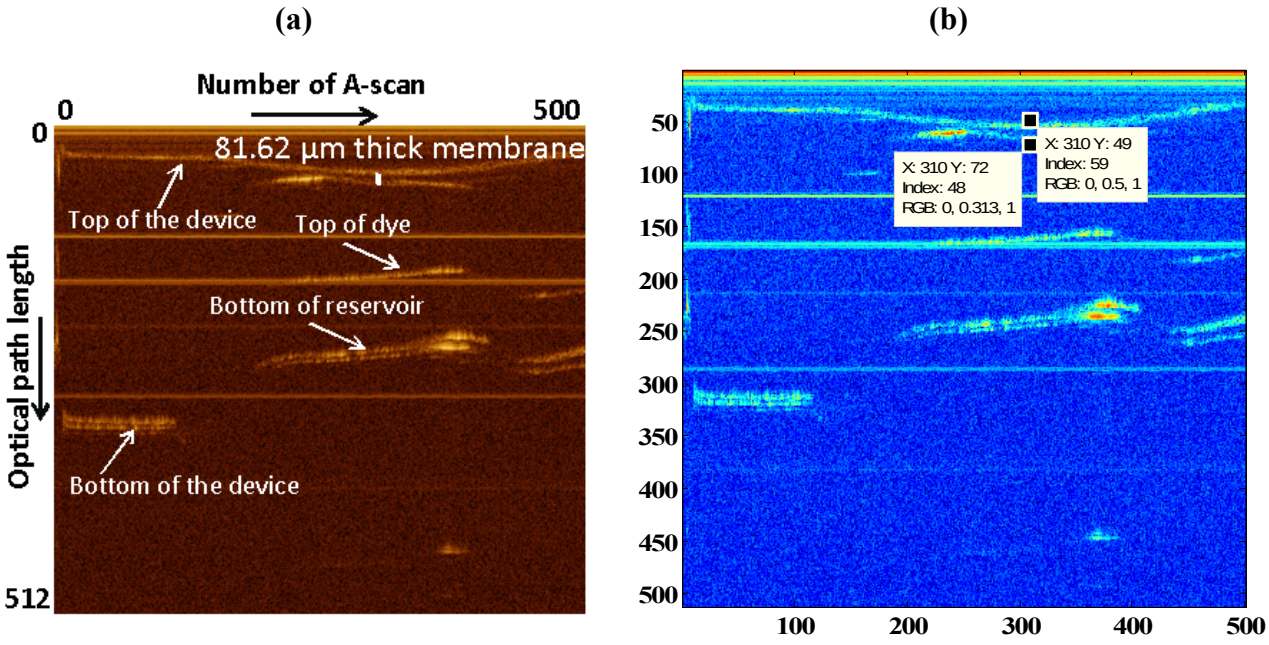

Figure B.1. Measurement of membrane thickness of the drug delivery device using (a) Spectral Domain Phase Sensitive Optical Coherent Tomography (SD-PSOCT), (b) pixel calculation using Matlab software from the SC image of the A-scan.

APPENDIX C: CONVERSION OF VOLUME TO CONCENTRATION

Currently the 10% Na Fluorescein dye present in the vitreous humor of the rabbit eye are measurement in volume. We need to calculate the concentration of the dye with respect to the vitreous humor of the rabbit eye. The concentration calculations are described below:

Conversion for 5 µL of 10% Na Fluorescein Dye:

Based on the size of the molecule of 10% Na fluorescein dye we can assume that 1 mL of dye is equivalent to 1 g. Thus, 5 µL is equivalent to 0.005 g.

We have 0.005 g of 10% Na Fluorescein dye in 3.3 mL vitreous humor of the pig eye

$$= \frac{0.005\ g\ of\ 10\%\ Na\ Fluorescein\ Dye}{3.3\ mL\ of\ Vitreous\ Humor}$$
$$= 0.001515\ g/mL$$
$$= 1.52\ mg/mL$$
$$= 1.52\ g/L$$

Na Fluorescein dye has molecular weight or molar mass of 376 daltons or g/mol

Thus, 10% Na Fluorescein dye has molar mass of 37.6 daltons or g/mol

Thus, concentration of the 5 µL dye in 3.3 mL vitreous humor

$$= \frac{1.52\ \frac{g}{L}\ of\ Na\ Fluorescein\ Dye\ in\ Vitreous}{37.6\ \frac{g}{mol}\ ofNa\ Fluorescein\ Dye}$$

$$= 0.04029 \frac{mole}{L}$$
$$= 40 \frac{mmole}{L}$$

Conversion for 3.82 µL of 10% Na Fluorescein Dye:

Based on the size of the molecule of 10% Na fluorescein dye we can assume that 1 mL of dye is equivalent to 1 g. Thus, 3.82 µL is equivalent to 0.00382 g.

We have 0.00382 g of 10% Na Fluorescein dye in 1.67 mL vitreous humor of the rabbit eye

$$= \frac{0.00382\ g\ of\ 10\%\ Na\ Fluorescein\ Dye}{1.67\ mL\ of\ Vitreous\ Humor}$$
$$= 0.002287\ g/mL$$
$$= 2.29\ mg/mL$$
$$= 2.29\ g/L$$

Na Fluorescein dye has molecular weight or molar mass of 376 daltons or g/mol

Thus, 10% Na Fluorescein dye has molar mass of 37.6 daltons or g/mol

Thus, concentration of the 3.82 µL dye in 1.67 mL vitreous humor

$$= \frac{2.29 \frac{g}{L} of\ Na\ Fluorescein\ Dye\ in\ Vitreous}{37.6 \frac{g}{mol} ofNa\ Fluorescein\ Dye}$$

$$= 0.06084 \frac{mole}{L}$$
$$= 60.84 \frac{mmole}{L}$$

Conversion for 0.7 µL of 10% Na Fluorescein Dye:

Based on the size of the molecule of 10% Na fluorescein dye we can assume that 1 mL of dye is equivalent to 1 g. Thus, 0.7 µL is equivalent to 0.0007 g.

We have 0.0007 g of 10% Na Fluorescein dye in 1.67 mL vitreous humor of the rabbit eye

$$= \frac{0.0007\ g\ of\ 10\%\ Na\ Fluorescein\ Dye}{1.67\ mL\ of\ Vitreous\ Humor}$$
$$= 0.000419\ g/mL$$
$$= 0.419\ mg/mL$$
$$= 0.42\ g/L$$

Na Fluorescein dye has molecular weight or molar mass of 376 daltons or g/mol

Thus, 10% Na Fluorescein dye has molar mass of 37.6 daltons or g/mol

Thus, concentration of the 0.7 µL dye in 1.67 mL vitreous humor

$$= \frac{0.42\ \frac{g}{L}\ of\ Na\ Fluorescein\ Dye\ in\ Vitreous}{37.6\ \frac{g}{mol}\ ofNa\ Fluorescein\ Dye}$$

$$= 0.01115 \frac{mole}{L}$$
$$= 11.15 \frac{mmole}{L}$$

Conversion for 3.4 µL of 10% Na Fluorescein Dye:

Based on the size of the molecule of 10% Na fluorescein dye we can assume that 1 mL of dye is equivalent to 1 g. Thus, 3.4 µL is equivalent to 0.0034 g.

We have 0.0034 g of 10% Na Fluorescein dye in 1.67 mL vitreous humor of the rabbit eye

$$= \frac{0.0034\ g\ of\ 10\%\ Na\ Fluorescein\ Dye}{1.67\ mL\ of\ Vitreous\ Humor}$$
$$= 0.002036\ g/mL$$
$$= 2.036\ mg/mL$$
$$= 2.036\ g/L$$

Na Fluorescein dye has molecular weight or molar mass of 376 daltons or g/mol

Thus, 10% Na Fluorescein dye has molar mass of 37.6 daltons or g/mol

Thus, concentration of the 3.4 µL dye in 1.67 mL vitreous humor

$$= \frac{2.036\ \frac{g}{L}\ of\ Na\ Fluorescein\ Dye\ in\ Vitreous}{37.6\ \frac{g}{mol}\ ofNa\ Fluorescein\ Dye}$$

$$= 0.05415\ \frac{mole}{L}$$
$$= 54.15\ \frac{mmole}{L}$$

Conversion for 0.4 µL of 10% Na Fluorescein Dye:

Based on the size of the molecule of 10% Na fluorescein dye we can assume that 1 mL of dye is equivalent to 1 g. Thus, 0.4 µL is equivalent to 0.0004 g.

We have 0.0004 g of 10% Na Fluorescein dye in 1.67 mL vitreous humor of the rabbit eye

$$= \frac{0.0004\ g\ of\ 10\%\ Na\ Fluorescein\ Dye}{1.67\ mL\ of\ Vitreous\ Humor}$$
$$= 0.00024\ g/mL$$
$$= 0.24\ mg/mL$$
$$= 0.24\ g/L$$

Na Fluorescein dye has molecular weight or molar mass of 376 daltons or g/mol

Thus, 10% Na Fluorescein dye has molar mass of 37.6 daltons or g/mol

Thus, concentration of the 0.4 µL dye in 1.67 mL vitreous humor

$$= \frac{0.24\ \frac{g}{L}\ of\ Na\ Fluorescein\ Dye\ in\ Vitreous}{37.6\ \frac{g}{mol}\ ofNa\ Fluorescein\ Dye}$$

$$= 0.00637\ \frac{mole}{L}$$
$$= 6.37\ \frac{mmole}{L}$$

REFERENCES

1. Bakutkin VV, Maksimova IL, Semyonova TN, Tuchin VV, Kon IL. Controlling of optical properties of sclera. SPIE Proceedings, 1995; 2393:137−141.

2. Tuchin VV, Maksimova IL, Zimnyahkov DA, Kon IL, Mavlutov AK, Mishin AA. Light propagation in tissues with controlled optical properties. *Proceedings SPIE*, 1996; 2925:118−142.

3. Tuchin VV, Maksimova IL, Zimnyakov DA., Kon IL, Mavlutov AH, Mishin AA. Light Propagation in tissues with controlled optical properties. *Journal of Biomedical Optics*, 1997; 2(4):401−417.

4. Zimnyakov DA, Tuchin VV, Mishin AA, Kon IL, Serov AN, In-vitrohuman sclera structure analysis using tissue optical immersion effect. Proceedings SPIE, 1996; 2673:233–247.

5. Stevenson R, Vaja N, Jackson J. Corneal transparency changes resulting from osmotic stress. *Ophthalmic Physiol. Opt.*, 1983; 3(1):33–39.

6. Chance B, Liu H, Kitai T, Zhang Y. Effects of solutes on optical properties of biological materials: models, cells, and tissues. Analytical Biochemistry, 1995; 227:351–362.

7. Liu H, Beauvoit B, Kimura M, Chance B. Dependence of tissue optical properties on solute-induced changes in refractive index and osmolarity. *Journal of Biomedical Optics*, 1996; 1(2):200–211.

8. *The Merck Index*, 12th Edition, Budavari S, O'Neil MJ, Smith A, Heckelman PE, Kinneary JF, editors, Merck Research Laboratories : Merck & Co., Inc., Whitehouse Station, NJ, 1996.

9. Keller MD, Majumder SK, and Mahadevan-Jansen A. Spatially offset Raman spectroscopy of layered soft tissues. Optics Letter. 2009; 34(7): 926-8.

10. Klein R, Klein BE, Jensen SC, Mares-Perlman JA, Cruickshanks KJ, Palta M. Age-related maculopathy in a multiracial United States population: the National Health and Nutrition Examination Survey III. Ophthalmology, 1999; 106:1056–1065.

11. Resnikoff S, Pascolini D, Etya'ale D et al. Global data on visual impairment in the year 2002. Bull World Health Organ, 2004; 82:844–851.

12. Klein R, Klein BE, Jensen SC, Meuer SM. The five-year incidence and progression of age-related maculopathy: the Beaver Dam Eye Study. Ophthalmology, 1997; 104:7–21.

13. Friedman DS, O'Colmain BJ, Munoz B et al. Prevalence of age-related macular degeneration in the United States. Arch Ophthalmology, 2004; 122: 564–572.

14. Varma R, Fraser-Bell S, Tan S, Klein R, Azen SP. Prevalence of age-related macular degeneration in Latinos: the Los Angeles Latino eye study. Ophthalmology, 2004; 111:1288–1297.

15. Anonymous Argon laser photocoagulation for senile macular degeneration. Results of a randomized clinical trial. Arch Ophthalmology, 1982; 100:912–918.

16. Gragoudas ES, Adamis AP, Cunningham ET Jr, Feinsod M, Guyer DR. Pegaptanib for neovascular age-related macular degeneration. New England Journal of Medicine, 2004; 351:2805–2816.

17. Brown DM, Kaiser PK, Michels M et al. Ranibizumab versus verteporfin for neovascular age-related macular degeneration. New England Journal of Medicine, 2006; 355:1432–1444.

18. Rosenfeld PJ, Brown DM, Heier JS et al. Ranibizumab for neovascular age-related macular degeneration. New England Journal of Medicine, 2006; 355:1419–1431.

19. Brown DM PIER study data. Retinal Physician 2006 Symposium, 2007.

20. Fung AE, Lalwani GA, Rosenfeld PJ et al. An optical coherence tomography-guided, variable dosing regimen with intravitreal ranibizumab (Lucentis) for neovascular age-related macular degeneration. American Journal of Ophthalmology, 2007;143:566–583.

21. Spaide RF, Laud K, Fine HF et al. Intravitreal bevacizumab treatment of choroidal neovascularization secondary to age-related macular degeneration. Retina, 2006; 26:383–390.

22. Macular Photocoagulation Study Group Laser photocoagulation for juxtafoveal choroidal neovascularization. Five-year results from randomized clinical trials. Arch Ophthalmology, 1994; 112:500–509.

23. Macular Photocoagulation Study Group Laser photocoagulation of subfoveal neovascular lesions of age-related macular degeneration. Updated findings from two clinical trials. Arch Ophthalmology, 1993; 111: 1200–1209.

24. Gragoudas ES, Adamis AP, Cunningham ET Jr, Feinsod M, Guyer DR. Pegaptanib for neovascular age-related macular degeneration. New England Journal of Medicine, 2004; 351, 2805–2816.

25. D'Amico DJ, Masonson HN, Patel M et al. Pegaptanib sodium for neovascular age-related macular degeneration: two-year safety results of the two prospective, multicenter, controlled clinical trials. Ophthalmology, 2006; 113:992–1001.

26. Vargas G, Chan EK, Barton JK, Rylander III HG, Welch AJ. Use of an agent to reduce scattering in skin. Lasers Surgery and Medicine, 1999; 24:133–141.

27. Ghosn MG, Tuchin VV, and Larin KV. Depth-resolved monitoring of glucose diffusion in tissues by using optical coherence tomography. Optics Letters 2006; 31(15): 2314−2316.

28. Vargas G, Readinger A, Dozier SS, Welch AJ. Morphological changes in blood vessels produced by hyper osmotic agents and measured by optical coherence tomography. Photochemistry and Photobiology 2003; 77(5): 541–549.

29. Bakutkin VV, Maksimova IL, Semyonova TN, Tuchin VV, Kon IL. Controlling of optical properties of sclera. Proc. SPIE 2393 1995; 137–141.

30. Tuchin VV, Maksimova IL, Zimnyahkov DA, Kon IL, Mavlutov AK, Mishin AA. Light propagation in tissues with controlled optical properties. Proc. SPIE 2925, 1996; 118–142.

31. Tuchin VV, Maksimova IL, Zimnyakov DA, Kon IL, Mavlutov AK, Mishin AA. Light propagation in tissues with controlled optical properties. Journal of Biomedical Optics 1997; 2: 401–417.

32. Vargas G, Chan KF, Thomsen SL, Welch AJ. Use of osmotically active agents to alter optical properties of tissue: effects on the detected fluorescence signal measured through skin. Lasers Surg.Med.2001; 29:213–220.

33. Choi B, Ramirez-San-Juan JC, Lotfi j, Nelson JS, Linear response range charactization and *in vivo* application of laser speckle imaging of blood flow dynamics. Journal of Biomedical Optics 2006; 11(4):041129.

34. Zhu D, Zhang J, Cui H, Mao Z, Li P, Luo Q. Short-term and long-term effects of optical clearing agents on blood vessels in chick chorioallantoic membrane. Journal of Biomedical Optics 2008; 13(2):021106.

35. Briers JD, Webster S. Laser speckle contrast analysis (LASCA): a nonscanning, full-field technique for monitoring capillary blood flow. Journal of Biomedical Optics 1996; 1:174–179.

36. Dunn AK, Bolay H, Moskowitz MA, Boas DA. Dynamic imaging of cerebral blood flow using laser speckle. Journal of Cerebral Blood Flow and Metabolism 2001; 21:195–201.
37. Fercher A, Briers J. Flow visualization by means of single exposure speckle photography. Opt. Commun. 1981; 37:326–329.

38. Yuan S, Devor A, Boas DA, Dunn AK. Determination of optical exposure time for imaging of blood flow changes with laser speckle contrast imaging. Applied Optics 2005; 44(10): 1823−1830.

39. Papenfuss HD, Gross JF, Intaglietta M, Treese FA. A transparent access chamber for the rat dorsal skin flap. Microvascular Research 1979; 18:311–318.

40. Dunn AK, Bolay H, Moskowitz MA, Boas DA. Dynamic imaging of cerebral blood flow using laser speckle. Journal of Cerebral Blood Flow and Metabolism 2001; 21:195–201.

41. Boyle R, and Thomas R. *Computer Vision:A First Course*, Blackwell Scientific Publications 1988; Chap. 5.

42. Shams R, Barnes N, and Harley R. Image registration in Hough space using gradient of images. IEEE Xplore on Digital Image Computing Techniques and Applications 2007; 226−232.

43. Chunhavittayatera S, Chitsobhuk O, and Tongprasert K. Image registration using Hough transform and phase correlation. International Conference on Advanced Communication Technology (ICACT) 2006; 973–977.

44. Cole-Rhodes A, Johnson K, LeMoigne J, and Zavorin I. Multiresolution registration of remote sensing imagery by optimization of mutual information using a stochastic gradient. IEEE Trans. on Image Processing 2003; 12(12):1495–1511.

45. Vargas G. Reduction of light scattering in biological tissue: implications for optical diagnostics and therapeutics. Doctoral Dissertation 2001; The University of Texas at Austin.

46. Barton JK. Predicting dosimetry for laser coagulation of *in vivo* cutaneous blood vessels. Doctoral Dissertation 1998; The University of Texas at Austin.

47. Wahl LM, Wahl SM. Inflammation. In Wound Healing, Biochemical and Clinical Aspects (Edited by I. K. Cohen, R. F. Diegelmann, and W. J. Lindblad), pp. 40–53. W. B. Saunders Co.,Philadelphia, 1992; [Chapter 3].

48. Walter JB, Israel MS. The inflammatory reaction. In General Pathology, 4th ed., (Edited by J. B. Walter) pp. 69–83. Churchill Livingston, London 1974; [Chapter 6].

49. Wang RK, Tuchin VV. Tissue clearing as a tool to enhance imaging capability for optical coherence tomography. Proc.SPIE 4619 2002; 22–25.

50. Boergen KP, Birngruber R, Gabel VP, and Hillenkamp F. Experimental studies on controlled closure of small vessels by laserirradiation. Proc. Lasers Surg. Med. Biol. Munich 1977; 5: 15.

51. Burek DG, Riva CE. Vasomotion and spontaneous low-frequency oscillations in blood flow and nitric oxide in cat optic nerve head. Microvascular Research 1998; 55: 103−112.

52. Wang Y, Okamura T, and Toda N. Mechanism of acetyl-choline-induced relaxation in dog external and internal ophthalmic arteries. Exp. Eye Res 1993; 57: 275−282.

53. Bertuglia S, Colantuoni A, and Dunn R Jr. Effect of L-NMMA and indomethacin on arteriolar vasomotion in skeletal muscle microcirculation of conscious and anesthetized hamsters. Microcirc. Res. 1994; 48: 68−84.

54. Abdi H. The Bonferonni and Sidak corrections for multiple comparisons. N.J. Salkind (ed.) Thousand Oaks, CA: Sage, *Encyclopedia of Measurement and Statistics 2007.*

55. Miller RG, Jr. Simultaneous Statistical Inference. NewYork: Springer. Verlog, 1991.

56. Shaffer JP. Multiple Hypothesis Testing. *Ann. Rev. Psych.* 9951; 46: 561−584

57. Bakutkin VV, Maksimova IL, Semyonova TN, Tuchin VV, Kon IL. Controlling of optical properties of sclera. Proc. SPIE 2393, 1995;137–141.

58. Tuchin VV, Maksimova IL, Zimnyahkov DA, Kon IL, Mavlutov AK, Mishin AA. Light propagation in tissues with controlled optical properties. Proc. SPIE 1996; 2925: 118–142.

59. Tuchin VV, Maksimova IL, Zimnyakov DA, Kon IL, Mavlutov AK, Mishin AA. Light propagation in tissues with controlled optical properties. Journal of Biomedical Optics, 1997; 2:401–417.

60. Tuchin VV, Optical Clearing of Tissues and Blood, PM 154, SPIE Press, Bellingham, WA, 2006 (Chapter 2, pp. 23−58 and subsection 8.3, pp. 188−191).

61. Bashkatov AN, Tuchin VV, Genina EA, Sinichkin YP, Lakodina NA, Kochubey VI. The Human Sclera Dynamic Spectra: *In Vitro* and *In Vivo* Measurements. Proc SPIE 1999; 3591: 311−319.

62. Tuchin VV, Culver J, Cheung C, Tatarkova SA, DellaVecchia MA, Zimnyakov D, Chaussky A, Yodh AG, Chance B. Refractive Index Matching of Tissue Components as a New Technology for Correlation and Diffusing-Photon Spectroscopy and Imaging. Proc. SPIE 1999; 3598: 111−120.

63. Tuchin VV. Coherent Optical Techniques for the Analysis of Tissue Structure and Dynamics. Journal of Biomedical Optics 1999; 4(1): 106−124.

64. Sacks ZS, Kurtz RM, Juhasz T, Mourau GA. High Precision Subsurface Photodisruption in Human Sclera. Journal of Biomedical Optics 2002; 7(3): 442−450.

65. Genina EA, Bashkatov AN, Sinichkin YP, Tuchin VV. Optical clearing of the eye sclera *in vivo* caused by glucose. Quantum Electronics 2006; 36 (12): 1119−1124.

66. Ghosn MG, Carbajal EF, Befrui N, Tuchin VV, Larin KV. Differential Permeability Rate and Percent Clearing of Glucose in Different Regions in Rabbit Sclera. Journal of Biomedical Optics 2008;13: 021110-1−021110-6.

67. Vargas G, Chan EK, Barton JK, Rylander III HG, Welch AJ. Use of an agent to reduce scattering in skin. Lasers Surgery and Medicine 1999; 24:133–141.

68. Vargas G, Chan KF, Thomsen SL, Welch AJ. Use of osmotically active agents to alter optical properties of tissue: effects on the detected fluorescence signal measured through skin. Lasers Surgery and Medicine 2001; 29: 213–220.

69. Vargas G. Reduction of Light Scattering in Biological Tissue: Implications for Optical Diagnostics and Therapeutics. Doctoral Dissertation 2001; The University of Texas at Austin.

70. Boergen KP, Birngruber R, Gabel VP, Hillenkamp F. Experimental studies on controlled closure of small vessels by laser irradiation. Proc. Lasers Surg. Med Biol. Munich 1977; 5: 15.

71. Zaman RT, Parthasarathy AB, Vargas G, Chen B, Dunn AK, Rylander III HG, Welch AJ. Perfusion in hamster skin treated with glycerol," Lasers in Surgery and Medicine, 2009; 41:492−503.

72. Rajaram N, Nguyen TH, Tunnell JW. Lookup table-based inverse model for determining optical properties of turbid media. Journal of Biomedical Optics Letters 2008; 13(5): 050501.

73. Mourant JR, Fuselier T, Boyer J, Johnson TM, Bigio IJ. Predictions and measurements of scattering and absorption over broad wavelength ranges in tissue phantoms. Applied Optics 1997; 36(4), 949−957.

74. Finlay JC, Foster TH. Effect of pigment packaging on diffuse reflectance spectroscopy of samples containing red blood cells. Optics Letter. 2004; 29(9): 965−967.

75. Van Veen RL, Verkruysse W, Sterenborg HJ. Diffuse-reflectance spectroscopy from 500 to 1060 nm by correction for inhomogeneously distributed absorbers. Optics Letter 2002; 27(4): 246−248.

76. Svaasand L, Fiskerstrand E, Kopstad G, Norvang L, Svaasand E, Nelson J, Berns M. Therapeutic response during pulsed laser treatment of port-wine stains: Dependence on vessel diameter and depth in dermis. Lasers Medical. Science 1995; 10(4): 235−243.

77. Vargas G, Readinger A, Dozier SS, Welch AJ. Morphological changes in blood vessels produced by hyper osmotic agents and measured by optical coherence tomography. Photochemistry and Photobiology 2003; 77(5): 541−549.

78. Stephenson RW. *Anatomy, Physiology and Optics of the Eye: A Textbook for Orthoptic Students*, Kimpton Publishers, 1973.

79. Nemeth SC. *Ocular Anatomy and Physiology*, Slack Incorporated Publishers, 2007.

80. Feng Y, Simpson TL. Corneal, limbal, and conjunctival epithelial thickness from optical coherence tomography. Optometry and Vision Science 2008; 85(9): 880−883.

81. Hayreh SS. Segmental nature of the choroidal vasculature. British Journal of Ophthalmology 1975; 59(11): 631−48.

82. Young AR. Chromophores in human skin. Phys. Med. Biol. 1997; 42:789−802.

83. Zaman RT, Diagaradjane P, Wang JC, Swartz J, Rajaram N**,** Gill-Sharp KL, Cho SH, Rylander HG, Payne DJ, Krishnan S, Tunnell JW. *In vivo* detection of gold nanoshells in tumors using diffuse optical spectroscopy. IEEE Journal of Selected Topics in Quantum Electronics, 2007; 13(6): 1715–1720.

84. Chan EK, Sorg B, Protsenko D, O'Neil M, Motamedi M, Welch AJ. Effects on compression on soft tissue optical properties. IEEE Journal of Selected Topics in Quantum Elcetronics, 1996; 2 (4): 940–950.

85. Farrell TJ, Patterson MS, Wilson B. A diffusion theory model of spatially resolved, steady-state diffuse reflectance for the noninvasive determination of tissue optical properties *in vivo*. Med. Phys. 1992; 19: 879−888.

86. Kienle A, Patterson MS. Improved solutions of the steady-state and the time-resolved diffusion equations for reflectance from a semi-infinite turbid medium. J. Opt. Soc. Am. A. 1997; 14: 246−254.

87. Rajaram N, Gopal A, Zhang XJ, Tunnell JW. Experimental validation of the effects of microvasculature pigment packaging on *in vivo* diffuse reflectance spectroscopy. Journal of Lasers in Surgery and Medicine, 2010; 42(7): 680–688.

88. Welch AJ, Gemert MJ. Appendix to Chap. 8 in *Optical-Thermal Response of Laser-Irradiated Tissue*, Plenum, New York, 1995.

89. Prahl S. Tabulated molar extinction coefficient for hemoglobin in water. http://omlc.ogi.edu/spectra/hemoglobin/index.html. Accessed 7/24/09.

90. West BT, Welch KB, Galecki AT. Linear mixed models: a practical guide using statistical software, Chapman & Hall/CRC, 2007.

91. Ethier CR, Johnson M, Ruberti J. Ocular Biomechanics and Biotransport. Annual Revision Biomedical Engineering, 2004; (6): 249−273.

92. Ghosn MG, Tuchin VV, Larin KV. Depth-resolved monitoring of glucose diffusion in tissues by using optical coherence tomography. Optics Letters, 2006; 31(15): 2314−2316.

93. Kiel JW. Endothelin modulation of choroidal blood flow in the rabbit. *Exp Eye Res*. 2000; 71:543–550.

94. Dallinger S, Dorner GT, Wenzel R, et al. Endothelin-1 contributes to hyperoxia-induced vasoconstriction in the human retina. *Invest Ophthalmol Vis Sci*. 2000; 41:864–869.

95. Zhu Y, Park TS, Gidday JM. Mechanisms of hyperoxia-induced reductions in retinal blood flow in newborn pig. *Exp Eye Res*., 1998; 67:357–369.

96. Takagi C, King GL, Takagi H, Lin YW, Clermont AC, Bursell SE. Endothelin-1 action via endothelin receptors is a primary mechanism modulating retinal circulatory response to hyperoxia. *Invest Ophthalmol Vis Sci*., 1996; 37:2099–2109.

97. Nishimura K, Riva CE, Harino S, Reinach P, Cranstoun SD, Mita S. Effects of endothelin-1 on optic nerve head blood flow in cats. *J Ocul Pharmacol Ther*. 1996; 12:75–83.

98. Kiel JW. Endothelin modulation of choroidal blood flow in the rabbit. Exp Eye Res., 2000; 71:543–550.

99. Brubaker RF. Measurement of aqueous flow by fluorophotometry. The Glaucomas. St. Louis, MO: C.V. Mosbey Co., 1989; 337−344.

100. Ninomiya H, Inomata T. Mirovascular anatomy of the pig eye: scanning electron microscopy of vascular corrosion casts. Journal of Veterinarian Medical Science, 2006; 68(11): 1149−1154.

101. Verkruyssa W, Khan M, Choi B, Svaasand LO, Nelson SJ. Measuring the effects of topically applied skin optical clearing agents and modeling the effects and consequences for laser therapies. Proc. SPIE, 2005; 5695: 278−287.

102. Walter JB, Israel MS. Chapter 6 in *The Inflammatory Reaction In General Pathology*, Churchill Livingston, London, 1974.

103. Wahl LM, Wahl SM. *Inflammation in wound healing. Biochemical and Clinical Aspects*, W. B. Saunders Co., Philadelphia, 1992; 40–53.

104. Ramanujam N, Richards-Kortum R, Thomsen S, Mahadevan-Jansen A, Follen M, Chance B. Low temperature fluorescence imaging of freezetrapped human cervical tissues. Optics Express, 2001; 8(6):335−343.

105. Romano V, Greber CM, Frenz M, Forrer M, Weber HP. Measurement of temperature distributions after pulsed IR-radiation impact in biological tissue models with fluorescent thing films. SPIE Proceeding paper, Laser Tissue Interaction II, 1991; (1427):16−26.

106. Buttemere CR, Chari RS, Anderson CD, Washington MK, Mahadevan-Jansen A, Lin W-C. *In vivo* assessment of thermal damage in the liver using optical spectroscopy. Journal of Biomedical Optics, 2004; 9(5):1018−1027.

107. Rajaram N, Kovacic D, Migden MF, Reichenberg JS, Nguyen TH, Tunnell JW. *In vivo* determination of optical properties and fluorophore characteristics of non-melanoma skin cancer. Proceedings of SPIE, 2009; 7161: 1021−1029.

108. Romano V, Zweig AD, Frenz M, Weber HP. Time-resolved thermal microscopy with fluorescent thin films. Applied Physics, 1989; 49:527−533.

109. Lin WC, Toms SA, Motamedi M, Jansen ED, Mahadevan-Jansen A. Brain tumor demarcation using optical spectroscopy; an *in vitro* study. Journal of Biomedical Optics, 2000; 5:214–220.

110. Ritz JP, Roggan A, Isbert C, Muller G, Buhr HJ, Germer CT. Optical properties of native and coagulated porcine liver tissue between 400 and 2400 nm. Lasers in Surgery and Medicine, 2001*;* 29: 205–212.

111. Ritz JP, Roggan A, Germer CT, Isbert C, Muller G, Buhr HJ. Continuous changes in the optical properties of liver tissue during laser-induced interstitial thermotherapy. Lasers in Surgery and Medicine, 2001; 28: 307–312.

112. Pickering JW, Posthumus P, and Gemert MJ van. Continuous measurement of the heat-induced changes in the optical properties (at 1,064 nm) of rat liver. Lasers in Surgery and Medicine, 1994; 15:200–205.

113. Germer CT, Roggan A, Ritz JP, Isbert C, Albrecht D, Muller G, Buhr HJ. Optical properties of native and coagulated human liver tissue and liver metastases in the near infrared range. Lasers in Surgery and Medicine, 1998; 23:194–203.

114. Pearce J, Thomsen S. Rate process analysis of thermal damage in *Optical-Thermal Response of Laser-Irradiated Tissue*, A. J. Welch and M. J. C. van Gemert, Eds., pp. 561–606, Plenum Press, New York, 1995.

115. Burstein EA, Abornev SM, Reshetnyak YK. Deconposition of protein tryptophan fluorescence spectra into log-normal components, I: decomposition algorithms. Biophysics Journal, 2001; 81:1699–1709.

116. Reshetnyak YK, Burstein EA. Decomposition of protein tryptophan fluorescence spectra into log-normal components, II: the statistical proof of discreteness of tryptophan classes in protein. Biophysics Journal 2001; 81:1710–1734.

117. Reshetnyak YK, Koshenvik Y, Burstein EA. Decomposition of protein tryptophan fluorescence spectra into log-normal components, III: correlation between fluorescence and micro environment parameters of individual tryptophan residues. Biophysics Journal 2001; 81:1735–1758.

118. Eftink MR. Fluorescence techniques for studying protein structure. Methods Biochemical Anal, 1990; 35:117–129.

119. Callis FR, Liu T. Quantitative prediction of fluorescence quantum yields for tryptophan in proteins. Journal of Physical chemistry B, 2004; 108:4248–4259.

120. Callis PR, Vivian JT. Understanding the variable fluorescence quantum yield of tryptophan in proteins using QM-MM simulations: quenching by charge transfer to the peptide backbone. *Chem Phys Lett*, 2003; 369:409–414.

121. Ababou A, Bombarda E. On the involvement of electron transfer reactions in the fluorescence decay kinetics heterogeneity of proteins. Protein Science 2001; 10: 2102–2113.

122. Adams PD, Chen Y, Ma K, Zagorski M, Sonnichsen FD, McLaughlin ML, Barkley MD. Intrmodelcular quenching of tryptophan fluorescence by the peptide bond in cyclic hexapeptides. Journal of American Chem Society, 2002; 124: 9278–9286.

123. Chen Y, Barkley MD. Toward understanding tryptophan fluorescence in proteins. Biochemistry, 1998; 37: 9976–9982.

124. Chen Y, Liu B, Yu H-T, Barkley MD. The peptide bond quenches indole fluorescence. Journal of American Chem. Society, 1996; 118: 9271–9278.

125. Mills, OE. Effect of temperature on tryptophan fluorescence of ß-Lactoglobulin B. *Biochimica et Biophysica Acta,* 1976; 434: 324–332.

126. Mills OE, Creamer LK. Biochim. Biophys. Acta, 1975; 379: 681–626.

127. Bakken EE, Heruth K. Temporal control of drugs, an engineering perspective. Ann. New York Acad. Sci., 1991; 618: 422–412.

128. Kost AJ, Langer R. Responsive polymeric delivery systems. Adv. Drug Delivery Revision, 1991; 6: 19–50.

129. Wu BM, Borland SW, Giordano RA, Cima LG, Sachs EM, Cima MJ. Solid free-form fabrication of drug delivery devices. J. Control Release, 1996; 40:77–87.

130. Katstra WE, Palazzolo RD, Rowe CW, Giritlioglu B, Teung P, Cima MJ. Oral dosage forms fabricated by Three Dimensional Printing. J Control Release, 2000; 66: 1–9.

131. Rowe CW, Katstra WE, Palazzolo RD, Giritlioglu B, Teung P, Cima MJ. Multimechanism oral dosage forms fabricated by three dimensional printing. J. Control Release, 2000; 66: 11–17.

132. Santoro N. Efficacy and safety of intravenous pulsatile gonadotropin-releasing hormone: Lutrepulse for injection. *Am J. Obstet. Gynecol*, 1990; 163: 1759–1764.

133. Creasy GW, Jaffe ME. Pulsatile delivery systems. *Ann. Ny Acad. Sci*, 1991; 618:548–557.

134. Creasy GW, Jaffe ME. Endocrine/reproductive pulsatile delivery systems. Adv. Drug Delivery Rev, 1991; 6: 51–56.

135. Sampath P, Brem H. Implantable slow-release chemotherapeutic polymers for the treatment of malignant brain tumors. Journal of the Moffitt Cancer, 1998; Center 5: 130–137.

136. Physician's Desk Reference (Ed,: R. Arky), Medical Economics Company, Montvale, NJ, USA, 1998; 2587–2589.

137. Physician's Desk Reference (Ed,: R. Arky), Medical Economics Company, Montvale, NJ, USA, 1998; 3139–3150.

138. Brown L, Langer R. Transdermal delivery of drugs. *Ann Rev. Med.*, 1988; 39: 221–229.

139. Siegel RA, Falamarzian M, Firestone BA, Moxley BC, pH-cobtrolled release from hydrophobic/polyelectrolyte copolymer hydrogels. J. Controlled Release, 1988; 8:179–182.

140. Kim JH, Kim JY, Lee YM, Kim KYJ. Controlled release of riboflavin and insulin through crosslinked poly (vinyl alcohol)/chitosan blend membrane. *Appl. Polym. Sci*., 1992; 44: 1923–1828.

141. Gutowska A, Bark JS, Kwon IC, Bae YH, Cha y, Kim SW. Squeezing hydrogels for controlled oral drug delivery. *J. Controlled Release*, 1997; 48: 141–148.

142. Bae YH, Okano T, Hsu R, Kim SW. Thermo-sensitive polymers as on-off switched for drug release. *Makromol. Chem. Rapid Commun.*, 1987; 8: 481–485.

143. Hoffman AS, Afrassiabi A, Dong LC. Thermally reversible hydrogels: II. Delivery and selective removal of substances from aqueous solutions. *J. Controlled Release*, 1986; 4: 213–222.

144. Okano T, Bae YH, Kim SW. Pulsed and Self-Regulated Drug Delivery, Ed.: J. Kost, CRC Press, Boca Raton, FL, USA 17–45, 1990.

145. Kost J, Lander R. Pulsed and Self-Regulated Drug Delivery, Ed.: J. Kost, CRC Press, Boca Raton, FL, USA 3–16, 1990.

146. Kost J, Leong K, Lander R. Ultrasound-enhanced polymer degradation and release of incorporated substances. *Proc. Natl. Acad. Sci.*,1989; 86: 7663–7666.

147. Fischel-Ghodsian F, Brown L, Mathiowitz E, Brandenburn D, Lander R. Enzymatically controlled drug delivery. *Proc. Natl. Acad. Sci.* 1988; 85: 2403–2406.

148. Mathiowitz E, Cohen MD. Polyamide microcapsules for controlled release vs. photochemical release. *J. Membr. Sci.,* 1989; 40: 67–86.

149. Kwon IC, Bae YH, Kim SW. Electrically erodible polymer gel for controlled release of drugs. *Nature*, 1991; 354: 291–293.

150. Bae YH, Kwon IC, Kim SW, in Polymeric Drugs and Drug Administration, Ed:, R. M. Ottenbrite, American Chemical Society, Washington, DC, USA, 98–110, 1994.

151. Milner LL. Electrochemically controlled release of drug ions from conducting polymers. *Mol. Cryst. Liq. Cryst.,* 1998; 160: 297–301.

152. Hepel M, Fijalek Z. in Polymetric Drugs and Drug Administration, Ed.: R.M. Ottenbrite, American Chemical Society, Washington, DC, USA, 79–97, 1994.

153. Schwendeman SF, Amidon GL, Levy RJ. Determinants of the modulated release of antiarrhythmic drugs by iontophoresis through polymer membranes. Macromolecules, 1993; 26: 2264–2272.

154. Edelman ER, Kost J, Bobeck H, Langer R. Regulation of drug release from polemer matrices by oscillating magnetic fields. *J. Biomed. Matter. Res.,* 1985; 19: 67–83.

155. Suzuki Y, Tanihara M, Nishimuru Y, Suzuki K, Kakimaru Y, Shimizu Y. A new drug delivery system with controlled release of antibiotic only in the presence of infection. *J. Appl. Biomat.,* 1998; 42:112–116.

156. Macular Photocoagulation Study Group Laser photocoagulation of subfoveal neovascular lesions of age-related macular degeneration. Updated findings from two clinical trials. Arch Ophthalmol, 1993; 111: 1200–1209.

157. Gragoudas ES, Adamis AP, Cunningham ET Jr, Feinsod M, Guyer DR. Pegaptanib for neovascular age-related macular degeneration. N Engl J Med, 2004; 351: 2805–2816.

158. D'Amico DJ, Masonson HN, Patel M et al. Pegaptanib sodium for neovascular age-related macular degeneration: two-year safety results of the two prospective. multicenter, controlled clinical trials. Ophthalmology, 2006; 113: 992–1001.

159. Geroski DH, Edelhauser HF, Invest. Ophthalmol. Vis. Sci., 2000**;** 41: 5.

160. Fraunfelder FT, JAMA, 1977; 237: 5 doi:10.1001/jama.237.5.446b

161. Fraunfelder FT, Ophthalmology, 1979; 86: 1.

162. Fraunfelder FT, Ophthalmology, 1980; 87: 2.

163. Fraunfelder FT, J. Am. Ophthalmol, 1990; 110: 4.

164. Stephenson RW. *Anatomy, Physiology and Optics of the Eye: A Textbook for Orthoptic Students*, Kimpton Publishers, 1973.

165. Nemeth SC. *Ocular Anatomy and Physiology*, Slack Incorporated Publishers, 2007.

166. Feng Y, Simpson TL. Corneal, limbal, and conjunctival epithelial thickness from optical coherence tomography. Optometry and Vision Science, 2008; 85(9): 880−883.

167. Hayreh SS. Segmental nature of the choroidal vasculature. British Journal of Ophthalmology, 1975; 59(11): 631−48.

168. Young AR, "Chromophores in human skin," Phys. Med. Biol., 1997; (42): 789−802.

169. Anderson J, Chiu D, Jackman R, Cherniavskaya O, McDonald J, Wu H, Whitesides S, and Whitesides G. Fabrication of Topologically Complex Three-Dimensional Microfluidic Systems in PDMS by Rapid Prototyping. Science, 1993; 261: 895.

170. McDonald J, Duffy D, Anderson J, Chiu D, Wu H, Schueller O, Whitesides G. Fabrication of microfluidic systems in poly (dimethylsiloxane). Electrophoresis, 2000; 21(1): 27–40.

171. http://www.microchem.com/products/su_eight.htm

172. Lo R, Li Po-Ying, Saati S., Agrawal RN, Humayun MS, Meng E. A passive MEMS drug delivery pump for treatment of ocular diseases. Biomed Microdevices, 2009; 11: 959–970.

173. Lo R, Kuwahara K, Li Po-Ying, Agrawal R, Humayun MS, Ellis Meng. A Passive Refillable Intraocular MEMS Drug Delivery Device. Proceedings of 2006 International Conference on Microtechnologies in Medicine and Biology Okinawa, Japan 9–12 May 2006.

174. Lavanya R, Teo L, Friedman DS, Aung HT, Baskaran M, Gao H, Alfred T, Seah SK, Kashiwagi K, Foster PJ, Aung T. Comparison of anterior chamber depth measurements using the IOLMaster, scanning peripheral anterior chamber depth analyser, and anterior segment optical coherence tomography. Journal of Ophthalmology, 2007; 91:1023–1026.

175. Gaudreault J, Fei D, Rusit J, Suboc P, Shiu V. Preclinical Pharmacokinetics of Ranibizumab (rhuFabV2) after a Single Intravitreal Administration. *Investigative Ophthalmology and Visual Science*, 2005; 46: 726–733.

176. McLaren JW, Brubaker RF. A Scanning Ocular Specfrofluorophotometer. Investigative Ophthalmology & Visual Science, 1988; 29(8).

177. Delori FC, Castany MA, Webb RH. Fluorescence characteristics of sodium fluorescein in plasma and whole blood. Exp Eye Res, 1978; 27:417.

178. The use of fluorescein in ophthalmological research. The Jonas S Friedenwald Memorial Lecture. Invest Ophthalmol, 1967; 6: 464–477.

179. Keijzer M, Jacques SL, Prahl SA, Welch AJ. Light distribution in artery tissue: Monte Carlo simulations for finite diameter laser beams. Lasers in Surgery and Medicine, 1989; 9: 148–154.

180. Jacques SL, Alter CA, Prahl SA. Angular dependence of HeNe laser light scattering by human dermis. Lasers Life Sci., 1987; 1: 309–333.

181. Maher EF. Transmission and absorption coefficients for the ocular media of the Rhesus monkey. SAM-TR-78-32, USAF School of Aerospace Medicine, 1978; 1–104.

182. Gardner CM, Jacques SL, Welch AJ. Fluorescence spectroscopy of tissue: recovery of intrinsic fluorescence from measured fluorescence. Applied Optics, 1996; 35(10): 1780–1792.

183. Keijzer M, Richard_Kortum R, Jacques SL, Feld MS. Fluorescence spectroscopy of turbid media: autofluorescence of the human aorta. Applied Optics, 1989; 28: 4286–4292.

184. McLaren JW, Brubaker RF. A Scanning Ocular Specfrofluorophotometer. Investigative Ophthalmology & Visual Science, 1988; 29(8).

185. Delori FC, Castany MA, Webb RH. Fluorescence characteristics of sodium fluorescein in plasma and whole blood. Exp Eye Res., 1978; 27:417–425.

186. Barsotti MF. The source of proteins in the aqueous humor in the eye. Doctoral thesis, Massachusetts Institute of Technology, 1990.

187. Romanchuk KG. Fluorescein. Physicochemical factors affecting its fluorescence. Diagnostic and surgical techniques, Survey of Ophthalmology, 1982; 26(5).

188. Mota MC, Carvalho P, Ramalho J, Leite E. Spectrophotometer analysis of sodium fluorescein aqueous solutions. Determination of molar absorption coefficient. International Ophthalmology, 1991; 15: 321–326.

189. Schwartz B, Feller MR. Temperature gradients in the rabbit eye, Investigative Ophthalmology, 1962; 1: 513.

190. Schwartz B. pH-temperature coefficient of rabbit anterior chamber aqueous humor. Division of Ophthalmology, Department of Surgery, State University of New York, Downstate Medical Center, Brooklyn, N. Y.

191. Lei B, Yao G. Spectral attenuation of the mouse, rat, pig, and human lenses from the wavelengths 360 nm to 1020 nm. Experimental Eye Research, 2006; 83: 610–614.

192. Brubaker RF. The flow of aqueous humor in the human eye.

193. Brubaker RF, Penniston JT, Grotte DA, et al. Measurement of fluorescein binding in human plasma using fluorescence polarization. Arch Ophthalmology, 1982; 100: 625–630.

194. Drezek R, Sokolov K, Utzinger U, Boiko I, Malpica A, Follen M, and Richards-Kortum R. J. Biomed. Opt., 2001; 6: 385–396.

195. Hung J, Lam S, LeRiche JC, Palcic B. Autofluorescnce of normal and malignant bronchial tissue. Lasers in Surgery and Medicine. 1991; 59: 930–933.

196. Holstein SV, Nilsson C, Andersson-Engels S, Willen R, Walther B, Svanberg K. Detection of adenocarcinoma in Barrett's oesophagus by means of laser induced fluorescence. Gut, 1996; 39: 711–716.

197. Huang Z, Zheng W, Xie S, Chen R, Zeng H, McLean DI, Lui H. Laser-induced autofluorescence microscopy of normal and tumor human colonic tissue. International Journal of Oncology, 2004; 24: 59–64.

198. McLaren JW, Brubaker RF. A scanning ocular spectrophotometer. Investigative ophthalmology and visual science, 1988; 29(8): 1284–1293.

199. Liu Q, Ramanujam N. Effect of fiber optic probe geometry on depth-resolved fluorescence measurements from epithelial tissues: a Monte Carlo simulation. Journal of Biomedical Optics, 2002; 27: 104–106.

200. Pfefer TJ, Schomacker KT, Ediger MN, Nishioka NS. Multiple-Fiber Probe Design for Fluorescence Spectroscopy in Tissue. Applied Optics, 2002; 41: 4712–4721.

201. Ghosh N, Majumder SK, Patel HS, Gupta PK. Depth-resolved fluorescence measurement in a layered turbid medium by polarized fluorescence spectroscopy Optics Letters, 2005; 30: 162–164.

202. Amelink A, Bard MPL, Burgers SA, and Sterenborg HJCM. Single-Scattering Spectroscopy for the Endoscopic Analysis of Particle Size in Superficial Layers of Turbid Media. Applied Optics, 2003; 42: 4095–4101.

203. Pfefer TJ, Matchette LS, Ross AM, Ediger MN. Selective detection of fluorophore layers in turbid media: the role of fiber-optic probe design. Optics. Letters, 2003; 28: 120–122.

204. Zhu CF, Liu Q, Ramanujam N. Sequential estimation of optical properties of a two-layered epithelial tissue model from depth-resolved ultraviolet-visible diffuse reflectance spectra. Journal of Biomedical Optics, 2003; 8: 237–247.

205. Utzinger U, Richards-Kortum R. Fiber optic probes for biomedical optical spectroscopy. Journal of Biomedical Optics, 2003; 8: 121–147.

206. Skala MC, Palmer GM, Zhu CF, Liu Q, Vrotsos KM, Marshek-Stone CL, Gendron-Fitzpatrick A, Ramanujam N. Investigation of fiber-optic probe designs for optical spectroscopic diagnosis of epithelial pre-cancers. Lasers in Surgery and Medicine, 2004; 34: 25–38.

207. Nieman L, Myakov A, Aaron J, Sokolov K. Compact beveled fiber optic probe design for enhanced depth discrimination in epithelial tissues. Applied Optics, 2004; 43: 1308–1319.

208. Q. Liu, and N. Ramanujam, *Opt. Letts*. 29, 2024–2026 (2004).

209. Schwarz RA, Arifler D, Chang SK, Pavlova I, Hussain IA, Mack V, Knight B, Richards-Kortum R, Gillenwater AM. Ball lens coupled fiber-optic probe for depth-resolved spectroscopy of epithelial tissue. Optics Letters, 2005; 30: 1159–1161.

VITA

Raiyan Tripti Zaman was born in Dhaka, Bangladesh, the youngest daughter of Amin-Uz-Zaman and Mahjuza Khanam. She ranked top 1% among 9 million students in the Higher Secondary Examination of Bangladesh. Raiyan published multiple poems and short stories in Bangladesh National Children Magazines during her stay in middle, junior, and high school. She was awarded second position out of 750 students in vocal music competition in Shisu Academy of Bangladesh. She was nominated for the National Merit Scholarship to study Pharmacy at the University of Punjab, Lahore, Pakistan. However, she enrolled as an undergraduate student at the University of Texas at Austin in Fall 1996. She received a Bachelor of Science degree in Electrical and Computer Engineering in 2000. During her undergraduate degree she was awarded as a College Scholar from the University of Texas at Austin. She also was nominated multiple times from the National Dean's List. She was a recipient of the President Scholarship and ECE Academic competitive Scholarship and became the life member of the National Society of Collegiate Scholar, the Golden Key National Honor's Society, and the National Society of Professional Engineers. Raiyan worked throughout her undergraduate study as an undergraduate research assistant with the Department of Electrical and Computer Engineering. After her graduation she started working as a Senior Applications Engineer for Semiconductor Product Sector of Motorola at Austin, Texas. During her stay at Motorola she received a BRAVO award for above and beyond performance. Raiyan started her graduate school in Fall of 2005 and completed the degree in Fall of 2006 and started her PhD under the supervision of Dr. Ashley J. Welch and Henry G. Rylander. During her PhD program she received Travel Grant Awards in four consecutive years from United State Air Force Academy for outstanding research paper in ASLMS conference, Research Excellence Award for best original research paper from Newport/Spectra Physics, Professional Development Award from the University of Texas at Austin, Travel Grant Award from Graduate Council for accepted paper in Laser and Elctro-optics conference. During her graduate program she was nominated twice from Chancellor's List for her academic excellence and had published her biography in Who's Who in America for outstanding achievement in her research filed and became a member of Magna Cum Laude Honor society. Raiyan has six journal and eight conference publications. She is currently finishing the requirements for the degree of Doctor of Philosophy in Engineering at the University of Texas at Austin.

Permanent Address: House 5, Road 11, Sector 4
Uttara Model Town,
Dhaka-1230, Bangladesh

This thesis was typed by the author.